



**HAL**  
open science

# Multi-scale study of tire-pavement interaction under rolling conditions based on the coupling of Finite element method and Discrete element method

Haitao Ge

► **To cite this version:**

Haitao Ge. Multi-scale study of tire-pavement interaction under rolling conditions based on the coupling of Finite element method and Discrete element method. Other. Université de Strasbourg, 2023. English. NNT: 2023STRAD004 . tel-04104716

**HAL Id: tel-04104716**

**<https://theses.hal.science/tel-04104716v1>**

Submitted on 24 May 2023

**HAL** is a multi-disciplinary open access archive for the deposit and dissemination of scientific research documents, whether they are published or not. The documents may come from teaching and research institutions in France or abroad, or from public or private research centers.

L'archive ouverte pluridisciplinaire **HAL**, est destinée au dépôt et à la diffusion de documents scientifiques de niveau recherche, publiés ou non, émanant des établissements d'enseignement et de recherche français ou étrangers, des laboratoires publics ou privés.

ÉCOLE DOCTORALE MSII (ED N°269)

laboratoire des sciences de l'Ingénieur, de l'Informatique  
et de l'Imagerie (ICUBE)-UMR 7357

**THÈSE** présentée par :

**Haitao GE**

soutenue le : 07 Mars 2023

pour obtenir le grade de : **Docteur de l'Université de Strasbourg**

Discipline / Spécialité : Mécanique / Génie Civil

**ÉTUDE MULTI-ÉCHELLE DE L'INTERACTION  
PNEU-CHAUSSÉE DANS DES CONDITIONS DE  
ROULEMENT BASÉE SUR LE COUPLAGE DE LA  
MÉTHODE DES ÉLÉMENTS FINIS ET DE LA  
MÉTHODE DES ÉLÉMENTS DISCRETS**

**THÈSE dirigée par :**

**M. CHAZALLON** Cyrille

Professeur, INSA de Strasbourg

**M. LE HOUEROU** Vincent

Professeur, Université de Strasbourg

**RAPPORTEURS :**

**M. HAMMOUM** Ferhat

Directeur de recherches, Université Gustave Eiffel

**M. RENOUF** Mathieu

Chargé de recherche (HDR), Université de Montpellier

---

**AUTRES MEMBRES DU JURY :**

**Mme. RAAB** Christiane

Professeur, EMPA de Zürich (Suisse)

**M. NELIAS** Daniel

Professeur, INSA Lyon

**M. QUEZADA** Juan Carlos

Maître de conférences, INSA de Strasbourg

**MEMBRE invité**

**M. SHIFERAW** Benjamin

Ingénieur de recherche et développement, Colas S.A.



UNIVERSITY OF STRASBOURG

**Multi-scale study of tire-pavement  
interaction under rolling conditions  
based on the coupling of Finite  
element method and Discrete element  
method**

by  
Haitao GE

A thesis submitted in partial fulfillment for the  
degree of Doctor of Philosophy

in the  
Doctoral School of MSII

March 2023



# *Acknowledgments*

As I near the completion of my Ph.D. dissertation, I am filled with a range of emotions as I reflect on the memories and experiences of the past three and a half years.

First and foremost, I extend my sincerest gratitude to my three supervisors for their invaluable guidance, unwavering support, and constant encouragement. Regarding my thesis supervisor, Prof. Cyrille CHAZALLON provided me with helpful advice in building a clear research framework for my thesis, and I am grateful to him for encouraging me to participate in many scientific communications, including international conferences. For my thesis co-supervisor, Prof. Vincent LE HOUREAU, I greatly admire his meticulous scientific attitude, and I would like to express my thanks to him for his valuable suggestions regarding hidden points in my research work that I had not noticed. I am deeply grateful to Associate Professor Juan Carlos QUEZADA GUAJARDO, my scientific co-supervisor, for his enlightening counsel and valuable contributions to my research, especially in numerical software use and development, throughout my Ph.D. study.

I also extend my great thanks to my office colleagues Léo COULON, Oussama HAMMOUD, Lei MA, Chong WANG, Xiang ZHANG, Victor DESLOGES, Marie FATAHIZADEH, and Renzhi WANG for the wonderful memories we shared together. I want to express special appreciation to my former colleagues Fujiao TANG, Anicet DANSOU, and Laura GAILLARD for all the unforgettable moments we shared at the beginning of my Ph.D. life. Additionally, I would like to thank my colleagues in the Group of Civil Engineering and Energy at INSA Strasbourg, Saïda MOUHOUBI, Georg Koval, Jian LIN, and Hossein NOWAMOOZ, for their hospitality and friendship during my Ph.D. study.

I would like to express my special appreciation to Mr. André MARC, with whom I frequently discussed after a day of work. Throughout my Ph.D. journey, he helped me practice my French a lot, and I learned a lot from him about French culture. We also shared many enjoyable times together.

I am also grateful to the China Scholarship Council (CSC), which provided

me with a full scholarship for three and a half years, guaranteeing the smooth completion of my thesis.

Lastly, I am deeply grateful to my family for their unwavering support and encouragement throughout my study.

In my future academic pursuits, I will continue to be guided by the principle of seeking truth from facts and strive to pursue further valuable scientific research.

# Résumé étendu

## Étude multi-échelle de l'interaction pneu-chaussée en conditions de roulement basée sur le couplage de la méthode des éléments finis et de la méthode des éléments discrets

Doctorant : Haitao GE

Directeur de Thèse : Cyrille CHAZALLON

Co-directeur de Thèse : Vincent LE HOUEROU

Encadrant scientifique : Juan Carlos QUEZADA

Université de Strasbourg, INSA de Strasbourg, CNRS, ICube, UMR 7357, F-67000 Strasbourg France

## Contexte

Alors que le trafic augmente à pas de géant, la détérioration des couches de surface d'enrobé apparaît comme la première cause des coûts du réseau routier. Une compréhension approfondie de l'interaction pneu-chaussée est essentielle pour optimiser la conception de la surface des chaussées en béton bitumineux dans le contexte d'infrastructure vieillissante et de ressources d'entretien limitées. Pour faire face aux difficultés découlant de la complexité et de l'inadéquation des méthodes expérimentales dans l'examen de l'interaction pneu-chaussée, les approches numériques telles que la méthode des éléments finis (FEM) et la méthode des éléments discrets (DEM) sont apparues comme un moyen prometteur et efficace de mieux comprendre les performances des enrobés bitumineux au cours des dernières décennies.

La plupart des études actuelles sur l'interaction entre le pneu et la chaussée ont été menées dans le cadre de la mécanique des milieux continus à l'aide de la méthode des éléments finis, qui présente des limites dans la modélisation de la nature discontinue des mélanges bitumineux. La DEM offre un moyen prometteur d'analyser les propriétés mécaniques des enrobés bitumineux à l'échelle des particules, mais elle n'est pas adaptée pour modéliser la structure déformable des pneus et déterminer les forces de contact réalistes des pneus



sur la surface de la chaussée. Ce travail de thèse est consacré à l'étude du système d'interaction entre le pneu et la chaussée sur la base de simulations numériques. Deux méthodes numériques principales, FEM et DEM, sont utilisées pour modéliser ce système à plusieurs échelles, de manière différente.

## Objectifs de la thèse

Pour simuler un système dynamique d'interaction mutuelle comprenant un pneu et un enrobé au niveau micro-structural, trois problèmes doivent être résolus principalement: Tout d'abord, rechercher une représentation réaliste de la charge du pneu; Deuxièmement, modéliser un enrobé en considérant explicitement les caractéristiques de ses différents composants (granulats irréguliers, liant bitumineux, etc.); Enfin, appliquer la charge du pneu roulant à la structure du mélange en couplant les deux modèles ci-dessus.

Cette thèse se consacre à l'étude du système d'interaction pneu-chaussée à partir de simulations numériques. Deux méthodes numériques principales, FEM et DEM, sont utilisées pour modéliser ce système à partir de multi-échelles, différemment. Enfin, des simulations de couplage FEM-DEM sont présentées pour étudier les réponses du mélange d'enrobé au niveau des particules, ce qui remplit l'objectif d'enquêtes multi-échelles sur les mécanismes d'interaction pneu-chaussée.

## Plan du Mémoire

Ce travail de thèse est divisée en sept chapitres. Le premier chapitre présente les objectifs, la portée de l'étude et les grandes lignes de la thèse. Le deuxième chapitre donne un aperçu des recherches précédentes sur l'analyse mécanique des réponses de la chaussée, l'interaction pneu-chaussée, la modélisation des mélanges bitumineux et les théories de simulation multi-échelles. En utilisant la théorie de la mécanique des milieux continus, le troisième chapitre décrit le couplage pneu-capteur-chaussée développé qui intègre les charges de roulement réelles des pneus dans la modélisation de la couche de béton bitumineux et analyse la réponse dynamique de cette couche sous diverses charges de roulement des pneus. Basé sur la méthode de la dynamique des contacts, le quatrième chapitre présente le modèle DEM développé pour les mélanges bitumineux, qui intègre une morphologie réaliste des agrégats et des

distributions granulométriques. Le cinquième chapitre présente un modèle de pneu développé utilisant la technique de scan laser 3D et FEM et propose en outre une simulation multi-échelle pour examiner les mécanismes d'interaction pneu-chaussée en incorporant les approches FEM et DEM. Le sixième chapitre développe un cadre de couplage FEM-DEM avancé pour analyser les réponses des mélanges bitumineux sous des charges de roulement de pneus d'un point de vue micro-mécanique, de manière cohérente, à l'échelle des particules. Le dernier chapitre résume les résultats et les conclusions de cette étude et discute des perspectives futures potentielles.

## Contraintes de contact entre le pneu et la chaussée

Des mesures expérimentales et une modélisation numérique des pneus ont été utilisées pour obtenir les contraintes de contact des pneus sur les surfaces des chaussées en béton bitumineux dans cette étude, comme indiqué au chapitre 3. Les principales conclusions sont présentées ci-dessous.

### Mesures expérimentales

Pour mesurer les contraintes de contact des pneus sur les surfaces de la chaussée, le système Tekscan a été utilisé. Il a été démontré que les contraintes de contact entre le pneu et la chaussée ne sont pas uniformes sur toute la surface de contact, et que la charge et la pression de gonflage du pneu affectent les valeurs des contraintes de contact et la surface de contact (Figure 1).

Par rapport à la pression de gonflage du pneu testé, les valeurs maximales de la contrainte de contact du pneu sont beaucoup plus élevées et concentrées au centre de l'empreinte du pneu. En outre, à mesure que les charges du pneu augmentent, la zone de contact passe d'une concentration centrale à un aplatissement latéral, tandis que la valeur maximale de la contrainte de contact augmente légèrement pour deux pressions de gonflage du pneu. En revanche, l'augmentation des pressions de gonflage des pneus accroît considérablement les contraintes de contact entre le pneu et la chaussée. Par rapport à la charge du pneu, la pression de gonflage semble avoir un impact plus significatif sur la distribution des contraintes de contact pneu-chaussée.

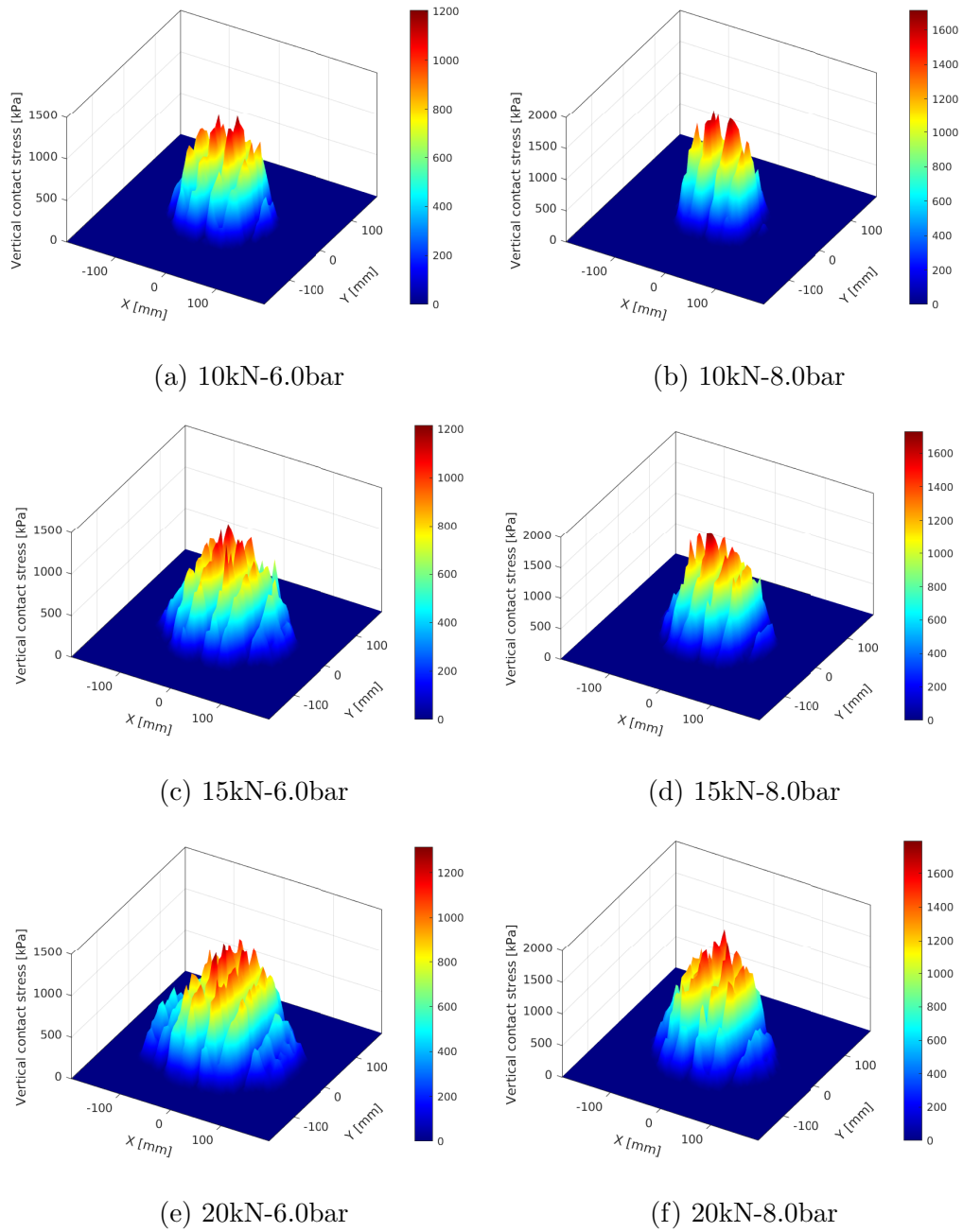


Figure 1: Distributions des contraintes de contact des pneus sous différentes charges et pressions de gonflage

## Modélisation numérique des pneus

En raison de la limitation des capteurs expérimentaux dans la mesure des contraintes de contact tangentielles des pneus sur la surface de la chaussée, une stratégie de modélisation numérique des pneus et sa calibration ont été développées afin d'obtenir les contraintes de contact pneu-chaussée, au chapitre 5.

Des techniques de scan laser 3D et de traitement d'image ont été utilisées pour reconstruire la géométrie du pneu. En utilisant la FEM, la structure du pneu a été construite sur la base de sa forme, et les paramètres pertinents ont été déterminés par des essais expérimentaux de compression. Compte tenu de ses performances et de sa stabilité numérique dans les simulations de systèmes non linéaires, la méthode de dynamique des contacts (CD) est utilisée pour résoudre les conditions de contact entre le pneu et la chaussée par le biais d'une formulation de contact implicite.

Dans des conditions de roulement libre et de freinage roue bloquée, le pneu induit trois composantes de contraintes de contact (verticale, transversale, longitudinale) et tous les types de contraintes de contact ne sont pas uniformes sur toute la surface de contact (Figures 2 et 3). La contrainte de contact verticale est beaucoup plus importante que les deux autres contraintes de contact tangentielles, que ce soit en roulement libre ou en freinage roue bloquée. En outre, en cas de freinage total, la contrainte de contact tangentielle sur la surface de la chaussée est beaucoup plus élevée qu'en cas de roulement libre.

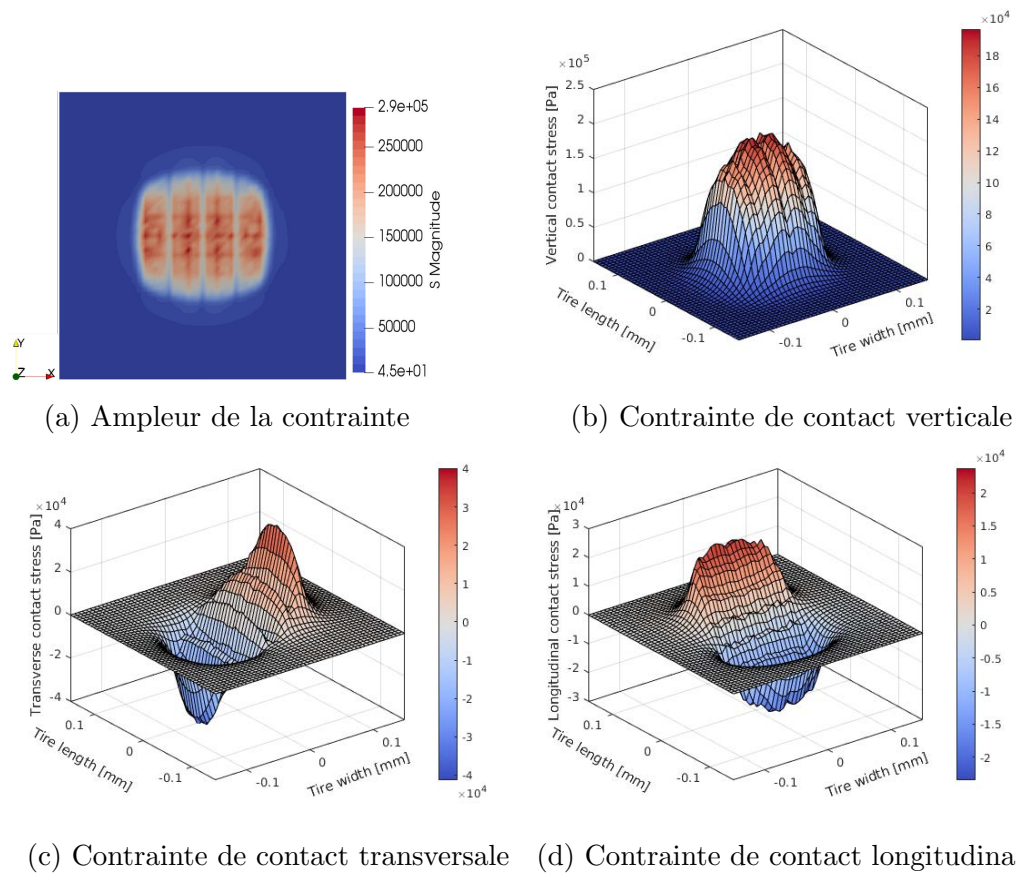


Figure 2: Contour de la distribution des contraintes de contact sous chargement de roulement libre

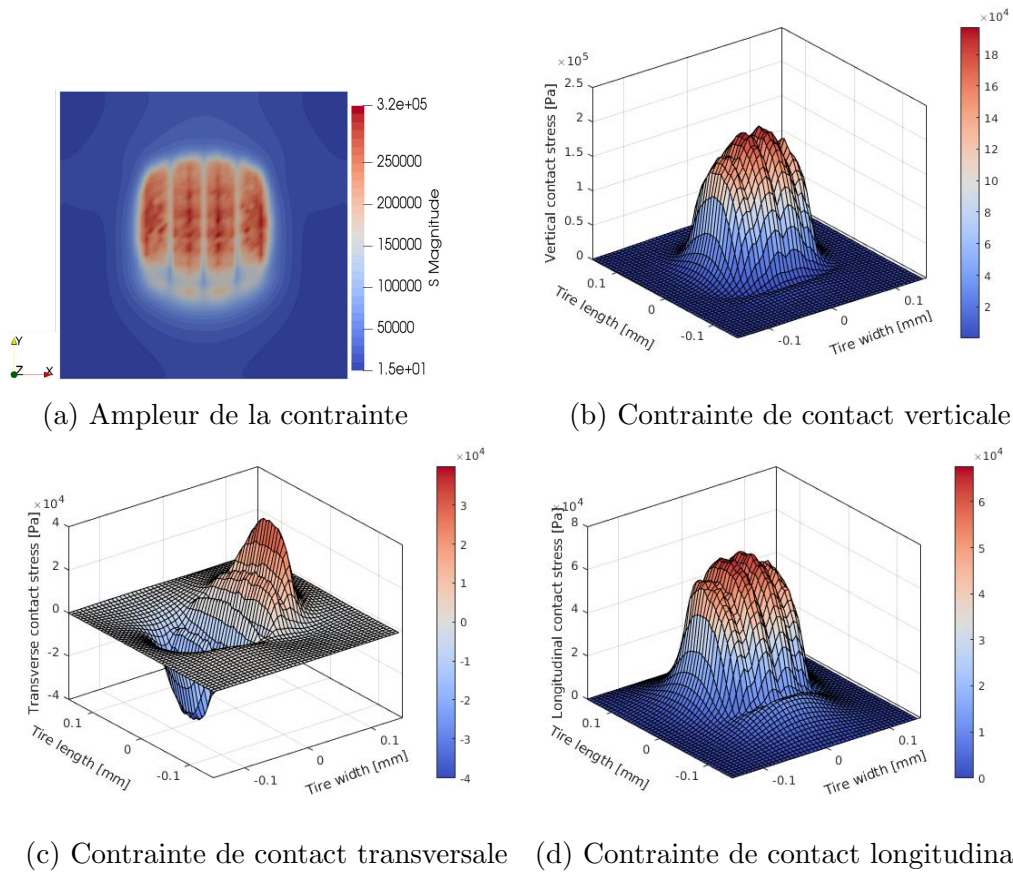


Figure 3: Contour de la distribution des contraintes de contact au freinage roue bloquée

## Modélisation des mélanges bitumineux

### Modèle FEM du mélange bitumineux

Le cadre de la mécanique des milieux continus a été utilisé pour effectuer des simulations macroscopiques des mélanges d'enrobés bitumineux, compte tenu du coût de calcul des simulations de chaussées en enrobés bitumineux, comme cela a été présenté dans le chapitre 3.

Dans les simulations numériques par éléments finis, le modèle VENO<sub>L</sub> (NON-Linear ViscoElastic) a été mis en œuvre pour caractériser les propriétés du mélange bitumineux en fonction de la fréquence, de l'amplitude de déformation et de la température.

D'après les résultats de la simulation numérique, ce modèle est capable de décrire avec précision les propriétés viscoélastiques du mélange bitumineux sous des températures et des fréquences variées pendant l'essai de module complexe, comme le démontrent les mesures du module complexe 2PB (Figure 4).

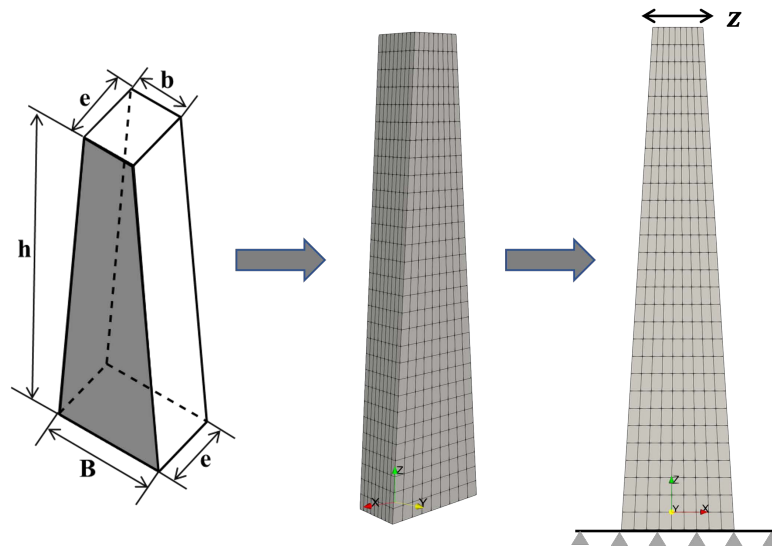


Figure 4: Essai numérique 2PB basé sur FEM

## Modèle DEM du mélange bitumineux

Comme décrit au chapitre 4, en raison de la structure hétérogène des mélanges bitumineux, la DEM a été adoptée pour décrire les réponses internes du mélange bitumineux à partir d'un niveau microscopique, de manière cohérente, au niveau des particules.

Une analyse statistique des caractéristiques morphologiques des agrégats a été réalisée à l'aide du scan laser 3D et du traitement d'image. Les résultats montrent que le coefficient d'allongement, d'aplatissement et la valeur de sphéricité des agrégats suivent tous des distributions normales.

Les échantillons de mélange d'enrobé ont été générés par une méthode de pavage de Voronoï en 3D, basée sur les statistiques de morphologie des particules, notamment le rapport d'aspect moyen et la valeur moyenne et l'écart type de la sphéricité.

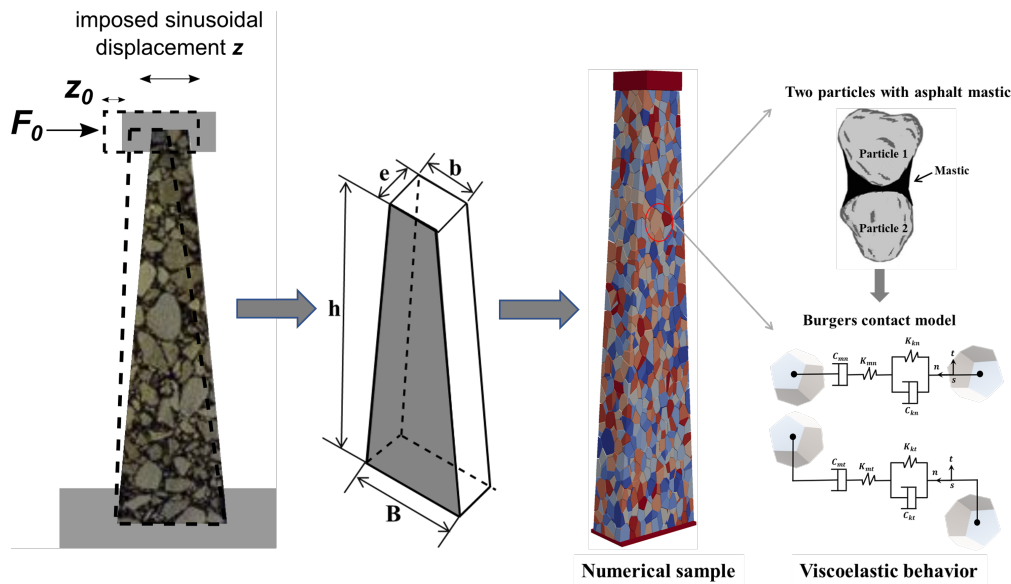


Figure 5: Montage de l'essai 2PB et modélisation numérique de l'échantillon

La méthode de la dynamique des contacts (CD) est introduite pour modéliser les mélanges bitumineux, car sa formulation permet de simuler des particules polyédriques réguliers et irréguliers. Le modèle de contact de Burgers est adopté pour rendre compte du comportement viscoélastique des mélanges bitumineux. Pour valider la précision du modèle, des essais expérimentaux et numériques du module complexe dans une configuration 2PB ont été réalisés



à différentes températures et fréquences (Figure 5). Les résultats ont montré un bon accord entre les courbes maîtresses numériques correspondantes et les résultats expérimentaux pour la norme du module complexe et l'angle de phase.

Après l'analyse microscopique, la force tangentielle et la force normale entre les particules semblent augmenter avec la diminution de la température et l'augmentation de la fréquence de chargement. En outre, la comparaison de la force tangentielle et de la force normale entre les particules pendant le chargement cyclique pourrait donner un aperçu du mécanisme d'initiation de l'endommagement pour les mélanges bitumineux.

## Réponses des mélanges bitumineux sous la charge des pneus

### Couplage pneu-capteur-chaussée

Pour l'analyse des réponses macroscopiques des enrobés bitumineux, un couplage pneu-capteur-chaussée a été proposé sur la base de la théorie de la mécanique des milieux continus, au chapitre 4. La réponse des couches de béton bitumineux à des conditions de travail variables, notamment la vitesse de roulement du pneu, la charge du pneu, la pression de gonflage et la température de l'environnement externe, a été examinée. La Figure 6 illustre le processus de chargement du pneu roulant sur la couche de béton bitumineux. D'après les résultats, le déplacement résiduel de la surface de la couche de béton bitumineux augmente avec la charge du pneu et la diminution de la vitesse du pneu, respectivement. En raison de leurs contributions opposées au déplacement résiduel, la charge du pneu et la surface de contact doivent être évaluées simultanément pour les effets de la pression de gonflage du pneu. Une augmentation significative du déplacement résiduel est observée à des températures élevées (lorsque la température dépasse 20 °C) pour les effets de la température sur les réponses de la couche de béton bitumineux. La zone d'influence du champ de distribution du déplacement résiduel augmente à mesure que la température augmente, surtout à des températures élevées.

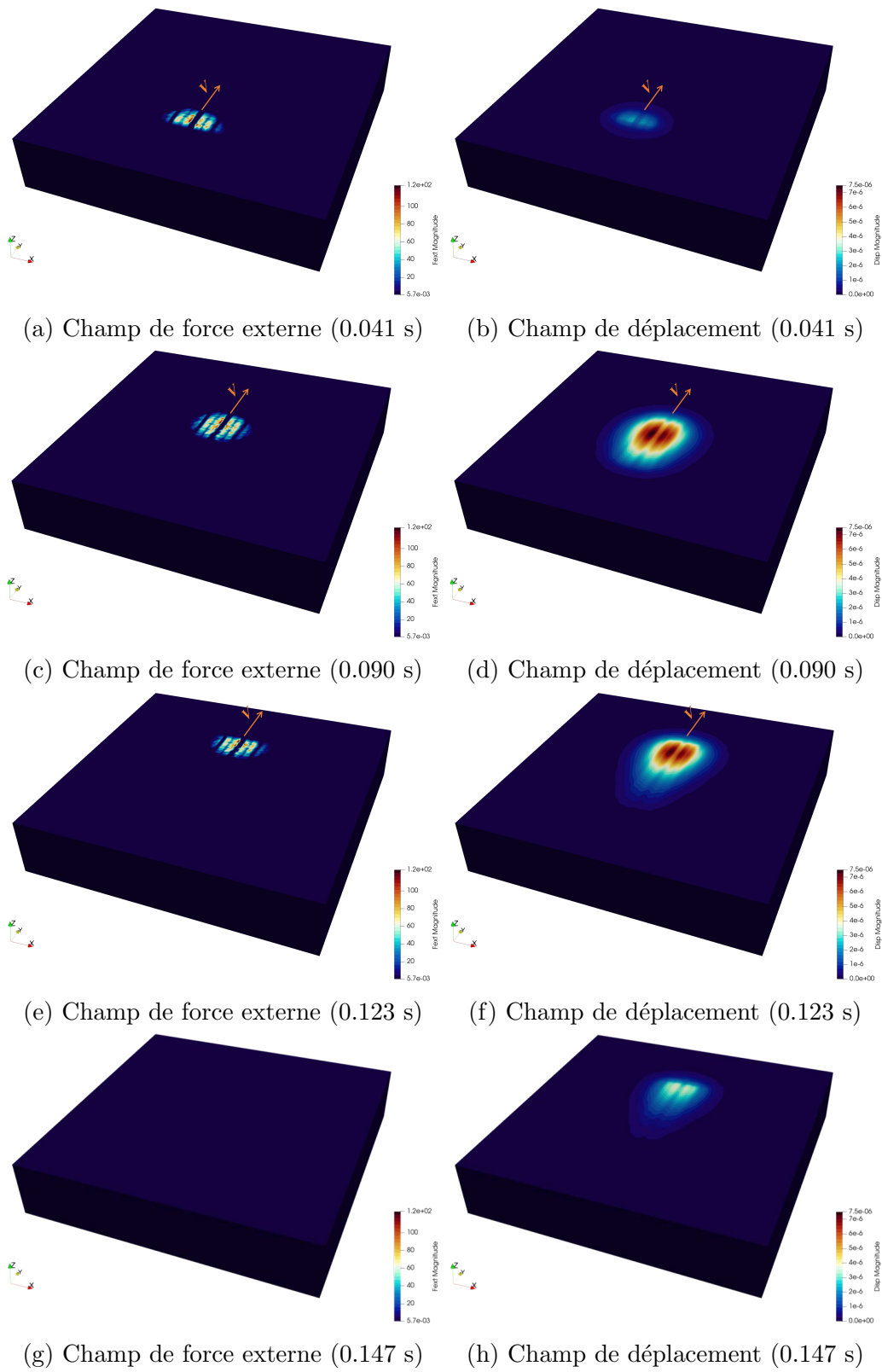


Figure 6: Processus de roulement des pneus sur la couche de béton bitumineux pour  $V=20$  km/h

## Du macro au micro : Le couplage FEM-DEM

### Simulation sous charges quasi-statiques des pneus

Au chapitre 5, nous avons proposé une stratégie de couplage de base pour analyser les réponses des mélanges bitumineux sous des charges quasi-statiques non uniformes de pneus. En construisant une série d'éléments de nervure sur la surface de la couche de béton bitumineux DEM, les contraintes de contact du pneu obtenues des simulations FEM pourraient être appliquées sur cette dernière comme un champ de force. En ajustant le nombre et la taille des éléments dans chaque élément de nervure, la forme exacte de la surface de contact du pneu à un niveau de charge donné peut être considérée.

Les résultats de la simulation montrent que dans des conditions de freinage total, les particules à l'intérieur du mélange bitumineux ont tendance à s'écouler dans la direction longitudinale et à tourner vers l'avant, ce qui entraîne une instabilité structurelle.

La distribution des valeurs de la force tangentielle en cas de freinage total est plus élevée que celle en cas de roulement libre, selon l'analyse de la force de contact des particules. Les résultats indiquent que dans des conditions de freinage total, les particules du mélange subissent un cisaillement plus important que dans des conditions de roulement libre, ce qui entraîne probablement une initiation plus précoce de l'endommagement.

L'effet de l'état de roulement des pneus sur le comportement des enrobés bitumineux a été vérifié dans une étude montrant que la force de contact des particules en cas de freinage roue bloquée est plus élevée qu'en cas de roulement libre.

Au niveau du plan de contact, le freinage total provoque un cisaillement important, ce qui peut conduire à un endommagement précoce. D'après la distribution du déplacement des particules, celles-ci ont tendance à s'écouler et à tourner dans la direction longitudinale en cas de freinage total, ce qui entraîne des perturbations structurelles.

### Simulation sous charges roulants

Au chapitre 6, une méthode avancée de couplage FEM-DEM est développée pour étudier les réponses des mélanges bitumineux au niveau des particules sous charges réelles de pneus roulants (Figure 7). Le noyau du couplage

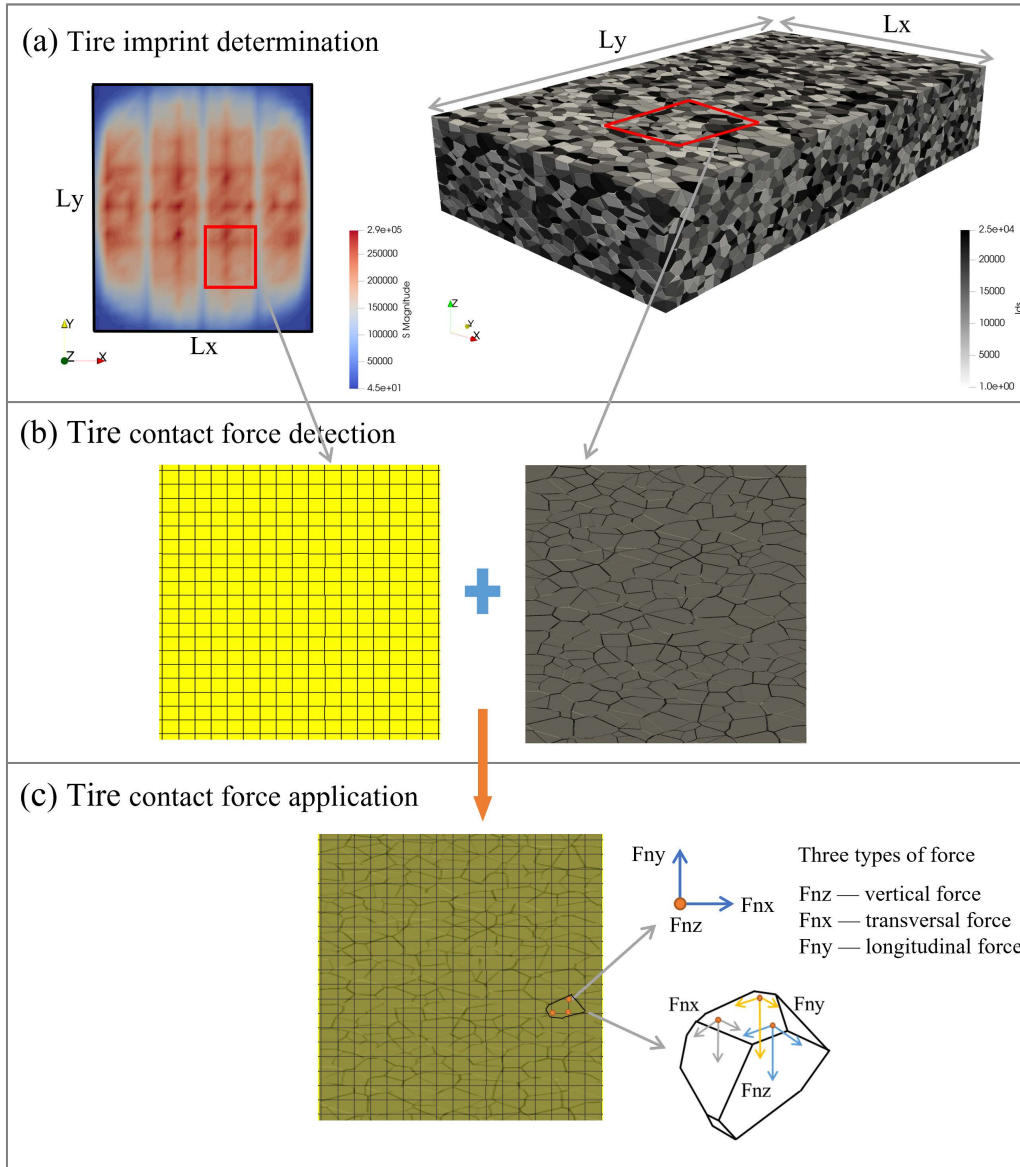
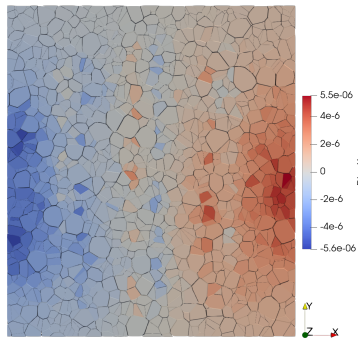


Figure 7: Simulation du couplage FEM-DEM : (a) détermination de l'empreinte du pneu (b) détection de la force de contact (c) application de la force de contact

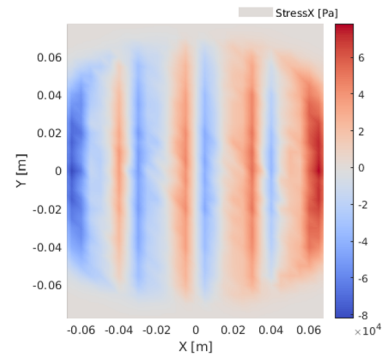
FEM-DEM consiste à détecter les particules correspondantes sur la couche de béton bitumineux, qui sont en contact avec les nœuds de l'aire de contact pneu-chaussée. À cette fin, la détection des contacts entre les particules et les nœuds du maillage est effectuée à deux niveaux. Tout d'abord, une détection grossière est effectuée à l'aide de l'algorithme *bounding box* afin d'identifier les particules dans le voisinage d'une zone maillée de référence. Lorsqu'un nœud de maillage se trouve à l'intérieur de la *bounding box*, une détection plus fine est effectuée à l'aide de la méthode du produit vectoriel afin de déterminer quelle surface de la particule est en contact direct avec le point nodal de la force de contact du pneu. Une fois les forces nodales de contact du pneu composées de trois éléments appliquées aux particules sur la surface de la couche d'enrobé bitumineux, la simulation du couplage a été réalisée à l'aide de calculs par itération temporelle.

L'efficacité de la méthode de couplage est validée en combinant l'analyse des distributions de déplacement des particules et des contraintes de contact pneu-chaussée dans trois directions (transversale, longitudinale et verticale), comme indiqué dans la Figure 8. Pendant le roulement du pneu sur la surface de la couche d'enrobé, le réseau de force des particules évolue de manière cohérente (Figure 9), ce qui montre l'efficacité des simulations de couplage.

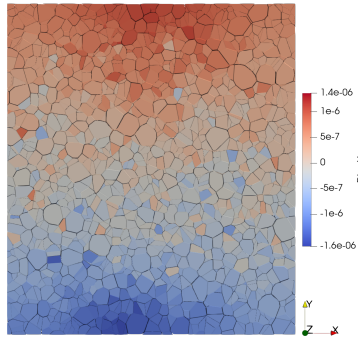
Il a été prouvé qu'une faible vitesse du pneu entraîne un important déplacement résiduel des particules, ce qui conduirait éventuellement à une déformation permanente et irrémédiable du mélange bitumineux. Des résultats similaires à ceux des simulations quasi-statiques mentionnées précédemment ont été observés lors de l'évaluation de l'effet de l'état de roulement des pneus sur le comportement du mélange bitumineux par l'analyse de la force de contact des particules (Figure 10). Au niveau du plan de contact, le freinage roue bloquée provoque une quantité significative de cisaillement, ce qui peut conduire à une initiation précoce de l'endommagement. Les particules ont tendance à s'écouler et à tourner dans la direction longitudinale lors d'un freinage roue bloquée, ce qui pourrait entraîner des perturbations structurelles. En outre, les particules soumises à un freinage roue bloquée ont tendance à avoir une composante de déplacement importante dans le sens longitudinal en raison des forces à la limite du pneu, ce qui pourrait entraîner une déformation permanente importante.



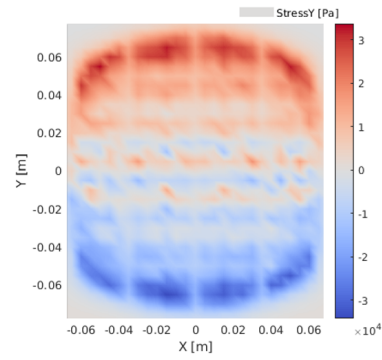
(a) Direction X



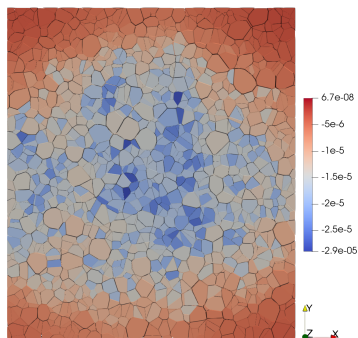
(b) Contrainte transversale



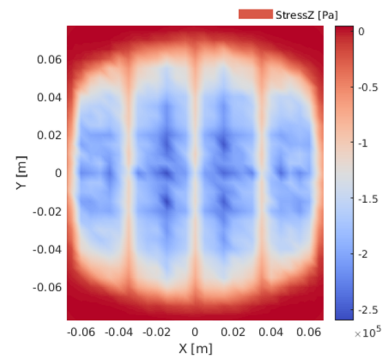
(c) Direction Y



(d) Contrainte longitudinale



(e) Direction Z



(f) Contrainte verticale

Figure 8: Comparaisons entre les distributions des déplacements de particules (à gauche) et les distributions des contraintes de contact pneu-chaussée (à droite) dans trois directions.

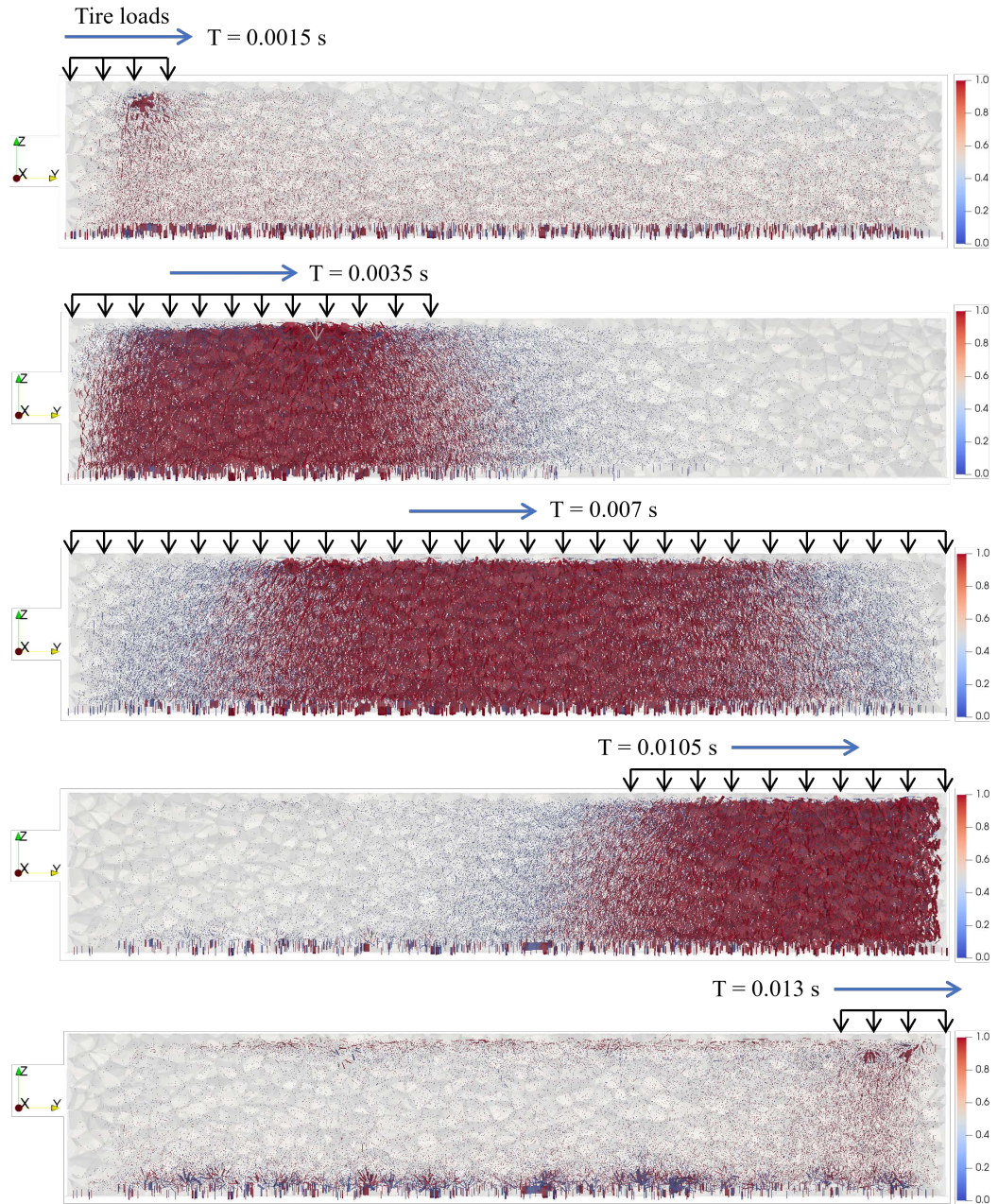


Figure 9: Évolution du réseau de forces de contact (force forte = 1.0 et force faible = 0.0) à une vitesse de roulement de 30 m/s.

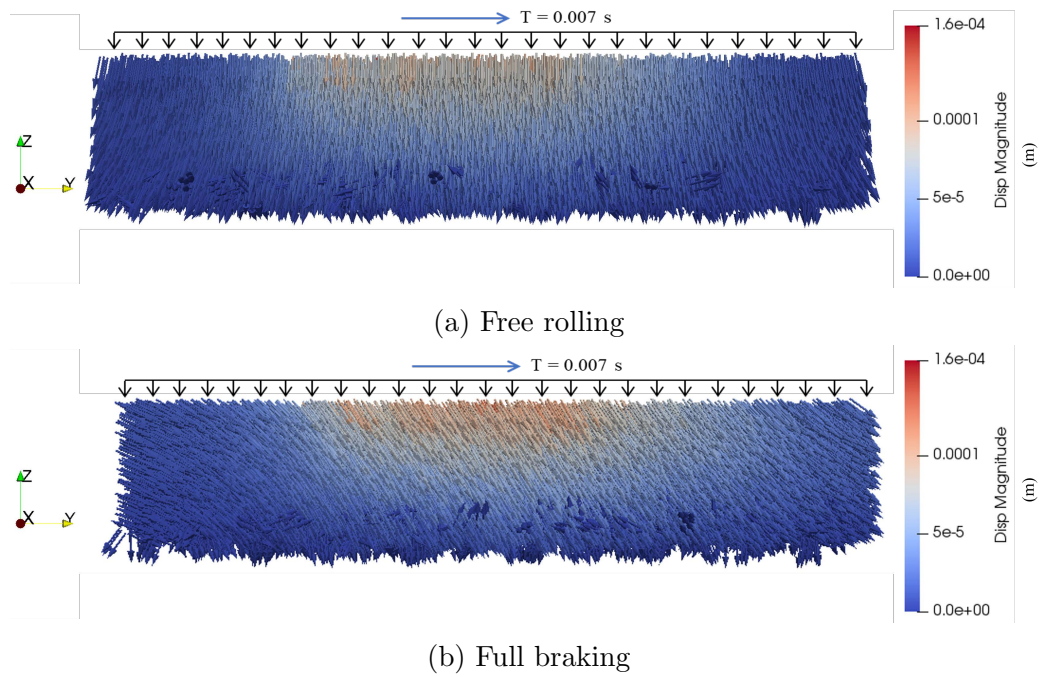


Figure 10: Distribution du déplacement des particules à 30 m/s pour différents états de roulement ( $T = 0.007 \text{ s}$ )



## Conclusions et perspectives

Cette étude est consacrée à la modélisation des mécanismes d'interaction pneu-chaussée à partir de plusieurs échelles d'observation. Les principales conclusions sont résumées ci-dessous :

Il existe deux façons d'obtenir les contraintes de contact entre le pneu et la chaussée : les mesures par capteurs et les modèles numériques. La méthode de modélisation numérique est plus souhaitable car elle permet de saisir les contraintes de contact pneu-chaussée dans les directions tangentielles.

Pour la modélisation des mélanges bitumineux, les méthodes FEM et DEM peuvent être utilisées pour des simulations à l'échelle macro et micro, respectivement. Dans la modélisation FEM, les mélanges bitumineux sont généralement supposés être homogènes et des lois constitutives complexes sont généralement requises. Le modèle NOnLinear ViscoElastic (VENoL) a été mis en œuvre avec succès dans les simulations numériques, et la précision a été atteinte dans la prédiction des propriétés des mélanges bitumineux en fonction de la fréquence et de la température.

Pour caractériser les structures hétérogènes des mélanges bitumineux, la méthode de modélisation DEM présentée dans cette étude fournit une base pour la simulation de haute précision des mélanges bitumineux contenant plusieurs phases, y compris les particules irrégulières et le mastic d'enrobé. Dans la simulation numérique, la morphologie et la distribution des tailles des agrégats sont incorporées dans la structure du mélange bitumineux. En outre, il réduit considérablement le coût de calcul de la préparation d'échantillons polyédriques en utilisant des techniques de pavage 3D. Elle peut être considérée comme une alternative intéressante aux méthodes de modélisation classiques dans les simulations de mélanges bitumineux.

Pour étudier les réponses des enrobés bitumineux sous la charge des pneus, il existe deux stratégies principales qui conviennent à des échelles et des objectifs différents. À l'échelle macroscopique, le couplage pneu-capteur-chaussée peut être appliqué pour étudier les processus d'interaction pneu-chaussée ainsi que la réponse du revêtement d'enrobé à différentes charges de pneus et conditions environnementales. À l'échelle microscopique, pour les parties qui nous intéressent (par exemple, la zone de contact pneu-chaussée) dans une macro-structure de chaussée, la stratégie de couplage FEM-DEM

proposée peut être utilisée pour effectuer la simulation de l'interaction pneu-chaussée. La méthode de couplage incorpore les avantages de la FEM pour simuler précisément les contraintes de contact sur la surface de la chaussée en béton bitumineux et de la DEM pour examiner les réponses internes du mélange à l'échelle des particules.

La présente étude fournit une méthode de simulation multi-échelle intégrant les méthodes FEM et DEM pour analyser les mécanismes d'interaction entre le pneu et la chaussée sous charges de roulement réalistes, ce qui offre un moyen prometteur de comprendre la détérioration de la surface de la chaussée et d'optimiser la conception des couches de surface.

En perspectives, un certain nombre de points reste à traiter :

- Modélisation d'un plus grand nombre de types de pneus, y compris diverses structures et bandes de roulement, afin de créer une base de données sur les contraintes de contact entre le pneu et la chaussée.
- Développer une base de données complète des réponses des chaussées en fonction de diverses conditions de chargement des pneus, des conditions environnementales et des caractéristiques des mélanges bitumineux, y compris les propriétés des composants internes.
- Poursuivre l'analyse de l'endommagement à l'échelle des particules et le relier aux prévisions macroscopiques de performance des chaussées.

## Publications principales

1. Ge, H., Quezada, J. C., Le Houerou, V., Chazallon, C. (2021). Three-dimensional simulation of asphalt mixture incorporating aggregate size and morphology distribution based on contact dynamics method. *Construction and Building Materials*, 302, 124124
2. Ge, H., Quezada, J. C., Le Houerou, V., Chazallon, C. (2022). Multiscale analysis of tire and asphalt pavement interaction via coupling FEM–DEM simulation. *Engineering Structures*, 256, 113925.
3. Ge, H., Quezada, J. C., Chazallon, C., Le Houerou, V. (2022). Modeling of asphalt mixture based on aggregate morphology distribution using the contact dynamics method. In *Eleventh International Conference on the*

Bearing Capacity of Roads, Railways and Airfields, Volume 2 (pp. 467-476). CRC Press.

4. Ge H, Quezada J C, Chazallon C, Le Houerou V, Investigation of Tire-pavement Interaction Based on Non-smooth Contact Dynamics Method[C]//7th World Tribology Congress, 2022, at Lyon in France, <https://www.wtc-2022.org>.
5. Ge, H., Quezada, J. C., Le Houerou, V., Chazallon, C. (2023). Three-Dimensional FEM-DEM Coupling Simulation for Analysis of Asphalt Mixture Responses Under Rolling Tire Loads[J]. Construction and Building Materials, 369, 130615.
6. Ge, H., Quezada, J. C., Le Houerou, V., Chazallon, C., Horny, P. (2023). A new tire-sensor-pavement coupling chain for investigating asphalt mixture responses under rolling tire loads. Road Materials and Pavement Design, 1-18.
7. Ge, H., Quezada, J. C., Le Houerou, V., Chazallon, C. (2023). From macro to micro: Asphalt mixture responses under realistic tire loads using FEM-DEM coupling [C]// 13th International Conference on Road and Airfield Pavement Technology, Accepted.

## **Prix**

1. Prix du meilleur poster: 7th World Tribology Congress, 2022.

# Contents

<b>Acknowledgments</b>	<b>i</b>
<b>Résumé étendu</b>	<b>iii</b>
<b>List of Figures</b>	<b>xxix</b>
<b>List of Tables</b>	<b>xxxvi</b>
<b>1 Introduction</b>	<b>1</b>
1.1 General background and motivation . . . . .	1
1.2 Objectives and scope . . . . .	2
1.3 Thesis outline . . . . .	3
<b>2 Literature review</b>	<b>5</b>
2.1 Traffic loads in asphalt pavement design . . . . .	6
2.2 Examination of tire loads on pavements . . . . .	7
2.2.1 Experimental measurements . . . . .	8
2.2.2 Numerical tire modeling . . . . .	8
2.3 Research methods for asphalt mixtures . . . . .	12
2.3.1 Experimental approaches . . . . .	12
2.3.2 Rheological models . . . . .	15
2.3.3 Finite element modeling of asphalt mixtures . . . . .	16
2.3.4 Discrete element modeling of asphalt mixture . . . . .	18
2.4 Asphalt mixture responses under tire loads . . . . .	29
2.4.1 Accelerated pavement testing analysis . . . . .	29

---

2.4.2	Analytical modeling analysis . . . . .	32
2.4.3	Finite element modeling analysis . . . . .	32
2.4.4	Discrete element modeling analysis . . . . .	34
2.5	Multi-scale coupling simulation . . . . .	37
2.6	Conclusions of the chapter . . . . .	40
<b>3</b>	<b>Tire-sensor-pavement coupling chain based on FEM</b>	<b>43</b>
3.1	Introduction . . . . .	44
3.2	Laboratory tests . . . . .	45
3.2.1	Tire contact stress distributions on the pavement surface	45
3.2.2	Asphalt mixture complex modulus test . . . . .	46
3.3	Asphalt mixture modeling and material characterization . . .	51
3.3.1	Viscoelastic material characterization for asphalt mixture	51
3.3.2	Validation of the VENO <sub>L</sub> model . . . . .	53
3.4	Coupling chain for the tire-sensor-pavement system . . . . .	56
3.4.1	Numerical asphalt layer building and coupling algorithm	56
3.4.2	Asphalt layer property identification under rolling tire loads . . . . .	57
3.4.3	Dynamic simulation of asphalt layer responses under rolling tire loads . . . . .	60
3.5	Asphalt layer responses under varied loading conditions . . . .	64
3.5.1	Dynamic responses of asphalt layer under different tire rolling velocity . . . . .	64
3.5.2	Dynamic responses of asphalt layer under different tire loads . . . . .	65
3.5.3	Dynamic responses of asphalt layer under different tire inflation pressures . . . . .	68

---

3.5.4	Dynamic responses of asphalt layer at different temperatures . . . . .	70
3.6	Conclusions of the chapter . . . . .	74
<b>4</b>	<b>Asphalt mixture modeling based on Contact Dynamics method</b>	<b>77</b>
4.1	Introduction . . . . .	78
4.2	Contact modeling theory . . . . .	79
4.3	Morphology distribution of aggregate particles . . . . .	82
4.3.1	Three-dimensional laser scanning of aggregate particles	82
4.3.2	Statistical analysis for aggregate shape . . . . .	82
4.3.3	Statistical analysis for aggregate angularity . . . . .	83
4.4	Asphalt mixture modeling . . . . .	85
4.4.1	Complex modulus test . . . . .	85
4.4.2	Irregular polyhedral particles simulation . . . . .	86
4.4.3	Burgers contact model and its calibration . . . . .	89
4.5	Numerical analysis . . . . .	96
4.5.1	Macro mechanical behavior . . . . .	96
4.5.2	Micro mechanical behavior . . . . .	97
4.6	Conclusions of the chapter . . . . .	104
<b>5</b>	<b>Multi-scale simulation of tire-pavement interaction</b>	<b>107</b>
5.1	Introduction . . . . .	107
5.2	Tire modeling and calibration . . . . .	108
5.2.1	Tire structure and model construction . . . . .	108
5.2.2	Model calibration . . . . .	110

---

5.3	Macro simulation of the tire induced-loading on the pavement surface . . . . .	111
5.3.1	Tire rolling contact model . . . . .	111
5.3.2	Tire contact stress distribution under free-rolling . . .	116
5.3.3	Tire contact stress distribution under full-braking . . .	116
5.4	Micro simulation of tire-pavement interaction . . . . .	119
5.4.1	Asphalt mixture modeling . . . . .	119
5.4.2	Non-uniform tire load simulation . . . . .	120
5.4.3	Particle displacement distribution . . . . .	123
5.4.4	Particle contact force analysis . . . . .	126
5.5	Conclusions of the chapter . . . . .	129
<b>6</b>	<b>Asphalt mixture responses under rolling tire loads</b>	<b>131</b>
6.1	Introduction . . . . .	132
6.2	FEM-DEM coupling for the dynamic tire-pavement interaction	132
6.2.1	Coupling algorithm . . . . .	133
6.2.2	Tire contact force detection . . . . .	133
6.2.3	Tire contact force application . . . . .	137
6.3	Validation of the coupling method . . . . .	138
6.4	Effects of tire rolling velocity . . . . .	142
6.4.1	Bottom boundary force . . . . .	142
6.4.2	Contact force network evolution . . . . .	142
6.4.3	Particle movement characteristics . . . . .	144
6.5	Effects of tire rolling status . . . . .	147
6.5.1	Bottom boundary force . . . . .	147
6.5.2	Particle contact force distribution . . . . .	148

---

6.5.3	Particle displacement distribution . . . . .	148
6.5.4	Average particle velocity . . . . .	150
6.5.5	Particle movement characteristics . . . . .	152
6.6	Conclusions of the chapter . . . . .	153
<b>7</b>	<b>Findings, conclusions and perspectives</b>	<b>155</b>
7.1	Findings . . . . .	155
7.1.1	Tire-pavement contact stresses . . . . .	155
7.1.2	Asphalt mixture modeling . . . . .	157
7.1.3	Asphalt mixture responses under tire loads . . . . .	158
7.2	Conclusions . . . . .	160
7.3	Perspectives . . . . .	161





# List of Figures

2	Contour de la distribution des contraintes de contact sous chargement de roulement libre . . . . .	viii
3	Contour de la distribution des contraintes de contact au freinage roue bloquée . . . . .	ix
4	Essai numérique 2PB basé sur FEM . . . . .	x
5	Montage de l'essai 2PB et modélisation numérique de l'échantillon . . . . .	xi
6	Processus de roulement des pneus sur la couche de béton bitumineux pour $V=20$ km/h . . . . .	xiii
7	Simulation du couplage FEM-DEM : (a) détermination de l'empreinte du pneu (b) détection de la force de contact (c) application de la force de contact . . . . .	xv
8	Comparaisons entre les distributions des déplacements de particules (à gauche) et les distributions des contraintes de contact pneu-chaussée (à droite) dans trois directions. . . . .	xvii
9	Évolution du réseau de forces de contact (force forte = 1.0 et force faible = 0.0) à une vitesse de roulement de 30 m/s. . . . .	xviii
10	Distribution du déplacement des particules à 30 m/s pour différents états de roulement ( $T = 0.007$ s) . . . . .	xix
2.1	Layered elastic analysis: inputs (blue), typical layer names and thicknesses, and outputs (red) . . . . .	7
2.2	(a) SIM configuration (b) tire loading process [28] . . . . .	8
2.3	TekScan system constituting of piezoresistive sensors(from <a href="https://www.tekscan.com/">https://www.tekscan.com/</a> ) . . . . .	9
2.4	Tire modeling process: from cross-section reconstruction to apply load on tire structure [36] . . . . .	10

2.5	(a) Calibration phase picture (b) Calibration procedure (c) Tire profile after surface reconstruction (d) Pressure distribution through SAM simulation [43] . . . . .	11
2.6	Process and data collection of a dynamic modulus test in the laboratory [49] . . . . .	12
2.7	(a) Test specimen dimensions (b) Schema of the complex modulus test device [51] . . . . .	14
2.8	Process of extracting the area of interest from digital tomographic image [80] . . . . .	18
2.9	The cross-section of the models containing aggregates with different angularities [80] . . . . .	19
2.10	(a) Marshall DEM specimen (b) Trabecular DEM specimen [92]	21
2.11	Simulating the splitting test by DEM: (a) the specimen preparation (b) the test set-up . . . . .	22
2.12	Configuration of the contact model in a DEM simulation [55] .	23
2.13	Burgers model in the local frame: (a) Normal components; (b) Tangential components [48] . . . . .	24
2.14	Generation process of asphalt mixture DEM model based on computer-aided algorithm [122] . . . . .	28
2.15	Variation of clump template influenced by distance [121] . . .	29
2.16	The MMLS3 applies repetitive loading through four wheels [129]	30
2.17	(a) HVS in FDOT's APT facility [3] (b) APT facility of IF-STTAR [131] (c) Natural Environment-Automatically Loaded Track (NE-ALT) system [4] (d) Full-scale loading test based on MLS66 equipment [132] . . . . .	31
2.18	(a) Discretisation of coupled ALE tire-pavement interaction model (b) Vertical displacements of pavement model at 5 km/h	33
2.19	Analysis model for transverse cracks under wheel load [145] . .	35
2.20	(a) Applied wheel loading assumption (b) Angular velocities of coarse aggregates [122] . . . . .	36

---

2.21	Multiscale tire–soil interaction simulation based on RVE using moving soil patch approach [153] . . . . .	38
2.22	(a) Initial soil bed and tire configurations (b) The tire during travel through the soil bed [155] . . . . .	39
3.1	The sensor measuring system (from <a href="https://www.tekscan.com/">https://www.tekscan.com/</a> ) (Left), Experimental test measuring process (Right). . .	46
3.2	Tire contact stress distributions under different loads and inflation pressures . . . . .	47
3.3	2PB test configuration . . . . .	48
3.4	Experimental results for the 2PB test . . . . .	50
3.5	VENoL model [67] . . . . .	51
3.6	VENoL model parameters and equations [67] . . . . .	52
3.7	Numerical 2PB test based on FEM . . . . .	54
3.8	Comparisons between numerical and experimental results . . .	55
3.9	Pavement layer and loading area . . . . .	56
3.10	Tire-sensor-pavement coupling . . . . .	57
3.11	Tire rolling process on the asphalt layer . . . . .	59
3.12	Tire rolling process on the asphalt layer for $V$ . . . . .	61
3.13	Cross section (Plane: $x = 0$ ) selection of asphalt layer . . . . .	62
3.14	Comparisons of the numerical surface deflection and the experimental rutting measurement . . . . .	63
3.15	Residual deformation (scale factor = 50000) for different tire rolling velocity . . . . .	64
3.16	Dynamic responses of the center element on the asphalt layer surface for $V$ . . . . .	66
3.17	Dynamic responses of the center element on the asphalt layer surface for different tire rolling velocity . . . . .	67

3.18	Residual deformation (scale factor = 50000) at inflation pressure of 8 bar for different tire loads at $V$ . . . . .	68
3.19	Dynamic responses of the center element on the asphalt layer surface for different tire loads at $V$ . . . . .	69
3.20	Residual deformation (scale factor = 50000) at tire load of 20 kN for different tire inflation pressures at $V$ . . . . .	70
3.21	Dynamic responses of the center element on the asphalt layer surface for different tire inflation pressures at $V$ . . . . .	71
3.22	Residual displacement field on the asphalt layer surface for different temperatures at $V = 20$ km/h and tire load of 20 kN and inflation pressure of 8 bar . . . . .	73
4.1	Comparison between the two contact modeling methods: Normal (left) and Tangential (right) . . . . .	80
4.2	Candidate/antagonist approach . . . . .	80
4.3	Contact situations that may occur between two polyhedral particles . . . . .	81
4.4	3D scanning process . . . . .	82
4.5	Original bounding box of an aggregate particle (left) and minimum bounding box cube of the aggregate particle (right) . . . . .	83
4.6	Probability distribution and normal fitting: (a) Elongation ratio (LI); (b) Flatness ratio (IS) . . . . .	84
4.7	Probability distribution and normal fitting of Sphericity ( $Sp$ ) . . . . .	85
4.8	Dynamic modulus and phase angles from experimental measurements of asphalt mixture . . . . .	87
4.9	Asphalt mixture and Voronoi tessellations . . . . .	88
4.10	Particle size distribution (PSD) of asphalt mixture . . . . .	89
4.11	Numerical modeling of test sample . . . . .	90
4.12	Burgers contact model between particles . . . . .	92

---

4.13	Relations between velocities and contact forces: (a) Normal components (b) Tangential components [48]. . . . .	94
4.14	Calibration process of Burgers model parameters. . . . .	95
4.15	Measured displacement $Z$ and corresponding force $F$ for 15 °C and 40 Hz . . . . .	96
4.16	Experimental and numerical master curve at $T_{ref} = 15^{\circ}C$ . . . .	97
4.17	Macro and micro behavior of asphalt specimen in one loading cycle . . . . .	98
4.18	Normal force probability distribution at 15 °C, 40 Hz . . . . .	99
4.19	Tangential force probability distribution at 15 °C, 40 Hz . . . . .	99
4.20	Average velocity of particles for 15 °C and 40 Hz . . . . .	100
4.21	Strong and weak contact force networks for 15 °C and 40 Hz .	101
4.22	Cumulative distribution for tangential force and normal force at T1, T3, 15 °C . . . . .	102
4.23	Cumulative distribution for tangential force and normal force at T1, T3, 40 Hz . . . . .	103
5.1	Tire scanning process . . . . .	109
5.2	Tire model and mesh refinement . . . . .	110
5.3	Comparisons between measured and calculated tire deflections	111
5.4	Tire driven forces during rolling (a) and pavement contact forces (b) [194] . . . . .	112
5.5	Asphalt surface layer and tire . . . . .	114
5.6	Contact stress distribution contours at free-rolling . . . . .	117
5.7	Contact stress distribution contours at full-braking . . . . .	118
5.8	Numerical modeling of asphalt mixture for 2PB complex modulus test . . . . .	120

---

5.9	Dynamic modulus and phase angles from experimental measurements and simulations at 15°C: (a) Dynamic modulus; (b) Phase angle . . . . .	121
5.10	Tire imprint, contact stresses under each rib and local coordinate system . . . . .	123
5.11	Boundary forces derived from free-rolling (a) Vertical force; (b) Longitudinal force; (c) Transverse force . . . . .	124
5.12	Pavement surface layer model: (a) Full model; (b) Half model along y-axis . . . . .	125
5.13	Particle displacement distribution under (a) free-rolling condition; (b) full-braking condition . . . . .	126
5.14	Maximum displacement comparison between free-rolling and full-braking . . . . .	127
5.15	Normal force distribution . . . . .	128
5.16	Tangential force distribution . . . . .	128
6.1	Coupling simulation of FEM and DEM: (a) Tire imprint determination; (b) Contact force detection; (c) Contact force application . . . . .	134
6.2	(a) Coarse detection: Bounding box; (b) Fine detection: Point in polyhedron . . . . .	136
6.3	(a) Plane-XY; (b) Plane-XZ; (c) Plane-YZ . . . . .	137
6.4	Comparisons between particle displacement distributions (left) and Tire-pavement contact stress distributions (right) in three directions . . . . .	140
6.5	(a) Particle displacement distribution; (b) Particle motion arrows . . . . .	141
6.6	Bottom boundary force characteristics . . . . .	143
6.7	Contact force network evolution (strong force = 1.0 and weak force = 0.0) at rolling velocity of 30 m/s . . . . .	145

---

6.8	Particle displacement for different tire rolling speeds . . . . .	146
6.9	Bottom boundary force characteristics for different rolling status	147
6.10	Particle contact force distribution at different tire rolling status	149
6.11	Particle displacement distribution at 30 m/s for different rolling status ( $T = 0.007$ s) . . . . .	150
6.12	Average particle velocities for different tire rolling status . . .	151
6.13	Particle displacement for different tire rolling status . . . . .	152





# List of Tables

2.1	Viscoelastic models for asphalt materials . . . . .	17
3.1	Particle size distribution (PSD) of asphalt mixture . . . . .	48
3.2	Modeling parameters for VENO <sub>L</sub> model . . . . .	54
4.1	Statistical parameters for aggregate morphology . . . . .	85
4.2	Particle size distribution (PSD) of asphalt mixture . . . . .	86
4.3	Dimensions of the specimens: EN 12697-26:2012 . . . . .	86
4.4	Burgers model parameters used in numerical simulations . . . . .	97
5.1	Burgers model parameters used in numerical simulations . . . . .	121



# Introduction

---

## Contents

<b>1.1</b>	<b>General background and motivation</b>	<b>1</b>
<b>1.2</b>	<b>Objectives and scope</b>	<b>2</b>
<b>1.3</b>	<b>Thesis outline</b>	<b>3</b>

---

This work was undertaken at the National Institute of Applied Sciences of Strasbourg (INSA Strasbourg), in the Engineering Science, Computer Science and Imaging Laboratory ICube, UMR7357. Firstly, the general background and motivation of the thesis are given in this chapter. Then, the objectives and research scope are discussed. Finally, an outline of the remainder of the thesis is presented.

## 1.1 General background and motivation

Road infrastructure is currently undergoing massive changes and challenges. Most existing roads are not sufficiently durable, and their lifespan is shorter than expected. The durability of the road infrastructure will also be negatively affected by the increase in traffic volume and climatic changes. Indeed, during most of its lifetime, the road is loaded with overrunning tires and exposed to climatic impact. During this time, failure processes (e.g., ruts and fractures) begin, which eventually lead to the end of the road's life. To obtain high-quality predictions of the performance of a road system over its lifetime, it is critical to simulate the real system as exactly as possible. The life cycle of a road begins with the raw materials used to manufacture it.

Asphalt mixtures are complex multi-phase composite materials extensively used in road construction, such as highways and urban pavements. A significant part of road network costs is related to surface degradation, which

tends to occur most frequently on asphalt surface layers. Due to its heterogeneous structure, the material response of an asphalt mixture is determined by the properties of its components (aggregates, asphalt binder, and air voids), changing environmental variables (temperature, moisture, etc.), and interaction with loading tires and underlying substrate. Therefore, it is crucial to assess the mixture responses at a micro-structural level under real tire load conditions in order to better understand and model its behavior.

Asphalt mixtures under rolling tire loads are subjected to three-dimensional stress states with varying stress levels in each dimension. Therefore, it is usually difficult to achieve such complex boundary conditions through laboratory tests due to the limited capabilities of testing equipment and measurement systems. Full-scale tests based on the Accelerated Pavement Testing (APT) method [1–4] are an effective approach for assessing macroscopic pavement performance under real tire loading. However, it is still a struggle to get insight into the internal mechanisms of the mixture damage from a microscopic point of view by using APT.

To cope with the difficulties arising from the complexity and inadequacy of experimental measurements, numerical approaches such as the Finite Element Method (FEM) and the Discrete Element Method (DEM) have emerged as a promising and effective way of gaining insight into asphalt mixture performance in recent decades.

## 1.2 Objectives and scope

For simulating a dynamic mutual interaction system comprising a tire and an asphalt mixture at the micro-structural level, three issues need to be addressed primarily: Firstly, seeking a realistic representation of the tire load; secondly, modeling an asphalt mixture while explicitly considering characteristics of its different components (irregular aggregate particles, asphalt binder, etc.); finally, applying the rolling tire load to the mixture structure by coupling the two models above.

This thesis is dedicated to the investigation of the tire-pavement interaction system based on numerical simulations. Two main numerical methods, FEM and DEM, are used to model this system from distinct multi-scales. Finally, FEM-DEM coupling simulations are presented to investigate asphalt mixture

responses at the particle level under tire loads, which fulfills the goal of multi-scale investigations of tire-pavement interaction mechanisms.

## 1.3 Thesis outline

This dissertation is divided into seven chapters.

The introduction chapter presents the objectives, scope of the study, and outline of the thesis.

The second chapter gives an overview of previous research on the mechanistic analysis of pavement responses, tire-pavement interaction, asphalt mixture modeling, and multi-scale simulation theories.

The following 4 chapters (from chapter 3 to chapter 6) are mainly based on four research papers related to this work.

Using continuum mechanics theory, the third chapter describes the developed tire-sensor-pavement coupling chain that integrates actual rolling tire loads into asphalt layer modeling and analyzes the dynamic response of the asphalt layer under various rolling tire loads. (Based on *Ge, H., Quezada, J. C., Le Houerou, V., Chazallon, C., & Horny, P. (2023). A new tire-sensor-pavement coupling chain for investigating asphalt mixture responses under rolling tire loads. Road Materials and Pavement Design, 1-18.*)

Based on the contact dynamics method, the fourth chapter introduces the developed DEM model of asphalt mixtures, which incorporates realistic aggregate morphology and size distributions. (Based on *Ge, H., Quezada, J. C., Le Houerou, V., & Chazallon, C. (2021). Three-dimensional simulation of asphalt mixture incorporating aggregate size and morphology distribution based on contact dynamics method. Construction and Building Materials, 302, 124124.*)

The fifth chapter presents a developed tire model using laser scanning technique and FEM and further proposes a multi-scale simulation for examining tire-pavement interaction mechanisms by incorporating both FEM and DEM. (Based on *Ge, H., Quezada, J. C., Le Houerou, V., & Chazallon, C. (2022). Multiscale analysis of tire and asphalt pavement interaction via coupling FEM-DEM simulation. Engineering Structures, 256, 113925.*)

The sixth chapter develops an advanced FEM-DEM coupling framework to analyze asphalt mixture responses under rolling tire loads from a micro-mechanical point of view, consistently, at the particle scale. (Based on *Ge, H., Quezada, J. C., Le Houerou, V., & Chazallon, C. (2023). Three-dimensional FEM–DEM coupling simulation for analysis of asphalt mixture responses under rolling tire loads. Construction and Building Materials, 369, 130615.*)

The final chapter summarizes the findings and conclusions of this study and discusses potential future perspectives.

# Literature review

---

## Contents

<b>2.1</b>	<b>Traffic loads in asphalt pavement design . . . . .</b>	<b>6</b>
<b>2.2</b>	<b>Examination of tire loads on pavements . . . . .</b>	<b>7</b>
2.2.1	Experimental measurements . . . . .	8
2.2.2	Numerical tire modeling . . . . .	8
<b>2.3</b>	<b>Research methods for asphalt mixtures . . . . .</b>	<b>12</b>
2.3.1	Experimental approaches . . . . .	12
2.3.2	Rheological models . . . . .	15
2.3.3	Finite element modeling of asphalt mixtures . . . . .	16
2.3.4	Discrete element modeling of asphalt mixture . . . . .	18
2.3.4.1	Two-Dimensional discrete element modeling . . . . .	20
2.3.4.2	Three-Dimensional discrete element modeling . . . . .	21
2.3.4.3	Contact model in asphalt mixture modeling . . . . .	22
2.3.4.4	Mesoscopic structure containing irregular particles . . . . .	26
<b>2.4</b>	<b>Asphalt mixture responses under tire loads . . . . .</b>	<b>29</b>
2.4.1	Accelerated pavement testing analysis . . . . .	29
2.4.2	Analytical modeling analysis . . . . .	32
2.4.3	Finite element modeling analysis . . . . .	32
2.4.4	Discrete element modeling analysis . . . . .	34
<b>2.5</b>	<b>Multi-scale coupling simulation . . . . .</b>	<b>37</b>
<b>2.6</b>	<b>Conclusions of the chapter . . . . .</b>	<b>40</b>

---



## 2.1 Traffic loads in asphalt pavement design

Asphalt pavements are subjected to vehicular traffic loads throughout their lifecycle, which leads to the continuous deterioration of pavement performance and further reduces their service life, and finally, increases maintenance costs.

A variety of distresses, including permanent deformation (rutting), fatigue cracks, low-temperature thermal cracks, potholes, raveling, and more, occur on asphalt pavements as a result of repeated vehicle loads and local environmental conditions [5–9].

A variety of factors contribute to pavement distress, including vehicle characteristics, pavement material properties, pavement structures, and most importantly, the load transfer mechanism from vehicles to pavements [10–13]. Tires are the only interface between vehicles and a pavement surface, so as asphalt pavements gradually deteriorate due to the tire-pavement interaction [14, 15]. It is therefore crucial to study the tire-pavement interaction to understand the load transfer mechanism.

In the conventional pavement design method, elastic layer theory is widely used in calculating critical pavement responses under traffic loads [16–18]. The layered elastic analysis utilizes an axisymmetric, isotropic, elastic layer model in which the bottom and sides are assumed infinite, and the wheel load is at the top. The thickness ( $t$ ) of each layer is parameterized, Young's modulus ( $E$ ) and Poisson's ratio ( $\nu$ ) are determined experimentally and applied to each layer, and the layer interface is permitted to have full to zero slip. As shown in Figure 2.1, the horizontal tensile strain ( $\epsilon_h$ ) at the bottom of the asphalt layer, and the vertical compressive strain ( $\epsilon_v$ ) at the top of the compacted soil layer are of crucial importance in the traditional pavement design.

An excessive value of  $\epsilon_h$  can cause the pavement surface to develop a fatigue crack that continues upwards to the surface of the pavement. As a result of excessive  $\epsilon_v$ , the compacted soil layer can become permanently deformed, which will be apparent on the surface of the pavement as rutting over time. Empirical relationships based on these two quantities are used to estimate fatigue and rutting [16].

As part of the design method, the tire contact area is considered as a circle,

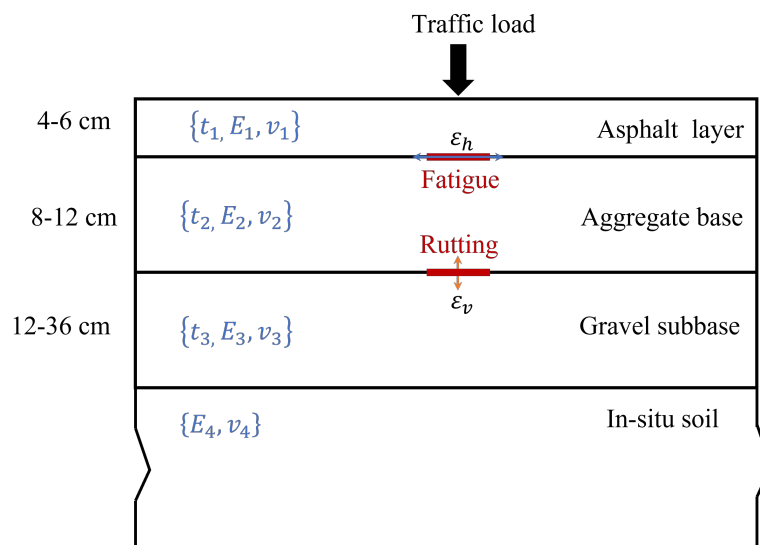


Figure 2.1: Layered elastic analysis: inputs (blue), typical layer names and thicknesses, and outputs (red)

and the tire load is assumed to be uniform and equal to the tire inflation pressure for the sake of computation simplicity [19, 20]. These assumptions have been proved to be practical to some extent in predicting some pavement distress such as fatigue crack and rutting. However, with the development of traffic technology and the increasing traffic loads, more and more asphalt layer surface damage occurs with interaction with vehicle tires, which is hardly predictable by using the traditional simplified design method.

Numerous studies have demonstrated that actual tire loads induce quite different pavement responses compared to uniform loads [21–23], particularly in terms of pavement surface degradation and near-surface crack development [24, 25]. This changing trend has shifted our attention in understanding the deformation mechanisms of pavement surfaces under actual tire loading.

## 2.2 Examination of tire loads on pavements

An accurate characterization of tire-pavement contact stress distribution is a prerequisite for understanding the degradation mechanism of asphalt surface layers and predicting the distress evolution. Many researchers conclude that the tire imprint shape and tire contact stress distributions are dependent on

tire loads and tire inflation pressures, and the tire contact stresses are not uniform across the contact area [26–28].

### 2.2.1 Experimental measurements

Sensor measuring systems provide an effective and precise solution for assessing tire contact stresses on the pavement surface. De Beer developed Stress-in-motion (SIM) system (Figure 2.2) to measure the tire contact stress distribution [28–30]. The SIM system was initially referred to as the Vehicle–Road Surface Pressure Transducer Array (VRSPTA) [20, 31].

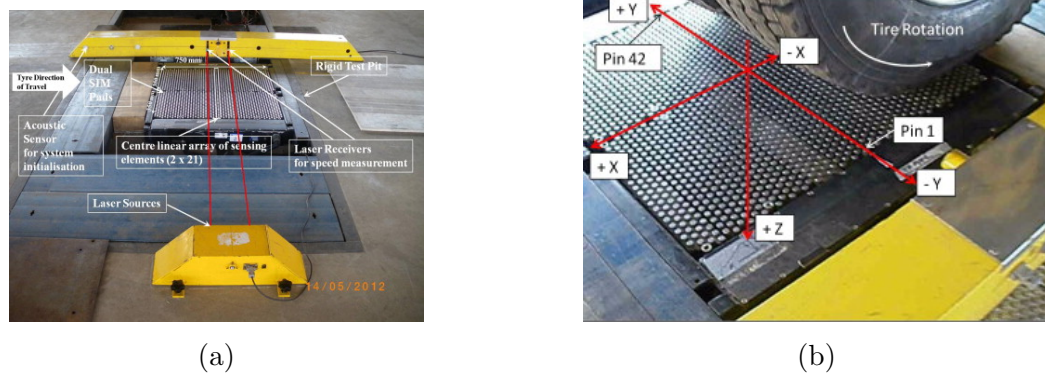


Figure 2.2: (a) SIM configuration (b) tire loading process [28]

In recent years, the Tekscan measuring system (Figure 2.3) was also widely used to get access to the tire contact stress distributions on the pavement surface. Prior research has proven that the Tekscan system is an efficient method to measure real tire contact pressures on pavement surfaces during a range of tire loading conditions [27, 32, 33].

Experiments have shown, however, that the real tire load is not uniform and that the stress distribution is not normal to the rolling surface since both vertical and tangential contact stresses are generated at the tire-pavement interface [26, 28, 34].

### 2.2.2 Numerical tire modeling

The tire-pavement interaction is an extremely complex contact problem. Experimental measurements are arduous because of their time-consuming ex-

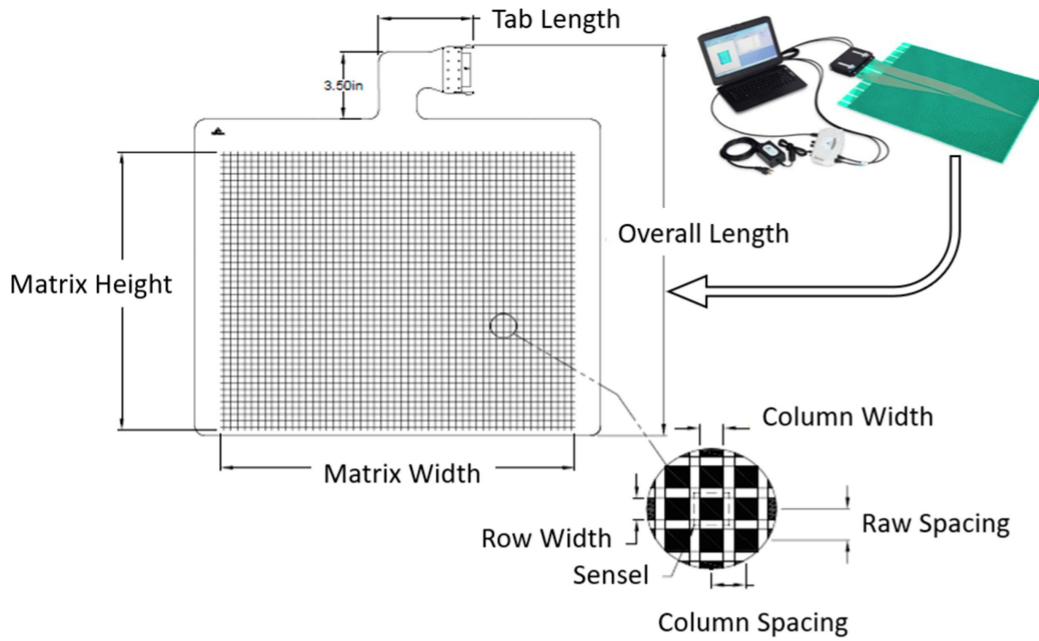


Figure 2.3: TekScan system constituting of piezoresistive sensors(from <https://www.tekscan.com/>)

penses and limitations in studying various boundary conditions of this interaction system. On the other hand, numerical tools provide an effective way to explore this system while taking into account the system's complexity.

Several FEM tire models were built to study tire contact stresses under different working conditions, such as the models developed by Korunović et al. [35], Wang et al. [36], Wollny et al. [37, 38], and Guo et al. [39, 40].

Wang et al. [36] validated the non-uniformity of tire contact stresses and localized tangential contact stresses based on the finite element method (FEM). Guo et al. [39, 40] analyzed the contact stress distribution of a bus tire on the pavement using FEM, and various tire work conditions were found to affect critical slip ratios and rolling resistance. Figure 2.4 shows an example of the numerical tire modeling process using FEM.

To reduce the cost of FEM computation, Manyo et al. [41, 42] proposed a fast tire-pavement modeling method combing photogrammetric techniques and the semi-analytical method (SAM) and studied pavement responses under different tire rolling conditions. They found that the maximum tensile strains caused by tire edges could lead to top-down cracking. Oubahdou et al. [32]

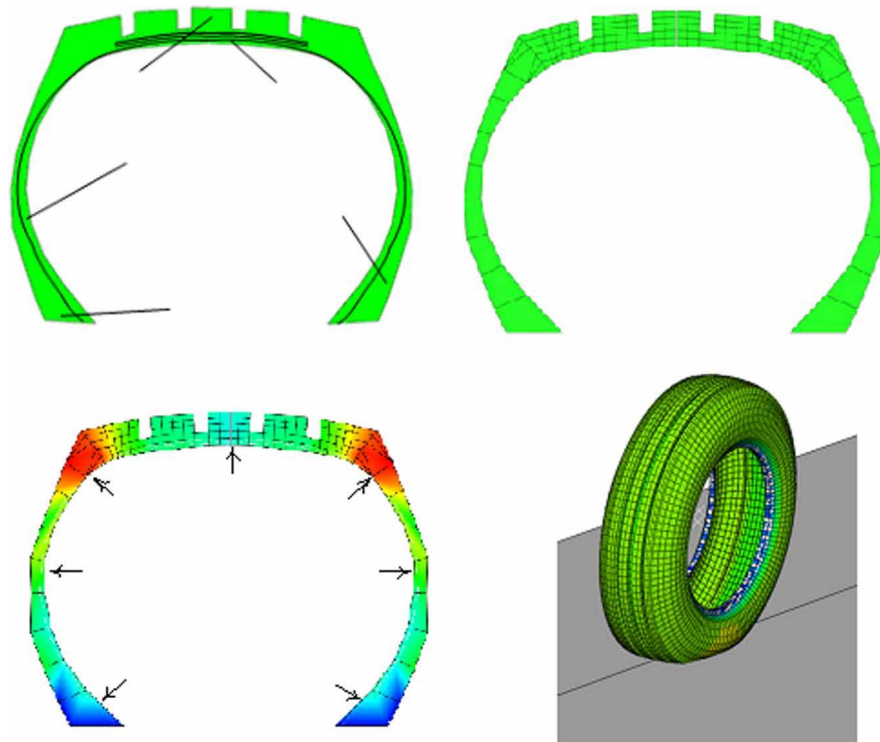


Figure 2.4: Tire modeling process: from cross-section reconstruction to apply load on tire structure [36]

studied tire contact stresses under various tire inclinations by combining SAM and sensor measurements, significant shear stresses were observed on the pavement surface as a result of tire turnings. Figure 2.5 shows the tire modeling based on photogrammetry and simulation results using SAM.

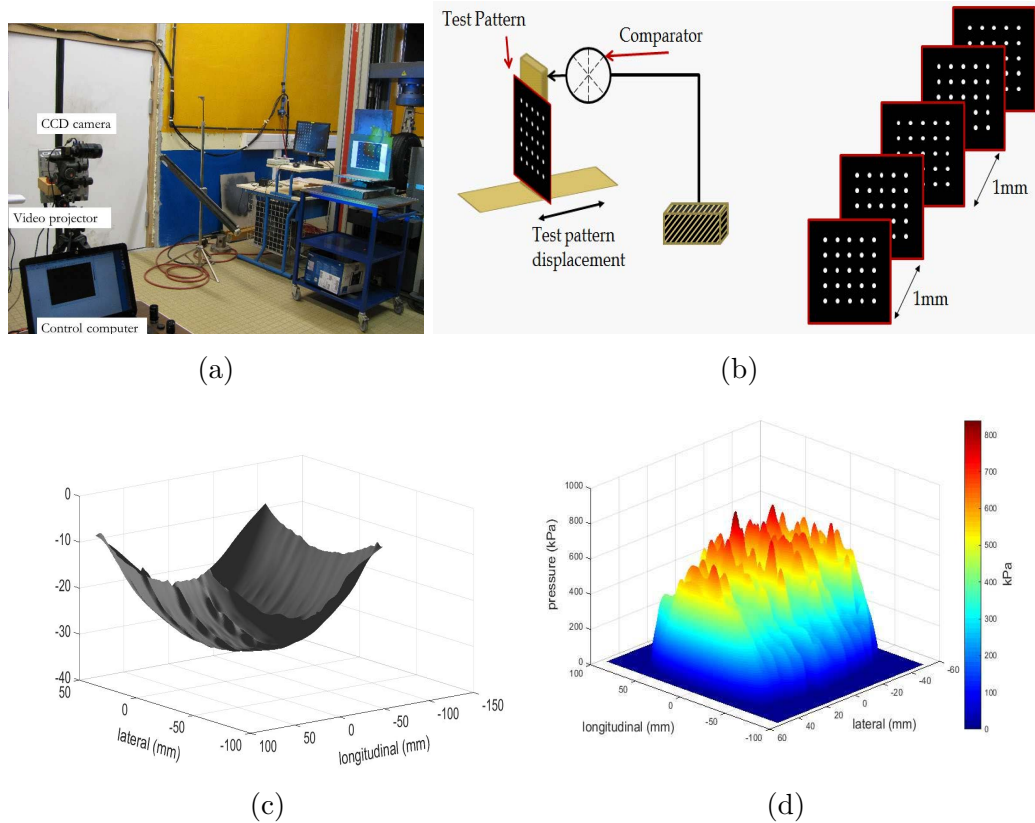


Figure 2.5: (a) Calibration phase picture (b) Calibration procedure (c) Tire profile after surface reconstruction (d) Pressure distribution through SAM simulation [43]

The simulation results above showed that tire contact stresses are influenced by multiple factors, including tire structure, inflation pressure, tire load, rolling states (free rolling, acceleration/braking, and cornering), rolling speed, friction, etc.

Compared with SAM simulations, FEM simulations have less computation efficiency, but much more flexibility in modeling complex composite tire and pavement structures, as well as assigning complex material behaviors, and are shown to be the most widely used and versatile method in tire-pavement

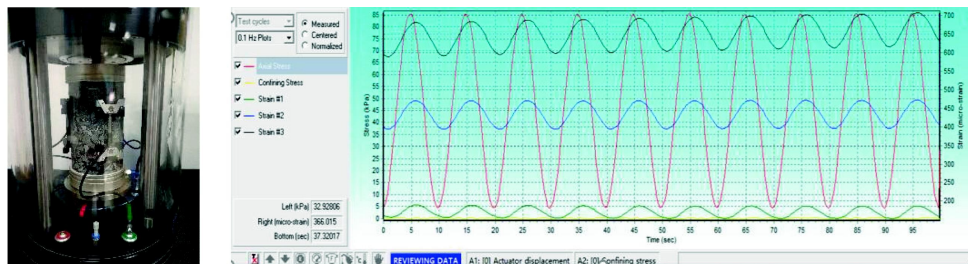
contact modeling [41]. However, in the most current FEM research, the pavement structure was assumed as rigid in the tire-pavement contact model, and the contact stresses on the tire were calculated to reflect tire load distribution on the pavement surface. Although this assumption could save computation time by avoiding massive contact detection between objects with different material properties, it may result in an inaccurate estimation of transmitted contact stresses on the pavement surface.

## 2.3 Research methods for asphalt mixtures

### 2.3.1 Experimental approaches

Experimental methods are commonly used to determine the macro material properties of asphalt mixtures. For pavement design, there are usually two main input parameters used to characterize the viscoelastic properties of an asphalt mixture: dynamic modulus and phase angle [44, 45].

These two parameters are also widely used in identifying asphalt mixture model effectiveness in numerical simulations [46–48]. Dynamic modulus tests are conducted under haversine or sinusoidal loading conditions. It is then measured at different temperatures and frequencies the output parameters (stress or strain). Finally, the dynamic modulus and phase angle are calculated based on formulations involving the stress and strain and other test parameters. The testing process of a dynamic modulus test is illustrated in Figure 2.6.



(a) Dynamic modulus test specimen (b) stress and strain under loading versus time

Figure 2.6: Process and data collection of a dynamic modulus test in the laboratory [49]

Complex modulus (at any temperature) is defined as the ratio of sinusoidal

stress amplitude to sinusoidal strain amplitude (at a given same time and frequency):

$$E^* = \frac{\sigma(t)}{\epsilon(t)} = \frac{\sigma_0 \sin(\omega t)}{\epsilon_0 \sin(\omega t - \phi)} = \frac{\sigma_0}{\epsilon_0} \cdot e^{i\phi} = |E^*| \cdot e^{i\phi} \quad (2.1)$$

Where,

- $E^*$  is the dynamic modulus;
- $\sigma_0$  is peak (maximum) stress;
- $\epsilon_0$  is the peak (maximum) strain;
- $\omega = 2\pi f$  is the angular velocity, in which  $f$  is the loading frequency;
- $\phi$  is the phase angle that represents the lag time between stress and strain;
- $t$  is the time;
- $i$  is the imaginary unit.

The complex modulus can also be defined as (EN 12697:26 [45]):

$$E^* = |E^*| \cdot (\cos\phi + i \cdot \sin\phi) = E_1 + iE_2 \quad (2.2)$$

The real component  $E_1$  represents the elastic behavior of the material while the imaginary component  $E_2$  describes the viscous material behavior.

Dynamic modulus  $|E^*|$  (the absolute value of the complex modulus) and the phase angle  $\phi$  (phase lag between stress and strain waveforms) can be calculated as:

$$|E^*| = \sqrt{(E_1^2 + E_2^2)} \quad (2.3)$$

$$\phi = \arctan(E_2/E_1) \quad (2.4)$$

The two components can be expressed in general terms as follows:

$$E_1 = \lambda \left( \frac{F}{z} \cos\phi + \frac{\mu}{10^3} \omega^2 \right) \quad (2.5)$$

$$E_2 = \lambda \left( \frac{F}{z} \sin\phi \right) \quad (2.6)$$

Where,



- $\lambda$  is the form factor as a function of specimen size and shape;
- $\mu$  is the mass factor, a function of the mass of the specimen ( $M$  in grams) and the mass of the movable parts ( $m$  in grams), that influence the resultant force by their inertial effects;
- $F$  is the applied force;
- $z$  is the displacement.

Depending on the type of test and the shape of the specimens,  $\lambda$  and  $\mu$  have different expressions. The dynamic modulus and phase angle provide critical information about the viscoelastic behavior of asphalt mixtures over a wide range of temperatures and loading frequencies.

These properties can be characterized in a variety of ways according to the European standards applicable to bituminous materials [45, 50]. The tests include two-point bending (2PB) on trapezoidal specimens, two-point bending on prismatic specimens, three-point bending on prismatic specimens, four-point bending on prismatic specimens, and compression-tension tests on cylindrical specimens. Figure 2.6 shows the scheme of the 2PB testing configuration.

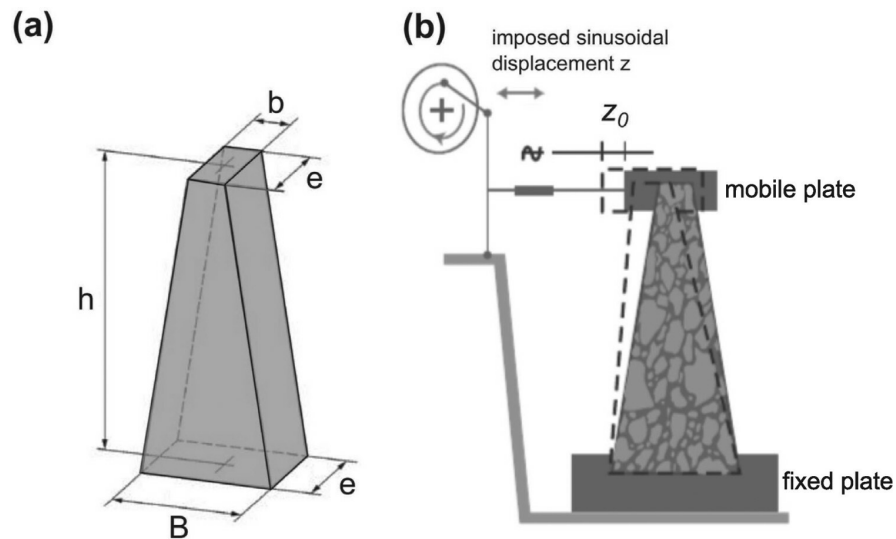


Figure 2.7: (a) Test specimen dimensions (b) Schema of the complex modulus test device [51]

### 2.3.2 Rheological models

Asphalt mixture is a temperature- and frequency-dependent material that has a classic visco-elastic nature [52–55]. Rheological models composed of various combinations of springs and dashpots can be used to describe materials that exhibit viscoelastic behavior. During recent decades, various rheological models have been used in order to describe the mechanical behavior of asphalt mixtures.

Maxwell and Kelvin-Voigt are two-parameter models that include a combination of springs and dashpots arranged in series and in parallel, respectively. Both models, however, are not adequate to describe well simultaneously the creep and relaxation behavior of asphalt mixtures. To address this, additional models were developed by combining the Maxwell and Kelvin models and increasing the number of elements in order to better simulate behaviors that were not considered in earlier models.

In this respect, improved models such as Generalized Maxwell, Generalized Kelvin-Voigt, Burgers, Huet-Sayegh, etc, were introduced in asphalt mixture modeling. The generalized model is composed of a number of different Maxwell and Kelvin elements connected in series [56, 57]. The Generalized Maxwell model comprises of a number spring and dashpot elements in series, while these elements are in parallel for the Generalized Kelvin model. Additionally, the Prony series can be used to represent both models [58]. The generalized models can correctly simulate the behavior of asphalt mixes including creep compliance and relaxation modulus [59, 60]. But it also requires a lot of rheological elements lacking clear physical meanings, which leads to difficulties in parameter identification. If only one Maxwell and Kelvin element is assigned in the generalized model, the Burgers model is obtained [61, 62]. Burgers model can describe viscoelastic behavior reasonably well within a considerably limited frequency range [63]. For the Huet-Sayegh model, it is composed of two parallel branches, where one consists of two parabolic dashpots and a spring of infinite stiffness in series and the other one consists of a single spring of small rigidity [60, 64]. This model is able to accurately describe the viscoelastic behavior of asphalt mixes over a wide range of temperatures and frequencies. However, it fails in describing the curve in the Black space at high temperature and low frequency [53] and in capturing the residual strain [64]. The correction of the Huet-Sayegh model

has been integrated into the 2S2P1D (2 Springs, 2 Parabolic elements, 1 Dashpot) model [65], this model can fit well the dynamic properties of asphalt materials. However, the fractional derivatives in this model are difficult to implement in a numerical simulation. Table 2.3.2 gives a summary of common analytical models used in characterizing viscoelastic material behaviors.

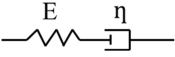
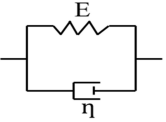
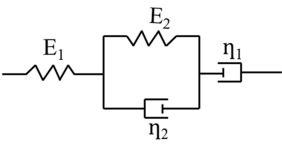
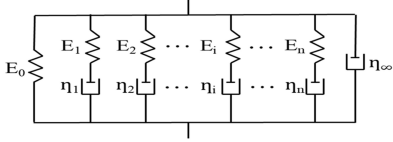
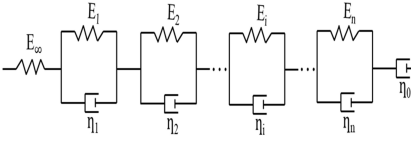
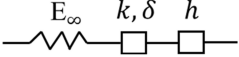
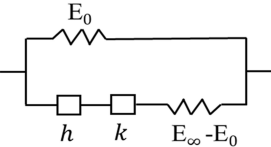
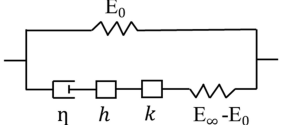
It is therefore desirable to develop a rheological model that is easy to implement in numerical simulations and that can characterize asphalt mixture behavior under dynamic loads for a wide range of frequencies and temperatures. Recently, VENoL (NONLinear ViscoElastic) model [66, 67] was developed to characterize the asphalt mixture behaviors. It is made up of two elements connected in parallel: a stiffness component related to the strain and a viscosity component related to the strain rate. This method incorporates the Time-Temperature Superposition Principle and the Time-Amplitude Semi-Superposition Principle to consider temperature and strain amplitude changes. Besides, based on a similar Kelvin–Voigt structure, the VENoL model can be easily implemented as a material law in numerical simulations. It is proven that this model is effective in reproducing instantaneous complex modulus tests for different strain amplitudes, as well as predicting the evolution of thixotropy during fatigue tests [68].

### 2.3.3 Finite element modeling of asphalt mixtures

Despite the fact that laboratory tests are able to determine the macro-scale properties of asphalt mixtures, these tests do not offer much insight into their micro-mechanical behaviors. During the last decades, Finite Element Method (FEM) has been widely used in a wide range of simulations to describe the overall behavior of asphalt mixtures based on continuum mechanics theory [69–76]. The FEM is the dominant discretization technique in continuum mechanics. A basic physical interpretation of the FEM is the subdivision of the physical model into simple geometric components called finite elements. Each element responds in terms of a finite number of degrees of freedom, representing a set of nodal points and the value of set functions. As a result, the physical model response is approximated by that of the model derived by connecting or assembling all the elements.

To capture the heterogeneity and micro-structure of an asphalt mixture,

Table 2.1: Viscoelastic models for asphalt materials

Name	Description	Schema
Maxwell model	A spring and a dashpot are connected in series. Describe the viscoelastic liquid behavior of the material.	
Kelvin-Voigt model	A spring and a dashpot are connected in parallel. Describe the viscoelastic solid behavior of the material.	
Burgers model	Consisting of the Maxwell model and Kelvin-Voigt model arranged as a series. Describe the viscoelastic material behavior in a limited range of temperatures and frequencies.	
Generalized Maxwell model	Consisting of a parallel group of n Maxwell elements, and possibly with a spring and a dashpot in parallel too.	
Generalized Kelvin-Voigt model	The structure is composed of a spring, n Kelvin-Voigt elements, and possibly with a spring and a dashpot in series.	
Huet model	Originally proposed for bitumen and asphalt mixtures. In this model, a spring is combined with two parabolic elements in series.	
Huet-Sayegh model	The model is an improvement over the previous one for simulating asphalt mixtures. It is capable of predicting the mechanical response of a wide range of bituminous materials.	
2S2P1D model	A comprehensive model that can accurately fit the mechanical response of most bituminous materials.	

FEM models were used to build an asphalt mixture with aggregates generated randomly by computer-aided algorithm [77, 78] or reconstructed by X-ray computed tomography (CT) [79, 80]. Figure 2.8 gives an example of using X-ray CT to reconstruct an asphalt mixture sample.

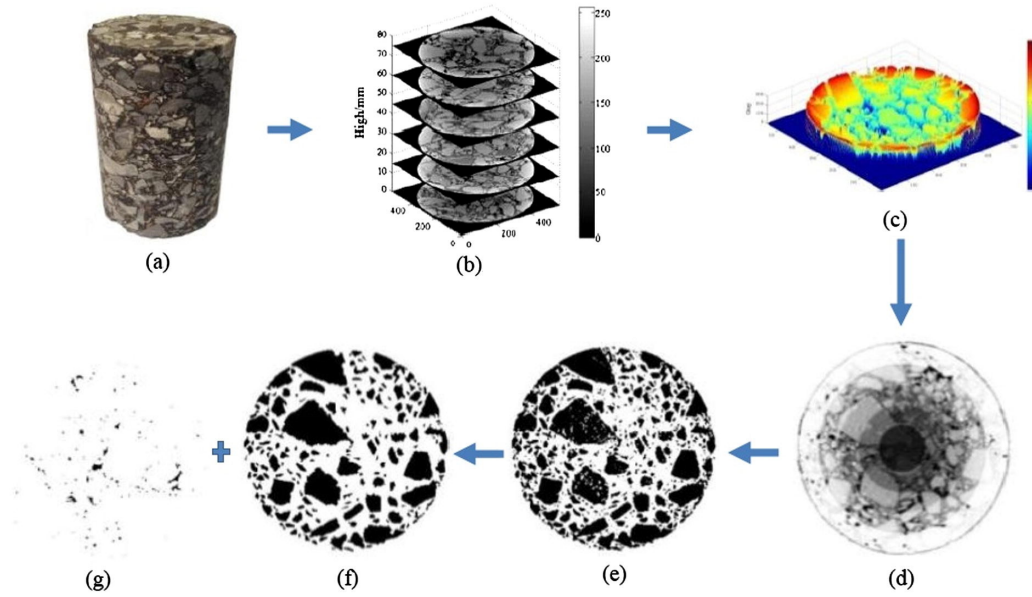


Figure 2.8: Process of extracting the area of interest from digital tomographic image [80]

Using a FEM model with reconstructed aggregates, it was demonstrated that the angularity and irregular shape of coarse aggregates can be addressed in asphalt mixtures. Figure 2.9 shows reconstructed samples with different angularities.

However, these models are based on continuum mechanics theory, which still has difficulties in modeling contact status changes between various asphalt components as they come in and out of contact as well as sliding between different particles when in contact.

### 2.3.4 Discrete element modeling of asphalt mixture

In contrast to FEM, Discrete Elements Method (DEM) considers the sample as an assembly of discrete bodies, rather than continuous media. The purpose of this technique is to solve discontinuous media problems by analyzing the

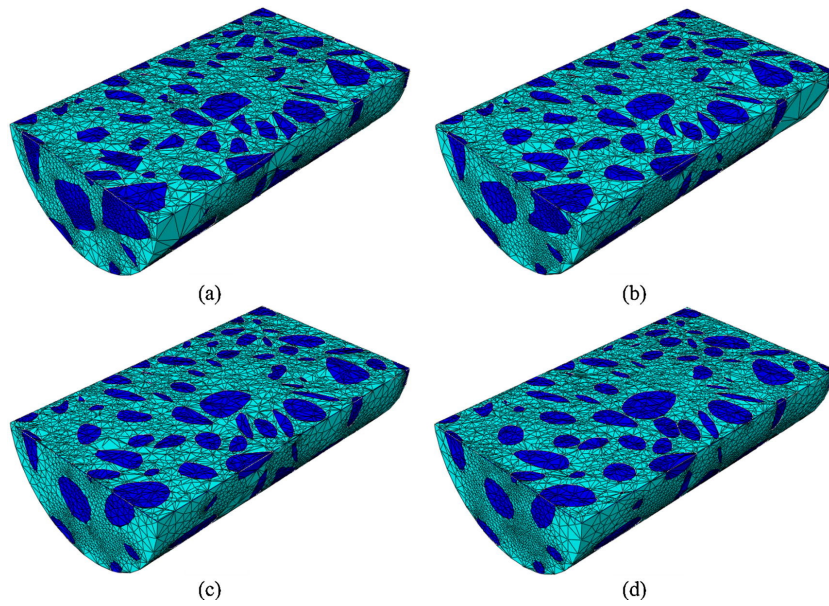


Figure 2.9: The cross-section of the models containing aggregates with different angularities [80]

contacts between discrete elements. Contact is deduced from its constitutive relation, and a consistent physical and mechanical model of that contact can be formulated. A simulation is then carried out based on Newton's second law of motion to simulate the movement including the translation and rotation of discontinuous and discrete elements.

In practice, there are two families of DEM:

The first one is referred to as the smooth and explicit method, assimilating grain interpenetration to possible deformation at the contact, which is derived from the pioneering work of Cundall [81], which could be also considered a modification of the genuine Molecular Dynamics method [82]. In this method, contact laws are handled explicitly by using regularization techniques. Due to explicit time integrators, small time steps are mandatory, and it may be challenging to choose parameters accordingly. Particularly, damping is necessary to guarantee the stability of explicit schemes.

The second one is called the nonsmooth and implicit method, based on Contact Dynamics (CD) method developed by Jean-Jacques Moreau [83], which takes into account shocks without grain interpenetration. The contact laws are thus non-differentiable and steep, and Non-Linear Gauss-Seidel algorithms (NLGS) are employed at each step to manage them implicitly. It

is possible to use large time steps while guaranteeing numerical stability, but each step takes time to complete.

Asphalt mixtures are complex multi-phase systems composed of aggregate particles and asphalt mastic. Due to the heterogeneous structure of asphalt mixtures, the discrete element method (DEM) has been widely adopted in the last decades as a complementary alternative for classical mesh-based methods [46, 84–86].

From a micro perspective, the DEM can explain the load transfer mechanism, damage situations, and failure processes of asphalt mixtures. At a macro scale, it is also capable of predicting rutting initiations, fatigue mechanisms, and fracture evolution for asphalt mixtures.

#### 2.3.4.1 Two-Dimensional discrete element modeling

Discrete element modeling began with 2D models, which have the advantage of fast calculations for complex systems. Despite the fact that some relatively complex experiments do not always yield consistent simulation results, 2D models can still be useful tools for experiments to analyze the general trend without the need for accurate data.

A 2D discrete element model, developed in [87], is used to examine the viscoelastic properties of asphalt mixtures with the Burgers model in mind. The dynamic modulus and phase angle of the asphalt mixtures were predicted through DEM simulations under sinusoidal loading, and the viscoelastic models were verified with experimental measurements. To understand the influence of the bond strength ratio and loading rate on the performance of the asphalt mixture, an indirect tensile test was performed using a 2D DEM method to simulate the tensile strength of the asphalt mixture [88]. Simulations of the splitting test were performed using the 2D DEM using aggregates with different properties and gradations [89]. The effects of air voids on the fracture behavior of asphalt mixtures were investigated using 2D discrete element simulations [90]. Using 2D simulations, the effect of horizontal aggregate distribution on splitting strength and maximum horizontal stress was also numerically assessed in [91]. Figure 2.10 displays 2D models of Marshall and Trabecular samples of asphalt mixture based on DEM.

These studies demonstrate that DEM simulations can provide more effective details than lab tests, such as changes in loading, displacements, and crack

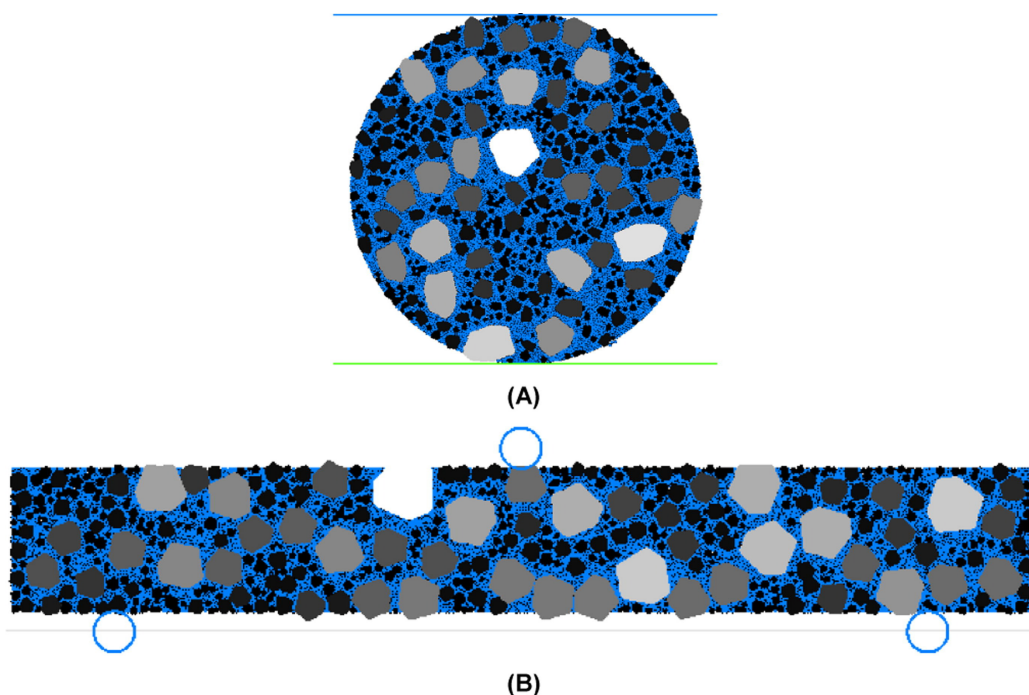


Figure 2.10: (a) Marshall DEM specimen (b) Trabecular DEM specimen [92]

propagation during load testing. However, they also revealed limitations of 2D simulations, such as the lack of geometric information present in the model, which may lead to some misinterpretations.

#### 2.3.4.2 Three-Dimensional discrete element modeling

Compared to 2D models, 3D models have more complex structures and interactions and are closer to reality than 2D ones from the perspective of morphology. Calculation time for 3D models is usually much longer than that for 2D models, and it depends on the number of elements in the simulation system.

Several studies have been conducted using 3D models to investigate the micromechanical behavior of asphalt mixtures, such as the use of a 3D DEM model to predict the dynamic modulus and phase angle of asphalt mixtures, in which the relative errors between laboratory and simulation results are within an acceptable range [47, 93]. It is also of note that another 3D DEM model was developed to simulate the creep test of the asphalt mixture in order to determine the stiffness and the response to the creep condition [94].



Some extended simulations were also conducted to analyze the effects of element size on the mechanical behavior of the asphalt mixtures [95].

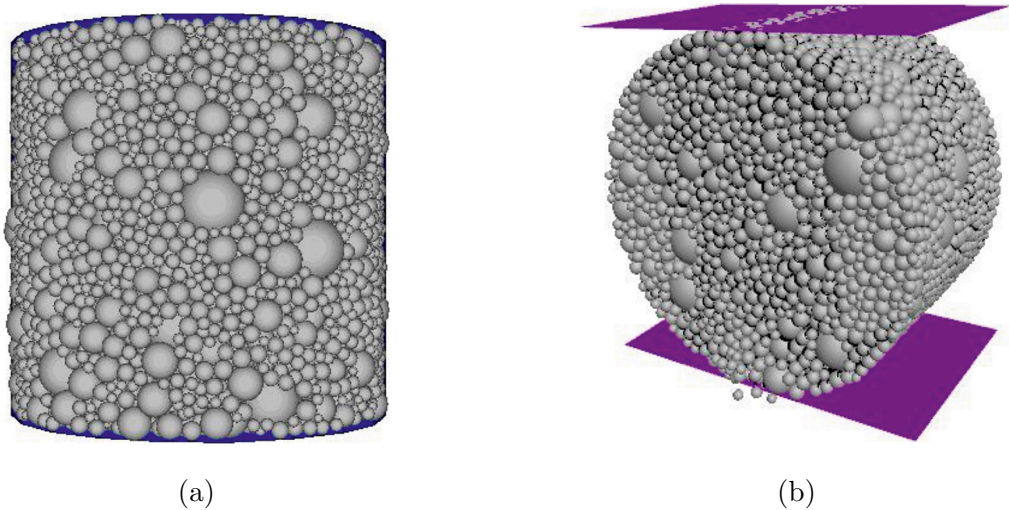


Figure 2.11: Simulating the splitting test by DEM: (a) the specimen preparation (b) the test set-up

#### 2.3.4.3 Contact model in asphalt mixture modeling

Different from FEMs that constitutive material behaviors that are usually assigned to the whole model at a macro scale, DEMs simulate mechanical material behaviors by defining contact models between particles for a packed granular assembly.

To characterize aggregate and asphalt mastic properties at the contact scale, a micro-fabric discrete element modeling approach was early developed based on linear elastic contact models [96]. Afterward, viscoelastic contact models gradually became widely used by researchers to model asphalt mastic [87, 97, 98], in order to evaluate the dynamic modulus [99, 100], creep [101] and compaction behavior of asphalt mixtures [102, 103].

Burgers model was widely used in DEM simulations of asphalt mixture in recent years and was demonstrated to be an effective way to characterize the viscoelastic behavior of asphalt mixtures [47, 48, 55, 87, 97, 101–103]. Figures 2.12 and 2.13 give contact model configurations in a DEM simulation of asphalt mixture.

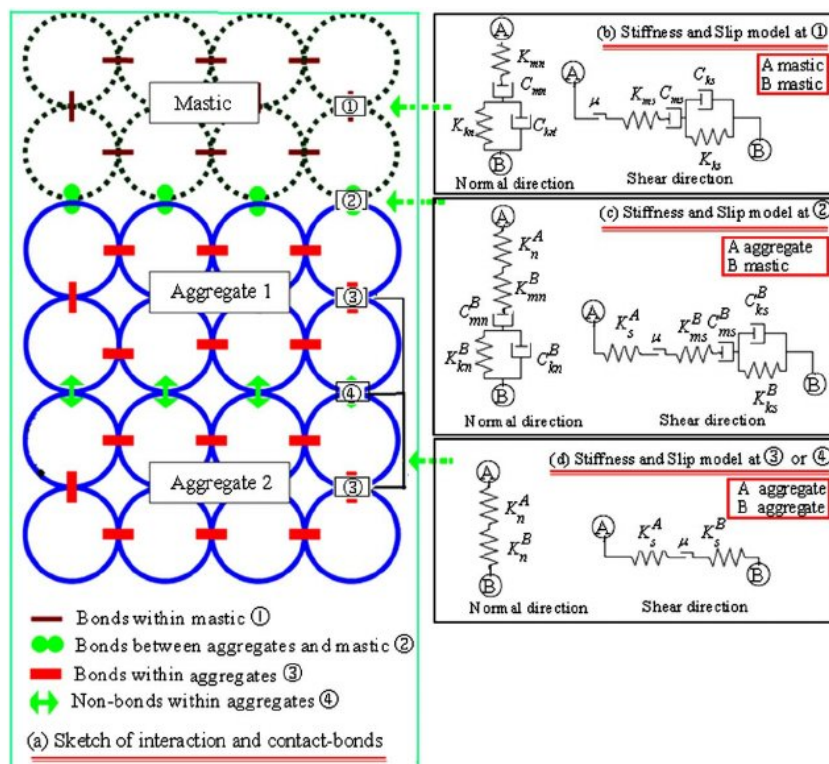


Figure 2.12: Configuration of the contact model in a DEM simulation [55]

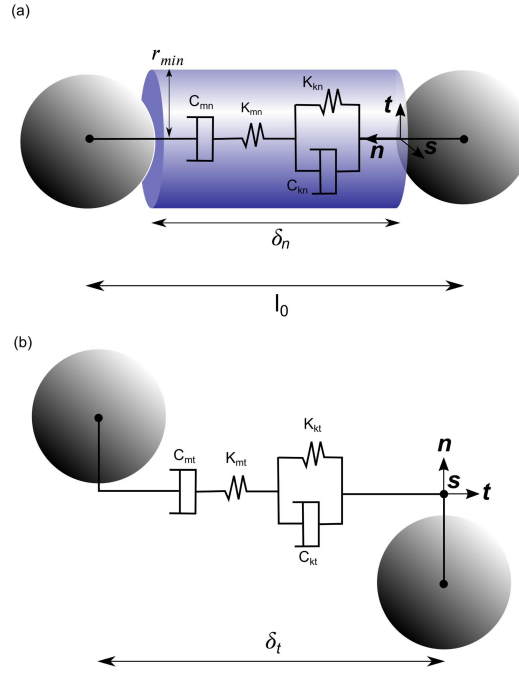


Figure 2.13: Burgers model in the local frame: (a) Normal components; (b) Tangential components [48]

By connecting the Kelvin-Voigt and Maxwell models in series, the Burgers model is able to consider the time-dependent properties of asphalt mixtures in a relatively simple and effective manner. Following is a hint as to how the Burgers model is correlated to the experimental dynamic modulus and phase angle from a macro perspective.

Total strain in the Burgers model can be written as:

$$\epsilon = \epsilon_{de} + \epsilon_{ie} + \epsilon_{cp} \quad (2.7)$$

Where,  $\epsilon_{de}$ ,  $\epsilon_{ie}$  and  $\epsilon_{cp}$  are elastic strain, viscous strain, and delayed elastic strain, respectively.

Then, the stress-strain relationship can be written as:

$$\sigma = E_1 \epsilon_{ie} = \eta_1 \frac{\partial}{\partial t} \epsilon_{cp} = E_2 \epsilon_{de} + \eta_2 \frac{\partial}{\partial t} \sigma_{de} \quad (2.8)$$

By substituting Eq. 2.8 into Eq. 2.7:

$$\epsilon = \frac{\sigma}{E_1} + \frac{\int \sigma dt + C_1}{\eta_1} + e^{\int -\frac{E_2}{\eta_2 dt}} \left( \int \frac{\sigma}{\eta_2} e^{\int -\frac{E_2}{\eta_2 dt}} dt + C_2 \right) \quad (2.9)$$

When asphalt mixtures subject to dynamic stress  $\sigma^* = \sigma_0 e^{i\omega t}$ , the resulting dynamic strain is described as  $\epsilon = \epsilon^* e^{i\omega t}$ .

The complex modulus is defined as the complex quantity:

$$\frac{\sigma^*}{\epsilon^*} = E^*(i\omega) = \left(\frac{\sigma_0}{\epsilon_0}\right) e^{i\phi} = E_1 + iE_2 \quad (2.10)$$

In which,  $\sigma_0$  is the stress amplitude,  $\epsilon_0$  is the strain amplitude, and  $\omega$  is the angular velocity, which is related to the frequency by  $\omega = 2\pi f$ .

The ratio of the stress and strain amplitudes  $\sigma_0/\epsilon_0$  defines the dynamic modulus  $|E^*(\omega)|$ , as shown in Eq. 2.11

$$|E^*(\omega)| = \sqrt{E_1^2 + E_2^2} = \frac{\sigma_0}{\epsilon_0} \quad (2.11)$$

Consequently, complex compliance, which is the reciprocal of the dynamic modulus, can be expressed using the following equation:

$$D^*(\omega) = \frac{\epsilon^*}{\sigma_0} = \frac{1}{K_m} + \frac{1}{i\omega C_m} + \frac{1}{K_m + i\omega C_k} \quad (2.12)$$

where,  $\sigma$  and  $\epsilon$  are the stress and strain at time equals zero,  $\omega$  is the radial frequency, and  $t$  is the elapsed time. The complex compliance consists of a real portion and an imaginary portion, and is normally written as:

$$D^*(\omega) = D'(\omega) + iD''(\omega) \quad (2.13)$$

$$D'(\omega) = \frac{1}{K_m} + \frac{K_k}{K_k^2 + \omega^2 C_k^2} \quad (2.14)$$

$$D''(\omega) = \frac{1}{\omega C_m} + \frac{K_k}{K_k^2 + \omega^2 C_k^2} \quad (2.15)$$

The dynamic compliance is determined as  $D^*(\omega) = \sqrt{(D')^2 + (D'')^2}$ , and the dynamic modulus is the reciprocals of the complex compliance, that is:

$$|E^*| = \frac{1}{|D^*|} = \frac{1}{\sqrt{(D')^2 + (D'')^2}} = \frac{1}{\sqrt{\left(\frac{1}{K_m} + \frac{K_k}{K_k^2 + \omega^2 C_k^2}\right)^2 + \left(\frac{1}{\omega C_m} + \frac{K_k}{K_k^2 + \omega^2 C_k^2}\right)^2}} \quad (2.16)$$

The phase angle  $\phi$  can be expressed as:

$$\phi = \tan^{-1} \frac{D''}{D'} = \tan^{-1} \left( \frac{K_m}{\omega C_m} \frac{K_k^2 + \omega^2 C_k^2 + \omega^2 C_k C_m}{K_k^2 + \omega^2 C_k^2} + K_k K_m \right) \quad (2.17)$$

Eqs. 2.7–2.17 describe the equations for determining the macro-scale parameters of asphalt mixtures. However, for the DEM simulations, the microscale parameters need to be determined further at the contact scale according to the macroscale parameters, and more details about the implementation of the Burgers model in the Contact Dynamics (CD) method will be given in the chapter 4.

#### 2.3.4.4 Mesoscopic structure containing irregular particles

For simulating an asphalt mixture, it is required to generate the mesoscopic structure of the mixture. As the geometries of aggregate particles play an essential role in the mixture performance [104–108], establishing a numerical model close to the real particle assembly is an issue that deserves much attention.

Image technique was widely adopted to characterize the internal structure of asphalt mixture for numerical simulation in the 2D [86, 99, 109, 110] and 3D DEM models [111–113]. However, image-based models are dependent on the prepared physical specimens; it is not capable of providing an absolute virtual environment for numerical simulations of asphalt mixtures. Sensitivity analysis of component properties such as aggregate morphology and spatial distribution based on this method is also limited due to the difficulty of controlling these factors precisely in the sample preparation.

Regarding the statistical assessment of the variation for mixture composition, the structure reconstruction based on image-based methods is limited [114]. Consequently, establishing a strategy to flexibly generate numerical samples resembling real asphalt specimens is suitable for creating a fully virtual environment and estimating systematically effective properties for asphalt mixtures.

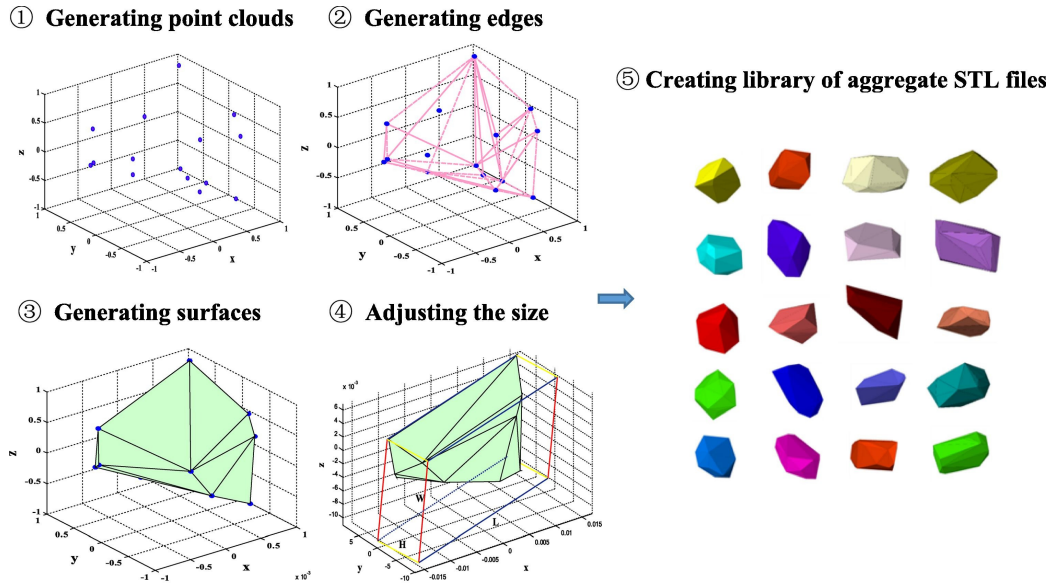
Currently, some research was conducted on the mixture simulation composed of random particle shapes, based on computer-aided algorithms [115–119] and laser scanning devices [120, 121].

The use of computer-aided algorithms allows the creation of large particle-shape databases in a short amount of time without requiring the use of laser scanners or other complex imaging techniques, which shows superior flexibility and independence compared with other methods. However, as the generated particles are usually created randomly, a large difference between the actual particle shape and the generated particle shape usually occurs. Figure 2.14 shows the generation process of particle shapes using computer-aided algorithms and the generated asphalt sample.

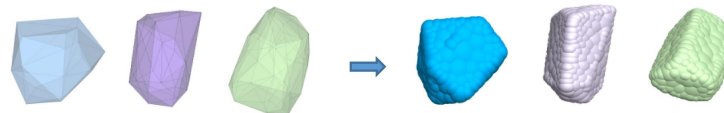
In most of these studies, after the particle geometry reconstruction, the particles were imported into numerical models and were modeled as simplified clumps composed of limited overlapping spheres or disks [123], neglecting crucial particle features such as angularity, as illustrated in Figure 2.15. This simplification may affect granular fabric properties such as porosity, contact anisotropy, and force chains network [124, 125]. In addition, although high-resolution particle clumps can properly simulate real particles, the huge computation cost is not affordable yet.

On the other hand, particle shapes used in a numerical model are usually selected from limited templates or created randomly in the simulation. The particle morphology distribution in the real mixture assembly cannot be represented adequately in the numerical specimens due to the rich variability of actual particle shapes. Indeed, as mentioned in section 2.3.3, the X-ray CT technique could be used to obtain the mesostructure of the whole asphalt sample, so that both particle morphology and size distributions would be better considered [100]. However, this method is physical specimen dependent, which can not provide a fully numerical environment for asphalt mixture modeling. Besides, the model accuracy is also highly dependent on the image processing technique, which is usually time-consuming. Moreover, the CT device is usually expensive and lacks flexible mobility.

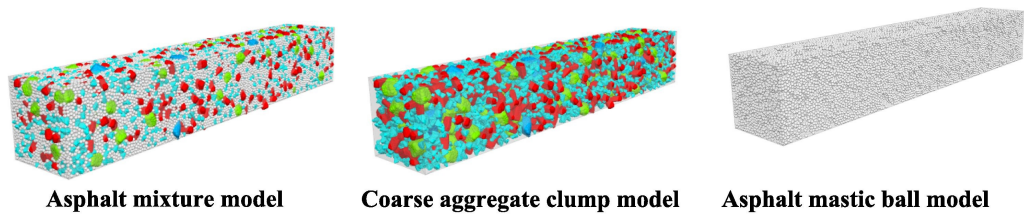
Moreover, the preparation of numerical samples composed of polyhedral particles is an extraordinarily time-consuming process: complex algorithms are required in contact detection and repulsive force computation during the preparation stages, such as gravity deposition, compaction, and stabilization of numerical samples.



(a) Step 1: generating polyhedron aggregate STL files



(b) Step 2: generating aggregate clump templates



(c) Step 3: generating asphalt mixture model

Figure 2.14: Generation process of asphalt mixture DEM model based on computer-aided algorithm [122]


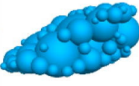
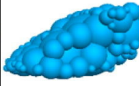
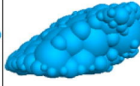




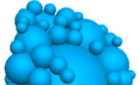
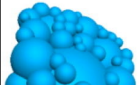
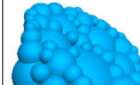
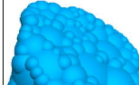
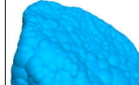

Geometry	Value of Distance					
	70	90	110	130	150	170
						
						

Figure 2.15: Variation of clump template influenced by distance [121]

## 2.4 Asphalt mixture responses under tire loads

### 2.4.1 Accelerated pavement testing analysis

For the evaluation of pavement performance under in-service traffic and environmental conditions, accelerated pavement testing (APT) facilities are traditionally used [126]. The design of these facilities is generally aimed at providing cost-effective solutions to improve pavement performance, as well as lowering life-cycle costs.

To test pavement response and performance under controlled, accelerated damage accumulation in a compressed time period, an APT involves applying a prototype wheel loading at or above the design load limit to an actual pavement structure.

It is possible to accelerate damage by performing repeated activities, altering loading conditions, imposing climatic conditions, and using various pavement structures or materials with reduced structural capacity.

There are two main types of APT systems: small-scale systems and full-scale systems.

For small-scale APT systems, a scaled-down version of the tire load is applied to the pavement system or test specimens. The model mobile load simulator



(MMLS3) has been developed as an accelerated pavement testing device on a small scale, which is capable of characterizing asphalt mixture performance including material bearing capacity and fatigue behavior when rolling tires in a repetitive motion for a huge amount cycles in a short period [127–129]. Figure 2.16 shows a working scheme of MMLS3.

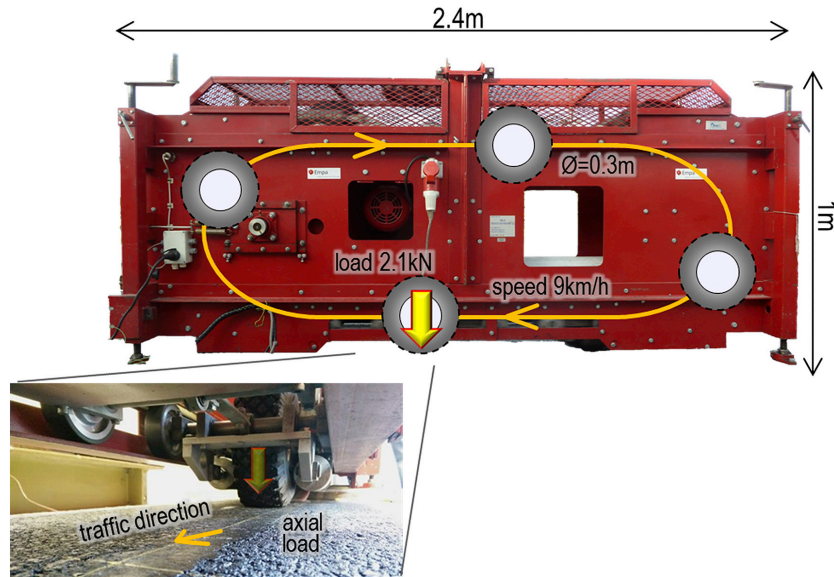


Figure 2.16: The MMLS3 applies repetitive loading through four wheels [129]

For accurate simulation of real-world conditions, full-scale test construction using conventional plants and processes is required [130]. Full-scale APT systems employ truck tires or combinations of tires to apply loads on pavements [1–4, 131]. Figure 2.17 shows some examples of different types of APT facilities used around the world.

Through APT facilities, an in-depth understanding of pavement performance, structure design, and construction process has been gained [133]. The APT also maintains a significant presence in the creation, design, rehabilitation, and innovation of pavement materials and designs.

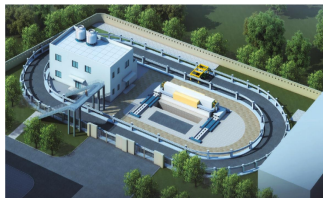
In summary, despite the high cost of both financial and construction resources from conducting full-scale APT tests, the full-scale APT method is an effective approach for assessing macroscopic pavement performance under real tire loading. Nevertheless, it is still a struggle to get insight into the internal mechanisms of the mixture damage from a microscopic point of view



(a)



(b)



(a) Layout of the entire system



(b) Loading vehicle in the NE-ALT system

(c)



(a)



(b)

(d)

Figure 2.17: (a) HVS in FDOT's APT facility [3] (b) APT facility of IFST-TAR [131] (c) Natural Environment-Automatically Loaded Track (NE-ALT) system [4] (d) Full-scale loading test based on MLS66 equipment [132]

by using APT.

### 2.4.2 Analytical modeling analysis

Due to the viscoelastic nature of asphalt mixtures, it is well known that the mechanical response of asphalt pavement under moving tires depends on time, loading rate, and the entire loading profile.

In early analytical models, limited by the computational capacity, it was often assumed that the tire load was a uniform static load, whereas the material constitutive relationship between each layer was assumed to be elastic in order to simplify the solution of the analytical model. Pavement analysis software packages, such as BISAR [134], KENLAYER [16] [135], LEAF [135] and ALIZÉ-LCPC [136, 137], were developed using this simplified model. It is efficient to use a simplified mechanical model based on linear elastic layer analysis. Nevertheless, the model is not applicable to the practical situation, which could result in inaccurate results.

There is therefore a great need for effective analytical solutions for the analysis of viscoelastic asphalt mixtures under complex loads. Several researchers have studied viscoelastic solutions of asphalt pavement analytically based on circular loads and rectangular loads [138–140]. However, these solutions focused on simplified loads which are not sufficient to describe complex loads. Considering realistic non-uniform tire loads and the viscoelastic properties of asphalt mixtures in an analytical model still remains challenging.

### 2.4.3 Finite element modeling analysis

The use of FEM has been proven successful in performing viscoelastic analysis and integrating complex loads [141]. For examining asphalt mixture responses under non-uniform tire loads, there are several studies proposed by researchers. Wang et al. [34] investigated the effects of tire types on pavement responses at the near-surface position and provided a reference for the truck tire optimization. After that, they further studied the near-surface cracking mechanism under critical loading conditions [25]. The results show that tire braking/acceleration and cornering induce high tangential contact stresses on the pavement surface, which could significantly accelerate the surface crack propagation. Wollny et al. [38] proposed a strategy to simulate a rolling tire on the pavement surface based on FEM and indicated

that tire rolling conditions have significant effects on macroscopic pavement performance. The relevant numerical model is shown in Figure 2.18.

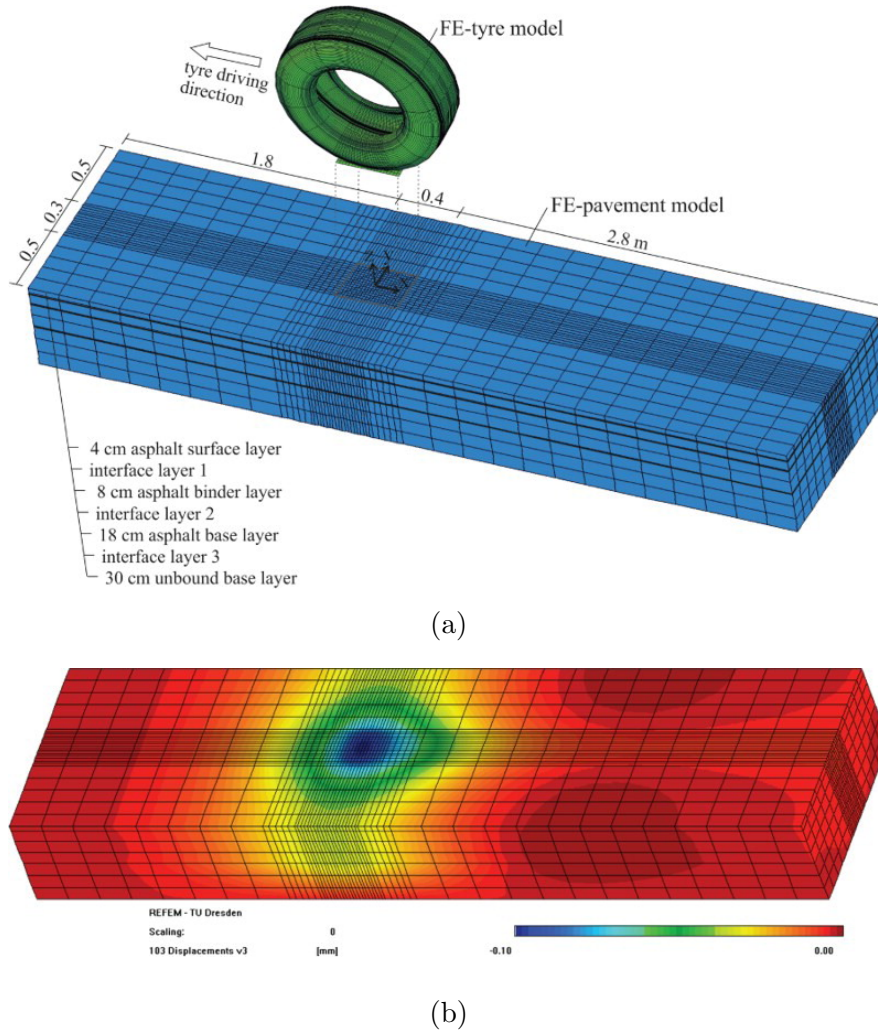


Figure 2.18: (a) Discretisation of coupled ALE tire-pavement interaction model (b) Vertical displacements of pavement model at 5 km/h

The effects of random non-uniform tire loads on asphalt pavement responses were examined using FEM simulations [142]. Using a constant uniform load without accounting for the random and spatial characteristics, the results indicate that the surface layer is underestimated for damage. According to the analysis of the impact of non-uniform tire-pavement contact stresses on asphalt pavement responses, shear contact stress plays a significant role in

controlling the evolution of rutting and longitudinal cracks [33].

Current research has primarily focused on macro simulations of the tire-pavement interaction, in which the asphalt pavement is usually assumed homogeneous due to the limitation of mesh-based methods in the continuum mechanics framework. For the calculation of tire contact stresses, in most of research works, the asphalt mixture is assumed as homogeneous. This assumption is rational when we focus on the tire load distribution on the pavement surface as tire contact stresses can be realistically represented through the mesh-based methods in the continuum mechanics framework. Indeed, Wollny et al. [143] proposed a consistent simulation chain based on FEM to examine the micro-structural asphalt model responses under realistic rolling tire loads. However, the simulation was conducted in the frame of FEM, which has limitations in describing contact status of individual particles. Moreover, when it comes to describing the internal asphalt mixture local responses, the homogenization assumption of asphalt mixture is insufficient as it cannot examine the mixture's mechanical performance from a microscopic level. Consequently, modeling a mixture structure while considering its different components and their respective properties explicitly is desired.

#### 2.4.4 Discrete element modeling analysis

This dissertation aims to examine asphalt mixture responses under various tire rolling conditions at the particle level. As introduced before, DEM offers an alternative way to assess asphalt mixture behavior at the particle scale. Several DEM models were built in 2D to investigate the asphalt layer responses under tire loads, including surface wear [144] and crack development [145]. Figure 2.19 shows the 2D model for transverse crack analysis.

However, the tire loading conditions used in current studies are usually uniform and simplified, which cannot reflect real non-uniform tire loads. Further, predicting the performance of asphalt mixtures based on 2D models might be unreliable due to the fact that they lack a full description of the heterogeneous structure of the asphalt mixture. Due to the computational costs involved in simulating tire load effects on asphalt mixtures using DEM in 3D, some DEM models simulate wheel tracking tests (WTTs) [117,122,146]

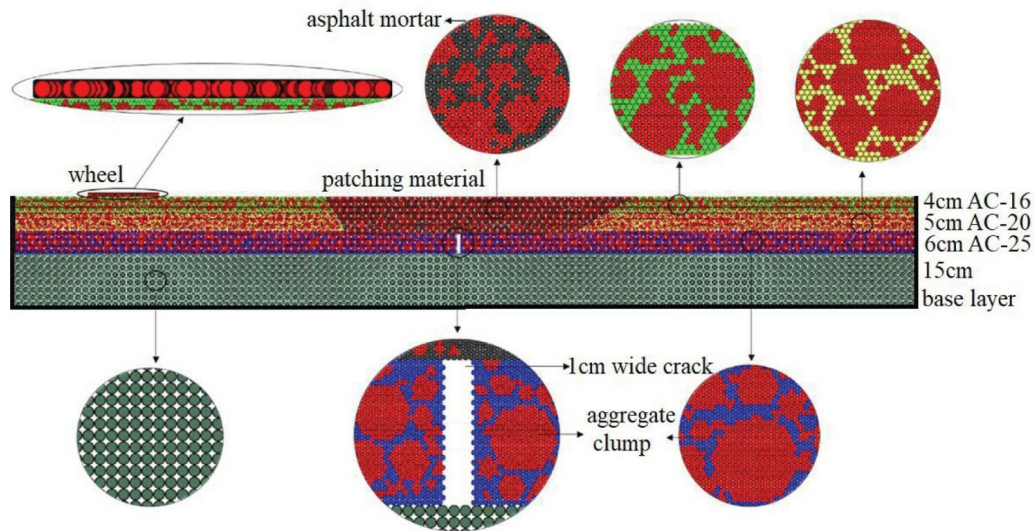


Figure 2.19: Analysis model for transverse cracks under wheel load [145]

to indirectly examine asphalt mixture responses under tire loads, as shown in Figure 2.20.

Nevertheless, these simulations are compromised by size effects and simplified boundary conditions that come from WTTs, which inhibit accurate predictions of mixture responses.

Despite its promise in examining the mechanical properties of asphalt mixtures at the particle level, DEM is inadequate to accurately simulate deformable tire structures and capture realistic tire contact forces on pavement surfaces.

Consequently, a coupling simulation incorporating FEM and DEM appears necessary to investigate non-uniform tire loads on asphalt mixtures at the particle level.

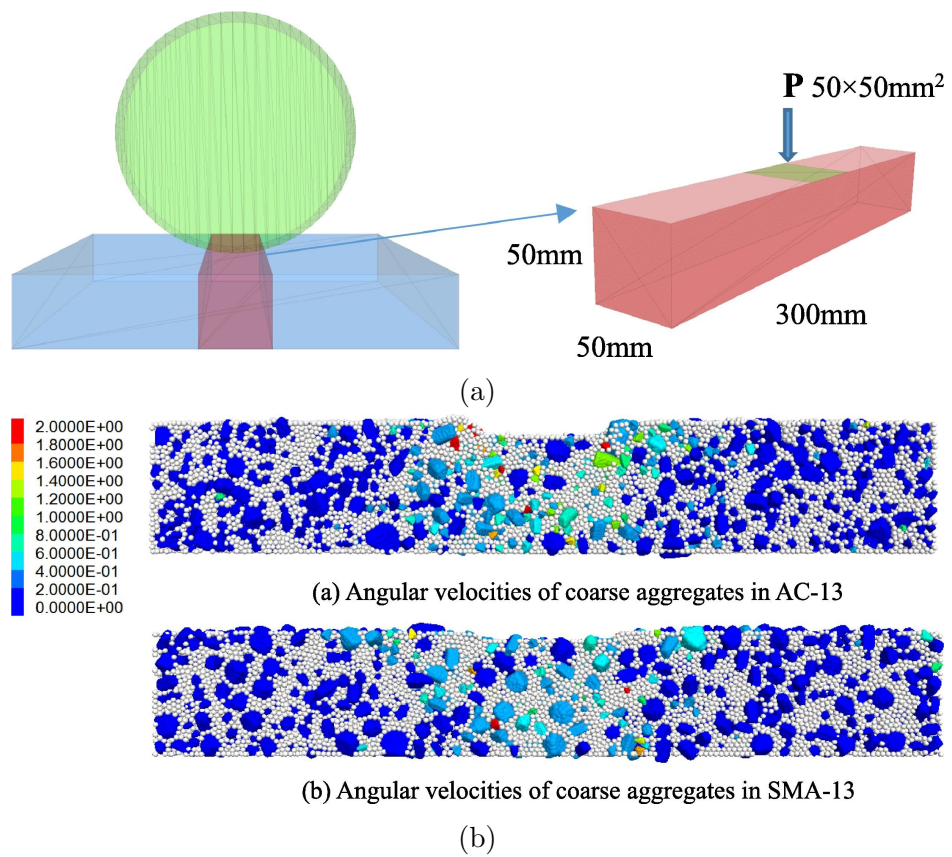


Figure 2.20: (a) Applied wheel loading assumption (b) Angular velocities of coarse aggregates [122]

## 2.5 Multi-scale coupling simulation

A number of studies have demonstrated that multiscale modeling significantly improves the accuracy of structural prediction with a significant reduction in computation effort [147–149]. As opposed to modeling the entire large scale, the multiscale model only considers properties of individual components of the mixture as well as microstructure characteristics at the smaller scale.

Multiscale approaches can be divided into two different types: for the first multiscale approach, a representative microscale sample of the heterogeneous material structure is used to represent the constitutive behavior of an infinitesimal point of material at the macroscale. The separation of scales is an important assumption of this multiscale approach [150]. It is therefore necessary to define a representative volume element (RVE), which is statistically representative for the entire heterogeneous composite. Considering that the inclusions should represent the overall composite behavior effectively [151], the RVE is therefore large compared to the characteristic dimensions of the microstructure (i.e., particle diameters), but relatively small in comparison to the entire macrostructure [152].

The multiscale modeling method proposed by Yamashita et al. [153] belongs to this first approach, as shown in Figure 2.21.

The RVE is used to simulate the soil status located at a Gauss point within a FEM element inside the road. Therefore, the dimensions of RVE are relatively very tiny compared to the tire contact area. As the soil materials are constituted of considerably fine grains (diameter  $< 0.002$  mm), the RVE is valid for this kind of material.

Nevertheless, the RVE application to the asphalt pavement is not proper since the aggregate size (grain size up to  $2\text{--}3$  cm) does not significantly differ from the macrostructural dimensions (asphalt layer thickness is usually between  $4\text{--}20$  cm).

For the second type of multiscale approach, the assumption of scale separation is not required. This approach links the microscale to macroscale structures directly, A number of studies have been conducted to explore the interaction between unbound materials and tires using this approach [154, 155]. The hierarchical refinement in macroscale subdomains is generally performed



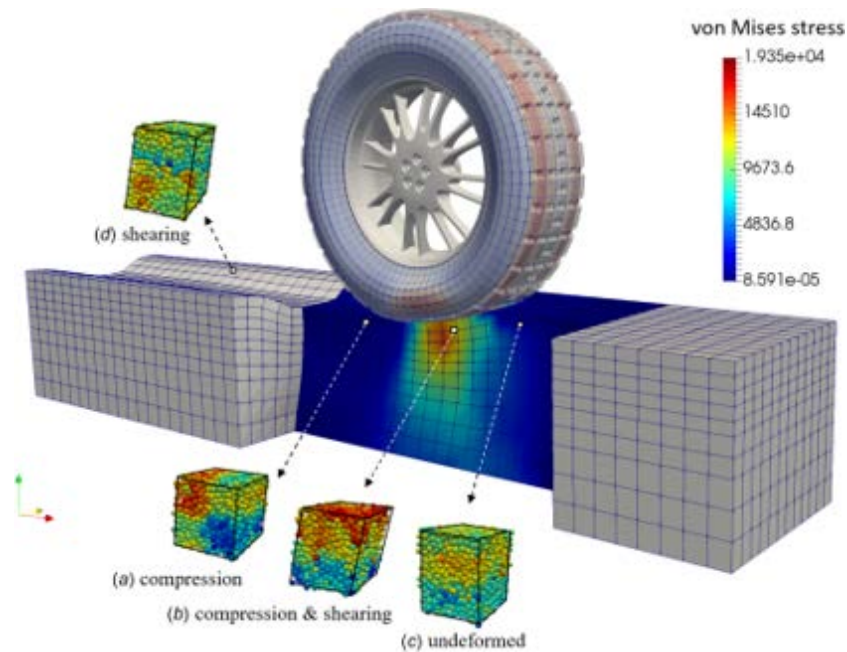
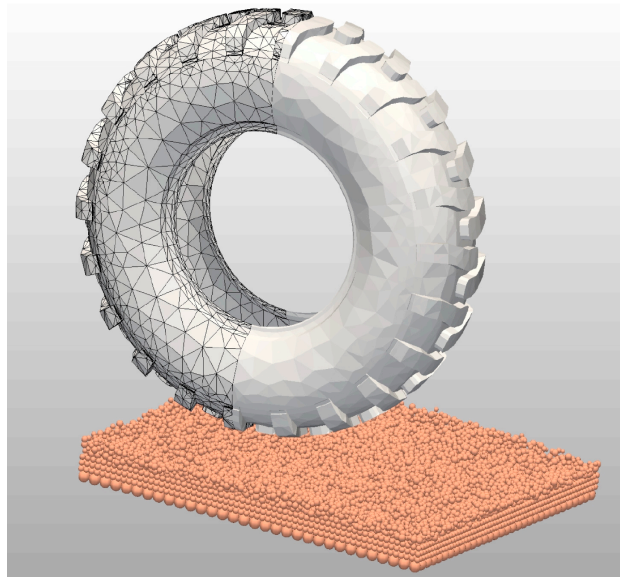


Figure 2.21: Multiscale tire–soil interaction simulation based on RVE using moving soil patch approach [153]

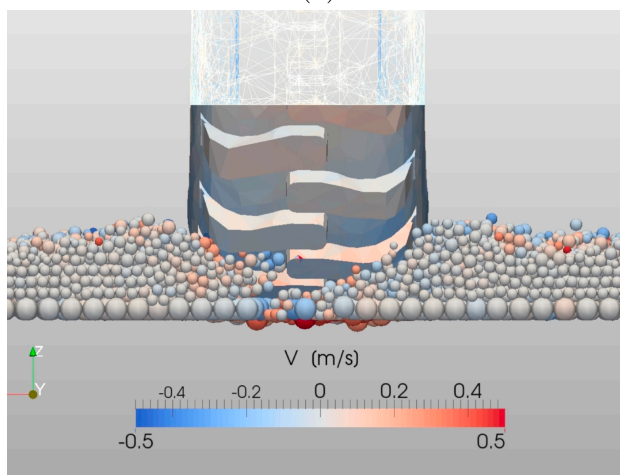
locally for some specific parts of the macroscale model. Figure 2.22 shows the multi-scale modeling of tire-soil interaction through using this approach.

However, the current research mainly focuses on the simulation of unbound materials such as sands, soils, and gravels. The contact laws used are mainly frictional and the particle shape is usually limited to spheres because of computation costs. Moreover, the road surface made with unbound materials is relatively soft compared to the asphalt pavement surface, which leads to different tire contact stress distributions on these two kinds of road surfaces.

Computation cost in the DEM simulation of asphalt mixtures considering both the visco-elastic contact model and irregular particle shapes is already huge. The massive contact detection between the FEM tire elements and DEM asphalt mixture particles, as well as the internal calculation of the FEM elements make a calculation based on a deformable FEM tire object in a DEM simulation at the same time is not affordable yet. Considering the visco-elastic nature and irregular particle shapes in an asphalt mixture, the current coupling simulation methods are inadequate for simulating asphalt pavement



(a)



(b)

Figure 2.22: (a) Initial soil bed and tire configurations (b) The tire during travel through the soil bed [155]

and tire interaction. Consequently, a new coupling framework dedicated to the interaction system between the tire and the asphalt pavement surface is required.

## 2.6 Conclusions of the chapter

In this chapter, we reviewed the literature for investigating the tire-pavement interaction system. The importance of using realistic tire loads in the pavement design was first emphasized, then the components of the tire-pavement interaction system including research on tire load determination, asphalt mixture models, and asphalt mixture responses under tire loads were extensively introduced and both experimentally and numerically discussed.

Currently, experimental measurements and numerical tire models are used to estimate tire-pavement contact stress, in which numerical methods have more flexibility than traditional experimental tests in describing various tire loading conditions. Numerical tire models vary in complexity according to their features and purpose. To predict precise tire-pavement contact stresses, deformable tire and pavement structures, as well as contact formulations between the rolling tire and the pavement surface, must be incorporated into the model.

For macro simulations of asphalt mixture responses, FEM analysis has been widely used because of its computation efficiency and high flexibility in describing complex loads and material behaviors. However, the asphalt pavement is usually assumed homogeneous in macro FEM simulations due to the limitation of mesh-based methods in the continuum mechanics framework. Asphalt mixtures are actually complex multi-phase systems composed of aggregate particles and asphalt mastic. Mesh-based methods can simulate tire contact stresses precisely on the pavement surface, but it is still a struggle to quantify internal mixture responses at the particle scale.

Even though DEM offers a promising way to examine asphalt mixture responses at the particle level, it is inadequate to represent deformable tire structures and capture realistic tire contact forces on pavement surfaces. Besides, DEM is typically only used for small-scale simulations as limited by its high computation costs. Furthermore, in most studies that generate mesoscopic asphalt mixture structures using DEM, particle shapes are selected

randomly or derived from limited templates. Due to the rich variability of actual particle shapes, the distribution of particle morphology in the real mixture assembly was not reproduced adequately in numerical specimens.

Although the aforementioned studies from the literature review enrich our understanding of tire-pavement interaction mechanisms, it is still challenging to integrate realistic rolling tire loading conditions into a numerical model that can evaluate asphalt mixture responses quantitatively from a microscopic scale, consistently, the particle scale. Consequently, using a coupling simulation incorporating FEM and DEM is imperative to investigate tire-pavement interaction from a macroscale to a microscale. For asphalt pavement and tire interaction simulation, the current coupling methods are not suitable due to the visco-elastic nature and complex mesoscopic structure of asphalt mixtures. Therefore, a coupling framework dedicated to the interaction between the tire and asphalt pavement surface is timely desired. In the following chapters, the dedicated multi-scale coupling simulations implementing FEM and DEM will be presented to examine internal asphalt mixture responses both macroscopically and microscopically under realistic non-uniform tire loads and rolling conditions.



# Tire-sensor-pavement coupling chain based on FEM

---

## Contents

---

<b>3.1</b>	<b>Introduction</b>	<b>44</b>
<b>3.2</b>	<b>Laboratory tests</b>	<b>45</b>
3.2.1	Tire contact stress distributions on the pavement surface	45
3.2.1.1	Experimental set-up	45
3.2.1.2	Measuring results	45
3.2.2	Asphalt mixture complex modulus test	46
3.2.2.1	Two point bending test configuration	46
3.2.2.2	Laboratory test results	49
<b>3.3</b>	<b>Asphalt mixture modeling and material characterization</b>	<b>51</b>
3.3.1	Viscoelastic material characterization for asphalt mixture	51
3.3.2	Validation of the VENO <sub>L</sub> model	53
<b>3.4</b>	<b>Coupling chain for the tire-sensor-pavement system</b>	<b>56</b>
3.4.1	Numerical asphalt layer building and coupling algorithm	56
3.4.2	Asphalt layer property identification under rolling tire loads	57
3.4.3	Dynamic simulation of asphalt layer responses under rolling tire loads	60
<b>3.5</b>	<b>Asphalt layer responses under varied loading conditions</b>	<b>64</b>
3.5.1	Dynamic responses of asphalt layer under different tire rolling velocity	64
3.5.2	Dynamic responses of asphalt layer under different tire loads	65

---

3.5.3	Dynamic responses of asphalt layer under different tire inflation pressures . . . . .	68
3.5.4	Dynamic responses of asphalt layer at different temperatures . . . . .	70
<b>3.6</b>	<b>Conclusions of the chapter . . . . .</b>	<b>74</b>

---

## 3.1 Introduction

As discussed in Chapter 2, linear elastic layer theory and uniform tire load assumption are widely used in conventional pavement design for calculating critical pavement responses. However, asphalt pavement surface damage occurred with interaction with vehicle tires is becoming hardly predictable by using traditional simplified design methods due to the development of traffic technology and the increasing traffic loads.

It has been demonstrated in a lot of research that actual tire loads induce quite different pavement responses compared with uniform loads [21–23], especially in investigating pavement surface deterioration [24,25]. It is therefore imperative to implement actual complex loads in numerical simulations to understand in-depth pavement responses under realistic tire loading conditions.

The use of finite element modeling (FEM) to investigate pavement performance at a macroscopic scale under various boundary conditions has been widely used for decades, especially for examining macroscopic asphalt pavement behavior.

Tekscan sensor measuring system has been proven to be an efficient way to measure tire-pavement contact stresses at varying tire loads, as discussed previously [27,32].

In the present chapter, we used the Tekscan system to capture realistic tire contact stress distributions on the asphalt pavement surface. Further, the asphalt mixture property was characterized using the so-called NOnLinear ViscoElastic (VENoL) model and the model reliability was validated by conducting the complex modulus test both experimentally and numerically based on the two-point bending configuration. As static loading is inadequate

to examine asphalt mixture responses under rolling tire loads, a new tire-sensor-pavement coupling chain was developed for integrating actual rolling tire loads in asphalt layer modeling. Finally, the dynamic response of the asphalt layer under rolling tire loads is analyzed and discussed.

## 3.2 Laboratory tests

### 3.2.1 Tire contact stress distributions on the pavement surface

#### 3.2.1.1 Experimental set-up

For measuring tire contact stresses on pavement surfaces, a pressure sensor measuring system named Tekscan (<https://www.tekscan.com/>) was used. This system is in the form of a thin film with dimensions of length  $\times$  width  $\times$  thickness = 704.1 mm  $\times$  625.9 mm  $\times$  0.102 mm, on which square elementary sensors of 7.112 mm side are distributed. Creating the sensor requires the use of two polyester sheets. The first sheet was composed of evenly separated piezoresistive materials (sensors). Similarly, the same sensors were placed on the second sheet, but perpendicular to the first sheet. Tekscan sensors operate according to the principle that their resistance varies depending on the applied stress. The electronic sheet is incompressible and operates between  $-40\text{ }^{\circ}\text{C}$  and  $60\text{ }^{\circ}\text{C}$ , with a moisture percentage ranging between 5 % to 90 %. Figure 3.1 shows the sensor measuring system and experimental test process. It should be noted that the pressure sensor device was calibrated with a load of 45 kN under a press system prior to carrying out the measurements. During sensor calibration, the software calculates an average applied pressure based on the area of the loaded sensor and the force applied until achieving acceptable convergence.

#### 3.2.1.2 Measuring results

In the present study, a truck tire (315/80 R 22.5) was chosen, and measuring tests were conducted under different tire loading conditions including two inflation pressures (6.0 bar and 8.0 bar) and three loads (10 kN, 15 kN, and 20 kN). Figure 3.2 shows the tire pressure measuring results for these loading conditions. As shown in the figure, tire contact stress distributions under all tire loading conditions are nonuniform across the whole contact



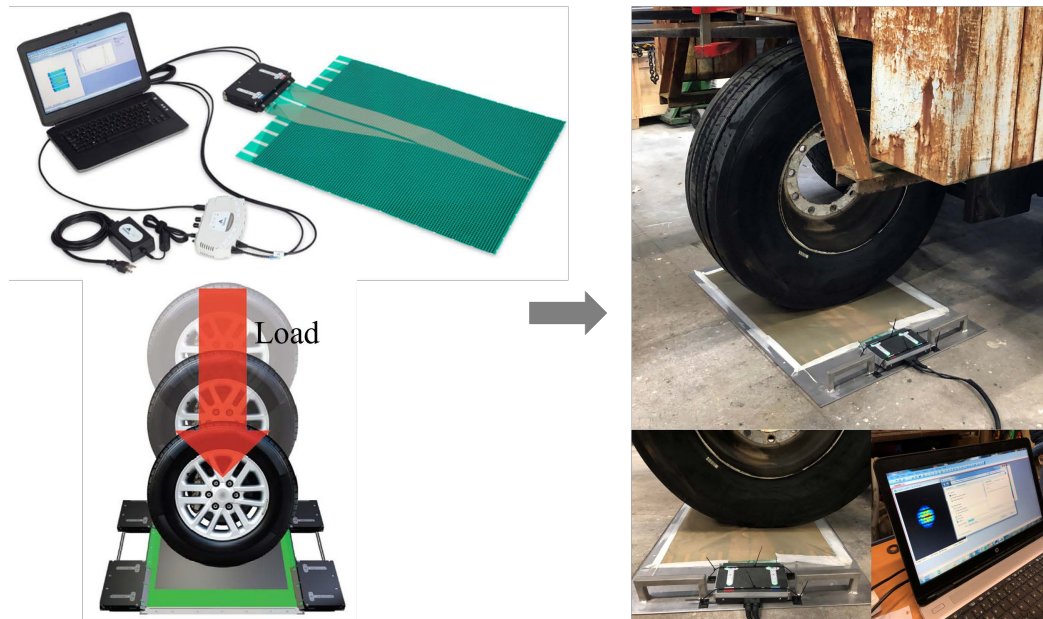


Figure 3.1: The sensor measuring system (from <https://www.tekscan.com/>) (Left), Experimental test measuring process (Right).

area. as expected, the peak values of tire contact stress concentrate on the center area of the tire footprint and they are much bigger than the tested tire inflation pressure. Besides, with the increment of tire loads, the contact area increases obviously from center-concentrated to side-flatted while the peak value of tire contact stress increases slightly for both tire inflation pressures. Additionally, the tire contact stresses significantly increase with increasing tire inflation pressures for all three tire loads. It seems that the tire contact stress distribution is more sensitive to tire inflation pressures compared with tire loads.

## 3.2.2 Asphalt mixture complex modulus test

### 3.2.2.1 Two point bending test configuration

The experimental campaign was conducted on trapezoidal samples, using a two-point bending (2PB) configuration according to the EN 12697-26:2012 specification [45]. Three trapezoidal samples were prepared with a French asphalt concrete type (BBMA 0/10), and the bitumen is 35/50 grade. The density of each trapezoidal sample is on average  $2.371 \text{ g/cm}^3$ , and the air

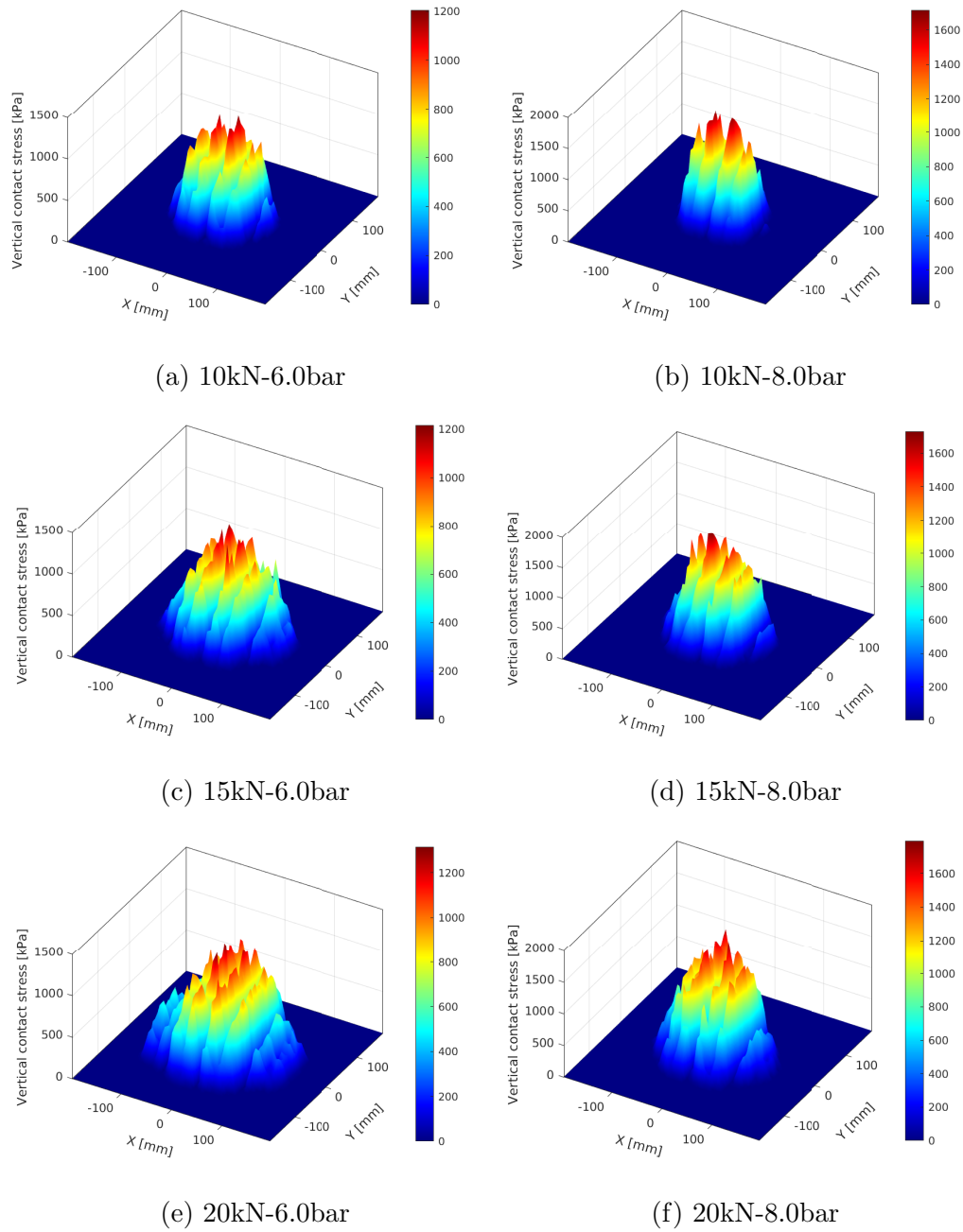


Figure 3.2: Tire contact stress distributions under different loads and inflation pressures

void is on average 1.57 %. Table 1 displays the particle size distribution (PSD) of the employed asphalt mixture.

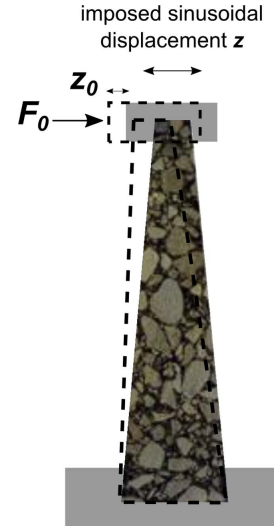
Table 3.1: Particle size distribution (PSD) of asphalt mixture

Diameter (mm)	12.5	10	8	6.3	4	2	1	0.5	0.25	0.125	0.063
PSD (%)	100	90	64	44	36	32	22	17	13	11	7.3

As shown in Figure 3.3, on each trapezoidal sample, a sinusoidal displacement  $z = z_0 \sin(\omega t)$  was imposed at the target frequency, with a peak displacement  $z_0$  of  $63 \times 10^{-6}$  m, corresponding to a strain amplitude of  $50 \times 10^{-6}$  at the top of the sample. The maximum force  $F_0$  and the phase angle  $\phi$  were measured during the last 10 seconds of the test.



(a) Experimental test device



(b) Test loading conditions [48]

Figure 3.3: 2PB test configuration

To identify the viscoelastic properties of the asphalt mixture, the real part  $E_1$  and the imaginary part  $E_2$  of the complex modulus  $E^*$  can be calculated by Equations (Eqs) 3.1 and 3.2:

$$E_1 = \gamma \left( \frac{F_0}{z_0} \cos(\phi) + 10^{-6} \mu \omega^2 \right) \quad (3.1)$$

$$E_2 = \gamma \frac{F_0}{z_0} \sin(\phi) \quad (3.2)$$

where  $\omega$  is the angular frequency,  $\gamma$  ( $mm^{-1}$ ) is a shape factor depending on the dimensions of the specimen:  $B = 56$  mm,  $b = 25$  mm,  $e = 25$  mm and  $h = 250$  mm, and  $u$  is the mass factor, both described by:

$$\gamma = \frac{12h^3}{e(B-b)^3} \left[ \left(2 - \frac{b}{2B}\right) \frac{b}{B} - \frac{3}{2} - \ln \frac{b}{B} \right] \quad (3.3)$$

$$u = 0.135M + m \quad (3.4)$$

where, the average total sample mass  $M$  is 0.6 kg, the mass of the mobile equipment overhead  $m$  is 0.235 kg.

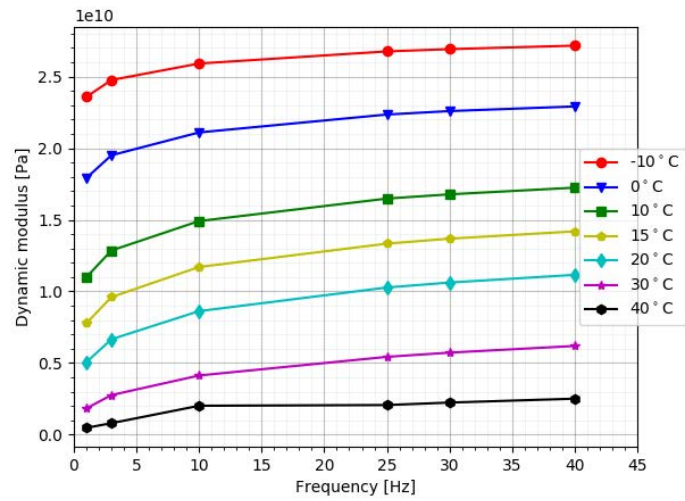
Finally, the dynamic properties can be determined as:

$$|E^*| = \sqrt{E_1^2 + E_2^2} \quad (3.5)$$

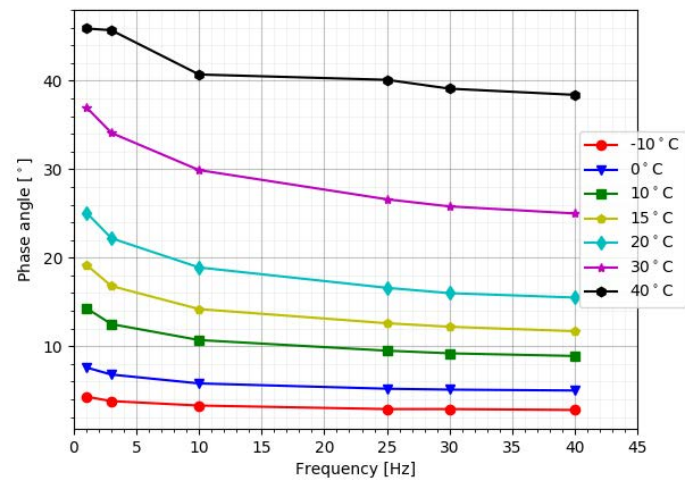
$$\phi = \arctan(E_2/E_1) \quad (3.6)$$

### 3.2.2.2 Laboratory test results

For the measurement of the dynamic modulus  $|E^*|$  and phase angle  $\phi$ , the frequency values tested were set as 1, 3, 10, 25, 30 and 40 Hz, while the selected temperature values were -10, 0, 10, 15, 20, 30 and 40 °C. The experimental results are shown in Figure 3.4. As it could have been expected, the dynamic modulus  $|E^*|$  decreases and the phase angle  $\phi$  increases with increasing temperature and decreasing frequency, respectively.



(a) Dynamic modulus



(b) Phase angle

Figure 3.4: Experimental results for the 2PB test

## 3.3 Asphalt mixture modeling and material characterization

### 3.3.1 Viscoelastic material characterization for asphalt mixture

Asphalt mixture is a complex composite exhibiting viscoelastic behavior. The VENoL (NOnLinear ViscoElastic) model [67] was adopted in this study to characterize the asphalt mixture behaviors. This model can represent the viscoelastic behaviour by calculating the instantaneous complex stiffness modulus according to the temperature  $T$  of the environment, the pulsation (or angular frequency)  $\omega$  and the strain amplitude  $\varepsilon_0$  of the imposed signal. Schematically, the VENoL model can therefore be represented with two elements  $\Re_E$  and  $\Im_\eta$  mounted in parallel (Figure 3.5).

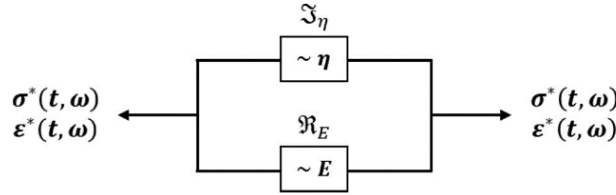
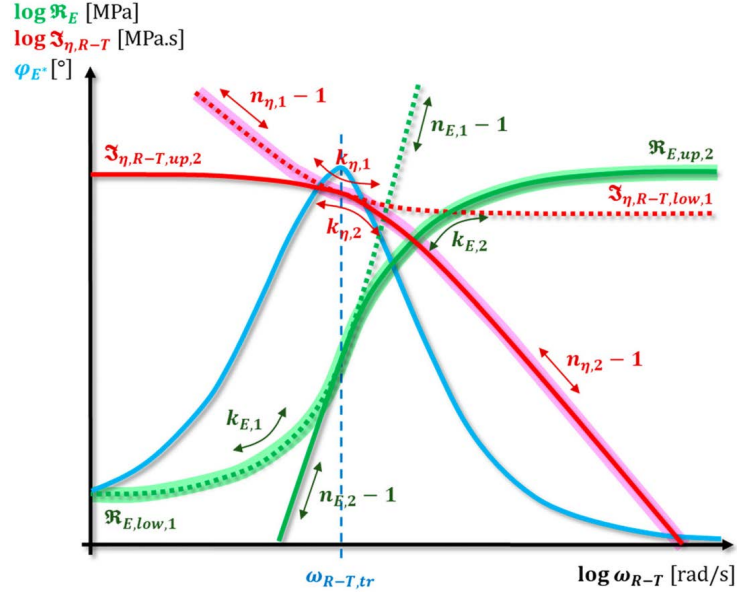


Figure 3.5: VENoL model [67]

In dynamic analysis, the complex stiffness modulus  $E^*(t)$  can be split into a real part  $\Re(E^*)$  and an imaginary part  $\Im(E^*)$ . Using  $\Im(E^*)$  divided by the signal pulsation  $\omega$ , we can calculate  $\Im_\eta$  as the "viscosity component". In the same way, we replace  $\Re(E^*)$  by  $\Re(E)$  named as the "stiffness component". Analogously, the general equation obtained naturally possesses a structure similar to the Kelvin-Voigt model. However, in the VENoL model, both the stiffness component  $\Re(E)$  and the viscosity component  $\Im_\eta$  depend on the environment temperature  $T$ , the pulsation  $\omega$  and the strain amplitude  $\varepsilon_0$  of the imposed signal.

By composing the Time-Temperature Superposition Principle (TTSP) [156, 157] with the Carreau–Yasuda (CY) model [158, 159], the illustration of VENoL model parameters and equations is given in Figure 3.6.

Figure 3.6a displays that the variations of the stiffness component  $\Re_E$  (green curves) and the reduced viscosity component  $\Im_{\eta, R-T}$  (red curves) are defined



(a) Evolution parameters

$$\mathfrak{R}_E(T, \omega) = \begin{cases} \text{if } \omega_{R-T} \leq \omega_{R-T,tr}, \\ \mathfrak{R}_{E,low,1} \cdot [1 + [\lambda_{E,R-T,1} \cdot \omega_{R-T}]^{k_{E,1}}]^{n_{E,1}-1} \\ \text{-----} \\ \text{if } \omega_{R-T} \geq \omega_{R-T,tr}, \\ \mathfrak{R}_{E,up,2} \cdot [1 + [\lambda_{E,R-T,2} \cdot \omega_{R-T}]^{k_{E,2}}]^{n_{E,2}-1} \end{cases}$$

$$k_{E,1} > 0; n_{E,1} > 1; k_{E,2} < 0; n_{E,2} > 1$$

$$\mathfrak{S}_{\eta,R-T}(T, \omega) = \begin{cases} \text{if } \omega_{R-T} \leq \omega_{R-T,tr}, \\ \mathfrak{S}_{\eta,R-T,low,1} \cdot [1 + [\lambda_{\eta,R-T,1} \cdot \omega_{R-T}]^{k_{\eta,1}}]^{n_{\eta,1}-1} \\ \text{-----} \\ \text{if } \omega_{R-T} \geq \omega_{R-T,tr}, \\ \mathfrak{S}_{\eta,R-T,up,2} \cdot [1 + [\lambda_{\eta,R-T,2} \cdot \omega_{R-T}]^{k_{\eta,2}}]^{n_{\eta,2}-1} \end{cases}$$

$$k_{\eta,1} < 0; n_{\eta,1} < 1; k_{\eta,2} > 0; n_{\eta,2} < 1$$

(b) Model equations

Figure 3.6: VENoL model parameters and equations [67]

as a function of the reduced pulsation  $\omega_{R-T}$ , below (dotted curves) and above (continuous curves) the transition reduced pulsation  $\omega_{R-T,tr}$ . CY parameters names are changed to correspond with the VENoL model (Equations in Figure 3.6b):  $\Re_{E,low,1}$ ,  $\Im_{\eta,R-T,low,1}$  and  $\Re_{E,up,2}$ ,  $\Im_{\eta,R-T,up,2}$  [Mpa, Mpa.s] are respectively lower and upper bounds;  $\lambda$  [s/rad] controls the position of the slop/bound intersection on the axis  $\omega_{R-T}$ ;  $n$  [-] is the slope coefficient and  $k$  [-] is the slope/bound transition coefficient. These parameters must be calibrated for the reference curve at a reference temperature  $T_{ref}$ .

### 3.3.2 Validation of the VENoL model

As shown in Figure 3.7, we built a 2PB test sample according to the experimental sample dimensions. Then, the open-source software gmsh (<https://gmsh.info/>) was used to mesh the numerical sample. The hexahedral mesh was used in the meshing process to obtain a good numerical convergence. Finally, the open-source software LMGC90 ([https://git-xen.lmgc.univ-montp2.fr/lmgc90/lmgc90\\_user/-/wikis/home](https://git-xen.lmgc.univ-montp2.fr/lmgc90/lmgc90_user/-/wikis/home)) was adopted to conduct the numerical simulations, in which the VENoL model is built-in. The material parameters were assigned to the non-linear model according to the experimental results, as detailed in Table 3.2. During the simulation, the bottom boundary was fixed and a sinusoidal displacement  $z = z_0 \sin(\omega t)$  was imposed on the top surface of the sample according to the test conditions. Considering the glass transition temperature of bitumen ( $T_g = -18$  °C), an equation similar to the Williams-Landel-Ferry (WLF) approach [160] was used to reconstruct the corresponding master curve for dynamic modulus and phase angle values of the asphalt mixture. A reference temperature  $T_{ref}$  was firstly chosen, then the translation of all isotherm values was performed by calculating the reduced frequency as  $f_r = a_T \times f$ , where  $f$  corresponds to each frequency value in each curve and  $a_T$  is the corresponding shift factor that could be fitted using the following WLF-like empirical equation.

$$\log a_T = \frac{-C_1(T - T_{ref})}{C_2 + (T - T_{ref})} \quad (3.7)$$

Where:

- $C_1$  and  $C_2$  are two constants, and  $T$  is the test temperature.

According to the experimental results for dynamic modulus and phase angle, Table 3.2 gives VENoL parameters for the asphalt mixture.



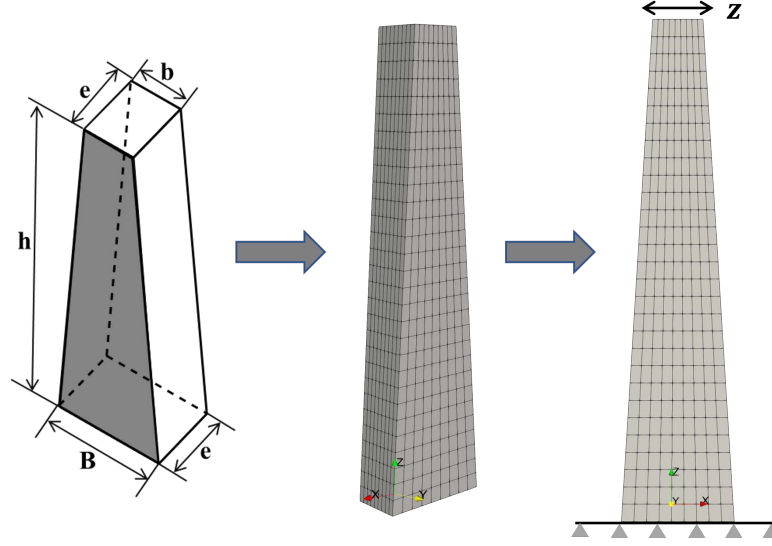


Figure 3.7: Numerical 2PB test based on FEM

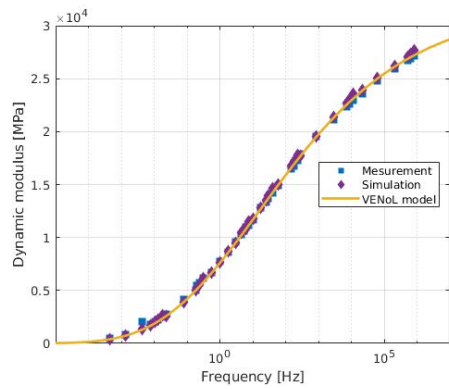
Table 3.2: Modeling parameters for VENO<sub>L</sub> model

Transition reduced pulsation:		$\omega_{R-T,tr} = 0$	
$\Re_E(\omega_{R-T})$		$\Im_{\eta,R-T}(\omega_{R-T})$	
$\omega_{R-T} \leq \omega_{R-T,tr}$	$\omega_{R-T} \geq \omega_{R-T,tr}$	$\omega_{R-T} \leq \omega_{R-T,tr}$	$\omega_{R-T} \geq \omega_{R-T,tr}$
$\Re_{E,low,1}$	$\Re_{E,up,2}=3.35 \times 10^4$	$\Im_{\eta,R-T,low,1}$	$\Im_{\eta,R-T,up,2}=1.1 \times 10^6$
$\lambda_{E,R-T,1}$	$\lambda_{E,R-T,2}=2.2 \times 10^4$	$\lambda_{\eta,R-T,1}$	$\lambda_{\eta,R-T,2}=8.3 \times 10^1$
$k_{E,1}$	$k_{E,2}=-0.163$	$k_{\eta,1}$	$k_{\eta,2}=0.25$
$n_{E,1}$	$n_{E,2}=2.96$	$n_{\eta,1}$	$n_{\eta,2}=-0.12$

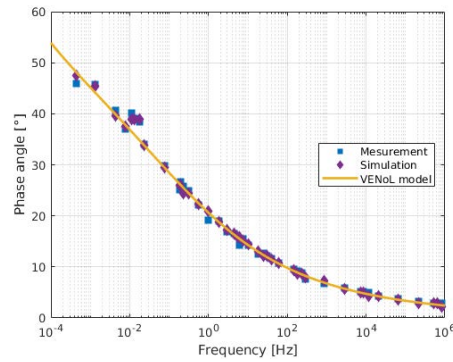
Herein,  $\omega_{R-T,tr}$  was set to 0.0 rad/s, only the parameters corresponding to  $\omega_{R-T} \geq \omega_{R-T,tr}$  were considered.

Figures 3.8a and 3.8b give the respective comparison of dynamic modulus and phase angle master curves ( $C_1 = 30$ ,  $C_2 = 198.4$  °C related to the current material, and  $T_{ref} = 15$  °C) for experimental, VENoL fitting, and numerical simulation results. These results agree quite well for both dynamic modulus and phase angle values.

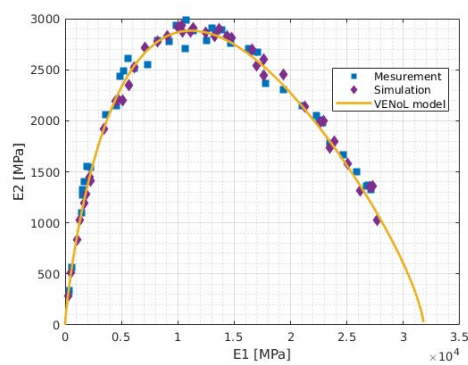
To verify the results in the Cole-Cole and Black spaces which are very sensitive to the parameter variation, Figures 3.8c and 3.8d show the results of experimental tests, VENoL fitting, and numerical simulations in the Cole-Cole and Black spaces respectively. As can be seen from these two figures, the fit for numerical simulations is in good agreement with VENoL fitting and experimental tests. The comparisons from Figure 3.8 validate the reliability of the fitting of the VENoL model for concerned viscoelastic asphalt mixtures.



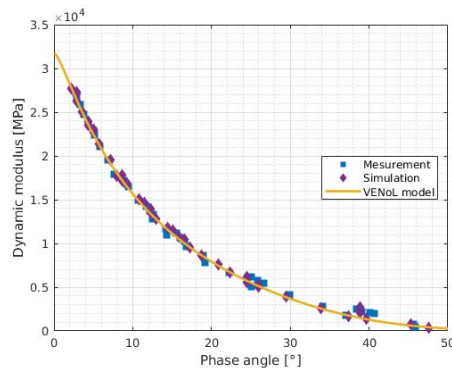
(a) Master curve for dynamic modulus



(b) Master curve for phase angle



(c) Cole-Cole plot



(d) Black diagram

Figure 3.8: Comparisons between numerical and experimental results

## 3.4 Coupling chain for the tire-sensor-pavement system

### 3.4.1 Numerical asphalt layer building and coupling algorithm

At first, we built an asphalt layer with dimensions along the x, y, and z-axis of 1 m, 1 m, and 0.2 m respectively (Figure 3.9). The hexahedral meshing process was carried out using the gmsht software. For the loading area in the center, we used a fine mesh whose size corresponds to the sensor dimensions, while for other parts, we used a coarse mesh to reduce the computation cost. Herein, for the loading area, the mesh element dimensions are 7.112 mm, 7.112 mm, and 10 mm in the x, y, and z directions respectively. For the entire simulation, for the sake of simplicity, only the asphalt layer bottom was fixed as a boundary condition.

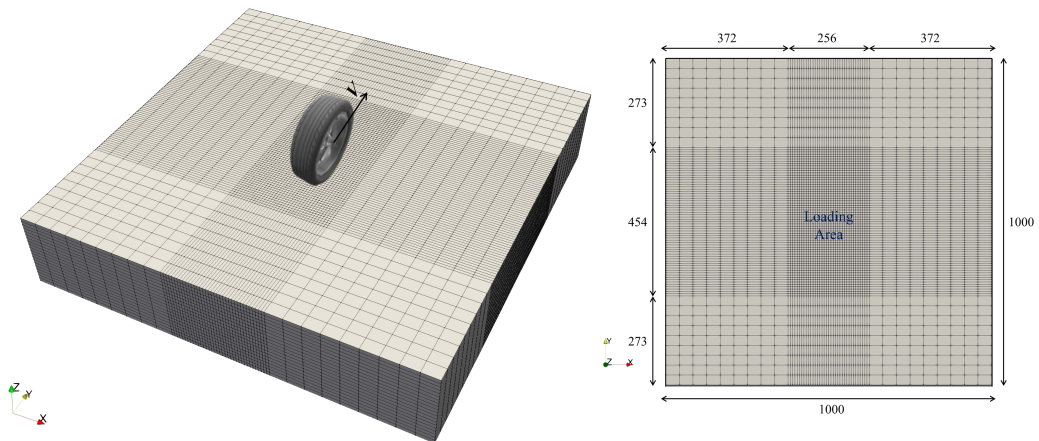


Figure 3.9: Pavement layer and loading area

To study the asphalt layer responses under real tire loads, we proposed a novel tire-sensor-pavement coupling chain that consists in applying the stress field obtained from the sensor measurement results to the pavement layer surface. The coupling chain is shown in Figure 3.10. In step 1, we conducted the experimental test of tire contact stress measurement by using the sensor measuring system. Then, the stress information was obtained and visualized in MATLAB. In step 2, the stress information from the previous step was transferred to nodal forces of the sensor matrix. In step 3, the asphalt layer

was reconstructed in FEM and the load area was refined according to the sensor dimensions. In step 4, the nodal forces were applied to the pavement surface at the corresponding nodes. In this step, a dynamic detection algorithm was used to determine the nodal force position on the FEM model. The general frame for this detection algorithm is listed in Algorithm 1.

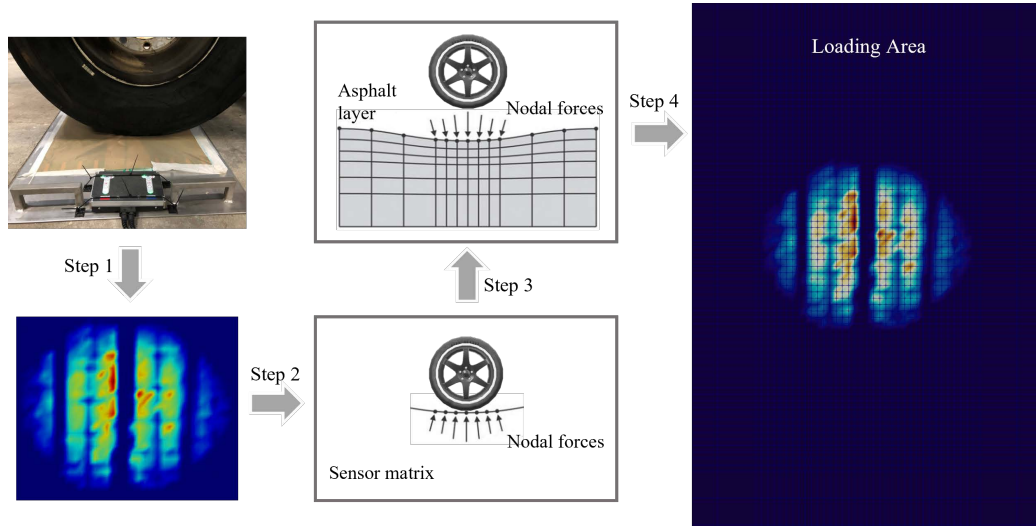


Figure 3.10: Tire-sensor-pavement coupling

### 3.4.2 Asphalt layer property identification under rolling tire loads

The tire rolling process is shown in Figure 3.11. Three critical time points (Starting time, Middle time and Ending time) describing the whole dynamic rolling process are shown in the figure.

Prior to simulating tire rolling on an asphalt layer surface, asphalt mixture properties must be identified under various tire loading conditions. As previously discussed, asphalt mixtures are viscoelastic materials sensitive to temperature and load frequency. This study investigated asphalt layer response under 15 °C which is the reference value used in the French pavement design method. However, the corresponding loading frequency for the complex modulus test must still be determined from the tire loading conditions. Accordingly, we used an equation proposed by Cheng et al. [161] to transfer vehicular loading velocity to the loading frequency during the complex

**Algorithm 1** General procedure of the detection algorithm

```

1. Asphalt layer surface node selection
1.1: Get node coordinates  $N_{coor}$  of the asphalt layer:
if  $N_{coorz} > -Ed_z$  then                                ▷  $Ed$  is the element dimensions
    Record the surface node id to an array [ID]
    Record the corresponding surface node coordinates to an array [ $NS_{coor}$ ]
end if
2. Data processing from Tekscan measurement
2.1: Transfer the stress signal of sensor to the nodal force of sensor, save
it to an array [ $F_{no}$ ].
2.2: Record the coordinates of the Tekscan sensor matrix to an array [ $T_{coor}$ ]
3. Detection and nodal force application to the asphalt layer
for  $t$  in range  $[0, t_{final}]$  do                                ▷  $t$  is the elapsed time
    while  $i$  in range  $[1, Num]$  do                                ▷  $Num$  is the length of [ID]
        if  $NS_{coory}[i] - Ed_y/2 = < T_{coory}[i] + v * t <= NS_{coory}[i] + Ed_y/2$ 
then
            if  $NS_{coorx}[i] - Ed_x/2 = < T_{coorx}[i] <= NS_{coorx}[i] + Ed_x/2$  then
                Apply the nodal force  $F_{no}[i]$  to this node with id of  $i$ 
            end if
        end if                                ▷  $v$  is the tire rolling velocity along the  $y$  direction
    end while
end for

```

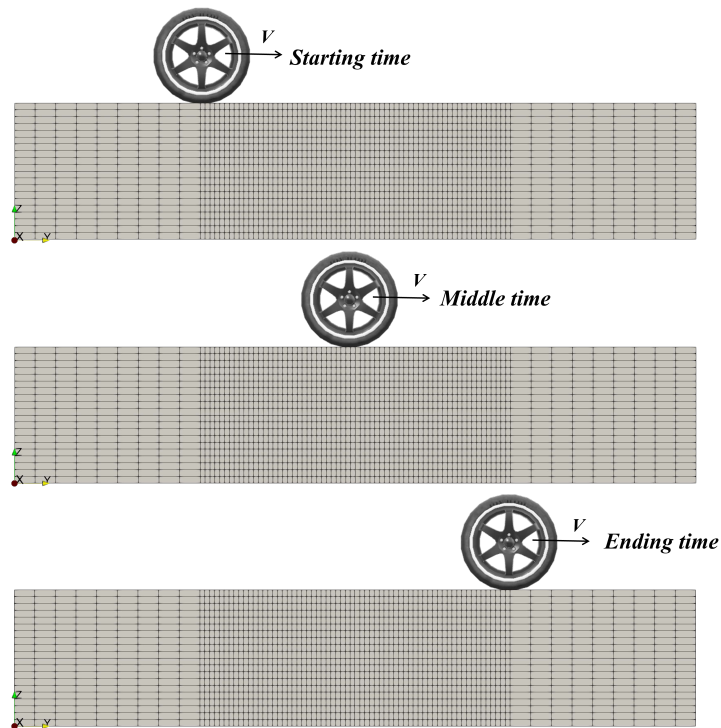


Figure 3.11: Tire rolling process on the asphalt layer

modulus test, as shown below:

$$f = 0.127V \quad (3.8)$$

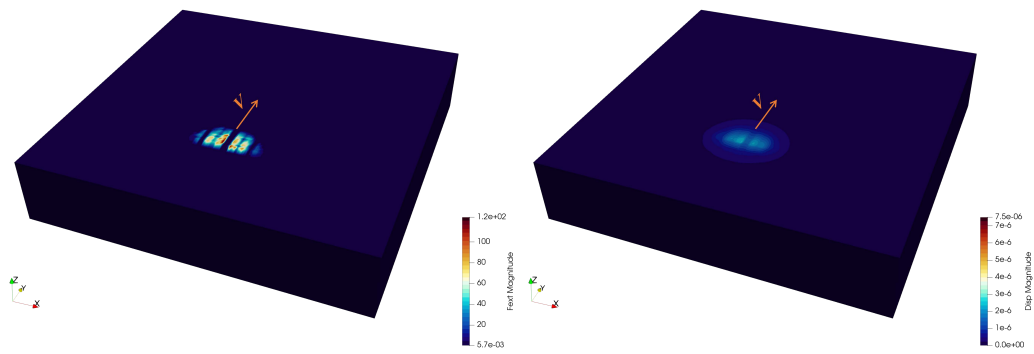
Where,  $f$  [Hz] is the frequency used in the complex modulus test and  $V$  [km/h] is the tire rolling velocity on the pavement surface.

Through validation of the full-scale accelerated pavement tests, the equation established in the original paper provides a good description of the frequency of test loading ( $f$ ) and tire motion speed ( $V$ ) for pavement temperatures not exceeding 31 °C. By using the equation above and the VENoL model built in the numerical simulation, we can easily identify the mixture properties of the asphalt layer model.

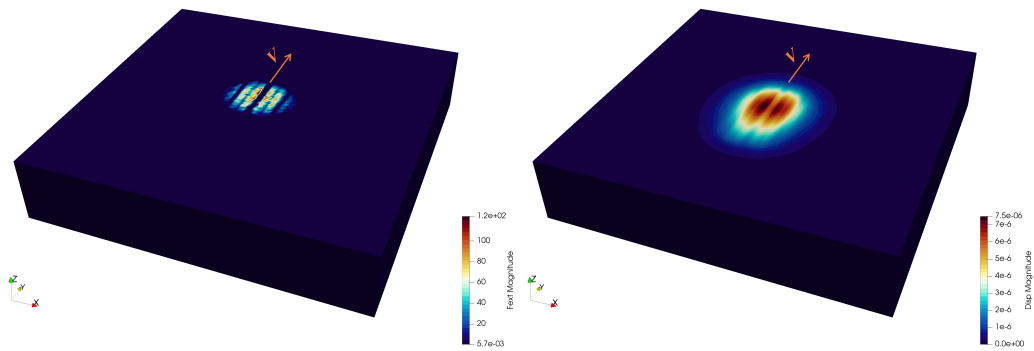
### 3.4.3 Dynamic simulation of asphalt layer responses under rolling tire loads

In steady-state tire rolling (angular and translational velocities are constant), tire loads are independent of time [38]. Previous studies have indicated that the influence of the velocity is relatively small on the tire tread deformation compared with the effects of the vertical force [162, 163], and tire rolling speeds have minor effects on tire contact stresses [164]. Herein, we assume that the tire rolling speed does not affect the tire loading state during the tire rolling.

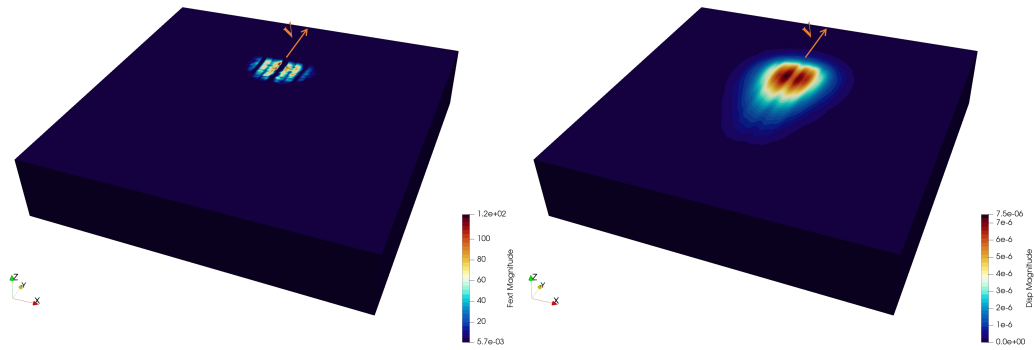
Figure 3.12 shows both the external force field and the displacement distribution field during the tire rolling process on the asphalt layer in 3D rendering, in which the tire inflation pressure was 8 bar and the tire load was 20 kN. As can be seen from the figure, the external tire load derived from the sensor measurements is non-uniform on the asphalt layer surface and advances along the y-direction, the whole moving process is consistent with Figure 3.11, which proves the reliability of the proposed tire-sensor-pavement coupling chain. Furthermore, we observed that there was a lag between the external force field and the displacement field throughout the whole tire rolling process, which originates from the viscoelastic nature of the asphalt mixture. As a result of the tire loading pass, a residual displacement field appears on the asphalt layer surface, which indicates a process of viscous material flow inside the asphalt mixture.



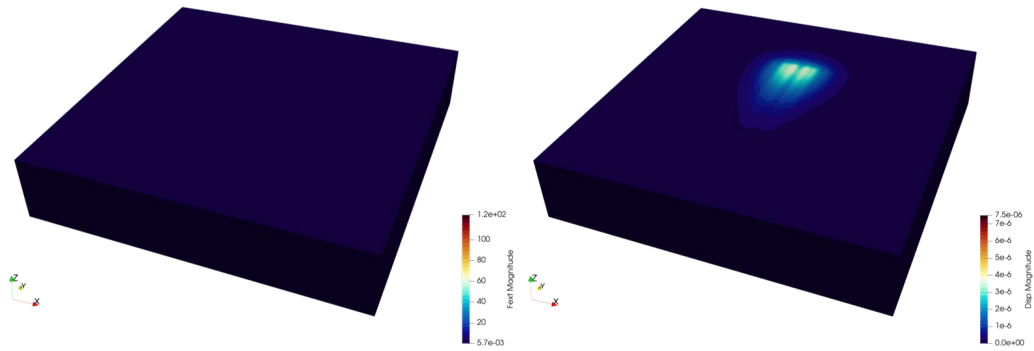
(a) External force field: Time = 0.041 s (b) Displacement field: Time = 0.041 s



(c) External force field: Time = 0.090 s (d) Displacement field: Time = 0.090 s



(e) External force field: Time = 0.123 s (f) Displacement field: Time = 0.123 s



(g) External force field: Time = 0.147 s (h) Displacement field: Time = 0.147 s

Figure 3.12: Tire rolling process on the asphalt layer for  $V = 20$  km/h



The deformation of the center section plane ( $x = 0$ ) as shown in Figure 3.13 was analyzed as a way of precisely describing the displacement distribution during the rolling process. As shown below in Figure 3.14, we validated

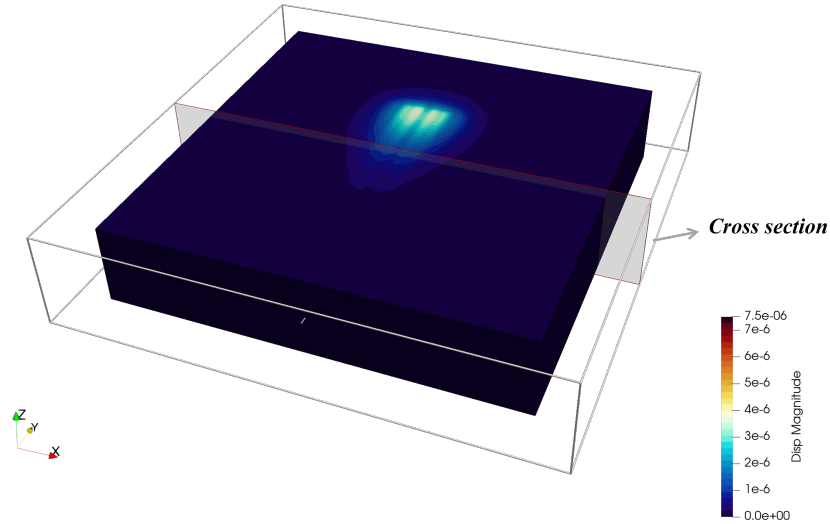
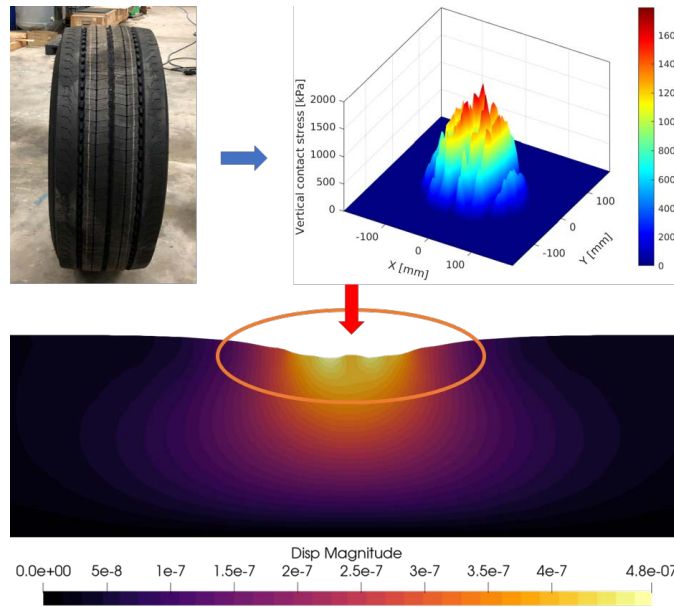
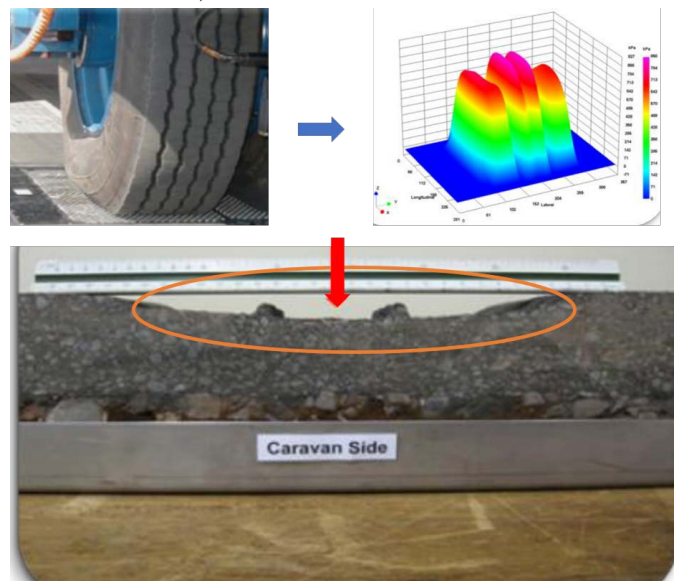


Figure 3.13: Cross section (Plane:  $x = 0$ ) selection of asphalt layer

the efficiency of the numerical model by comparing the surface deflection from the numerical simulation to the rutting deformation from the experimental tests. The non-smooth surface deflection observed in Figure 3.14a is associated with a non-uniform tire contact stress and a non-smooth tire texture, contrasting with the smooth deformation shape obtained in previous simulations employing the uniform load assumption [165, 166]. Figure 3.14b shows the asphalt rutting deformation induced by truck tire loads after long-term loading periods. The non-smooth tire surface texture, along with non-uniform tire contact stresses, also produces a non-smooth surface. Rutting is a result of the accumulation of residual deflection in the surface after a long period of loading. The measured rutting shape shows similarities to the surface deflection measured from the numerical simulation, which confirms the validity of the model and its performance. Establishing a relationship between the residual surface deflection and the final rutting deformation after long-term loading cycles is encouraging based on the proposed high-precision model to predict asphalt surface deterioration.



(a) Residual displacement after load passing (scale factor = 50000)



(b) Asphalt rut deformation under real tire loads [30]

Figure 3.14: Comparisons of the numerical surface deflection and the experimental rutting measurement

## 3.5 Asphalt layer responses under varied loading conditions

### 3.5.1 Dynamic responses of asphalt layer under different tire rolling velocity

In this part, the effect of the tire rolling velocity on the asphalt layer responses was examined. Figure 3.15 depicts the respective status of the cross-section before and after the tire loading pass for a tire rolling velocity of 20 km/h at the tire inflation pressure of 8 bar and the tire load of 20 kN.

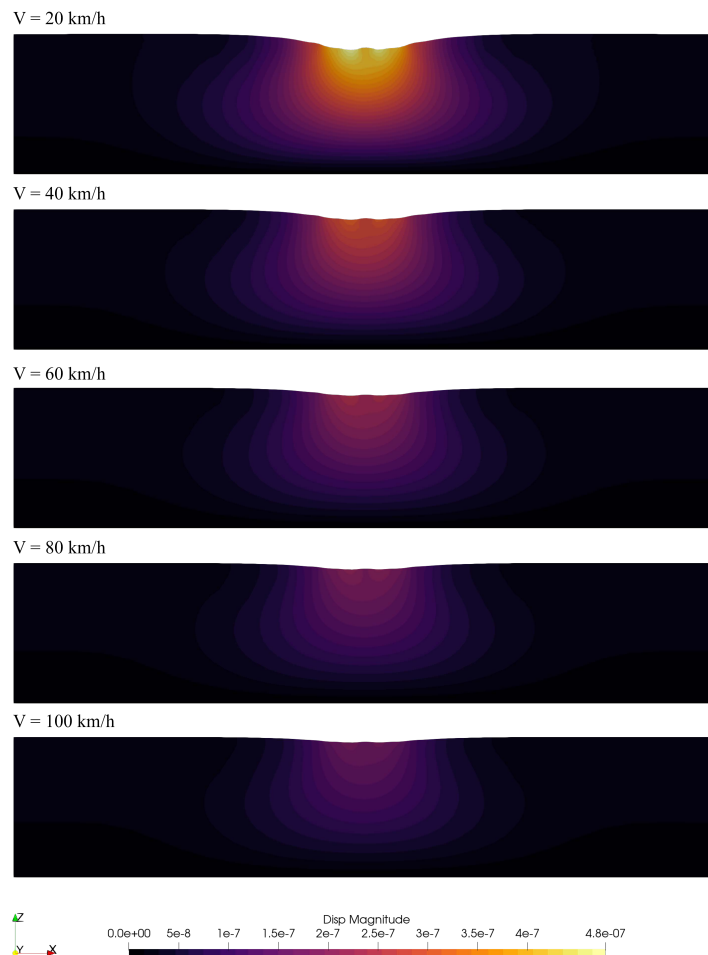


Figure 3.15: Residual deformation (scale factor = 50000) for different tire rolling velocity

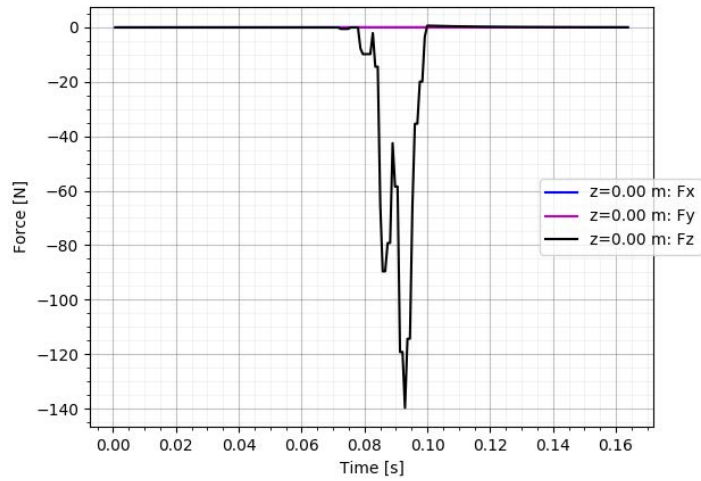
The dynamic responses for the center element of the asphalt layer surface were further analyzed. Figure 3.16 gives the result of the force and displacement signals of the center elements. Figure 3.16a illustrates that the vertical force is dominant during the whole tire rolling process. Additionally, when the tire arrives at the corresponding cross-section, the element subjects the tire load; after a short period, the signal disappears as the tire load passes the cross-section. Figure 3.16b shows that the main displacement lies in the vertical direction, which is consistent with the dominant vertical force signal. The displacement increases with elapsed time and decreases after the peak value, and it approximates the Haversine curve, but the element displacement does not return to its original value (a residual displacement occurs) after the load pass because of the viscous material behavior.

Figure 3.17 gives further comparisons of the vertical force and displacement signals of the center element for different velocities. Figure 3.17a shows that the peak force value seems to not change due to the same load utilized. It appears that the force signal curve shape becomes stretched with decreasing tire rolling velocity as a slower tire rolling velocity results in a longer time-lapse. Figure 3.17b shows that the low tire rolling velocity induces the increment of both peak displacement and residual displacement. The reason comes from that the viscous flow of asphalt mixture accumulates over a long elapsed time during the rolling process at low tire velocity.

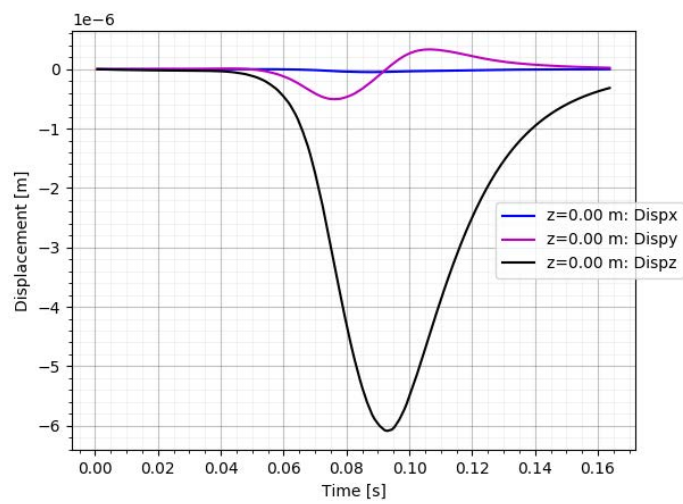
### 3.5.2 Dynamic responses of asphalt layer under different tire loads

Figure 3.18 plots the residual displacement distribution across the cross section lying on the center ( $x=0$ ). As shown in the figure, heavy tire loads cause a wide influencing zone and large residual displacement.

Figure 3.19 further gives the displacement characteristics of the center element lying on the center of the asphalt layer surface. It illustrates that big tire loads induce the increment of both a big peak and residual element deformation.



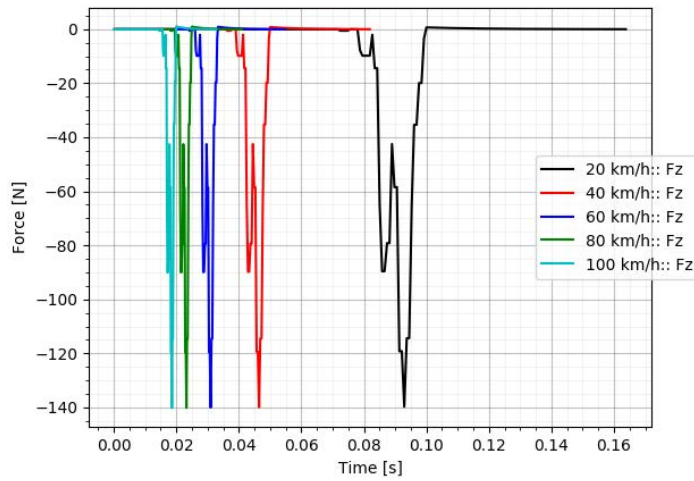
(a) Force signal



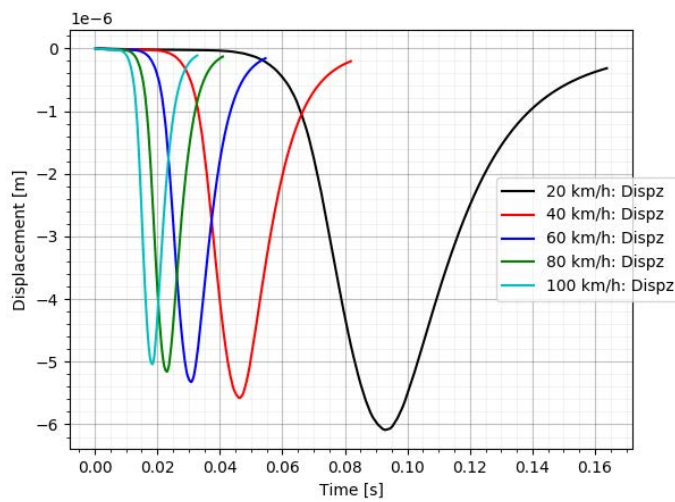
(b) Displacement signal

Figure 3.16: Dynamic responses of the center element on the asphalt layer surface for  $V$

$$= 20 \text{ km/h}$$



(a) Force signal



(b) Displacement signal

Figure 3.17: Dynamic responses of the center element on the asphalt layer surface for different tire rolling velocity

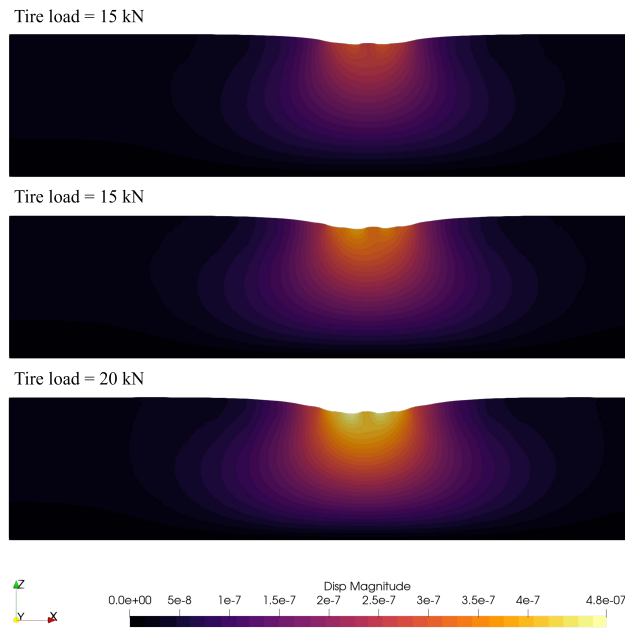
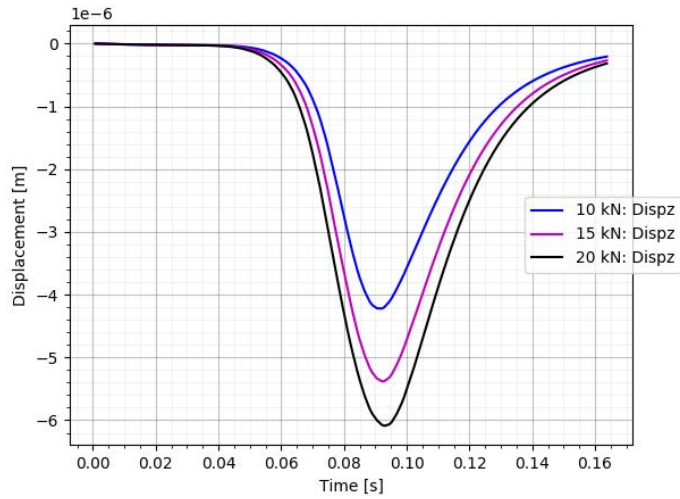


Figure 3.18: Residual deformation (scale factor = 50000) at inflation pressure of 8 bar for different tire loads at  $V = 20$  km/h

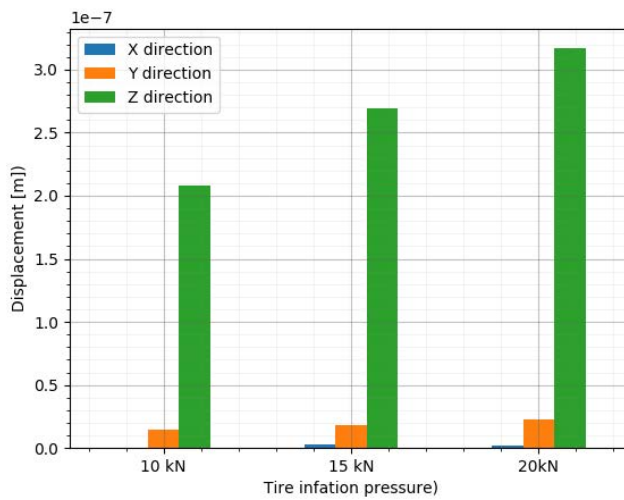
### 3.5.3 Dynamic responses of asphalt layer under different tire inflation pressures

Figure 3.20 plots the displacement distribution of the cross section. From the figure, it is hard to quantitatively evaluate the deformation characteristics as the difference is not obvious.

Figure 3.21 further gives the residual displacement of the center element. It shows that high tire inflation pressure causes increased peak deformation compared with low tire inflation pressure. Both tire inflation pressures reach the same level for residual displacement. The results display the combined effect of tire loads and inflation pressures. Compared to the high tire inflation pressure, low tire inflation pressure results in a longer tire loading period. The small contact area patch of the tire leads to a short rolling duration as well as high tire loads leading to large deformation. A low inflation pressure causes a large contact area between the tire and pavement, which leads to a long period of the tire rolling over the pavement and resulting in heavy deformation accumulation. Tire inflation pressure contributes to both tire



(a) Vertical displacement signals



(b) Residual displacement comparison

Figure 3.19: Dynamic responses of the center element on the asphalt layer surface for different tire loads at  $V = 20$  km/h



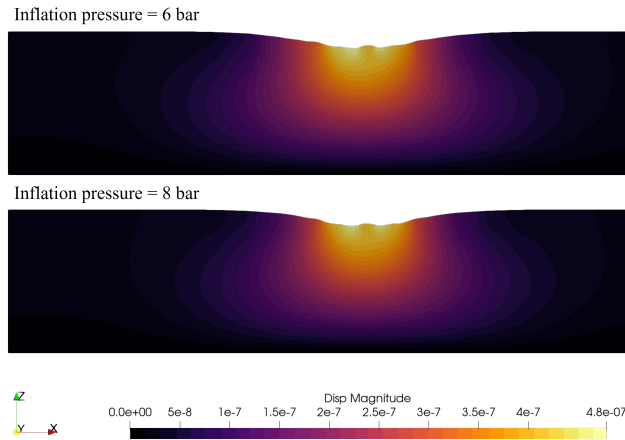


Figure 3.20: Residual deformation (scale factor = 50000) at tire load of 20 kN for different tire inflation pressures at  $V = 20$  km/h

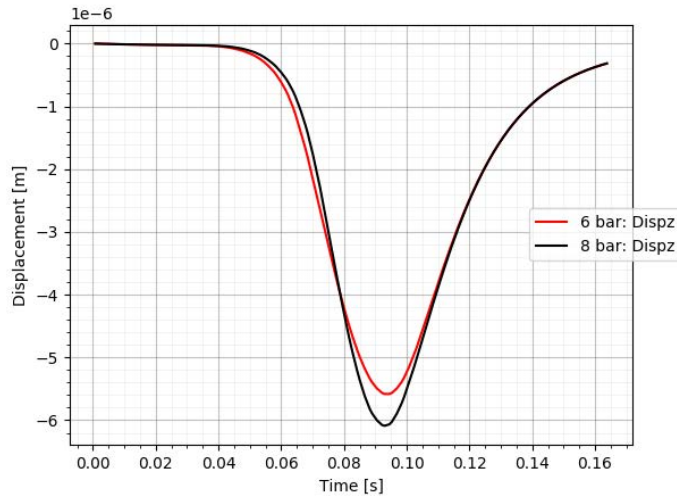
loads and tire contact patch area. These two contributions are opposite, so both effects should be considered concurrently when evaluating the residual deformation of the asphalt layer.

### 3.5.4 Dynamic responses of asphalt layer at different temperatures

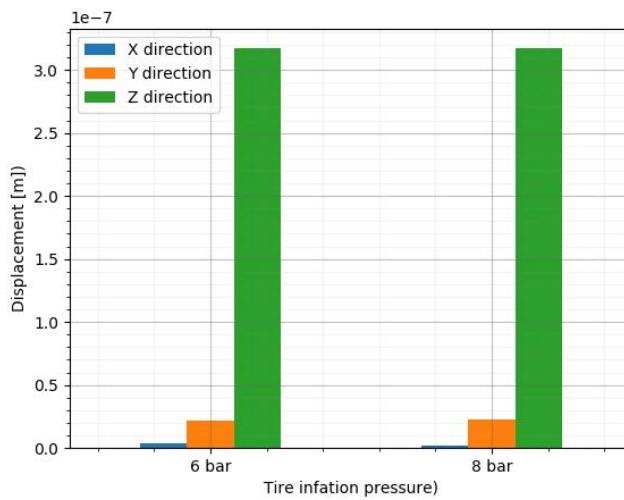
Asphalt mixture properties are also dependent on the environmental temperature. Thanks to the VENoL model introduced before, we also conducted simulations for asphalt layer responses under rolling tire loads at different temperatures.

Figures 3.22a to 3.22e give examples of the residual displacement filed on the asphalt layer surface after tire loading passe at different temperatures (from  $-10$  °C to  $30$  °C). Based on these figures, it can be seen that the influencing field of residual displacement widens as the temperature increases, especially at a high temperature ( $30$  °C herein), the residual displacement field is widely distributed on the asphalt layer surface. Figure 3.22f gives the comparison for the maximum residual displacement at different temperatures. The figure illustrates that the peak value of residual displacement increases with increasing temperatures and that the increment becomes drastic after  $20$  °C.

The results above illustrate that the asphalt mixture responses are sensitive



(a) Vertical displacement signals



(b) Residual displacement comparison

Figure 3.21: Dynamic responses of the center element on the asphalt layer surface for different tire inflation pressures at  $V = 20$  km/h

to temperature due to the viscoelastic mixture nature. The viscous material flow of the asphalt layer becomes non-negligible as the temperature increases, particularly at high temperatures when residual deformation increases dramatically.

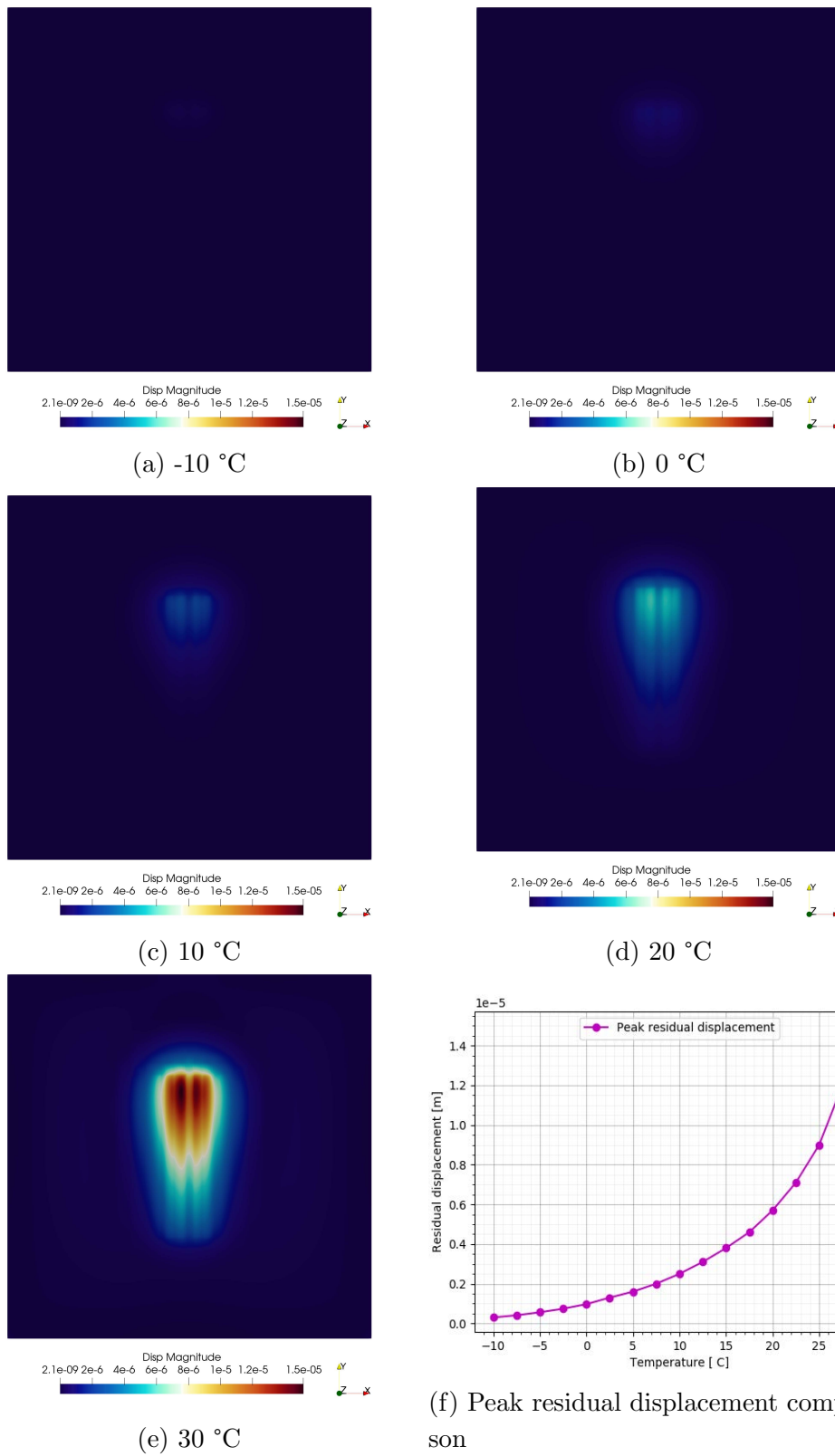


Figure 3.22: Residual displacement field on the asphalt layer surface for different temperatures at  $V = 20$  km/h and tire load of 20 kN and inflation pressure of 8 bar

### 3.6 Conclusions of the chapter

The aim of this chapter is to examine macro asphalt pavement responses under realistic tire loading conditions at the most accurate level. From tire contact stress determination and asphalt mixture property characterization through dynamic simulation of asphalt layer responses under rolling tire loads, this chapter introduces a tire-sensor-pavement coupling chain to integrate measured tire contact stress into asphalt pavement models using FEM.

A sensor measuring system was used to capture tire contact stresses on the pavement surface. The test results show that the non-uniformity and values of tire contact stress, as well as the corresponding tire contact area on the pavement surface, are depending on the tire load and inflation pressures. Additionally, tire contact stress distribution appears to be more sensitive to tire inflation pressure than to tire load.

For characterizing the frequency- and temperature- dependent asphalt mixture properties, the NOnLinear ViscoElastic (VENoL) model was integrated into FEM simulations. Based on 2PB complex modulus test measurements, the numerical simulation results fit well with experimental results and analytical calculations in describing the viscoelastic properties of the asphalt mixture under various temperatures and frequencies during the complex modulus tests, which proves the effectiveness of VENoL model implementation in FEM.

The general frame of the tire-sensor-pavement coupling chain was proposed to investigate asphalt layer responses under rolling tire loads. In the tire rolling process, a lag between the external force field and the displacement field occurs due to the viscoelastic nature of the asphalt mixture. After the tire rolling, a non-smooth residual surface deflection on the asphalt layer is observed as a result of non-uniform tire loads.

Asphalt layer responses at different working conditions including tire rolling velocity, tire load, inflation pressure, and external environment temperature were investigated. The results show that the residual displacement of the asphalt layer surface increases with increasing tire loads and decreasing tire velocities respectively; for the effects of tire inflation pressure, both tire load and contact area should be evaluated simultaneously because of their two-

---

side opposite contributions to the residual displacement. For the temperature effects on the asphalt layer responses, it shows that the influencing zone of the residual displacement distribution field increases as the temperature increases, especially at a high temperature (when the temperature exceeds 20 °C), a drastic increment in residual displacement is observed.

The following paper summarizes the main results of this chapter:

Ge, H., Quezada, J. C., Le Houerou, V., Chazallon, C., & Horny, P. (2023). A new tire-sensor-pavement coupling chain for investigating asphalt mixture responses under rolling tire loads. *Road Materials and Pavement Design*, 1-18. [[167](#)].



# Asphalt mixture modeling based on Contact Dynamics method

## Contents

<b>4.1</b>	<b>Introduction</b>	<b>78</b>
<b>4.2</b>	<b>Contact modeling theory</b>	<b>79</b>
<b>4.3</b>	<b>Morphology distribution of aggregate particles</b>	<b>82</b>
4.3.1	Three-dimensional laser scanning of aggregate particles	82
4.3.2	Statistical analysis for aggregate shape	82
4.3.3	Statistical analysis for aggregate angularity	83
<b>4.4</b>	<b>Asphalt mixture modeling</b>	<b>85</b>
4.4.1	Complex modulus test	85
4.4.2	Irregular polyhedral particles simulation	86
4.4.3	Burgers contact model and its calibration	89
<b>4.5</b>	<b>Numerical analysis</b>	<b>96</b>
4.5.1	Macro mechanical behavior	96
4.5.2	Micro mechanical behavior	97
4.5.2.1	Contact force distribution	97
4.5.2.2	Particle velocity distribution and contact force networks	100
4.5.2.3	Normal and tangential force analysis	101
<b>4.6</b>	<b>Conclusions of the chapter</b>	<b>104</b>



## 4.1 Introduction

As we explored in the previous chapter, when using FEM to study asphalt mixture response under tire loads, the mixture is assumed to be homogeneous and the mixture behavior is usually characterized by complex constitutive material models.

Nevertheless, the mechanical behavior of asphalt mixture composed of aggregates, bitumen, and air depends highly on the properties of its components in interaction [168]. Considering the local responses of asphalt mixtures from a microscopic level, the homogenization assumption concerning the asphalt mixture is insufficient because it cannot examine asphalt mixture responses mechanically from a particle scale. Therefore, it is necessary to model an asphalt mixture structure while explicitly considering its different components and their properties.

Experiments are generally used to determine viscoelastic material properties from a macro scale. However, it is still a challenge to study the micro-mechanical behavior of the material through laboratory measurements. With the continuous advances in computation capacity, numerical methods are widely used for examining micro-mechanically material performances. The discrete element method (DEM) has been demonstrated to be an effective method to simulate granular systems including asphalt mixtures at the particle scale in recent years [46, 84–86].

For a simulation of the asphalt mixture, it is required to generate the mesoscopic structure of the mix close to the real assembly. In this chapter, based on the acquisition of aggregate shapes through 3D laser scanning, the morphological characteristics for a large number of real particles were analyzed statistically by using image processing technology. The contact dynamics (CD) method was introduced to simulate irregular particles because of its suitability for polyhedron modeling. The numerical asphalt mixture specimens were generated by a tessellation method considering both the aggregate size distribution and morphology data. The numerical and experimental complex modulus tests were carried out with different temperatures and loading frequencies to confirm the model's reliability. Finally, the micro-mechanical analysis was conducted to investigate the contact force distribution between particles and lead to reveal the essence of mixture damage initiation at the particle scale.

## 4.2 Contact modeling theory

In computational contact mechanics, the contact problem is an extremely non-linear, non-smooth, and non-differential problem. A unilateral contact problem can be modeled using Signorini's condition and Coulomb's friction law (Figure 4.1). As seen here, the contact conditions are essentially infinite steep, which makes them non-differentiable.

For a classical solution to the contact problem, the reaction force ( $R$ ) is defined as a function of the gap ( $g$ ), where  $g$  represents the penetration of two contacting surfaces. The relation between  $g$  and  $R$  can instead be replaced with steep mapping graphs and thus be solved by non-linear differential equations. Replacing the infinite steep formulation with some smooth relations could be considered mathematically as a regularization or numerically as a penalty method. With this strategy, contact conditions are modeled as a sequence of steep laws using regularization techniques, and the nonlinear laws being thus handled by means of an explicit time integrator. It is adopted widely for solving contact problems in FEM [169] and explicit smooth DEM simulations pioneered by P. Cundall [81, 170] because of its simplicity and easy implementation in numerical algorithms.

There are, however, some weaknesses to this method from its principles: 1) The time step is mandatory small in order to ensure the calculation stability, especially when dealing with high contact stiffness; 2) Damping must be introduced, either through the contact laws or as a numerical trick, to ensure the stability of explicit schemes. 3) The equilibrium state is hard to achieve via an explicit method when considering the tangential friction force. 4) Penetration is inevitable. The constraint condition is satisfied precisely when the penalty parameter tends to infinity. However, the resulting equations could be ill-conditioned if the penalty parameter is too large and thus choosing the relevant parameters could be tricky; Differently, Jean-Jacques Moreau developed the Non-smooth Contact Dynamics method (NSCD), shortly Contact dynamics (CD) in 1984 for the implicit non-smooth interaction model [83] and this method has proved to be an effective tool for modeling a large number of contacting rigid or deformable bodies [171–173]. Unlike the method described above, the CD method uses non-differential steep laws to define the relationship between relative velocities  $U$  and impulses  $I$ . Signorini's condition and Coulomb's friction law are cited as the foundations of contact

laws. Figure 4.1 compares the CD method and the classical penalty method for solving contact conditions.

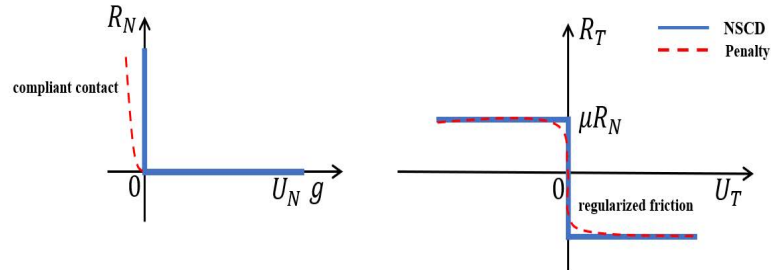


Figure 4.1: Comparison between the two contact modeling methods: Normal (left) and Tangential (right)

At the local frame, the contact management between two objects is based on the so-called candidate/antagonist approach (Figure 4.2). According to this approach, it is assumed that one is able to define for each point ( $C$ ) of the candidate boundary its (unique) nearest point ( $A$ ) on the antagonist boundary, a local reference frame ( $\mathbf{n}, \mathbf{t}, \mathbf{s}$ ) attached to the antagonist body is defined at the contact point  $A$ . For deformable objects, one has to consider contact elements composed of a node versus the discretized antagonist face boundaries.

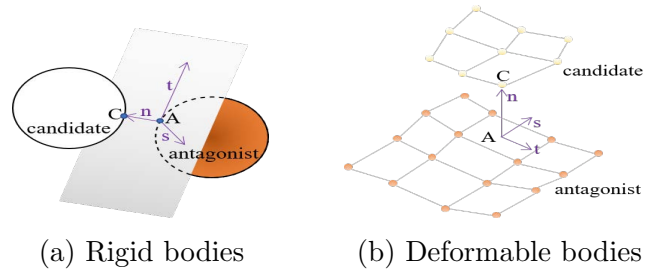


Figure 4.2: Candidate/antagonist approach

The contact laws are managed with an implicit integration scheme using a Non-Linear Gauss-Seidel algorithm (NLGS) at each time step. Kinematic constraints arising from contacts are calculated simultaneously by combining them with dynamics equations, in order to determine all the velocities and contact forces in the system. Furthermore, the regularized parameters such as damping are removed from the local contact frame. As a result, the

implicit method can be used to find equilibrium states more accurately than explicit methods [174]. In comparison to explicit DEMs, the CD method allows using larger time steps since it determines the characteristic system time of particle dynamics.

As shown schematically in Figure 4.3, three main types of contact may occur between two polyhedral particles: point contact, line contact, and surface contact. The line (edge–face) contacts can be modeled by two points, while three points can model surface (face–face) contacts since they involve equal geometric unilateral constraints between the two faces. There are several steps involved in the determination of the contacts between two polyhedral particles. In the first step, we compute a list of neighboring pairs using a “bounding box” method. Then, an overlap calculation is done for each pair, using the “common plane” method. [175]. Contact planes are determined by their intersection in the case of an overlap. This detection method allows simulating large samples composed of polyhedral particles in a relatively short time [176, 177]. Finally, for each potential contact point, the local impulsion and velocity are calculated independently, and the resultant force is then assigned to the contact.

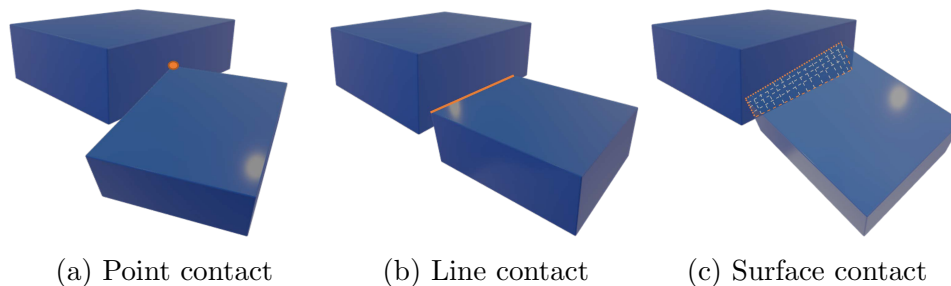


Figure 4.3: Contact situations that may occur between two polyhedral particles

Considering its advantages, we used the CD method to simulate the aggregate particles in asphalt mixtures and the later tire-pavement interaction simulations. The open-source software LMGC90 is adopted in which the CD method is built-in.

## 4.3 Morphology distribution of aggregate particles

### 4.3.1 Three-dimensional laser scanning of aggregate particles

In this study, aggregate particles with sieving sizes from 4 mm to 31.5 mm were randomly selected from the stockyard. A three-dimensional laser scanner (FARO Edge ScanArm HD) was used to obtain real geometrical data of the selected 500 aggregates. Surface point coordinates of particles were collected and transmitted to the computer during the scanning process. After the scanning and data acquisition of all specimens, the point cloud data obtained by the laser scanner were imported into MATLAB to further process individually, as Figure 4.4 shows.

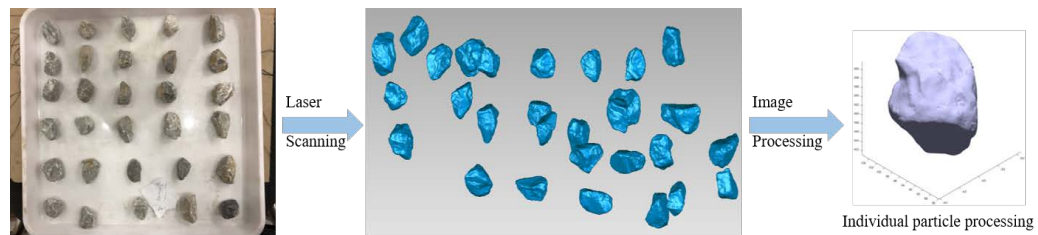


Figure 4.4: 3D scanning process

### 4.3.2 Statistical analysis for aggregate shape

The traditional method usually divides particle morphology into three scales: contour form, angularity, and surface texture [178], among which contour form and angularity belong to the macroscopic and mesoscopic scale, respectively, while surface texture belongs to the microscopic scale. Shape characteristics of particles with different scales affect various aspects of the mixture performance [179–181]. In the numerical particle-based simulation, the surface texture of particles can be indirectly implemented by setting a friction coefficient of mutual interaction. In the conventional simulation, the friction coefficient is usually set to a constant value [182, 183]. Accordingly, in this study, particle surface texture statistics have not been carried out.

The aggregate form is used to describe the dimension characteristics of a

particle, defined by the ratios of three linear dimensions: length (L), width (I), and thickness (S). Elongation ratio ( $LI=L/I$ ) and Flatness ratio ( $IS=I/S$ ) evaluate how a particle resembles a column or a plate [184]. If the value of LI and IS is close to 1, the aggregate is not slender. Otherwise, the particle is elongated or flatted. The minimum bounding box algorithm [185] was performed to calculate the minimum bounding box for a particle so that the dimension values of L, I, and S can be extracted. Schematic drawings of one aggregate in different bounding boxes are illustrated in Figure 4.5.

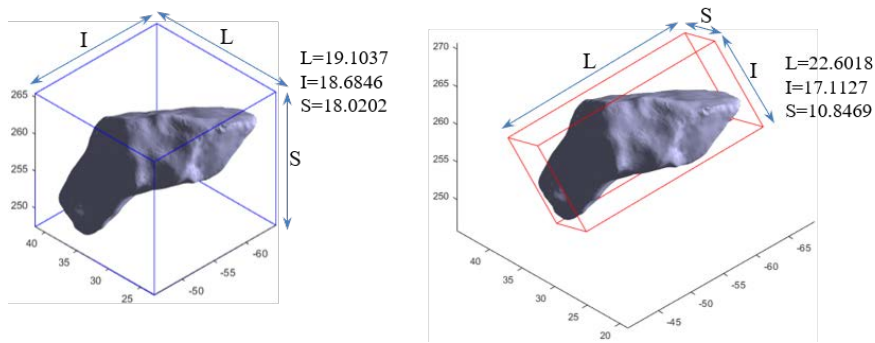
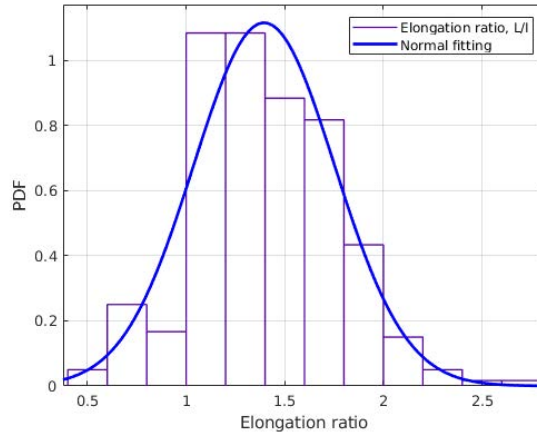


Figure 4.5: Original bounding box of an aggregate particle (left) and minimum bounding box cube of the aggregate particle (right)

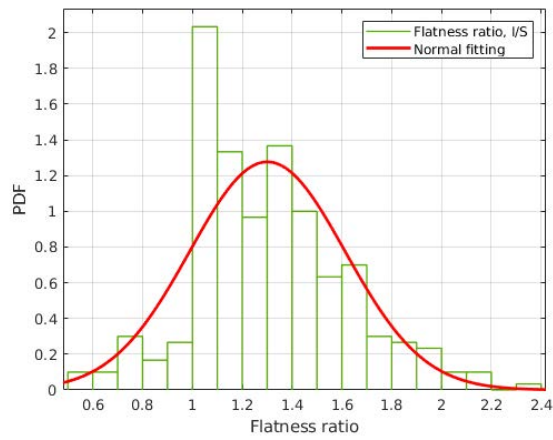
Statistical features of LI and IS of all particles were analyzed. Figure 4.6a and Figure 4.6b show the probability distribution histogram (PDF) of the LI and IS, respectively. As shown in the figures, both LI and IS of aggregate particles obey a normal distribution. Aggregates with IS less than 0.6 are defined as flaky particles and constitute about 5% of the overall samples, which fulfills the French standard stating flaky aggregates used in road construction should be less than 15% (NF P18-545 [186]).

### 4.3.3 Statistical analysis for aggregate angularity

Angularity belongs to mesoscopic shape characteristics. If particles show sharp edges, it will be more favorable to the mixture interlocking. If aggregates are rounded, the overall mixture strength will be significantly reduced, even with better gradation. The Sphericity value ( $Sp = \sqrt[3]{36\pi V^2/SA}$ ), where  $V$  and  $SA$  represent particle volume and surface area, respectively, witnesses the angularity of aggregate particles [80, 187]. The closer this value to 1, the more spherical a particle, and the lower the particle angularity.



(a)



(b)

Figure 4.6: Probability distribution and normal fitting: (a) Elongation ratio (LI); (b) Flatness ratio (IS)

The statistics of  $Sp$  were analyzed using the same method as mentioned above, as Figure 4.7 reports. The results show that the  $Sp$  obeys quite well a normal distribution. Table 4.1 gives the statistical results of aggregate morphology. The average aspect ratio (L: I: S) for aggregates is about 1.815: 1.301: 1, the mean and standard deviation of the  $Sp$  are 0.8013 and 0.0428 respectively.

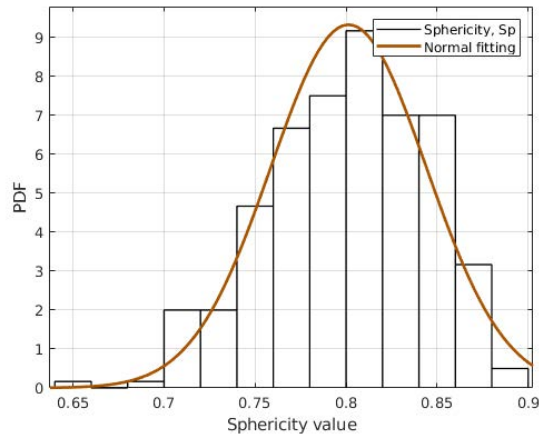


Figure 4.7: Probability distribution and normal fitting of Sphericity ( $Sp$ )

Table 4.1: Statistical parameters for aggregate morphology

Parameters	Distribution type	Mean	Standard deviation
LI	Normal	1.3951	0.3578
IS	Normal	1.3009	0.3124
Sp	Normal	0.8013	0.0428

## 4.4 Asphalt mixture modeling

### 4.4.1 Complex modulus test

To identify the mechanical properties of asphalt mixtures, complex modulus tests were conducted in a two-point bending (2PB) configuration. The slab specimens were prepared according to the asphalt mixture gradation (Table 4.2) and the trapezoidal samples were cut from the slab according to the dimensions given in Table 4.3.



Table 4.2: Particle size distribution (PSD) of asphalt mixture

Diameter (mm)	12.5	10	8	6.3	4	2	1	0.5	0.25	0.125	0.063
PSD (%)	100	90	75	58	44	31	20	15	12	9	6.5

Table 4.3: Dimensions of the specimens: EN 12697-26:2012

Dimensions of the specimens	Type of mixture $D \leq 14 \text{ mm}$
B	$56 \pm 1 \text{ mm}$
b	$25 \pm 1 \text{ mm}$
e	$25 \pm 1 \text{ mm}$
h	$250 \pm 1 \text{ mm}$

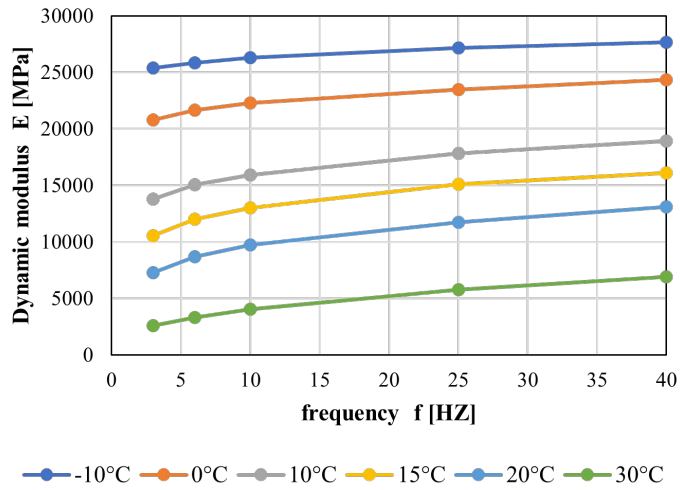
Note:  $D$  is the maximum aggregate size.

In the 2PB tests, the loading frequencies ranged from 3 Hz up to 40 Hz, and temperatures varied between  $-10 \text{ }^\circ\text{C}$  and  $30 \text{ }^\circ\text{C}$ . For each couple temperature-frequency, a sinusoidal horizontal displacement  $Z = A \sin(\omega t)$  was measured on the top of each sample and the amplitude  $A$  was  $63 \text{ }\mu\text{m}$  leading to a maximum strain  $\epsilon$  less than  $50 \times 10^{-6}$  to prevent fatigue damage.

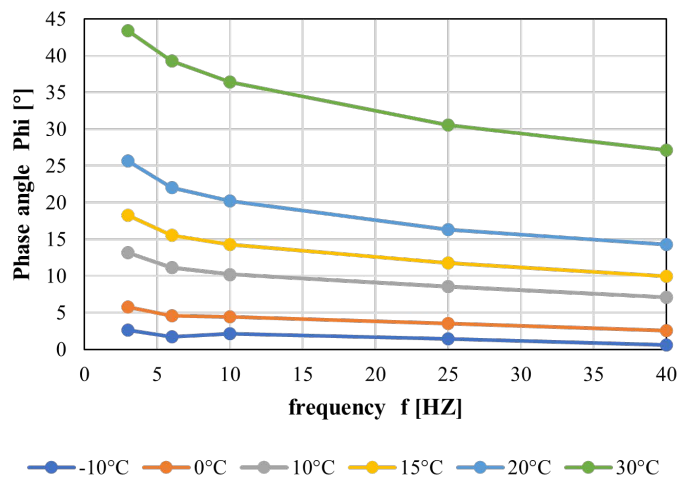
The dynamic modulus  $|E^*|$  and phase angle  $\phi$  were measured at six temperatures ( $-10, 0, 10, 15, 20$  and  $30 \text{ }^\circ\text{C}$ ) and five loading frequencies (3, 6, 10, 25, and  $40 \text{ Hz}$ ), the results are shown in Figure 4.8.

#### 4.4.2 Irregular polyhedral particles simulation

Asphalt mixtures are complex multi-phase systems composed of aggregates, bitumen and air, where aggregates occupy almost 95% of the mass in the mix. Consequently, asphalt mixture can be seen as a system of irregular particle tessellations from a geometrical point of view (Figure 4.9), and particles interact with each other through a viscoelastic mastic phase containing bitumen and air between them [80,114,188]. Therefore, the open-source software NEPER (<https://neper.info/>) was adopted to generate particle tessellation samples. It offers support for Voronoi tessellations in both 2D and 3D, large tessellations can be easily created, and any convex domain shape can be used [189,190]. Moreover, tessellations can also be written in various formats for different simulations.



(a) Dynamic modulus



(b) Phase angle

Figure 4.8: Dynamic modulus and phase angles from experimental measurements of asphalt mixture

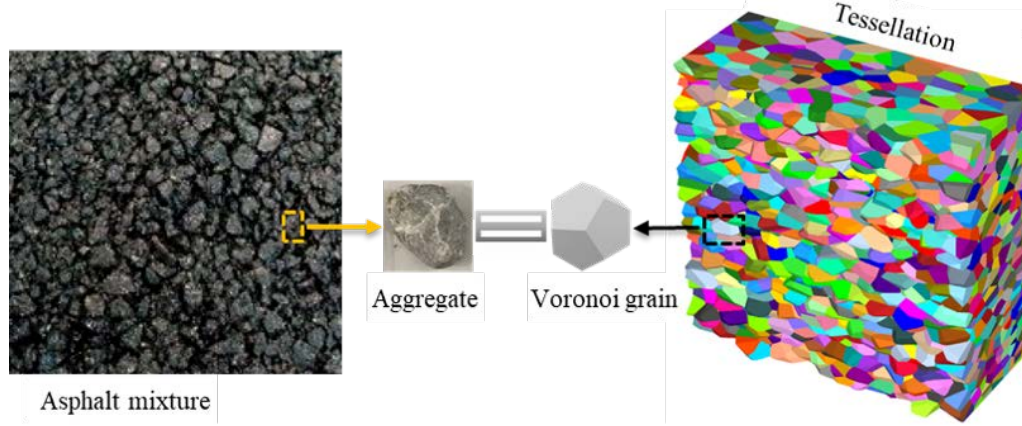


Figure 4.9: Asphalt mixture and Voronoi tessellations

Before generating the trapezoidal numerical specimen for a 2PB test, two main parameters need to be input. The first is particle size: we input the size of aggregates according to the PSD results (Figure 4.10) to simulate aggregate gradation. The second is particle morphology: we input the aggregate shape parameters from the statistics reported in Table 4.1, including aspect ratio and sphericity and its distribution. Using this procedure, we can achieve the goal of incorporating the aggregate morphology and aggregate size in the numerical simulation of asphalt mixtures. After the generation, about 5,680 tessellations were created following the experimental gradation cut at 2 mm to reduce the total quantity of particles in the sample, so that finer aggregates are included in the asphalt mastic. For particles between 2 mm and 4 mm, we assume that they have the same morphology distribution as other particles. Then, the vertices of each tessellation were imported in LMGC90 to build numerical models. In this stage, particles were generated based on the convex hull of vertices from the tessellation. The initial generated tessellation is not proper for modeling the asphalt mixture because there are no gaps between grains and particles touch seamlessly. Therefore, the original particle size from net tessellation is shrunk by multiplying a correction factor  $f_{cr}$  (Eq. 4.1 [51, 188]) in order to create gaps accommodating the mastic phase among particles. As Figure 4.11 shows, rigid particles interact with each other through the viscoelastic asphalt mastic.

$$f_{cr} = \left(1 - \frac{T_L \rho_S}{100 \rho_L}\right)^{\frac{1}{3}} \quad (4.1)$$

Where:  $T_L$  is the binder content (4.7%),  $\rho_S$  the initial density of particles

( $2.6Mg/m^3$ ) and  $\rho_L$  the density of binder ( $1.03Mg/m^3$ ).

After the sample generation, the contact model was activated between particles. To simulate the mobile loading parts in the experimental device, a top plate was generated with mass of 0.235 kg and put over the sample. Finally, the system was stabilized by activating gravity. Following this entire process, numerical samples were prepared with the same geometrical properties as those identified on experimental specimens. Figure 4.10 and Figure 4.11 show the final gradation and snapshot of the numerical sample reconstructed in LMGC90 software, respectively.

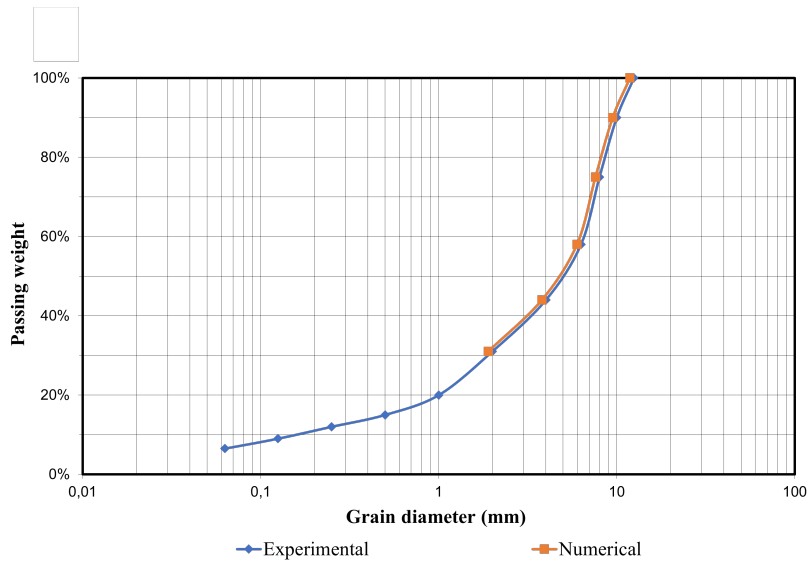


Figure 4.10: Particle size distribution (PSD) of asphalt mixture

#### 4.4.3 Burgers contact model and its calibration

Asphalt mixture is a complex composite material showing a viscoelastic behavior, thus a viscoelastic contact model based on the Burgers model was adopted in the simulation. This model comprises a Maxwell model in series with a Kelvin-Voigt model (Figure 4.12), the normal and tangential properties including stiffnesses and the viscosities for the Maxwell and the Kelvin-Voigt parts correspond to  $K_{mi}$ ,  $C_{mi}$ ,  $K_{ki}$ , and  $C_{ki}$ , respectively, where  $i$  stand for  $n$ ,  $t$  or  $s$ .

For a viscoelastic material under cyclic loading, it is possible to determine

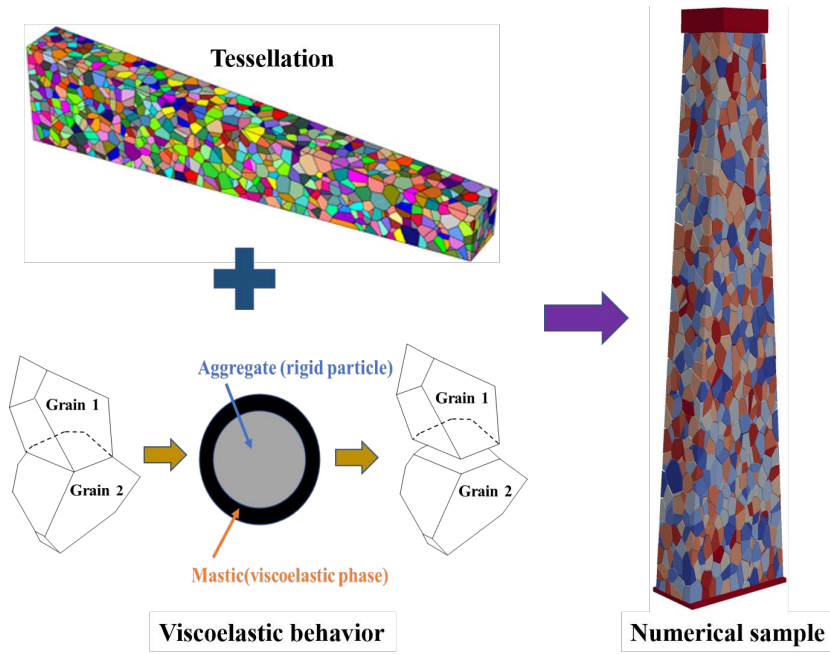


Figure 4.11: Numerical modeling of test sample

the complex compliance from the resulting strain and stress as following:

$$|D^*| = \sqrt{D'(\omega)^2 + D''(\omega)^2} \quad (4.2)$$

$$D'(\omega) = \frac{1}{E_m} + \frac{E_k}{E_k^2 + \omega^2 \eta_k^2} \quad (4.3)$$

$$D''(\omega) = \frac{1}{\omega \eta_m} + \frac{\omega \eta_k}{E_k^2 + \omega^2 \eta_k^2} \quad (4.4)$$

Where:

- $E_m$ ,  $\eta_m$ ,  $E_k$  and  $\eta_k$  correspond to the macroscopic Maxwell and Kelvin-Voigt stiffnesses and viscosities respectively.
- $|D^*|$  is the complex compliance,  $D'$  and  $D''$  are the real and the imaginary parts of the complex compliance, and  $\omega$  is the pulsation.

The normal components of the microscopic parameters at the particle-scale can be assessed by:

$$K_{mn} = A_c E_m / l_0 \quad (4.5)$$

$$C_{mn} = A_c \eta_m / l_0 \quad (4.6)$$

$$K_{kn} = A_c E_k / l_0 \quad (4.7)$$

$$C_{kn} = A_c \eta_k / l_0 \quad (4.8)$$

Where:

- $A_c$  is the cross-section area of two particles in contact and  $l_0$  is the initial distance between the particles.

On the other hand, the tangential components of the contact model for both tangential directions t and s can be computed from the above normal parameters, as:

$$K_{mt} = K_{ms} = \frac{K_{mn}}{2(1 + \nu)} \quad (4.9)$$

$$C_{mt} = C_{ms} = \frac{C_{mn}}{2(1 + \nu)} \quad (4.10)$$

$$K_{kt} = K_{ks} = \frac{K_{kn}}{2(1 + \nu)} \quad (4.11)$$

$$C_{kt} = C_{ks} = \frac{C_{kn}}{2(1 + \nu)} \quad (4.12)$$

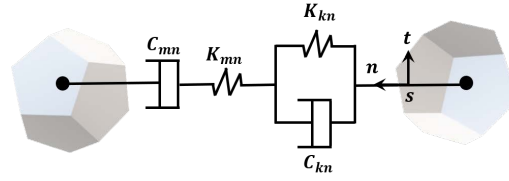
Where:

- $\nu$  is the Poisson's ratio, this ratio was set to 0.35 [48].

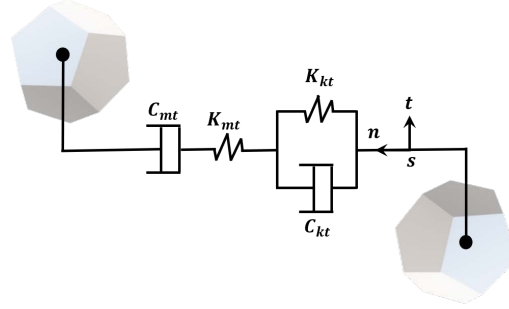
In the contact dynamics (CD) method, the contacting laws are non-differential steep laws defining the relation between relative velocities  $\mathbf{U}$  and impulses  $\mathbf{R}$ . These laws are based on the Signorini condition and Coulomb's friction law for perfectly rigid bodies. The CD formulation of solving the non-smooth contact problem above can be written as:

$$U^+ = U^- + WR^+ dt \quad (4.13)$$

Where:



(a) Normal components



(b) Tangential components

Figure 4.12: Burgers contact model between particles

- $U^+$  and  $U^-$  are the relative velocities at times  $t$  and  $t + dt$ , where  $dt$  is the time step;
- $W$  is the Delassus matrix, which contains the values of the inverse reduced inertia;
- $R^+$  is the vector of contact forces at time  $t + dt$ .

Adding the complementary velocities generated into the Burgers model to the general CD formulation for frictional contacts (Eq. 4.13, leads to the following equation of motion:

$$U^+ = U^- + U_k^+ + U_{mk}^+ + U_{mc}^+ + WR^+ dt \quad (4.14)$$

Where:

- $U_k^+$  is the complementary relative velocity generated by the Kelvin-Voigt model.
- $U_{mk}^+$  and  $U_{mc}^+$  are the complementary relative velocities generated by the stiffness and viscosity parts of the Maxwell model.

The contact forces generated within the Burgers model can be determined for

each section as function of the complementary relative velocities, as follows:

$$R^+ = R_k^+ = R_{mk}^+ = R_{mc}^+ \quad (4.15)$$

$$R_{ki}^+ = -K_{ki}\delta_{ki}^+ - C_{ki}U_{ki}^+ \quad (4.16)$$

$$R_{mki}^+ = -K_{mi}\delta_{mki}^+ \quad (4.17)$$

$$R_{mci}^+ = -C_{mi}U_{mci}^+ \quad (4.18)$$

Where:

- $R_k^+$ ,  $R_{mk}^+$  and  $R_{mc}^+$  correspond to the local reaction vectors at time  $t + dt$  generated by the Kelvin-Voigt and the Maxwell properties, respectively.

Replacing the complementary velocity terms obtained from Eq. 4.16 to 4.18 into Eq. 4.19, leads to a modified equation of motion in the CD formulation, obtained as a function of the parameters of the Burgers model as:

$$U_i^+ = U_i^- - \frac{K_{ki}\delta_{ki}}{C_{ki}} + \frac{R_i^-}{dtK_{mi}} + [W_{ii} + (-\frac{1}{dtK_{mi}} + \frac{1}{C_{mi}} + \frac{1}{C_{ki}})]R_i^+ dt \quad (4.19)$$

This formulation is solved implicitly by means of an iterative procedure based on the Non-Linear Gauss-Seidel algorithm (NLGS) method. The relations between velocities and contact forces for the Burgers model in CD method are plotted in Figure 4.13. More details about the numerical implementation of this contact model in CD method can be found in [48].

The macroscopic model parameters allow determining the dynamic modulus as  $|E^*| = |D^*|^{-1}$  and the phase angle by  $\phi = \arctan(D''/D')$ . Using the established analytical expressions for  $|E^*|$  and  $\phi$ , the best fit of macroscopic parameters regarding experimental data can be estimated. The parameter calibration of Burgers model for each temperature was based on an optimization iterative procedure, as follows:

- Performing the numerical simulation based on initial Burgers parameters under each loading frequency;
- Computing the numerical  $|E^*|$  and  $\phi$  values from simulation results according to Eqs. 3.1 to 3.6;



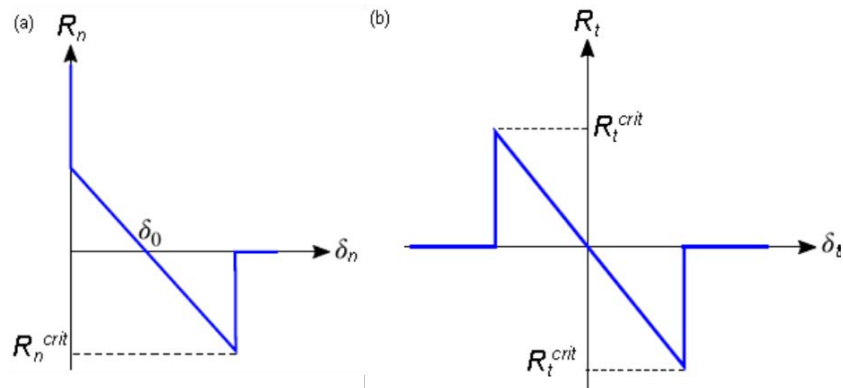


Figure 4.13: Relations between velocities and contact forces: (a) Normal components (b) Tangential components [48].

(iii) Correcting the analytical model (Eqs. 4.2 to 4.4) with the same parameters to fit the numerical values. After the calculation, a difference between the analytical and the numerical values could be observed. The correction step compensating the difference was processed by an optimization algorithm implemented in Python programming language based on the least-squares method;

(iv) Using the corrected expressions above to fit the experimental  $|E^*|$  and  $\phi$  values;

(v) Evaluating the error between experimental and numerical  $|E^*|$  and  $\phi$  values, the parameters fitted from this iteration step can be used to perform a new iteration step until the convergence criterion is achieved. Finally, after several iterations of model parameters adjustment, the model parameters were fitted optimally to the experimental data.

The flow chart of the calibration process is shown in Figure 4.14. After several iterations of model parameters adjustment, the model parameters were fitted optimally to the experimental data.

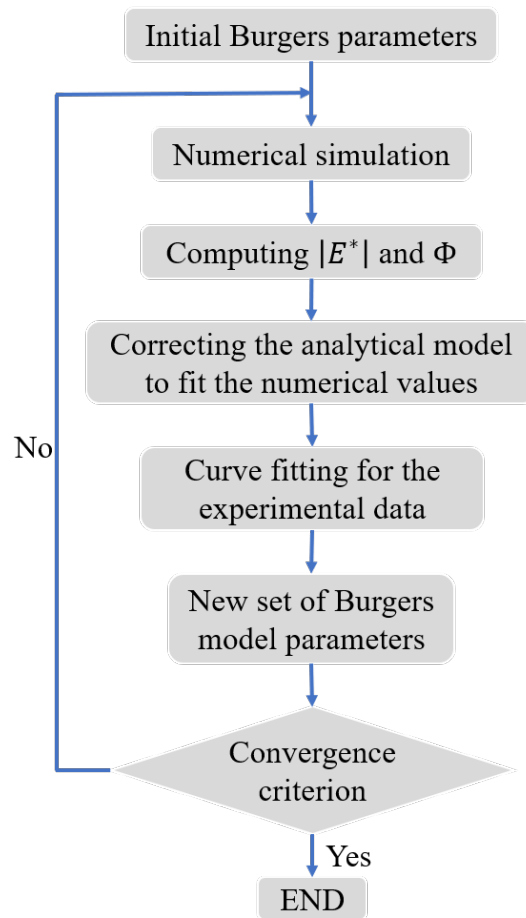


Figure 4.14: Calibration process of Burgers model parameters.

## 4.5 Numerical analysis

### 4.5.1 Macro mechanical behavior

Figure 4.15 shows an example of the measured displacement and the corresponding force at the top plate for five loading cycles. As expected, both the force and displacement curves follow the sinusoidal wave. The phase angle between these two curves allows calculating  $\psi$ .

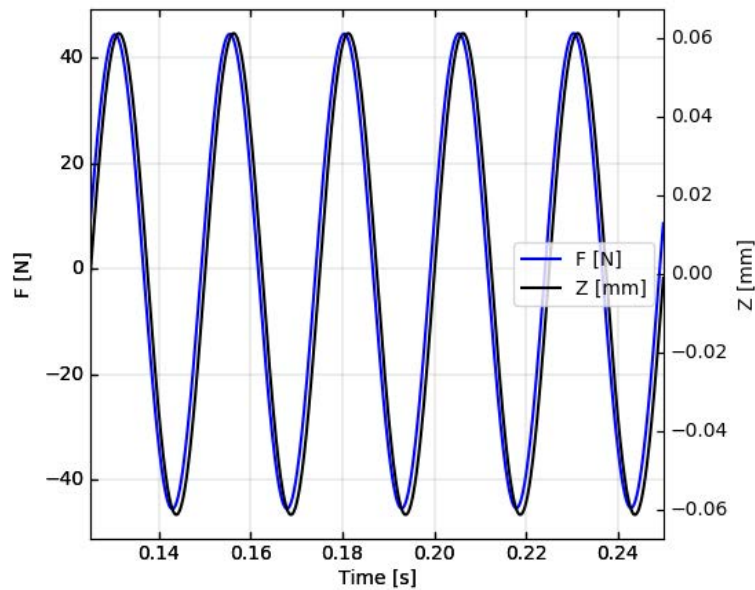


Figure 4.15: Measured displacement  $Z$  and corresponding force  $F$  for 15 °C and 40 Hz

The master curve describing the loading time dependency of asphalt mixtures can be built according to the time-temperature superposition principle [156, 157]. The equation (Eq. 3.7) defined in Chapter 3 was used to build the corresponding master curve for the asphalt mixture. Figure 4.16 shows the experimental and numerical results for the master curve with  $C_1 = 28$  and  $C_2 = 206.8$  °C, at the reference temperature of 15 °C, which is a referenced value in French pavement design [45].

The numerical values from simulations are in good agreement with experimental values for  $|E^*|$  and  $\phi$  for all the tested frequencies, despite some

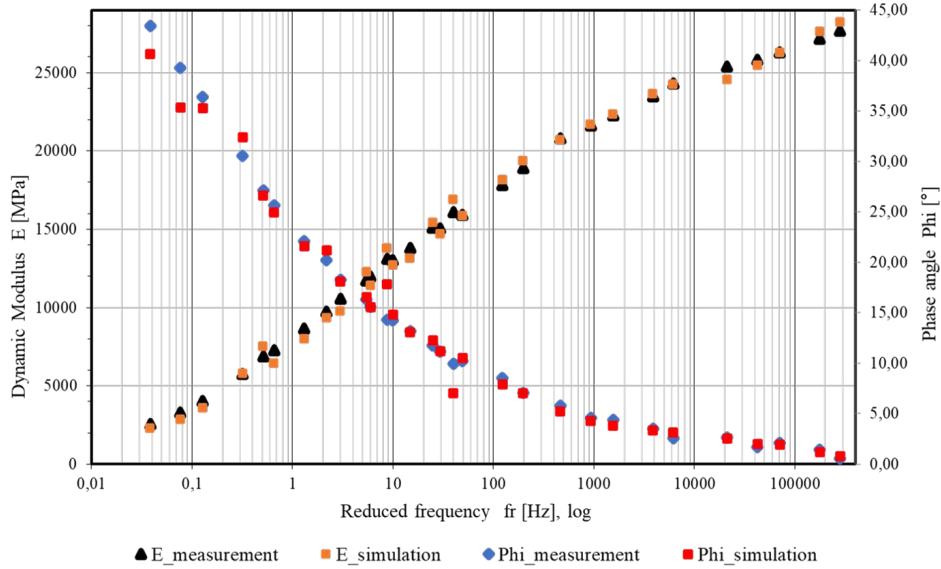


Figure 4.16: Experimental and numerical master curve at  $T_{ref} = 15^{\circ}C$

fluctuations around the average values. The best fitting parameters for the Burgers contact model are listed in Table 4.4.

Table 4.4: Burgers model parameters used in numerical simulations

$T$ ( $^{\circ}C$ )	$E_m$ (Pa)	$\eta_m$ (Pa.s)	$E_k$ (Pa)	$\eta_k$ (Pa.s)
-10	$1.34 \times 10^8$	$1.79 \times 10^8$	$2.55 \times 10^9$	$3.26 \times 10^7$
0	$1.18 \times 10^8$	$6.86 \times 10^7$	$9.36 \times 10^8$	$1.03 \times 10^7$
10	$1.02 \times 10^8$	$1.93 \times 10^7$	$2.80 \times 10^8$	$3.05 \times 10^6$
15	$9.48 \times 10^7$	$1.02 \times 10^7$	$1.70 \times 10^8$	$1.79 \times 10^6$
20	$8.64 \times 10^8$	$4.81 \times 10^6$	$1.02 \times 10^8$	$1.05 \times 10^6$
30	$7.18 \times 10^7$	$8.84 \times 10^5$	$3.39 \times 10^7$	$2.80 \times 10^5$

## 4.5.2 Micro mechanical behavior

### 4.5.2.1 Contact force distribution

After the calibration, the previous stabilized specimens were submitted to dynamic loading. Figure 4.17 illustrates the macro- and micro-mechanical behavior of an asphalt specimen in one loading cycle. At the macro-mechanical scale, repeating compression and tension states in the specimen lead to fa-

tigue cracks inside the sample. On the other hand, at the contact-scale, there are two main types of force between particles: the tangential force inducing shearing in the interfacial plane of contact and the normal force lying perpendicular to this plane. Both forces contribute to the fatigue damage of asphalt mastic between particles, playing a major role in contact breakage and particle movement, finally initiating and propagating macro-cracks inside the mixture.

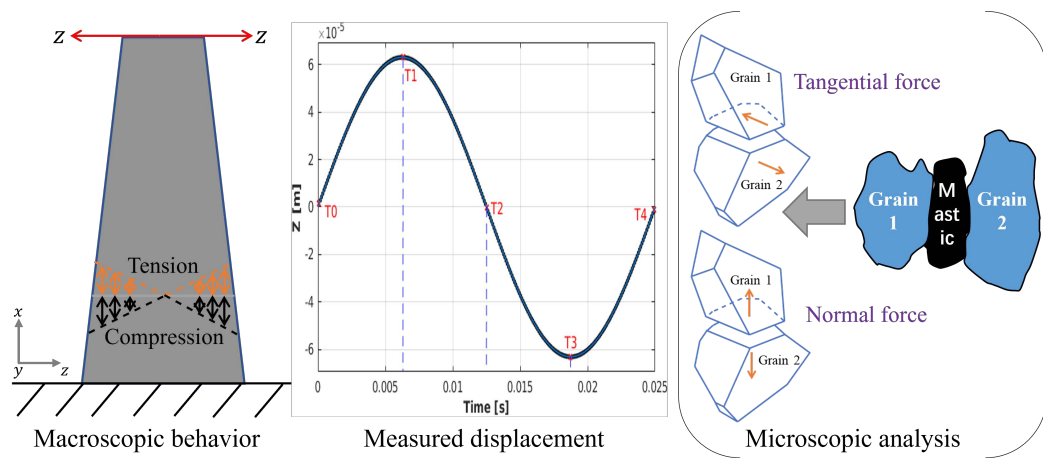


Figure 4.17: Macro and micro behavior of asphalt specimen in one loading cycle

Figures 4.18 and 4.19 show the normal stress and tangential stress distribution in one loading cycle, respectively. Both normal force value and tangential force value converge at zero at  $T_4$ , which is consistent with the end loading condition. For the other loading points from  $T_0$  to  $T_3$ , the distribution of the normal force values follows a normal distribution centered at zero, while the tangential force values develop an asymmetric distribution on one side of the  $x$ -axis. These distributions imply that the normal forces are symmetric around zero (tension-compression) during the loading cycle, while tangential forces change the direction and intensity as the loading condition changes. The horizontal displacement achieves a maximum value when both normal and tangential force are close to their maximums (because of the phase lag), according to  $T_1$  and  $T_3$ .

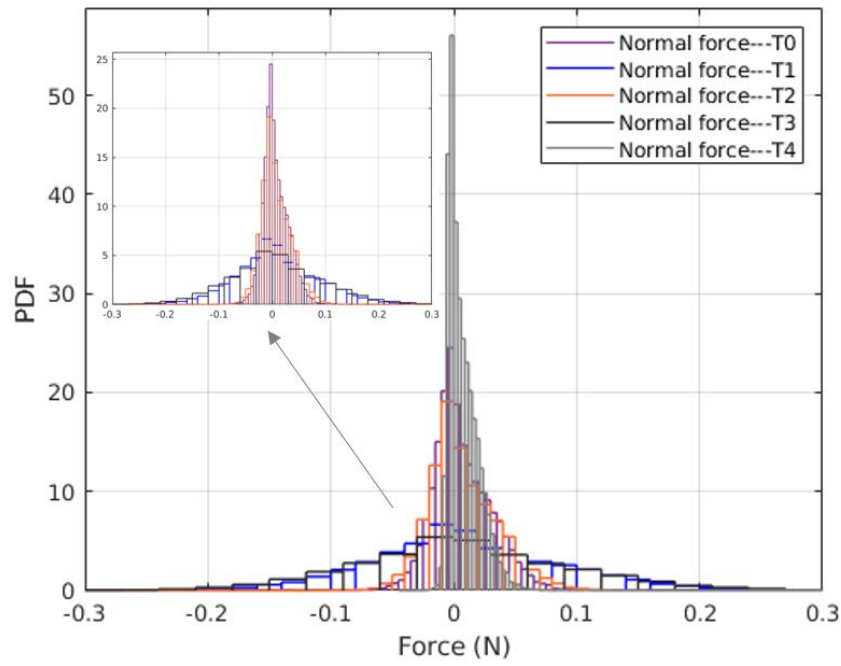


Figure 4.18: Normal force probability distribution at 15 °C, 40 Hz

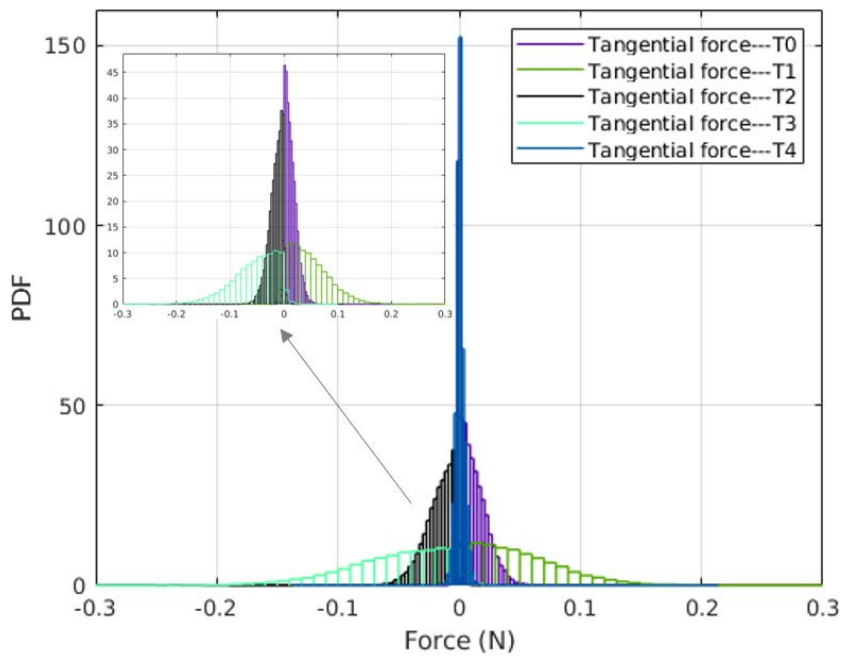


Figure 4.19: Tangential force probability distribution at 15 °C, 40 Hz

#### 4.5.2.2 Particle velocity distribution and contact force networks

The numerical sample follows the loading condition and responding particle movement behaves accordingly. Figure 4.20 depicts different stages during one loading cycle in the numerical test. The particle velocity achieves the maximum value at T1 and T3 when the displacement amplitude is the maximum, and it is close to zero at T4 due to the balance calculation at the end of the loading. For T0 to T3, the average particle velocity displays an increasing trend along with the specimen height, from a minimum value for particles lying on the bottom plate up to a maximum value for particles bonded to the top loading plate.

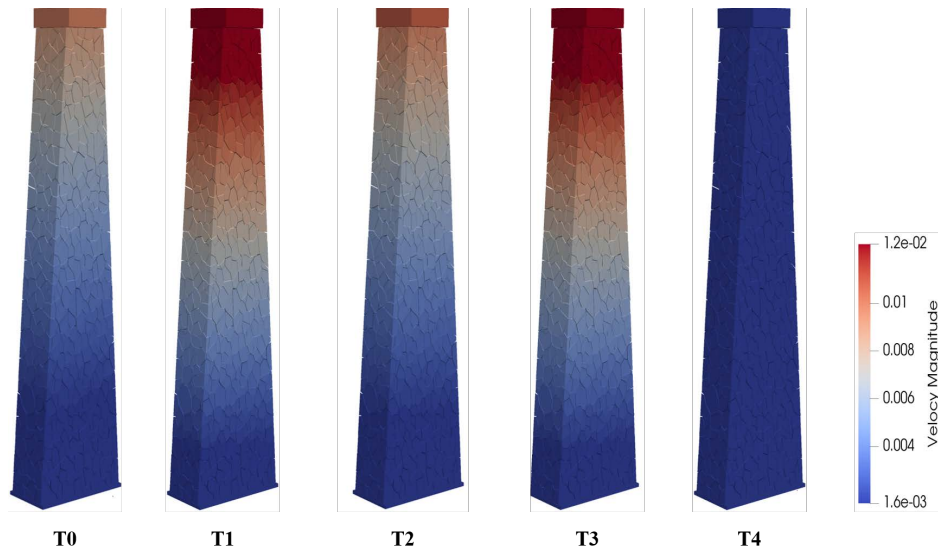


Figure 4.20: Average velocity of particles for 15 °C and 40 Hz

In particle-based methods, the contact force network reflects the transmission of external loads in granular materials. Previous observations show that T1 and T3 are two characteristic points for the loaded specimen; therefore it is rewarding to visualize the contact force networks at these two points. Strong and weak contacts are always coexisting in a contact network, which forms the corresponding networks of strong contact forces, i.e. forces above the mean normal force ( $f_n > \langle f_n \rangle$ ), and weak contact forces ( $f_n < \langle f_n \rangle$ ) [125]. Figure 4.21 shows the strong and weak force distribution at T1 and T3. Both strong (red) and weak forces (blue) change direction following the change in direction of the tangential force. This is consistent with the inference above.

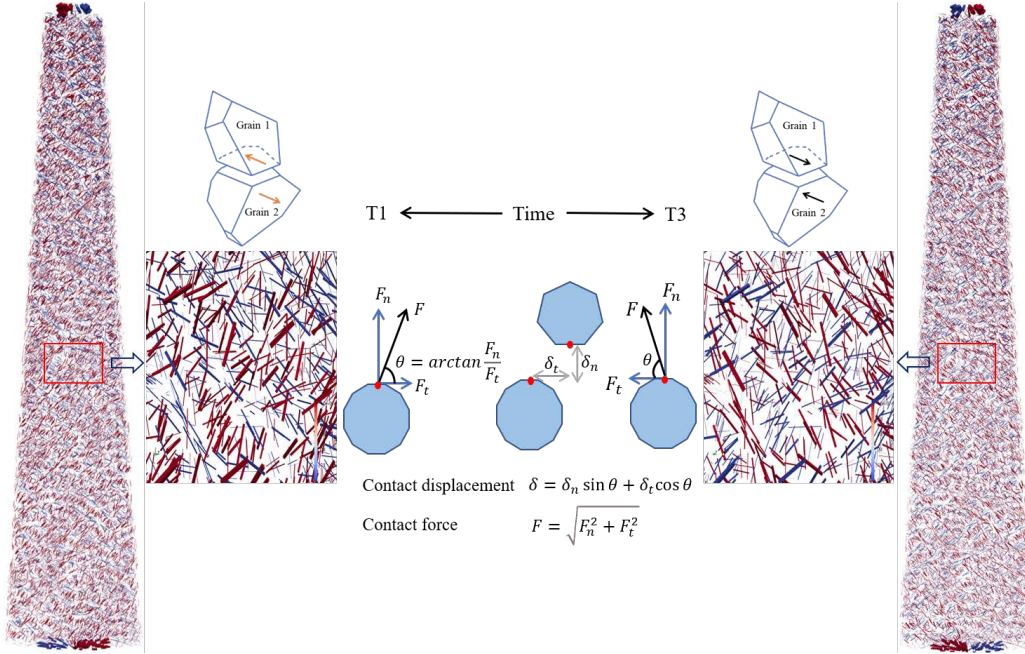


Figure 4.21: Strong and weak contact force networks for 15 °C and 40 Hz

#### 4.5.2.3 Normal and tangential force analysis

As previously evoked, both normal and tangential forces between particles can be considered for the set up of a damage contact model. In this part, we examine the changing trend of the tangential and normal forces for different loading frequencies and temperatures. From the above analysis, we choose T1 and T3 as the critical time to process force analysis. Figure 4.22 shows the changing trend of the two types of force at 15 °C for different frequencies. The tangential force reaches positive values at T1, where the measured displacement is maximum following the horizontal loading direction. After a half loading cycle, the tangential force achieves negative values at T3, where the displacement reaches a maximum value in the opposite direction. The higher the frequency, the larger the magnitude of tangential force at T1 and T3 will be. The normal force has a wider distribution range than the tangential force and distributes symmetrically along the Y-axis ( $x=0$ ). Besides the range increases as the frequency increases, which indicates the magnitude of the normal force shows the same trend as the tangential force.



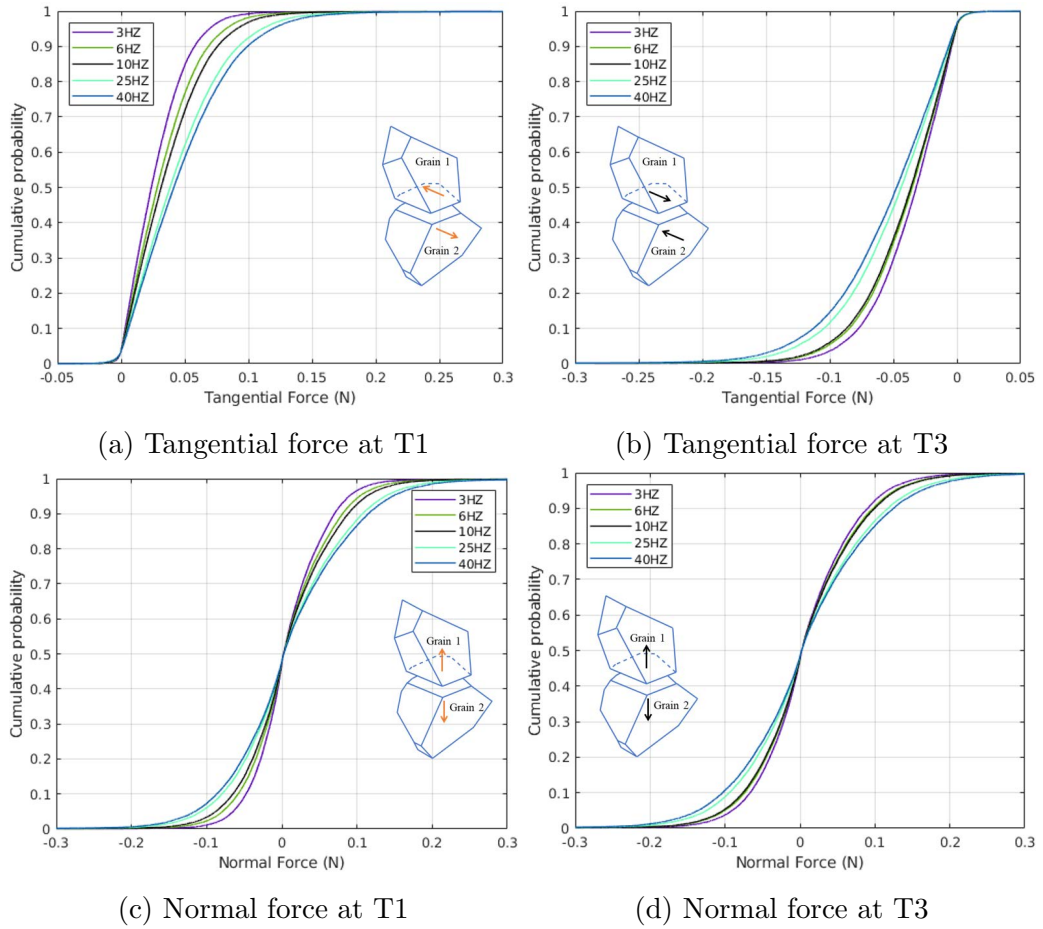


Figure 4.22: Cumulative distribution for tangential force and normal force at T1, T3, 15 °C

Figure 4.23 shows the changing trend of the tangential force and normal force at 40 Hz loading frequency for different temperatures. It can be seen that the magnitude of the tangential force decreases when the temperature increases. Similarly, the magnitude of normal force behaves in the same downtrend as the tangential force as the temperature increases. It also illustrates that the asphalt mixture is sensitive to temperature and loading frequency, due to its viscoelastic nature.

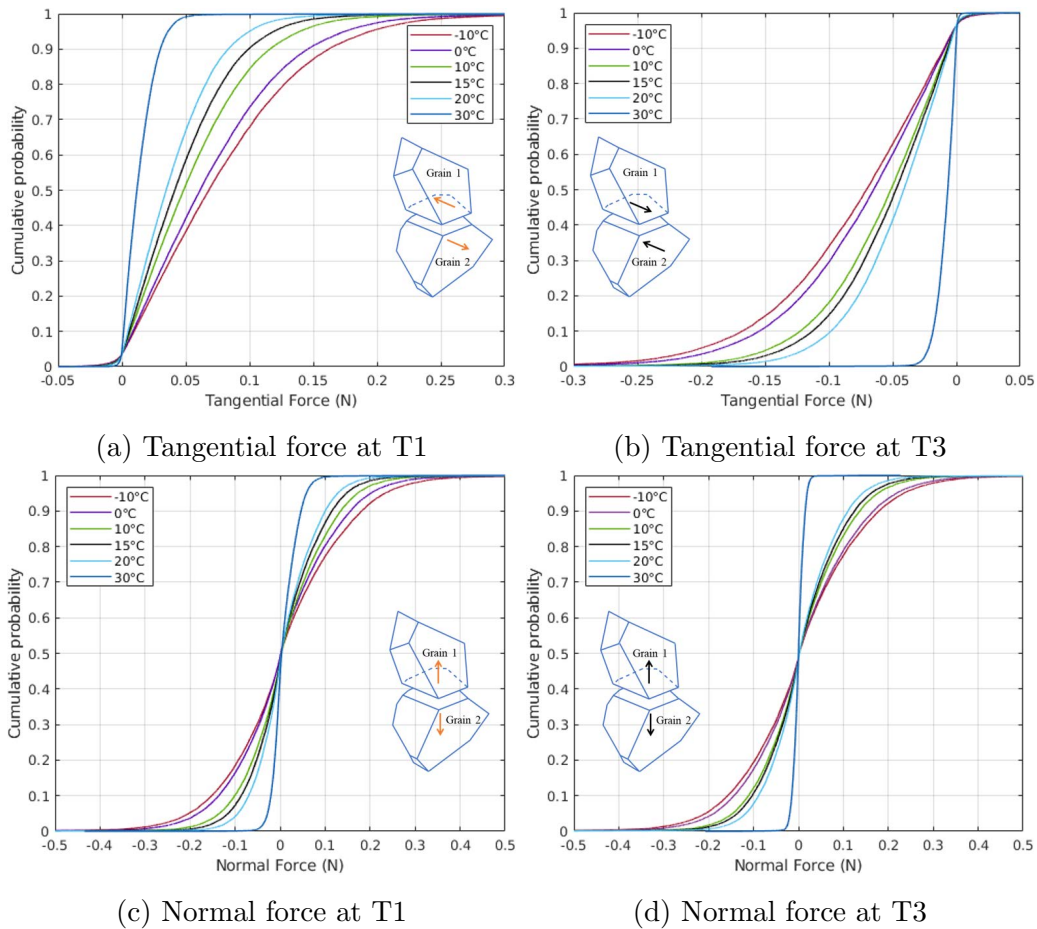


Figure 4.23: Cumulative distribution for tangential force and normal force at T1, T3, 40 Hz

At the macroscopic scale, asphalt materials have a stiffer behavior at higher frequencies or lower temperatures. During a performance test of asphalt mixtures, the specimen exchanges compression and tension in loading cycles. The specimen is subjected to a higher stress level at higher frequencies or

lower temperatures, which induces earlier damage initiation. From the microscopic analysis at the contact scale above, we can conclude that the specimen withstanding lower frequency or higher temperature tends to exhibit better resisting performance to adhesive failure because of lower tangential force and lower normal force between particles.

Particle forces analysis above reveals the micro-mechanism of mixture failure initiation at the contact scale. By using the presented numerical method, some earlier failure patterns of asphalt mixtures could be envisaged. The findings here are also encouraging for further prediction of damage evolution in future studies. Long-term performance tests such as laboratory fatigue tests are always time-consuming and expensive. Due to the limitation of computation capacity, it is still challenging to reproduce long-term performance tests with larger numbers of loading cycles in numerical tests. The proposed numerical modeling method might be used to study mixture damage evolution if a damage model of bonds between particles with the cycle number is added in the numerical simulation process.

## 4.6 Conclusions of the chapter

In this chapter, combining laser scanning and image processing, morphology features of aggregates were collected and analyzed statistically. Aggregate flatness ratio, elongation ratio, and Sphericity value all obey normal distributions. The average aspect ratio ( $L : I : S$ ) for aggregates and the mean and standard deviation of the Sphericity value were obtained as input particle shape parameters in the numerical simulation.

The contact dynamics method was introduced to model asphalt mixtures because of its superior capability in polyhedron simulation. Asphalt mixture specimens were generated by a tessellation method based on particle morphology statistics. The modeling method incorporates the aggregate morphology and size distribution in the numerical simulation. It also reduces the computational time significantly during the preparation stages for polyhedral samples, such as deposition by gravity and compaction.

Experimental and numerical 2PB tests under different temperatures and frequencies were carried out to validate the model reliability. The dynamic modulus and the phase angle were calculated to analyze the viscoelastic be-

havior. The corresponding numerical master curves were in good agreement with the experimental data.

Through the microscopic analysis, both the tangential force and the normal force between particles have an apparent increasing trend with increasing loading frequency and decreasing temperature. Comparing the trends of the tangential force and normal force between the particles during cyclic loading, the mechanism of damage initiation for viscoelastic materials could be assessed at the particle scale.

The following paper summarizes the main results of this chapter:

Ge, H., Quezada, J. C., Le Houerou, V., & Chazallon, C. (2021). Three-dimensional simulation of asphalt mixture incorporating aggregate size and morphology distribution based on contact dynamics method. *Construction and Building Materials*, 302, 124124. [[191](#)].



# Multi-scale simulation of tire-pavement interaction

---

## Contents

---

<b>5.1</b>	<b>Introduction</b>	<b>107</b>
<b>5.2</b>	<b>Tire modeling and calibration</b>	<b>108</b>
5.2.1	Tire structure and model construction	108
5.2.2	Model calibration	110
<b>5.3</b>	<b>Macro simulation of the tire induced-loading on the pavement surface</b>	<b>111</b>
5.3.1	Tire rolling contact model	111
5.3.2	Tire contact stress distribution under free-rolling	116
5.3.3	Tire contact stress distribution under full-braking	116
<b>5.4</b>	<b>Micro simulation of tire-pavement interaction</b>	<b>119</b>
5.4.1	Asphalt mixture modeling	119
5.4.2	Non-uniform tire load simulation	120
5.4.3	Particle displacement distribution	123
5.4.4	Particle contact force analysis	126
<b>5.5</b>	<b>Conclusions of the chapter</b>	<b>129</b>

---

## 5.1 Introduction

The tire-pavement interaction is an extremely complex contact problem in the contact mechanics domain. In the chapter 3, we adopted Tekscan to measure the tire contact stresses experimentally, this method is adequate when we focus on the free-rolling tire loading condition as the tangential contact

stresses are negligible, as the dominant vertical tire contact stress can be well characterized through measurements. However, when we shift our attention to braking/acceleration cases, the experimental method has limitations in obtaining tangential tire contact stresses. Due to these limitations of experimental measurements in studying different kinematic cases, experimental approaches struggle to examine this interaction system adequately.

On the other hand, numerical tools provide an effective way to explore this system while taking into account the system complexity. However, current research has primarily focused on macro simulations of the tire-pavement interaction based on mesh-based methods such as FEM [34, 36, 38–40, 143] and SAM [32, 41, 42], in which the asphalt pavement is usually assumed homogeneous due to the limitations of mesh-based methods in the continuum mechanics framework. Mesh-based methods can simulate tire contact stresses precisely on the pavement surface, but it is still a struggle to quantify internal mixture responses at the particle scale.

As introduced in the previous chapter, asphalt mixtures are complex multi-phase systems composed of aggregate particles and asphalt mastic. DEM is an effective method to model the interacting components of asphalt mixture and to understand the mixture responses from the particle level.

In this chapter, we report a multiscale simulation method to examine the tire-pavement interaction combining FEM and DEM approaches based on the Contact Dynamics (CD) method. The multiscale modeling approach brings the benefit that FEM can provide precise tire contact stresses on the pavement surface, while DEM can evaluate effectively the internal discontinuity behavior of the asphalt mixture. This method proposes an innovative and promising way to simulate the tire-pavement interaction and to explore degradation mechanisms of the asphalt pavement surface under different tire loads at the particle scale.

## 5.2 Tire modeling and calibration

### 5.2.1 Tire structure and model construction

The tire structure is extraordinarily complex. For a typical radial tire, it comprises components at several scales such as ribs, grooves, beads, sidewalls,

and belt piles, and every part has its own material properties. Numerical simulations have a universal purpose of capturing the main features of a problem and ignoring its secondary factors. A wheel can be divided into two parts from the point of its functionality: a deformable part that models the tire itself and air together, which interacts with the pavement surface directly, and a rigid rim serving as the driven system following the tire motion that supports the loading, and transmits acceleration and braking. We adopted this strategy in tire modeling for its efficiency and simplicity.

In the modeling, a passenger tire (185/65R15) was chosen and a three-dimensional laser scanner (FARO Freestyle3D) was employed to reconstruct the tire geometry (Figure 5.1).

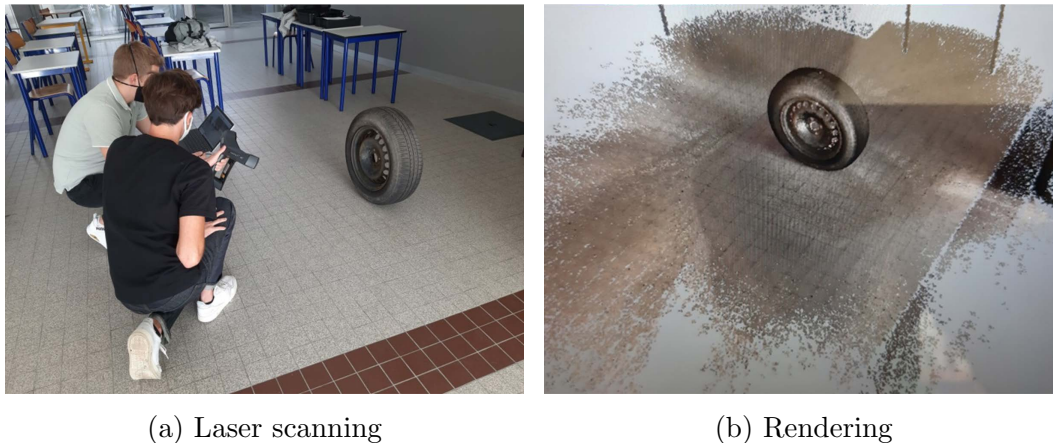


Figure 5.1: Tire scanning process

After the scanning procedure, the open-source software Meshlab (<https://www.meshlab.net/>) was used to process the cloud points and reconstruct the tire shape. Raw tire data are very noisy and have many textures, which are not conducive to numerical simulation since it produces geometrical non-linear complexity. The tire data were handled based on a method proposed elsewhere [192]. Based on the scanning results, the longitudinal tire grooves were retained, whereas the transverse textures were omitted by image processing, and the rigid rim part was replaced for the sake of simplicity by a cylinder inheriting the same diameter. Then, the open-source software Gmsh was used to conduct the meshing process. A fine mesh (5 mm characteristic length) was defined for the outer tire part and a coarse one was chosen for



the inner tire part (30 mm characteristic length) to achieve a good precision while saving the computation time. Figure 5.2 shows the generated tire model.

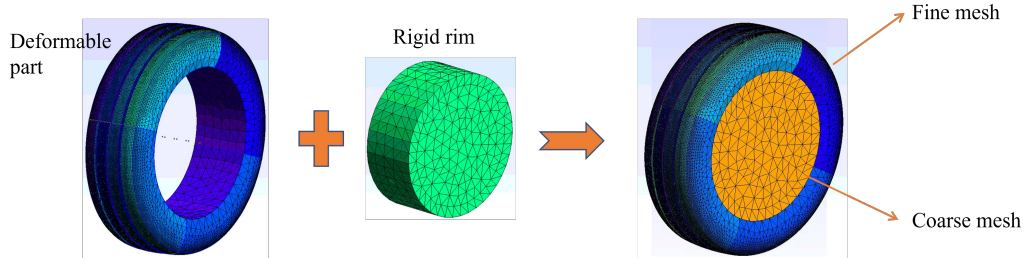


Figure 5.2: Tire model and mesh refinement

### 5.2.2 Model calibration

The rim part was assumed to be rigid, and the deformable part was modeled via a linear elastic material. The degree of freedom of these two objects was fixed by setting a coupled contact law so that the deformable and rigid parts can stick together and prevent sliding. To identify elasticity parameters of the deformable part, a tire compression test [193] was performed.

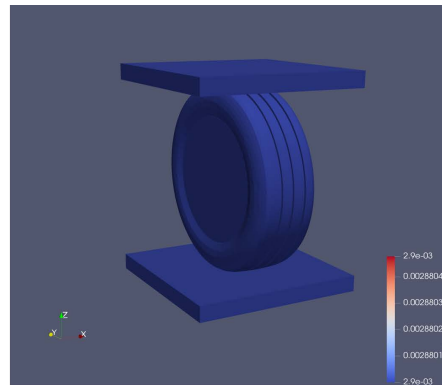
In the experiment, the tire was placed between two rigid plates, the force sensor was set on the top plate. We then recorded the force value ( $F$  [N]) and displacement ( $z$  [mm]) of the top plate. We measured the displacement values of the top plate at four force levels ( $F = 1, 2, 3, 4$  kN), then the tire load-deflection test results were used furthermore to calibrate the tire bulk behavior through numerical simulations.

During the numerical simulation of the reproduced test, Signorini's condition and Coulomb's friction law were adopted as the contact law between the tire and the rigid plates, and the friction coefficient was set as close to zero considering the slippery feature of the plate surface. A numerical top rigid plate was then subjected to the same vertical velocity as in the experimental test. As a final step, the numerical load-deflection curve of the rigid top plate was recorded during the simulation and then compared with the experimental results. The material properties were calibrated in the numerical simulation to fit the experimental deflection values. Figure 5.3 presents the compression test process and calibration results, where the tire inflation pressure was equal

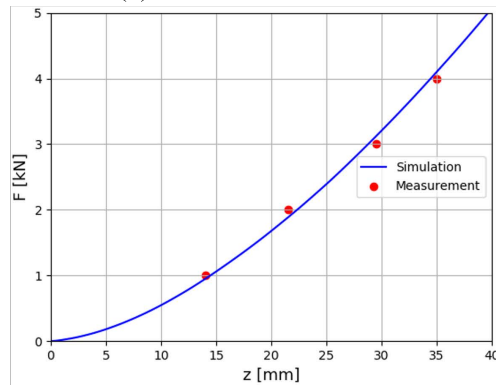
to 2.2 bar. The predicted load-deflection curve agrees with the experimental data, where the obtained material parameters for the numerical simulation were a Young's modulus of 1.0 MPa and a Poisson's ratio of 0.36. It is worth to note that the deformable part is compressible since it models rubber and air together. The nonlinear load-deflection curve comes from the geometric nonlinearity.



(a) Tire compression test



(b) Numerical simulation



(c) Load-deflection curve

Figure 5.3: Comparisons between measured and calculated tire deflections

## 5.3 Macro simulation of the tire induced-loading on the pavement surface

### 5.3.1 Tire rolling contact model

Pavement surfaces degrade primarily due to traffic loads, where tires are the interface between a vehicle and the road surface. Pavement degradation anal-

ysis requires contact stress distributions of a tire on the pavement surface. Depending on the driving state and direction, a vehicle tire could withstand forces and torques in every directions. Figure 5.4 illustrates the force status of a rolling tire and the contact mechanical actions transmitted to the pavement surface. The vertical force is given by the weight of the vehicle and depends on the dynamic behavior of the suspension. The longitudinal force is generated when the tire is traveling in a straight line, during acceleration or braking. The side (lateral) force is generated when the tire is changing direction, during cornering.

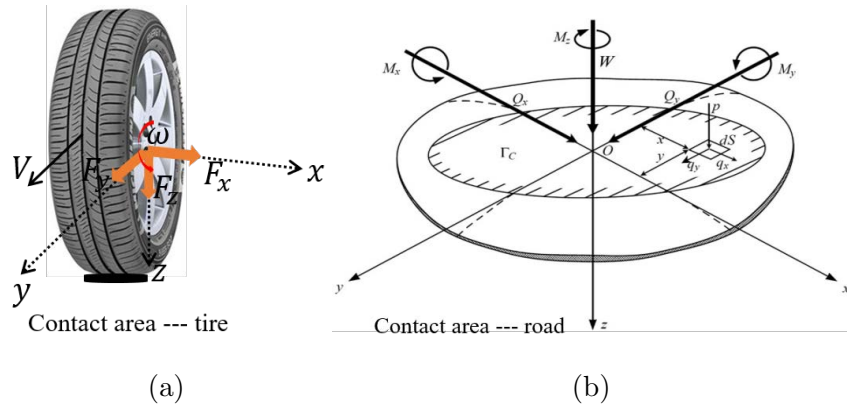


Figure 5.4: Tire driven forces during rolling (a) and pavement contact forces (b) [194]

where:

- $F_x$  [N] — lateral tire force.
- $F_y$  [N] — longitudinal tire force.
- $F_z$  [N] — vertical tire force.
- $\omega$  [rad/s] — tire angular velocity.
- $V$  [m/s] — tire longitudinal velocity.
- $Q_x, Q_y, W$  — contact forces on the pavement surface.
- $M_x, M_y, M_z$  — contact moments on the pavement surface.

The contact stresses on the pavement surface including the normal and tan-

genital parts were solved by the balance formulations below:

$$W = \int_{\Gamma_c} p(x, y) dS = F_z \quad (5.1)$$

$$Q_x = \int_{\Gamma_c} q_x(x, y) dS = F_x \quad (5.2)$$

$$Q_y = \int_{\Gamma_c} q_y(x, y) dS = F_y \quad (5.3)$$

where:

- $W$  [N] — normal load applied.
- $Q_x, Q_y$  [N] — tangential load applied.
- $p(x, y)$  [Pa] — normal contact pressure at a point(x,y).
- $q(x, y)$  [Pa] — tangential contact pressure at a point(x,y).
- $\Gamma_c$  [m<sup>2</sup>] — contact area.

After the construction of formulations solving the contact problem between the tire and pavement surface, it is possible to study the pavement surface responses under various tire loading conditions.

A pavement surface layer interacting with the tire was built and shown in figure 5.5. A dimension of 0.3 m×0.3 m×0.04 m in x, y, and z-direction was chosen for the modeling of a typical pavement wearing course. The y-axis represents the tire moving direction, and the x-axis represents the transverse (or lateral) direction, the spatial mesh size was chosen as 5 mm×5 mm×10 mm in x, y and z respectively, the mesh size of the contact zone under the tire matches the mesh size of the tire outer part to capture the stress distribution accurately.

Asphalt mixtures exhibit complex visco-elastic and visco-plastic behaviors regarding loading conditions, mainly including temperature and loading frequency. For the sake of computation efficiency, the elasticity modulus and Poisson's ratio of the surface layer was chosen to be 13,000 MPa and 0.35 respectively according to the experimental complex modulus test results at 15 °C and 10 Hz [191]. Thus the asphalt mixture was assumed as an elastic

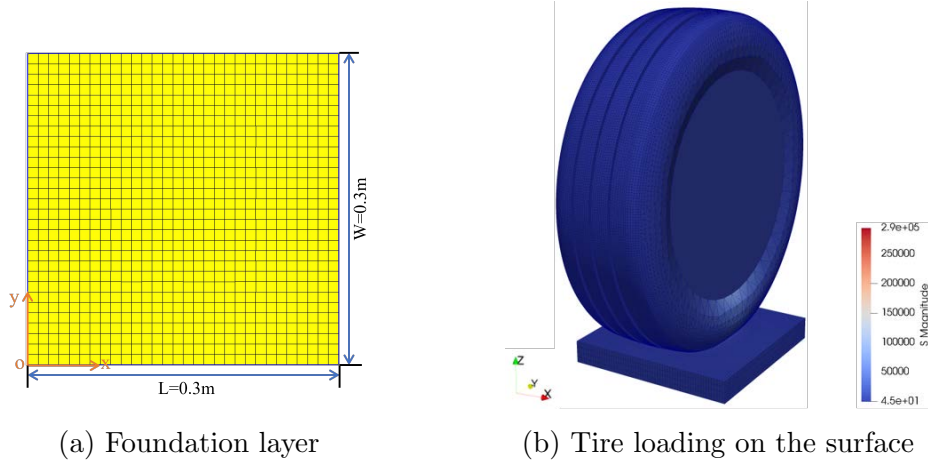


Figure 5.5: Asphalt surface layer and tire

material in the modeling [45]. We used Coulomb's friction law to describe the contact between the tire and the pavement surface, and the friction coefficient was chosen as  $\mu=0.8$ , where this value is commonly used as reference value for tire-pavement friction. For simulating tire axial loads, the driven forces were applied on the rim part of the calibrated tire model. During the entire simulation, the bottom of the layer was used as a fixed boundary condition.

The weight of a four-wheeled passenger car was assumed to be equally distributed between tires, the vertical load  $F_z$  of a tire can then be calculated as follows:

$$F_z = G_v/4 = m_v \cdot g_a/4 \quad (5.4)$$

Where,

- $G_v$  [N] — vehicle weight.
- $m_v$  — vehicle mass, it was set to 2.0 t in this study.
- $g_a$  — gravitational acceleration ( $9.8 \text{ m} \cdot \text{s}^{-2}$ ).

In this study, we examined the longitudinal tire behavior, including braking and acceleration. For a rolling tire without cornering, its longitudinal velocity can be calculated as:

$$V_{y0} = r_w \cdot \Omega_0 \quad (5.5)$$

where:

- $V_{y0}$  [m/s] — rolling tire longitudinal velocity.
- $r_w$  [m] — rolling tire radius.
- $\Omega_0$  [rad/s] — rolling tire angular velocity.

When a torque is applied to the tire, either for acceleration or braking, a longitudinal slip ( $k$ ) occurs between the tire and the vehicle [195], calculated as:

$$k = \begin{cases} -\frac{V_{y0} - r_w \cdot \Omega}{V_{y0}} = -\frac{\Omega_0 - \Omega}{\Omega_0}, a_v < 0 \\ \frac{r_w \cdot \Omega - V_{y0}}{r_w \cdot \Omega} = -\frac{\Omega - \Omega_0}{\Omega}, a_v > 0 \end{cases} \quad (5.6)$$

where:

- $k$  [-] — longitudinal tire slip.
- $\Omega$  [rad/s] — braking/accelerating tire angular velocity.
- $a_v$  [m/s<sup>2</sup>] — vehicle acceleration.

During braking, if the tire is completely locked ( $\Omega = 0$ ), the  $k$  parameter will reach a minimum value equals to -1. During acceleration, if the vehicle is activating but the tire is at standstill ( $\Omega_0 = 0$ ), the  $k$  parameter reaches its maximum value of 1.

For  $k$  different from zero, it corresponds to the acceleration ( $k > 0$ ) or braking ( $k < 0$ ) states, and the tire is subjected to longitudinal forces. For  $k = 0$ , it corresponds to the free-rolling state. When the tire is rolling in a steady-state (angular and translational velocities are constant), the dynamic process of the tire rolling is time-independent [38]. In the steady-state simulation, there is no requirement for the tire to move over the FEM mesh of the pavement, which makes it possible to calculate this interaction system numerically efficiently. Furthermore, it also allows the use of a dense mesh within the contact area of the pavement and the tire, which allows the accurate capture of tire contact stresses on the pavement surface. The tire loading state during rolling is also determined by the tire rolling speed. According to previous studies, for a passenger tire, the rolling tire radius  $r_w$  changes slightly when the tire experiences different rolling speed (from 0 to 5 km/h) [40]; and tire

rolling speed (from 15 to 90 km/h) has a negligible effect on the tire contact stresses [162]. Herein, we assume that the tire rolling speed does not affect the tire loading state. Consequently, the tire rolling contact can be considered to be stationary in the steady-state. As declared above, there are therefore two coupled effects: a normal effect caused by vertical loads, and a tangential effect caused by tangential loads (mainly from tire acceleration or braking).

### 5.3.2 Tire contact stress distribution under free-rolling

When a tire is in a free-rolling state, only vertical load  $F_z = 5$  kN acts on the tire. Figure 5.6a shows the magnitude of tire contact stresses on the pavement surface. This contour shows that the tire-pavement contact area is close to an ellipse. Figure 5.6b shows that the vertical contact stress is not uniform across the whole contact area. The distribution of the vertical stress is symmetric along the y-axis (tire length), and the maximum stress values concentrate at the tire center ribs.

Figures 5.6c and 5.6d demonstrate that the tire also induces contact stress components in lateral and longitudinal directions, affecting pavement responses together. The longitudinal contact stress distributes symmetrically along the y-axis, their peak values locate at the tire center ribs. The lateral contact stress distributes symmetrically along the x-axis (tire width) and the stress values achieve maximum at the tire edge ribs. In terms of peak values, the ratio between vertical, lateral, and longitudinal contact stress is about 1: 0.18: 0.14; the tangential contact stresses are considerably low compared to the vertical contact stress as expected for free-rolling conditions.

### 5.3.3 Tire contact stress distribution under full-braking

Since the longitudinal forces associated with a tire are similar for acceleration and braking, this study analysed tire contact stresses in braking conditions. In braking, the direction of the braking torque is opposite to the tire moving direction. If the tire slip reaches its minimum value ( $k=-1$ ), it means that the tire is fully locked (hence full-braking), and the longitudinal force  $F_y$  can

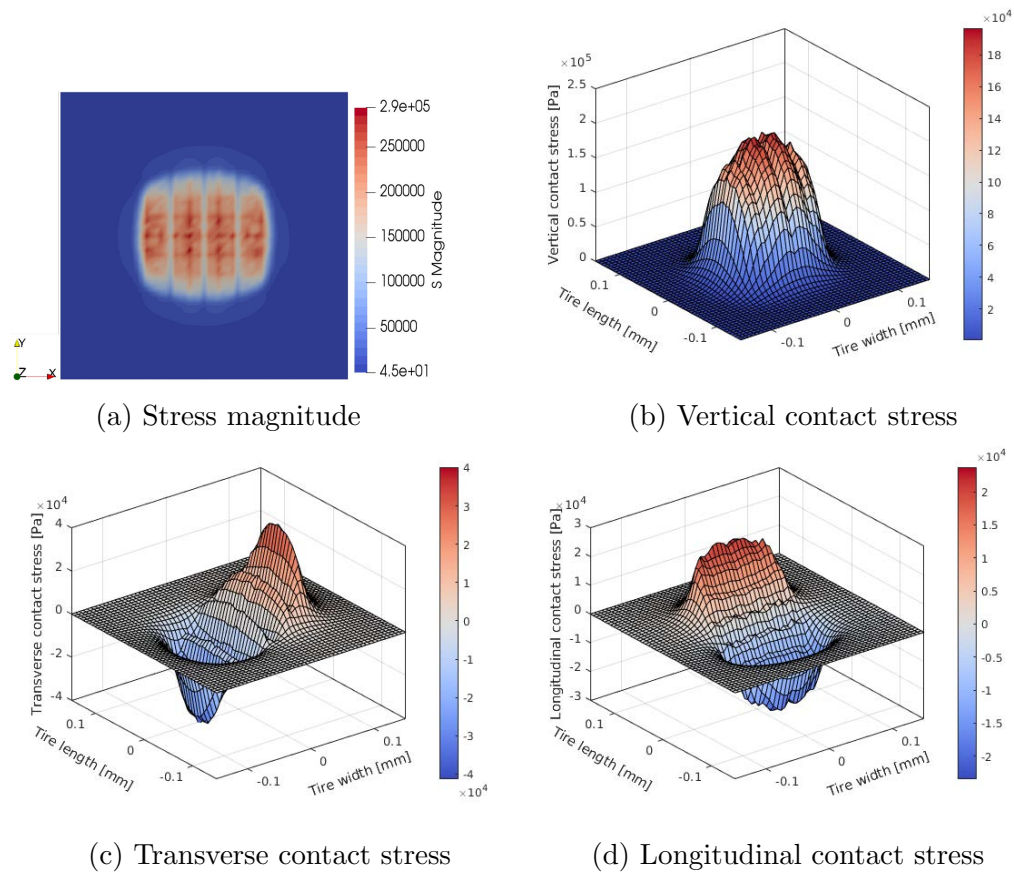


Figure 5.6: Contact stress distribution contours at free-rolling



then be calculated as follows:

$$F_y = \mu \cdot F_z \quad (5.7)$$

Where:

- $\mu$  [-] — friction coefficient between tire and pavement surface.

During full-braking, both the vertical force  $F_z = 5$  kN and longitudinal force  $F_y = 4$  kN act on the tire rim. Figure 5.7 illustrates the distribution of tire contact stresses under full-braking. The tire contact area shows a shape similar to the free-rolling condition, but the intensity of the distribution of contact stresses differs. As a result of braking force action, the maximum contact stress area is concentrated along the negative y-axis.

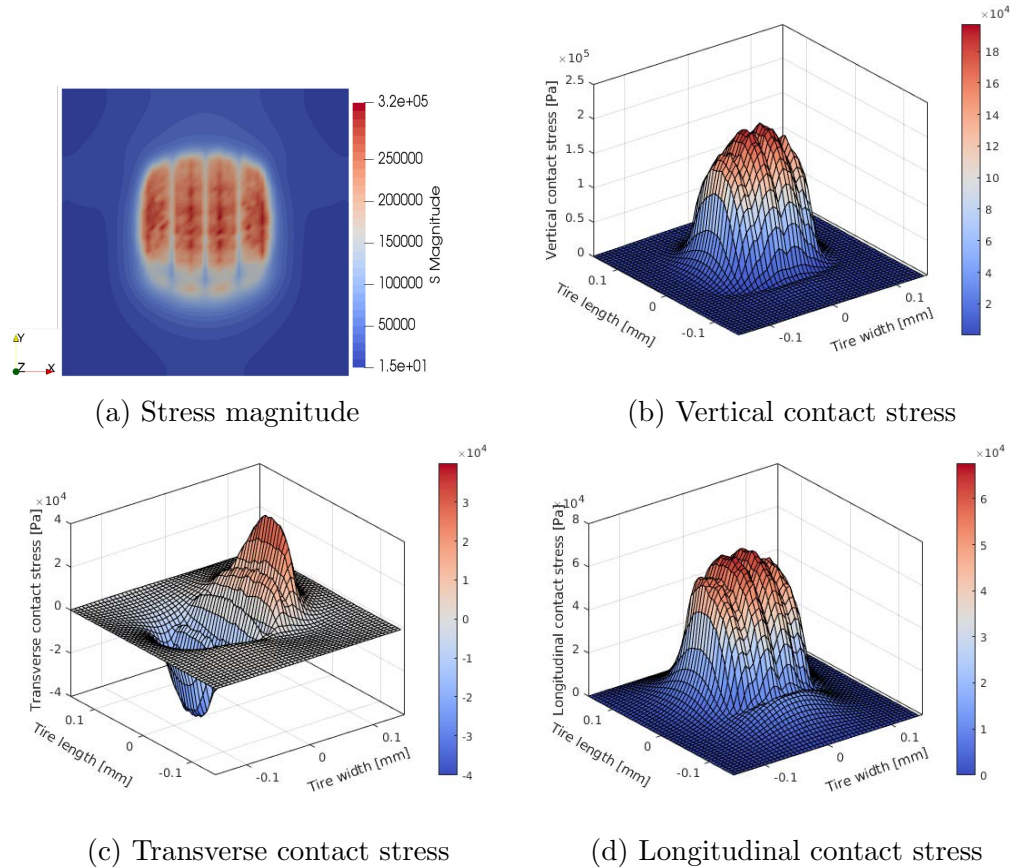


Figure 5.7: Contact stress distribution contours at full-braking

Referring to Figures 5.7b and 5.7c, both vertical and transverse stresses of

full-braking condition are very similar to those of free-rolling condition as there is no lateral force acting on the tire under two conditions. However, Figure 5.7d shows that the magnitude of longitudinal contact stress increases drastically in the full-braking condition in comparison with the free-rolling condition. Additionally, the longitudinal stresses are symmetric in free-rolling and go from a negative minimum to a positive maximum while they are exclusively positive in full-braking. The average ratio of peak vertical, lateral, and longitudinal contact stress values is about 1: 0.18: 0.37. The increment of tangential contact stresses could accelerate the pavement surface deterioration.

## 5.4 Micro simulation of tire-pavement interaction

### 5.4.1 Asphalt mixture modeling

The macro-scale model of the tire-pavement surface interaction above was used to study further the effect of various tire rolling conditions on pavement responses at the particle scale. This section describes the creation of a DEM pavement surface layer via CD method, the main work of the DEM modeling for asphalt mixtures is based on 4.

The open-source software NEPER was adopted to generate tessellation samples of the surface layer based on the particle size distribution (PSD) (Table 4.2) and the morphology properties.

The following steps were followed to generate the mixture sample:

- i) Tessellations were created following the aggregate morphology statistics and PSD cut at 2 mm to reduce the total quantity of particles in the sample, so that finer aggregates are included in the asphalt mastic;
- ii) The vertices of each tessellation were imported in LMGC90 to build numerical models. At this stage, particles were generated based on the convex hull of vertices from the tessellation;
- iii) The particles from the original tessellation were shrunk by multiplying a reduction factor in order to create gaps accommodating the mastic phase among particles.

Figure 5.8 gives the generated asphalt mixture sample for complex modulus tests based on two-point bending (2PB) configuration, where rigid particles interact with each other through the viscoelastic asphalt mastic.

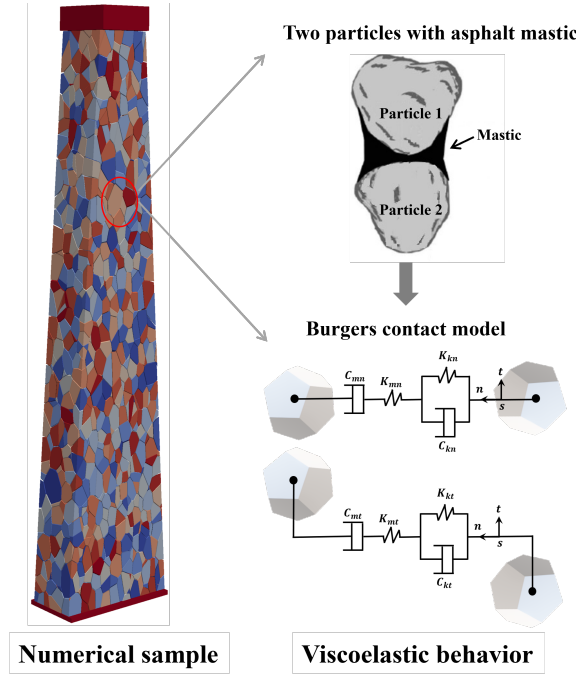


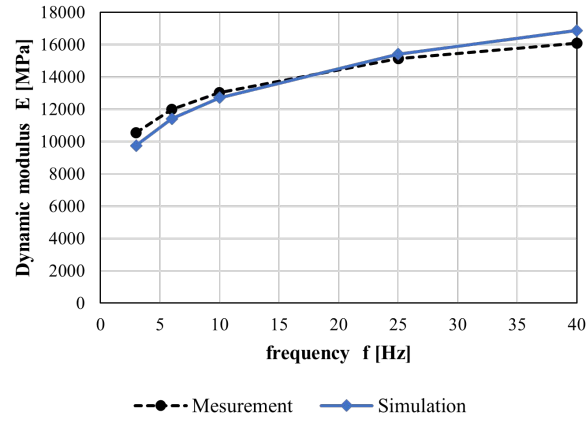
Figure 5.8: Numerical modeling of asphalt mixture for 2PB complex modulus test

Finally, the Burgers contact model was employed to simulate the viscoelastic behavior of asphalt mastic. The normal and tangential properties of the Burgers contact model include stiffnesses and viscosities for the Maxwell and the Kelvin-Voigt parts, corresponding to  $K_{mi}$ ,  $C_{mi}$ ,  $K_{ki}$ , and  $C_{ki}$ , respectively, where  $i$  stands for  $n$ ,  $t$  or  $s$ .

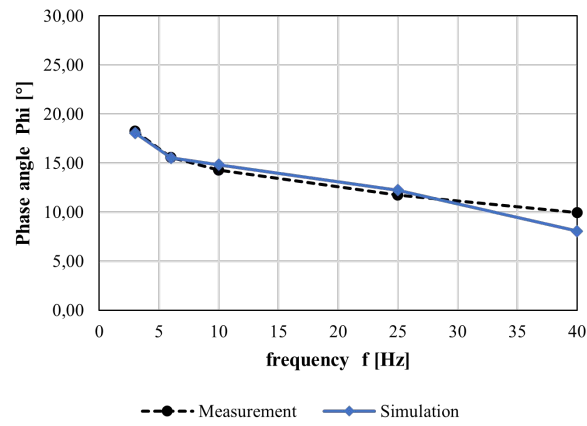
Regarding the experimental values for dynamic modulus  $|E^*|$  and phase angle  $\phi$  for 15 °C, Figure 5.9 shows that numerical results are in good agreement with experimental measurements for  $|E^*|$  and  $\phi$  for all the tested frequencies. The parameters for the Burgers contact model are listed in Table 5.1.

#### 5.4.2 Non-uniform tire load simulation

Research about the simulation of non-uniform tire loads in DEM models is rare. Herein, we proposed a strategy to simulate non-uniform boundary



(a)



(b)

Figure 5.9: Dynamic modulus and phase angles from experimental measurements and simulations at 15°C: (a) Dynamic modulus; (b) Phase angle

Table 5.1: Burgers model parameters used in numerical simulations

Temperature (°C)	$E_m$ (Pa)	$\eta_m$ (Pa.s)	$E_k$ (Pa)	$\eta_k$ (Pa.s)
15	$9.48 \times 10^7$	$1.02 \times 10^7$	$1.70 \times 10^8$	$1.79 \times 10^6$

conditions on a particle assembly inspired by previous studies of FEM simulations [25, 196]. As a result of the relatively large pavement stiffness compared to the tire, when a tire is in motion on a pavement surface for a short period of time, the pavement surface deforms negligibly. So we can make an assumption that the pavement structure has no effects on the tire contact stresses during the tire rolling process.

Therefore, for a rolling tire in a steady-state, we applied directly the force field obtained from the contact stress distributions of the FEM tire model on the DEM asphalt layer surface. The coupling method allows for the computation to be efficiently solved while keeping accuracy, as it eliminates the massive contact detection between the tire elements and asphalt mixture particles and the internal calculation of the tire elements. Moreover, another advantage is that real particle shapes can be taken into account in the asphalt mixture simulation via DEM tools owing to the saving computation cost.

In the DEM model, the measured tire contact stresses (vertical, transverse, and longitudinal) under each rib were applied, respectively, on the tire contact area ( $L_x = 0.13$  m,  $L_y = 0.22$  m), as Figure 5.10 shows. By adjusting the number and size of elements within each rib, the exact shape of the tire contact patch at a given load level could be considered. Depending on their locations based on the tire contact area, all elements along a tire rib have varying contact stresses along with the vertical, longitudinal and lateral directions. For an accurate capture of tire contact stresses, in particular longitudinal contact stress, while conserving calculation efficiency, the element length and width were equal to the tire thread width and the groove gap, respectively. The contact stresses were converted to equivalent concentrated forces using element shape functions as implemented into the FEM calculations, where all forces were assumed constant throughout the calculation.

Figure 5.11 displays an example of derived tire contact forces at free-rolling. It can be found that these boundary forces present a consistent distribution as the tire contact stresses aforementioned, which proves the method effectiveness.

After the mixture calibration described in the previous part, we generated a pavement surface layer composed of polyhedral particles consistent with the tire contact dimensions (Figure 5.12a), where the bottom particles were fixed

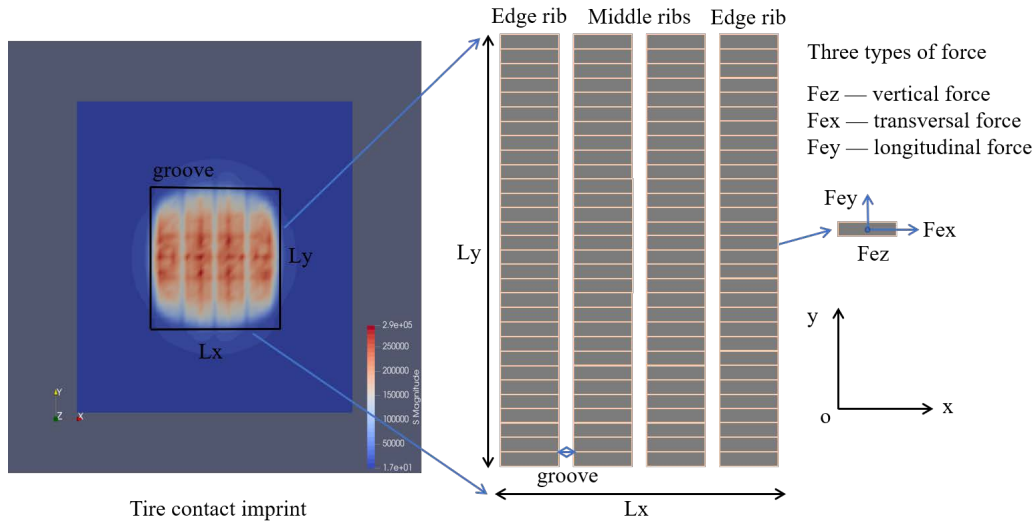


Figure 5.10: Tire imprint, contact stresses under each rib and local coordinate system

using a fixing boundary wall. Considering the viscoelastic contact between particles, the full pavement model comprised about 25,000 polyhedrons, leading to a large computation cost. As described before, the spatial distribution of tire contact stresses under both free-rolling and full braking is symmetrical along the longitudinal axis. Regarding the symmetrical boundary conditions, a symmetrical simulation strategy was adopted in the simulation in order to reduce the computational cost. The simulation only considers the half pavement model during the calculation, simultaneously, the freedom of x-direction for particles located on the center surface was fixed, as shown in Figure 5.12b. Finally, the tire loads were applied to the half pavement model as force boundary conditions, we studied the pavement responses after a short loading time ( $1 \times 10^{-2}$  s) in order to simulate an instantaneous dynamic loading.

### 5.4.3 Particle displacement distribution

Figure 5.13a shows the particle displacement distribution under free-rolling condition. The arrows in the figure represent the particle moving direction, and the color of the arrows indicates the magnitude of the particle displacement. It can be seen that particle displacements distribute non-uniformly in the mixture, where particles near the center have larger displacements than

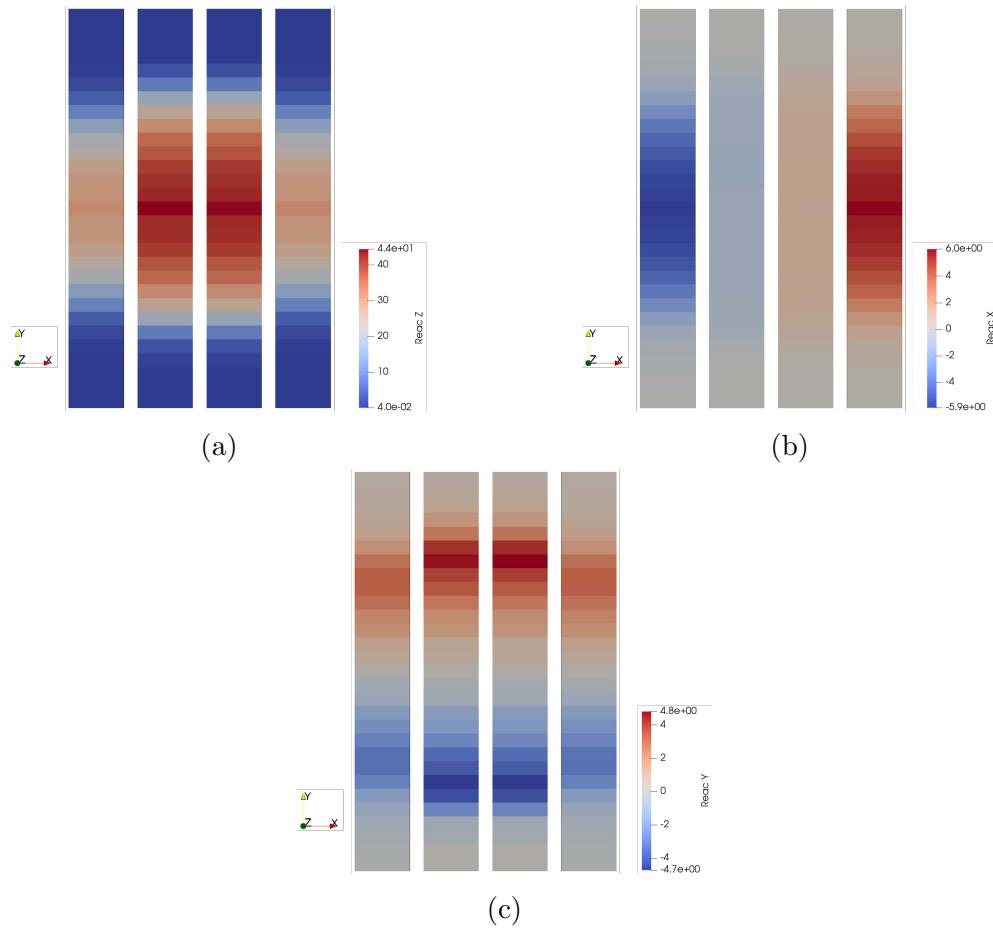


Figure 5.11: Boundary forces derived from free-rolling (a) Vertical force; (b) Longitudinal force; (c) Transverse force

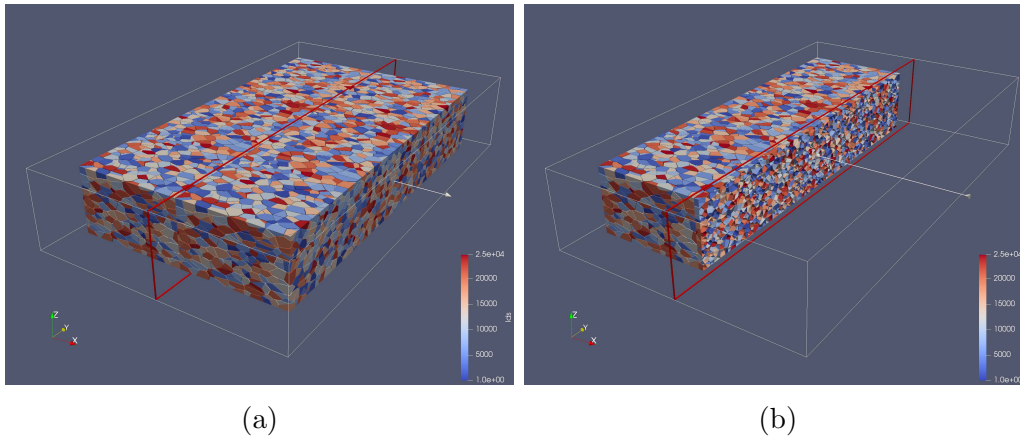


Figure 5.12: Pavement surface layer model: (a) Full model; (b) Half model along y-axis

those in other regions, which is consistent with the stress concentration under the free-rolling condition. In general, the arrow direction is essentially vertical since vertical contact stress dominates the entire tire contact stresses, whereas particles that lie under both sides have a horizontal component of particle displacement due to the existence of longitudinal and lateral contact stresses.

Figure 5.13b shows the particle displacement distribution under full-braking condition. The peak displacements appear concentrated on one side of the model along the longitudinal direction. Particles have an obvious longitudinal displacement component owing to the significant longitudinal contact stress. Note that particles under both free-rolling and full-braking conditions have a similar lateral displacement distribution since the lateral tire contact stresses occur in a comparable pattern on the pavement surface for the two loading conditions.

Comparing the particle displacement distribution under free-rolling and full-braking conditions, the whole particle displacement under full-braking is larger than that under free-rolling. Figure 5.14 gives the comparison for peak values of the particle displacement and their components in the three directions under free-rolling and full-braking. Despite the similarities of their lateral components (x-direction) and vertical components (z-direction), the particle displacements are quite different along y-direction due to the differences in longitudinal tire contact stresses. Under full-braking loading, the



displacement of particles becomes intensified, especially in the longitudinal direction. The imposed loading condition of contact stresses causes particles to rotate around the lateral direction, possibly leading to structural instability and high tensile strain and stress of the mixture.

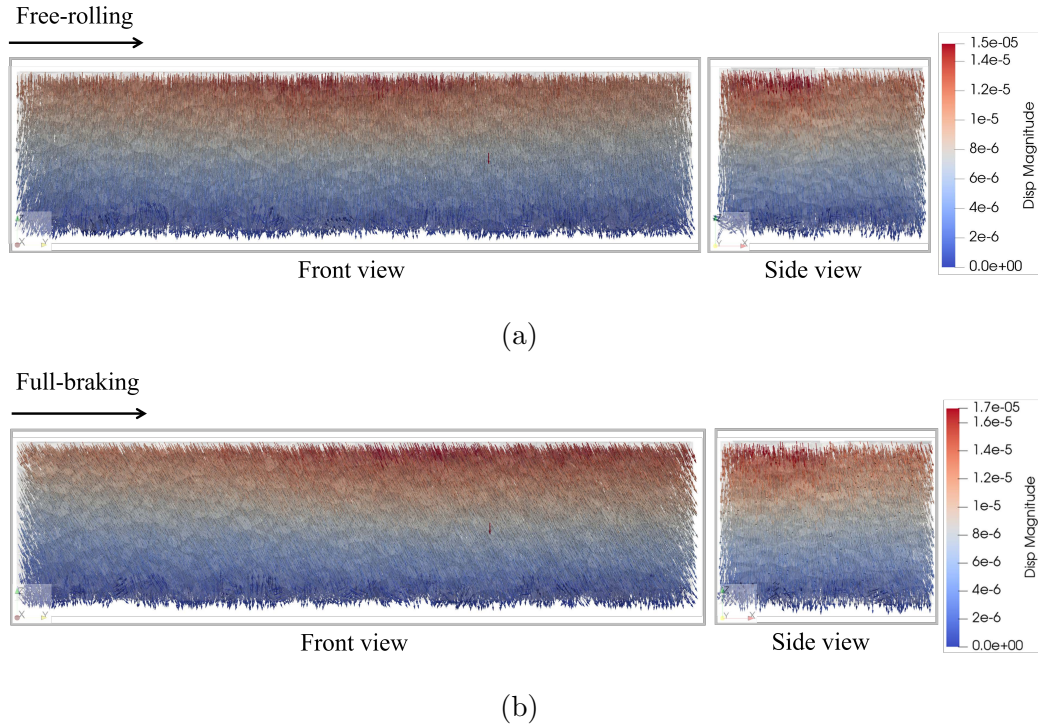


Figure 5.13: Particle displacement distribution under (a) free-rolling condition; (b) full-braking condition

#### 5.4.4 Particle contact force analysis

At the contact plane between two particles, there are two main types of forces: the tangential force that induces shearing in the contact plane, and the normal force lying perpendicular to that plane. Both forces contribute to particle contacts being damaged, causing contact breakage and particle movement, leading to macro-cracks forming and propagating inside the mixture. Figure 5.15 shows the normal force distribution for particles subjected to free-rolling and full-braking conditions. The normal force values for full-braking and free-rolling conditions distribute asymmetrically along the y-axis

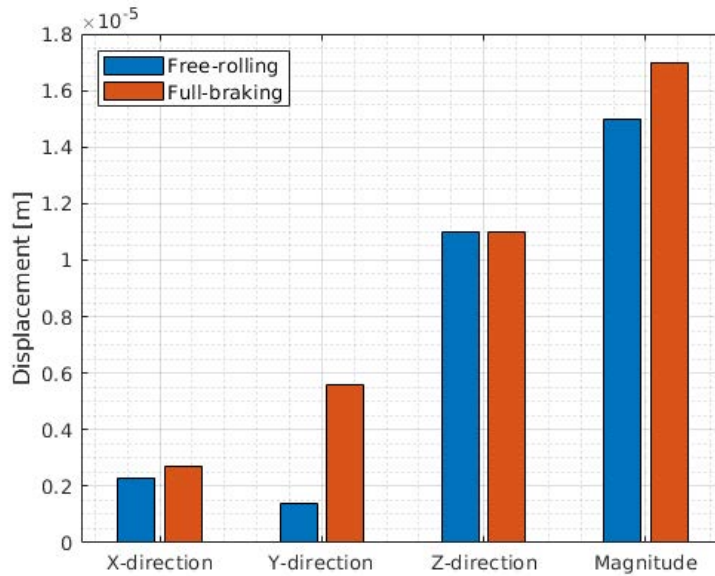


Figure 5.14: Maximum displacement comparison between free-rolling and full-braking

( $x=0$ ), due to the fact that particles undergo mainly a compression state under both loading conditions owing to the vertical contact stresses and the normal force distributes primarily in one side of the axis.

Figure 5.16 shows the distribution of tangential force values under different loading conditions. The tangential force values for both full-braking and free-rolling conditions follow approximately a normal distribution centered at zero. A larger magnitude range of tangential force values is observed under full-braking than that under free-rolling, which indicates that full-braking loading induces a stronger shear effect among particles than free-rolling loading, resulting in possible earlier damage initiation within the mixture.

Pavement design methods traditionally consider only the vertical tire load and assume that the load is uniformly distributed. Nevertheless, based on the above multiscale analysis, these assumptions could be unreliable for investigating the degradation mechanisms of the asphalt pavement surface. The contact stresses distribute non-uniformly across the contact area; the tangential contact stresses caused by the tire are inevitable, particularly in acceleration or braking, which is crucial to the asphalt mixture responses.

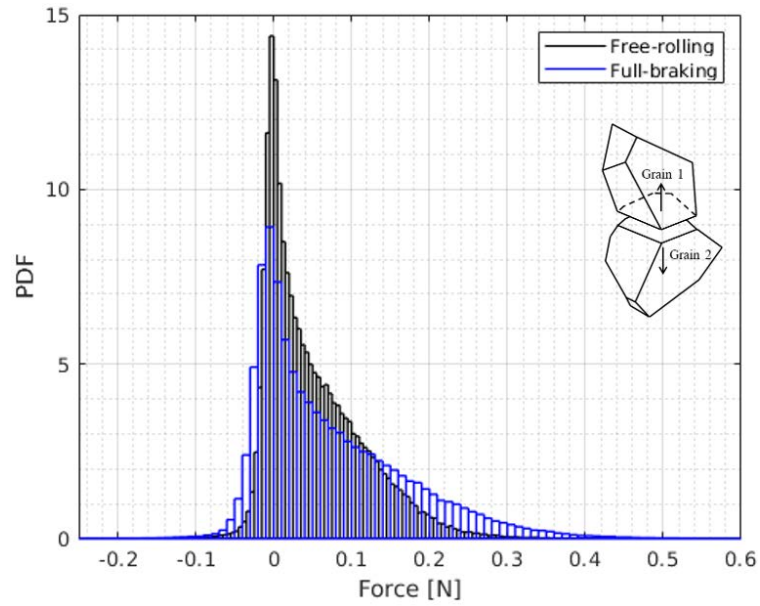


Figure 5.15: Normal force distribution

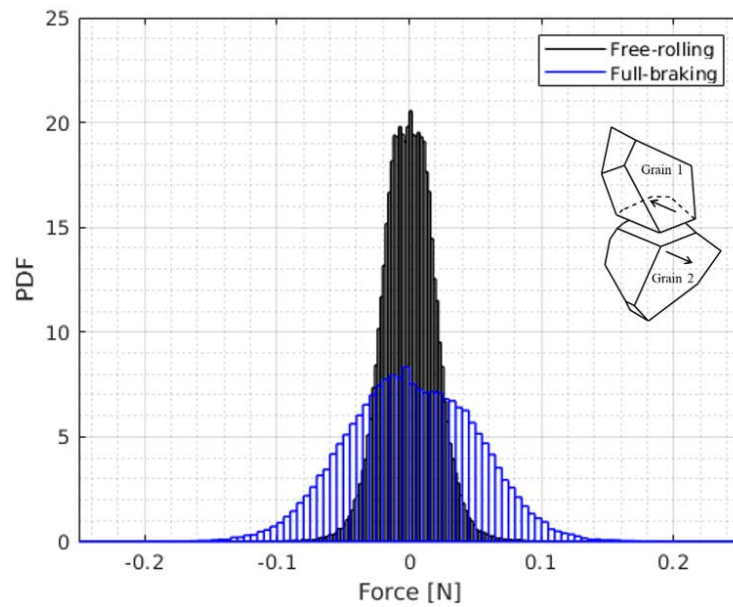


Figure 5.16: Tangential force distribution

For predicting surface failures such as top-down cracks, taking only vertical contact stress into account and assuming uniform contact stress appears inadequate, as it could lead to misinterpretations of pavement responses under tire loading.

## 5.5 Conclusions of the chapter

This chapter has introduced the CD method to conduct a multiscale FEM-DEM simulation for the tire-pavement interaction investigations. The main conclusions drawn are as follows:

The tire modeling strategy and its calibration were detailed. The tire geometry was reconstructed via laser scanning and image processing techniques. The tire structure was built by FEM according to its function and the relevant parameters were identified with a compression test.

The contact stress distributions under free-rolling and full-braking reveal that the tire induces contact stresses in three directions (vertical, transverse, longitudinal) and the contact stresses are not uniform across the contact area as expected. The tangential contact stress on the pavement surface under full-braking is obviously much higher than that under free-rolling.

The internal mixture responses under tire loads were investigated by modeling a pavement surface layer via DEM. Under the full-braking condition, particle displacement distribution illustrates that particles tend to flow along the longitudinal direction and rotate ahead, which may lead to structural instability of the mixture. According to the analysis of particle contact forces, the tangential force values under full-braking have a wider distribution range than those under free rolling. It indicates that the full-braking condition induces a greater shear effect within particles in the mixture than the free-rolling condition, and may thereby result in earlier damage initiation.

The following paper summarizes the main results of this chapter:

Ge, H., Quezada, J. C., Le Houerou, V., & Chazallon, C. (2022). Multiscale analysis of tire and asphalt pavement interaction via coupling FEM-DEM simulation. *Engineering Structures*, 256, 113925. [197].



# Asphalt mixture responses under rolling tire loads

---

## Contents

---

<b>6.1</b>	<b>Introduction</b>	<b>132</b>
<b>6.2</b>	<b>FEM-DEM coupling for the dynamic tire-pavement interaction</b>	<b>132</b>
6.2.1	Coupling algorithm	133
6.2.2	Tire contact force detection	133
6.2.3	Tire contact force application	137
<b>6.3</b>	<b>Validation of the coupling method</b>	<b>138</b>
<b>6.4</b>	<b>Effects of tire rolling velocity</b>	<b>142</b>
6.4.1	Bottom boundary force	142
6.4.2	Contact force network evolution	142
6.4.3	Particle movement characteristics	144
<b>6.5</b>	<b>Effects of tire rolling status</b>	<b>147</b>
6.5.1	Bottom boundary force	147
6.5.2	Particle contact force distribution	148
6.5.3	Particle displacement distribution	148
6.5.4	Average particle velocity	150
6.5.5	Particle movement characteristics	152
<b>6.6</b>	<b>Conclusions of the chapter</b>	<b>153</b>

---

## 6.1 Introduction

In the previous chapter, we proposed a multi-scale method to investigate the tire-pavement interaction mechanism under quasi-static tire loads. The multi-scale method incorporates the advantages that FEM can simulate contact stresses precisely on the asphalt pavement surface and DEM is capable of examining internal responses of the asphalt mixture at the particle scale. However, due to the limitation of quasi-static loading conditions, the dynamic asphalt mixture responses were not fully examined.

In this chapter, an advanced 3D FEM-DEM coupling simulation is presented to examine internal asphalt mixture responses micromechanically under transient rolling tire loads. Within the simulation, advanced algorithms were developed to handle the contact detection between mixture particles and tire contact forces and also to achieve the application of rolling tire loads on the asphalt mixture layer.

Then we analyzed statistically the micro-mechanical responses including particle movement characteristics, displacement and velocity distributions, contact forces, and individual particle displacement in an asphalt mixture under different tire rolling conditions. The current study proposes an innovative method for exploring dynamic tire-pavement interaction under rolling tire loads, which could help revealing degradation mechanisms of asphalt pavement surfaces under realistic rolling tire loads at the particle level.

## 6.2 FEM-DEM coupling for the dynamic tire-pavement interaction

As introduced in Chapter 5, we proposed a multi-scale method to investigate tire-pavement interaction, rib elements are used to transfer tire loads derived from the FEM tire model to the DEM model of asphalt mixture. This method is struggling when examining asphalt mixture responses under transient rolling tire loads as the load transfer media, the rib elements, are unsuitable for moving. In order to fully understand asphalt mixture failure mechanisms, it is essential to examine dynamic asphalt mixture responses under transient rolling tire loads. Herein, we developed an advanced coupling strategy to achieve the dynamic tire-pavement interaction process

under rolling tire loads.

### 6.2.1 Coupling algorithm

The kernel of the advanced FEM-DEM coupling is based on the detection between tire contact forces and particles. This detection is conducted to determine which particle is in contact with the tire contact force ( $\vec{F}_n$ ), where  $\vec{F}_n$  is derived from the nodal force on the pavement surface from the FEM tire-pavement model, thus  $\vec{F}_n$  is composed of three component  $F_{nx}$ ,  $F_{ny}$ ,  $F_{nz}$ . The coupling process is shown in Figure 6.1.

At first, we focused on the contact area of the tire and pavement surface, so we extracted the tire footprint dimensions from the tire model (Figure 6.1a). When the vertical tire force  $F_{nz}$  is lower than zero, the force position is deemed to be inside the tire-pavement surface contact area. After scanning all the force coordinates of the pavement surface, a square boundary area ( $L_x \times L_y$ ) circumscribing all the contact force points could be obtained (Figure 6.1b). Then, according to the square boundary dimensions, we created an asphalt mixture wearing layer with a thickness of 4 cm by using the calibrated asphalt mixture parameters. Afterward, the contact detection between the tire contact forces and asphalt mixture aggregates was performed during the simulation. Finally, the tire contact forces were applied to the particles on the asphalt mixture layer surface and the coupling simulation was conducted based on the time-iteration calculation frame. The general procedure is shown in algorithm 2.

### 6.2.2 Tire contact force detection

For the tire contact force detection, we perform a detection at two levels: coarse detection and fine detection. As shown in Figure 6.2, for a particle located on the asphalt layer surface, we first extracted its geometry information including polyhedron vertices. Then, we calculated the bounding box (minimal and maximal coordinates of vertices in x, y and z direction) of this particle and compared the tire contact force coordinates ( $F_{coord}$ ) with the horizontal range of the bounding box, as shown in Figure 6.2a. If the tire contact force is outside the bounding box, it is judged that the contact force is outside all the particle surfaces. The tire contact force may also lie outside the particle surfaces while being in the bounding box, so we need to perform



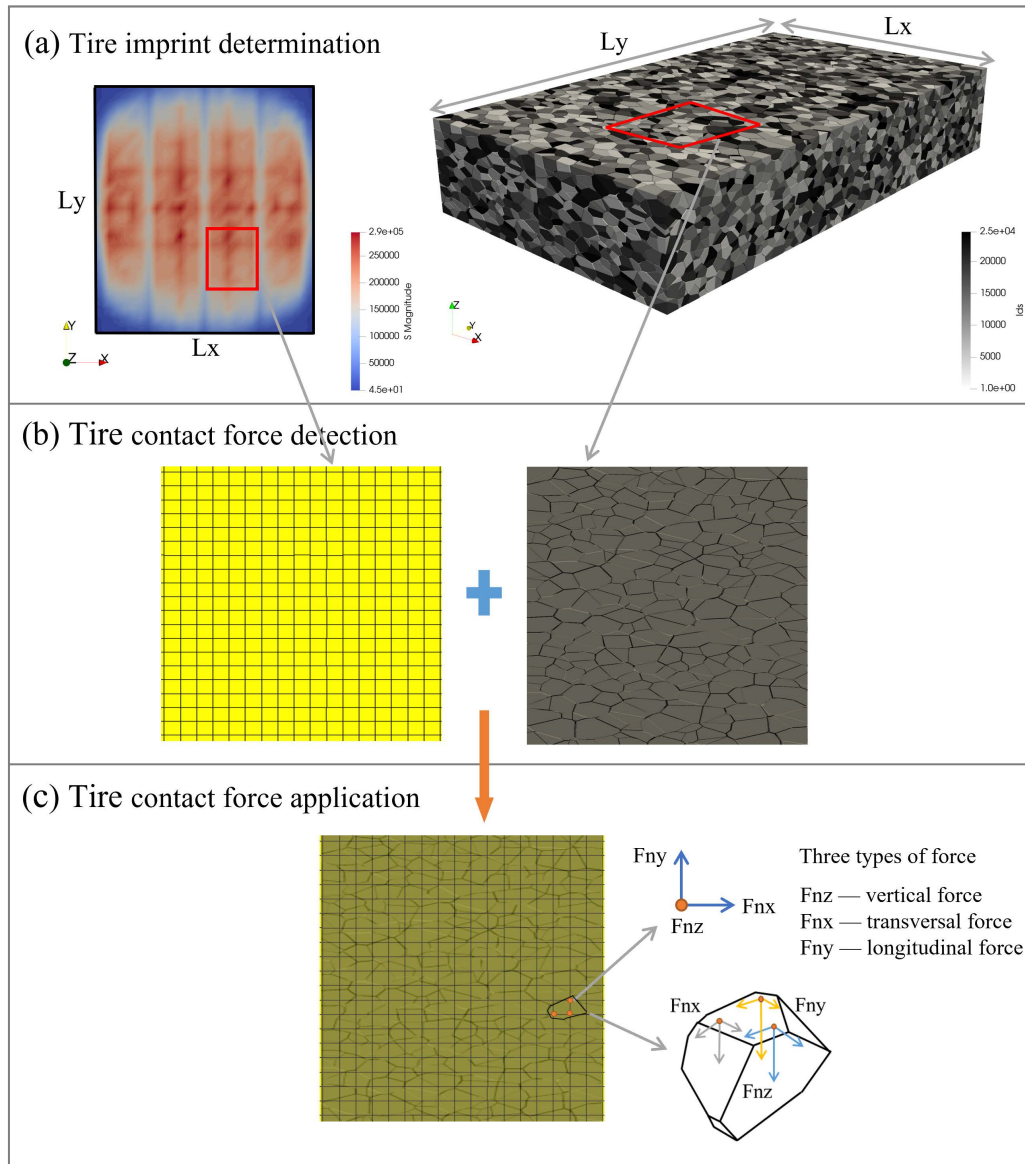


Figure 6.1: Coupling simulation of FEM and DEM: (a) Tire imprint determination; (b) Contact force detection; (c) Contact force application

---

**Algorithm 2** General procedure of the coupling algorithm

---

1. Tire imprint determination
  - if**  $F_{nz} \leq 0$  **then**
    - 1.1: Get coordinates of the contact force:  $F_{coorx}$ ,  $F_{coory}$  and  $F_{coorz}$**end if**
  - 2: Calculate the range of the contact force field:  $L_x = \max(F_{coorx}) - \min(F_{coorx})$  and  $L_y = \max(F_{coory}) - \min(F_{coory})$
  - 3: Asphalt mixture modeling according to the range.
  - loop**
    4. Tire contact force detection on the surface layer
    - if** Tire contact force is inside the force field **then**
      - 4.1: Coarse detection
      - 4.2: Fine detection**end if**
    5. Tire contact force application on the asphalt mixture sample
    - if** The tire contact force is on a particle surface **then**
      - 5.1: Applying the force and moments to the particle**end if**
    - 6: Running next step simulation based on the time iteration algorithm
-

a further accurate detection, the fine detection. To perform fine detection, we extracted particle surfaces and compute a dot product to determine if the tire contact force is located on the particle surface. As shown in Figure 6.2b, a particle surface (ABC) is taken as an example. If the tire contact force point (P) is inside the triangle surface, the results of all the cross products ( $\overrightarrow{AB} \times \overrightarrow{AP}$ ,  $\overrightarrow{BC} \times \overrightarrow{BP}$ ,  $\overrightarrow{CA} \times \overrightarrow{CP}$ ) must be higher than zero. The detection procedures are listed in the algorithm 3.

---

**Algorithm 3** Tire contact force detection on the particle

---

1. Coarse detection  
**if**  $\min(Xvertex) \leq F_{coorx} \leq \max(Xvertex)$ , and  $\min(Yvertex) \leq F_{coory} \leq \max(Yvertex)$  **then**  
     Particle is on the bounding box surface of the particle
  2. Fine detection  
**if**  $\overrightarrow{AB} \times \overrightarrow{AP} \geq 0$ , and  $\overrightarrow{BC} \times \overrightarrow{BP} \geq 0$ , and  $\overrightarrow{CA} \times \overrightarrow{CP} \geq 0$  **then**  
     Force is on the particle surface  
**else**  
     Force is outside the particle surface  
**end if**
  - else**  
     Force is outside the particle surface  
**end if=0**
- 

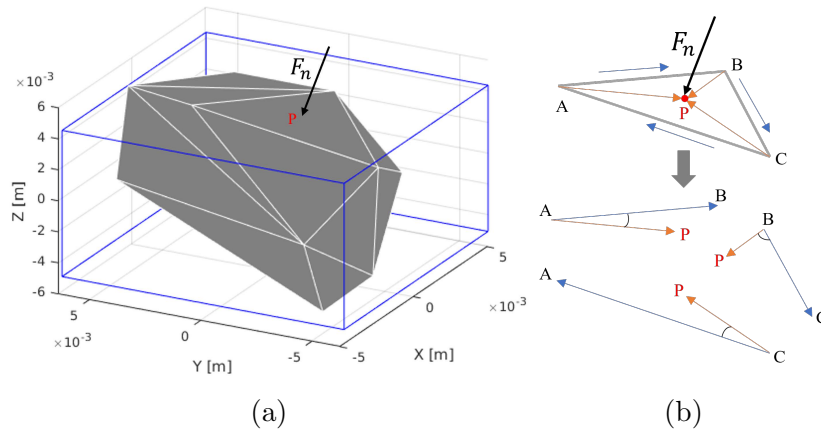


Figure 6.2: (a) Coarse detection: Bounding box; (b) Fine detection: Point in polyhedron

### 6.2.3 Tire contact force application

After the contact detection procedure, we need to apply the tire contact forces on particles located on the asphalt layer surface. For the contact force application, we applied external tire contact forces to the mass center of polyhedron particles. As shown in Figure 6.3, as a tire contact force  $\vec{F}_n$  has three components ( $F_{nx}$ ,  $F_{ny}$  and  $F_{nz}$ ), it also has three associated components of moments ( $M_x$ ,  $M_y$  and  $M_z$ ) on the particle.

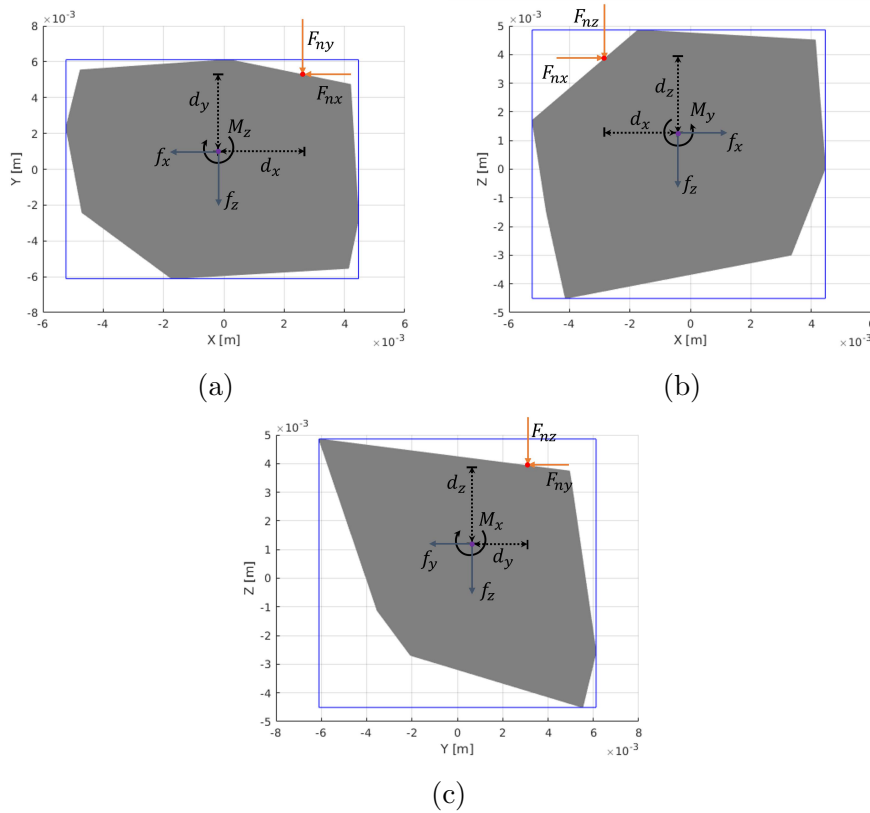


Figure 6.3: (a) Plane-XY; (b) Plane-XZ; (c) Plane-YZ

By using the algorithm 4, the tire contact forces can be transmitted equally to the mass center as external forces and moments.

Finally, following the construction of the coupling frame, the mechanical response of the asphalt mixture layer under varying tire rolling conditions including rolling velocity and rolling status could be further investigated, as introduced in later sections. All the simulations were conducted in LMGC90

**Algorithm 4** Tire contact force application to the particle

---

```

1. External particle force  $f$  calculation
if Tire contact force point is on the particle surface then
     $f_x = F_{nx}$ 
     $f_y = F_{ny}$ 
     $f_z = F_{nz}$ 
2. External particle moment  $M$  calculation
     $M_x = F_{ny} * dz + F_{nz} * dy$ 
     $M_y = F_{nx} * dz + F_{nz} * dx$ 
     $M_z = F_{nx} * dy + F_{ny} * dx$ 
end if

```

---

at  $T_{ref} = 15$  °C, which is a referenced value in French pavement design [45]. The Burgers contact law was activated between particles in the asphalt mixture, related contact parameters as listed in Table 5.1 of Chapter 5 were assigned in the model.

### 6.3 Validation of the coupling method

To verify the effectiveness of the proposed modeling approach, numerical simulations at static tire loads were further conducted. Using the coupling method, the tire loads were applied to the asphalt layer model as force boundary conditions. We studied the pavement responses after a short loading time ( $1 \times 10^{-2}$  s) in order to simulate instantaneous dynamic loading. The time step was set to  $5 \times 10^{-5}$  s during the entire simulation to ensure numerical stability. For the entire simulation, the bottom particles in the asphalt layer model were fixed by a rigid wall, which provides a bottom boundary condition.

Comparisons between contact stresses and particle displacements for different directions (X, Y, Z) were made, as shown in Figure 6.4.

Figures 6.4b, 6.4d, and 6.4f demonstrates that the tire induces non-uniform contact stresses in three directions including transverse, longitudinal and vertical components, affecting pavement responses together. In terms of peak values for vertical, transverse, and longitudinal contact stresses, the vertical contact stress is much bigger than the other two tangential contact stresses.

The vertical stress distribution is symmetric along the y-axis (tire length), and maximum values are concentrated at the tire center ribs. The transverse contact stress occurs as a result of restricted horizontal movement of the tire ribs, the maximum stress value occurs at the ribs of the tire. The longitudinal contact stress is mainly caused by friction between tire and pavement and reaches its peak values at the center tire ribs.

As a result of applied tire-pavement contact stresses on the asphalt layer surface, particles move consistently in three directions, as shown in corresponding figures 6.4a, 6.4c, and 6.4e, proving the model reliability and effectiveness of the coupling method. In addition, there are differences in the contour color between particle displacements and applied contact stresses. The difference is caused by the non-uniformity of particle size distribution and particle contact-bearing capacity, big particles usually have more contacts from their surrounding particles and therefore provide them more resistance to external forces and finally induce less fluctuation of particle motion.

Figure 6.5a shows further the distribution of particle displacement magnitude under real tire loads. Particle displacements are observed to be non-uniform on the asphalt layer surface. Particles near the center having greater displacements than particles in other regions, which is consistent with the tire-pavement contact stress concentration. Figure 6.5b illustrates the directions of particle movement represented by arrows, and the color of the arrows indicates the magnitude of particle displacement. Due to the fact that the vertical contact stress dominates the entire tire contact stress, the arrow direction is primarily vertical, indicating particles move mainly along the negative Z-direction. In contrast, particles lying under both sides have noticeable horizontal components of particle displacement as a result of existing longitudinal and lateral contact stresses.

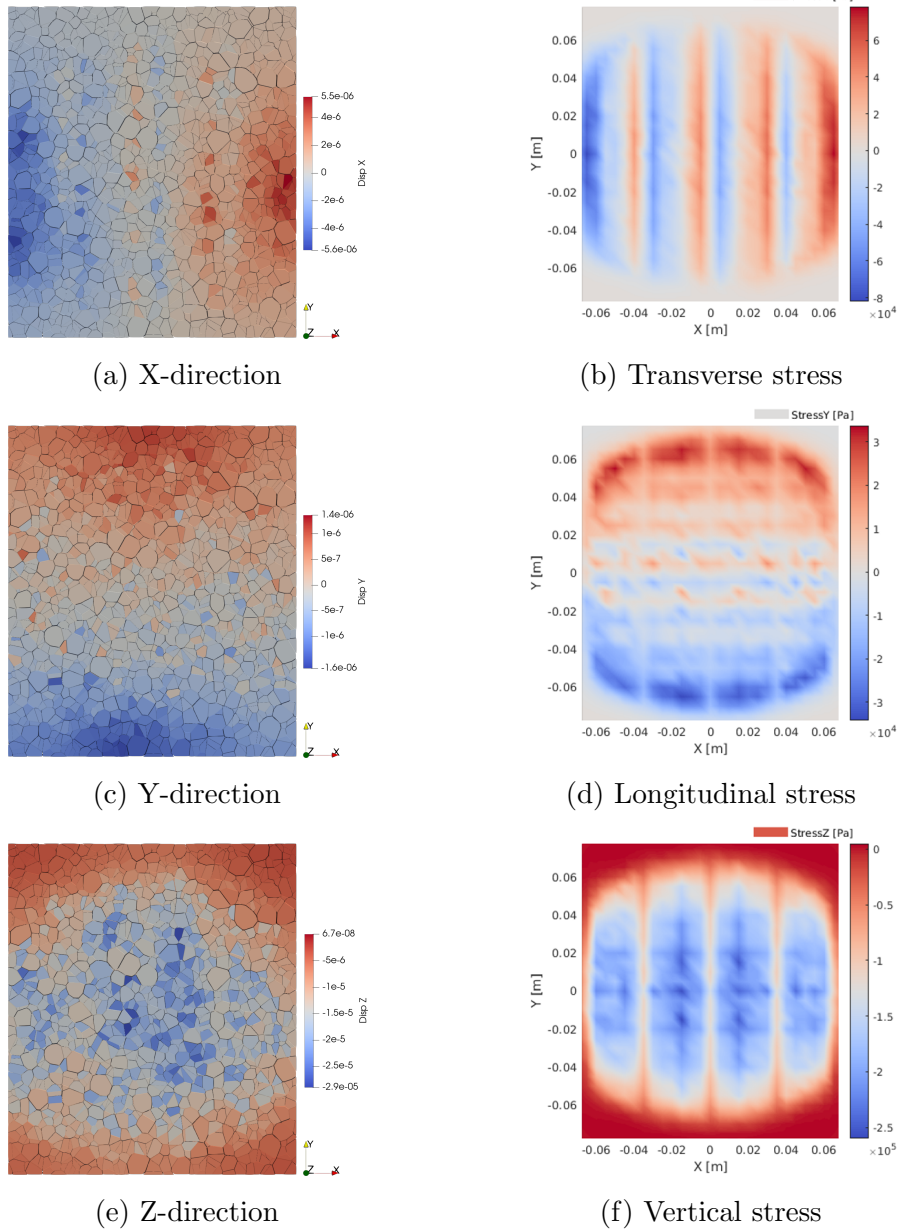
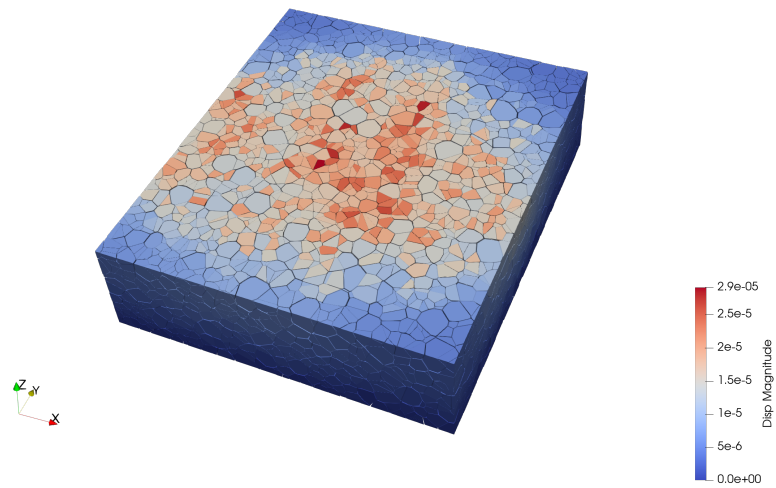
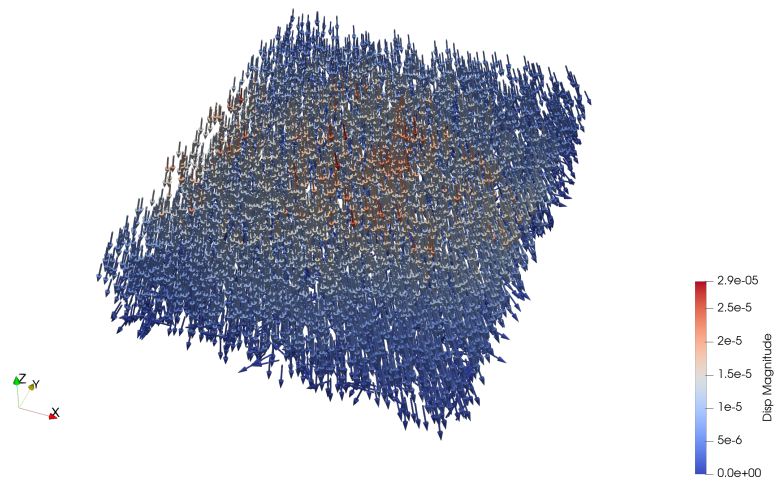


Figure 6.4: Comparisons between particle displacement distributions (left) and Tire-pavement contact stress distributions (right) in three directions



(a)



(b)

Figure 6.5: (a) Particle displacement distribution; (b) Particle motion arrows



## 6.4 Effects of tire rolling velocity

### 6.4.1 Bottom boundary force

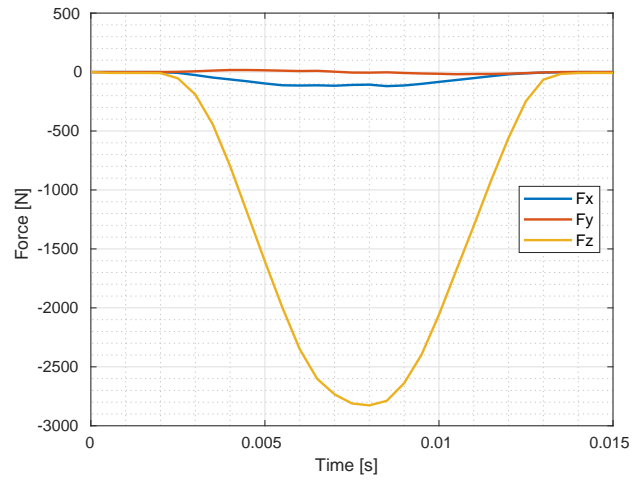
Following the validation of the coupling method, we investigate further how the asphalt layer responds to rolling tire loads. In contrast with the static simulation, rolling simulation requires the external force field to advance on the asphalt layer surface over time. Thus, a rolling load algorithm based on time-step calculation is used to conduct this rolling process. The coordinates of the external force field move step by step according to the applied tire rolling velocity over time through time advancement. Thanks to the symmetric distribution of tire contact stresses, a symmetric simulation strategy was adopted to reduce the computation cost. The simulation used only half of the layer model along the y-axis, whereas the x-direction of particles on the center surface was fixed simultaneously to provide a lateral boundary condition. Three tire rolling velocities (10, 20, and 30 m/s) were applied to the coupling model at the free rolling condition to investigate the effect of tire rolling velocity on mixture layer responses. Figure 6.6a gives evolution results for the bottom boundary force at tire velocity of 30 m/s along the time. All the force values first increase until they reach their peak values, and then they all decrease gradually down to zero. Besides, the vertical force is dominating the mixture layer, while tangential forces are relatively lower.

Figure 6.6b compares  $F_z$  (vertical component of the boundary force) at different tire velocities. A similar evolution trend can be observed for  $F_z$  under different tire loading velocities, with a similar peak value achieved in the middle of the loading time for each tire velocity. It seems that the velocity has no significant influence on the  $F_z$  peak value as it could have been expected.

### 6.4.2 Contact force network evolution

In particle-based methods, contact force networks reflect external loads transmitted through granular materials. Coexisting strong and weak contacts form a contact network, which is made up of the corresponding strong contact forces, i.e. forces above the mean normal value ( $f_n > \langle f_n \rangle$ ), and weak contact forces ( $f_n < \langle f_n \rangle$ ) [125].

Figure 6.7 shows the strong and weak force distribution during the rolling



(a) Boundary force at free rolling (30 m/s)

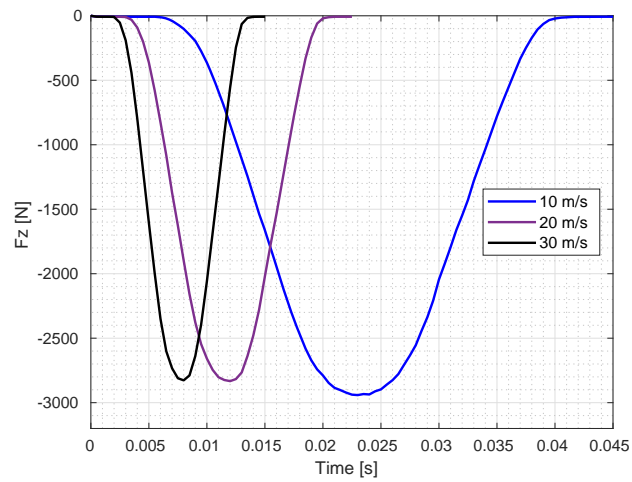
(b) Comparison for  $F_z$  at different rolling speeds

Figure 6.6: Bottom boundary force characteristics

process at a tire velocity of 30 m/s. In response to moving tire load, strong (red) and weak (blue) forces evolved. At the initial stage of rolling ( $T = 0.0015$  s), the contact force network is considerably loose because only a little range of tire load activates on the layer surface. When the tire load is fully distributed on the mixture layer ( $T = 0.007$  s), the strong contact force network reaches its maximum distribution range. After that, as the tire load passes from the layer surface, the strength of force networks starts to diminish. A relatively equal balance of force states is finally achieved (after  $T = 0.013$  s) when the tire load fully passes the layer surface. An analysis of the evolution of the contact networks shows how the tire is moving on the asphalt layer surface, demonstrating the accuracy of the coupling algorithm.

### 6.4.3 Particle movement characteristics

Further, we investigate the movement of individual particles during the rolling process under different tire velocities. Figure 6.8 depicts the movement evolution of one particle located on the center of the surface layer under various tire rolling speeds. Throughout the loading duration, particle displacement increases, and it reaches its peak value halfway through the loading time. It then decreases gradually until it reaches its residual value. It can be found that particle displacement is mainly caused by vertical particle movement due to strong vertical tire contact forces. Figures 6.8a, 6.8b and 6.8c illustrate that the value of particle displacement cannot return to zero after a tire load passes, which indicates that the tire load causes residual strains due to the viscous flow occurring within the asphalt mixture. The accumulation of the particle displacement after multiple tire load cycles could finally lead to macroscopic non-recoverable plastic deformation such as rutting. Tire load-induced plastic deformation is referred to as permanent displacement here. Figure 6.8d illustrates the permanent displacement of the particle at different tire speeds. According to the results, low tire speed induces high permanent displacement for particles, which is in agreement with the measurement observations that low tire speed causes severe rutting.

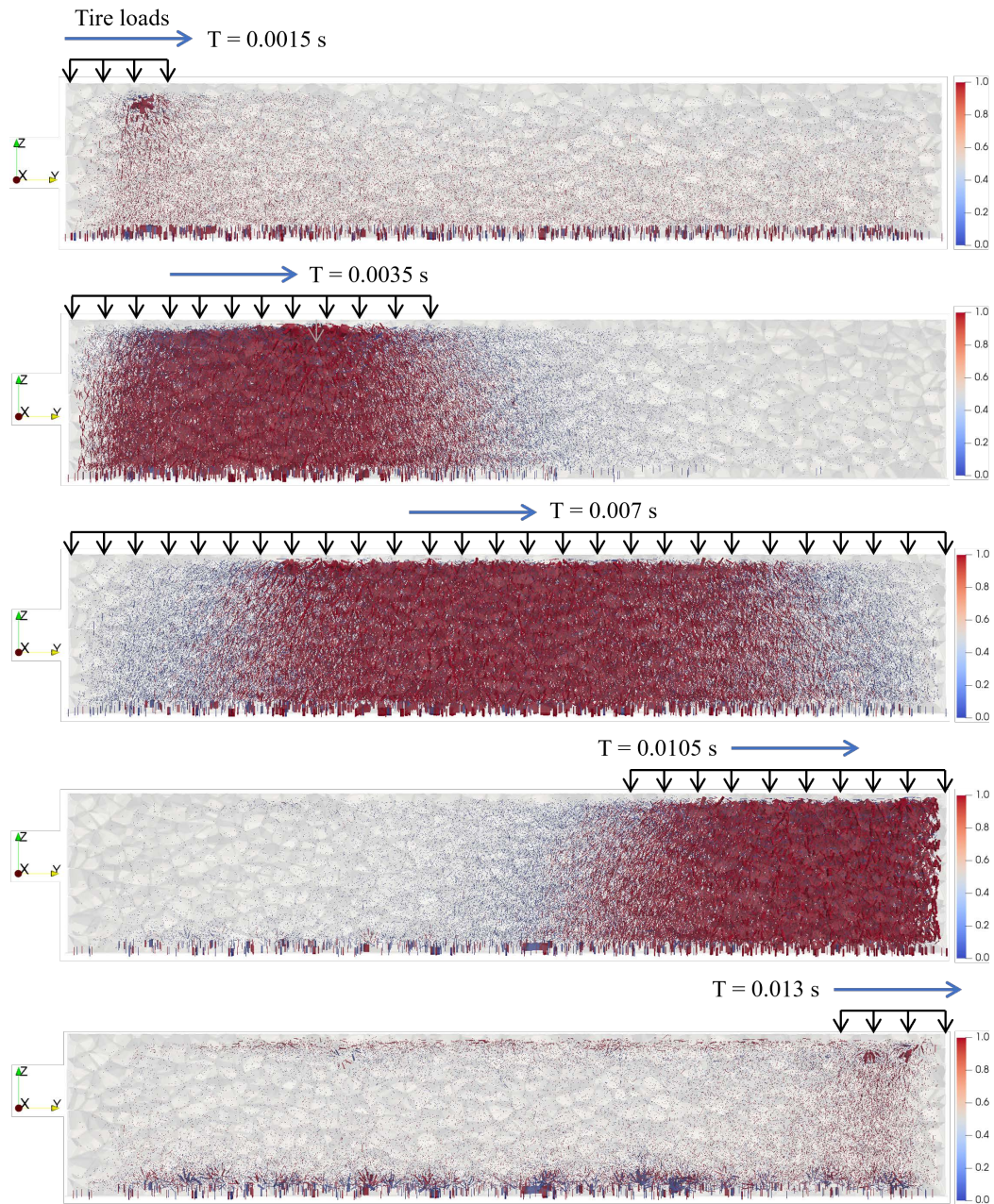
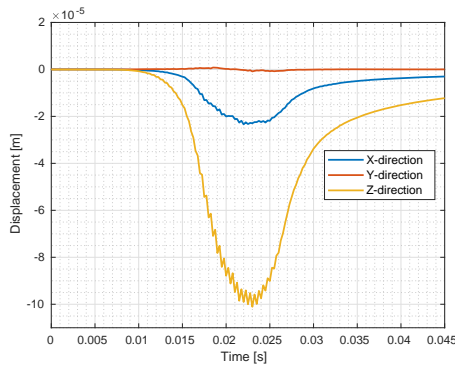
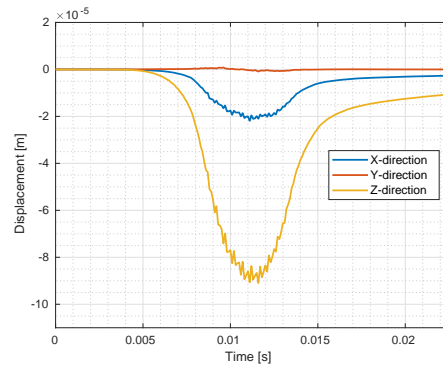


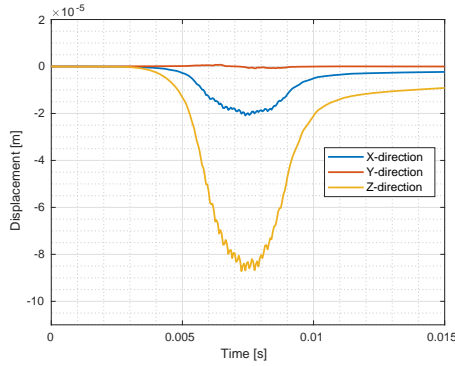
Figure 6.7: Contact force network evolution (strong force = 1.0 and weak force = 0.0) at rolling velocity of 30 m/s



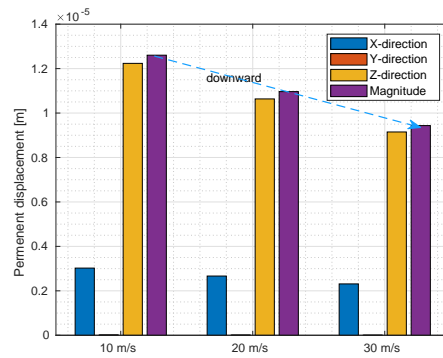
(a) 10 m/s



(b) 20m/s



(c) 30 m/s



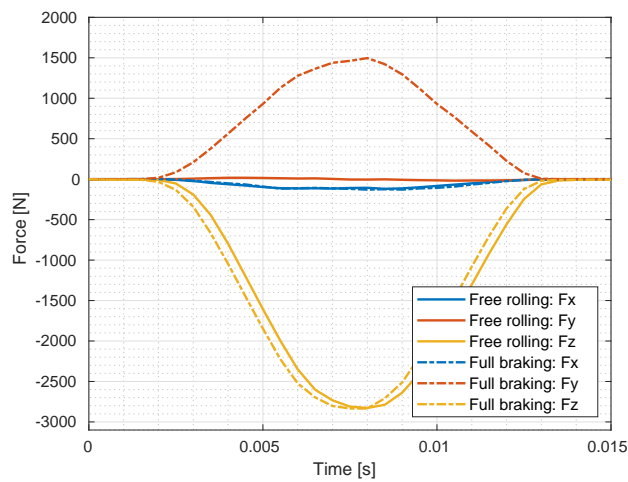
(d) Comparison for the permanent displacement

Figure 6.8: Particle displacement for different tire rolling speeds

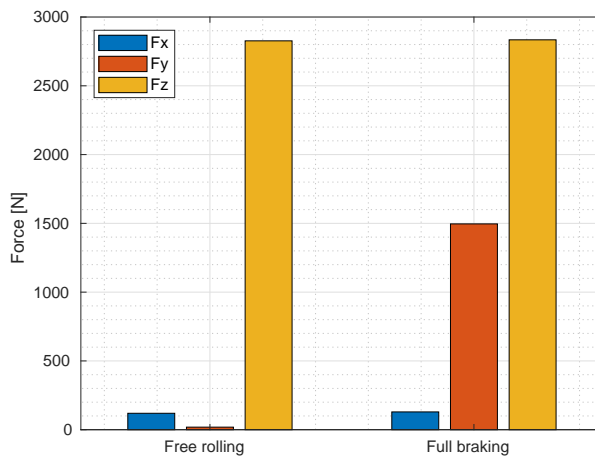
## 6.5 Effects of tire rolling status

### 6.5.1 Bottom boundary force

Figure 6.9 shows the boundary force comparison for free rolling and full brake conditions. Compared to the free rolling condition, the boundary force has a significant component along the longitudinal axis (y-axis) at full braking, which could result in particle disturbances in the mixture.



(a) Boundary force  $F$  comparison



(b) Peak force value comparison

Figure 6.9: Bottom boundary force characteristics for different rolling status

### 6.5.2 Particle contact force distribution

Furthermore, the particle contact force distribution under two loading conditions was analyzed. The time points corresponding to the peak boundary values were selected as critical times to study the particle contact force distribution.

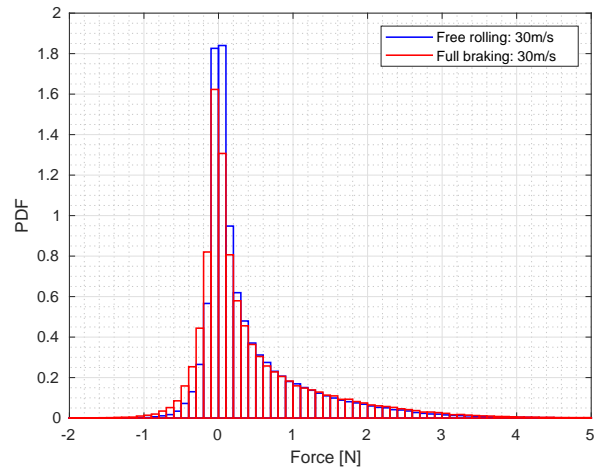
There are two types of forces acting at the particle contact plane: the tangential force that induces shearing, and the normal force lying perpendicular to the contact plane. The combination of both forces can result in particle contact breakage and particles moving, resulting in macro-cracks forming and propagating within the mix. A comparison of normal contact force distributions for particles at free rolling and full braking conditions is shown in figure 6.10a. As a result of the similar vertical contact stresses at two loading conditions, normal force value distributions are mostly asymmetric along the y-axis ( $x = 0$ ). The main reason being that particles under both loading conditions generally suffer from a compression state.

As shown in figure 6.10b, the tangential contact force values vary depending on the loading conditions. For both free rolling and full braking conditions, the tangential contact force values follow approximately a normal distribution with zero at the center. Under the full braking condition, the magnitude range of tangential force values is greater than that under the free rolling condition, which indicates that full braking induces a stronger shear effect between particles, which may lead to earlier initiation of damage within the mixture.

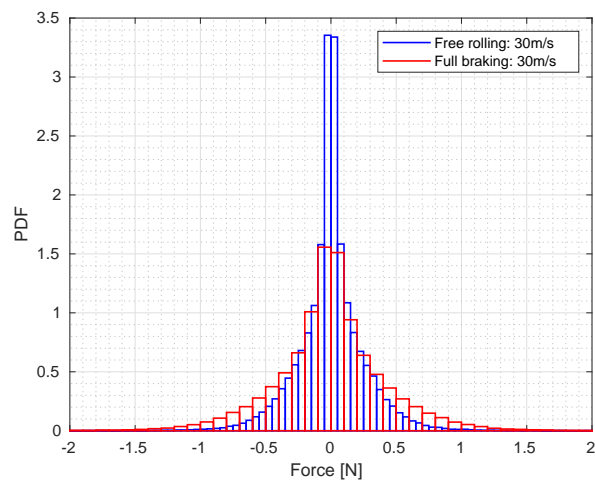
### 6.5.3 Particle displacement distribution

Figure 6.11 presents the particle displacement distribution for both loading conditions. The particle displacement distribution under free rolling is shown in figure 6.11a. The arrows in the figure indicate particle movement direction, and their colors indicate particle displacement magnitude. The particle displacements are not distributed uniformly in the mixture, with particles near the center displacing more than those in other regions, which is consistent with the concentration of stresses under free rolling.

Figure 6.11b shows the particle displacement distribution under the full braking condition. There is a visible concentration of peak displacements on one



(a) Normal contact force



(b) Tangential contact force

Figure 6.10: Particle contact force distribution at different tire rolling status



side of the model along the longitudinal axis. As a result of the significant longitudinal contact stress, particle displacement arrows also have an obvious longitudinal component.

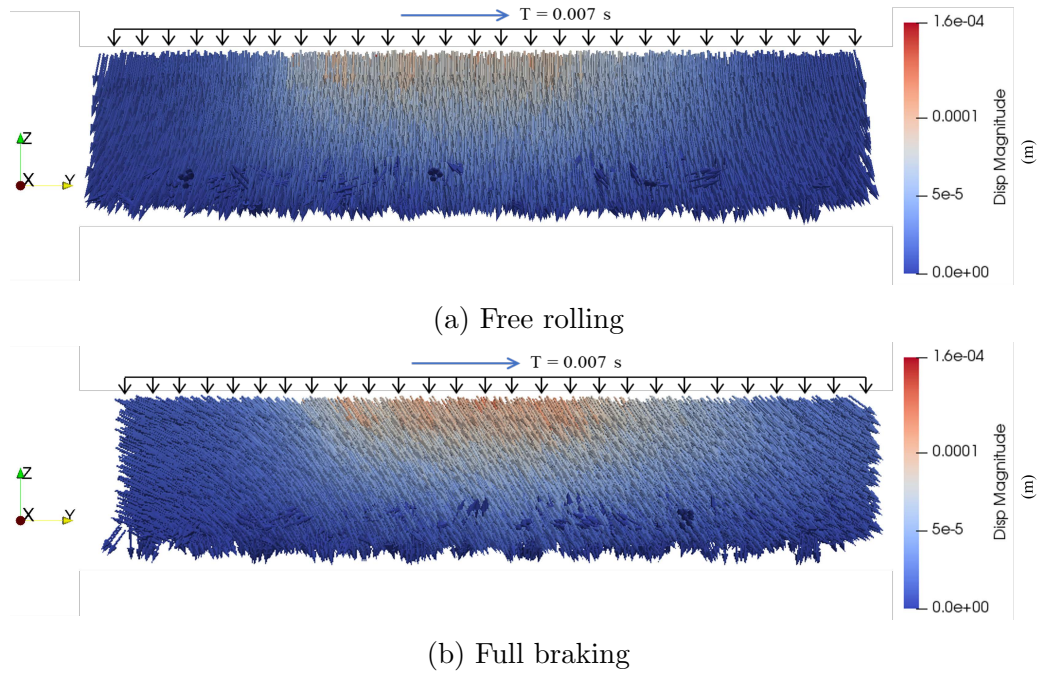
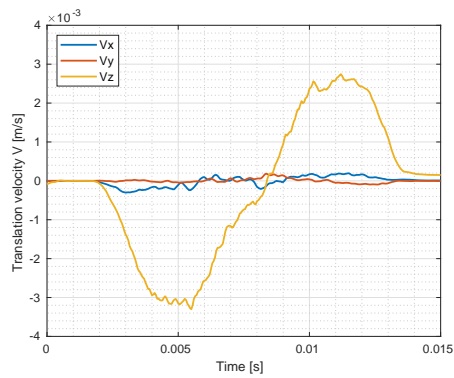


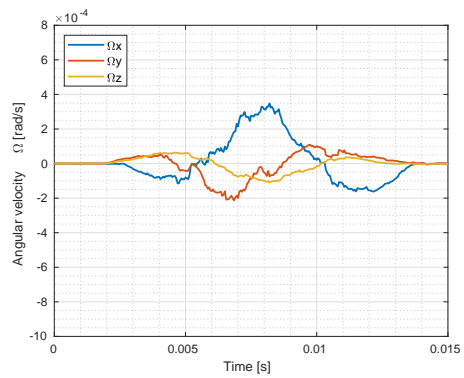
Figure 6.11: Particle displacement distribution at 30 m/s for different rolling status ( $T = 0.007$  s)

#### 6.5.4 Average particle velocity

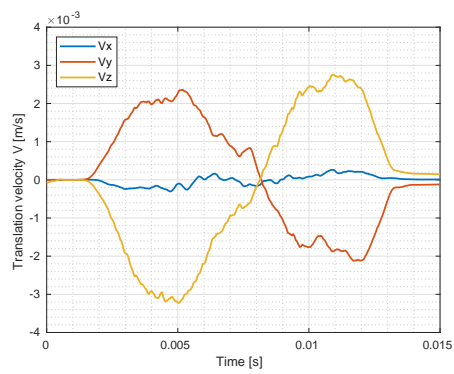
Figure 6.12 gives the evolution of average particle velocity including translation velocity and angular velocity for two loading conditions. The alignment of the translation velocity at full braking (figure 6.12c) exhibits a higher component of velocity along the y-axis than that at free rolling (figure 6.12a), which indicates that particles tend to move along the y-axis during full braking. The comparison of the angular velocity characteristics at two loading conditions shows the particles tend to have a noticeable rotation along the x-axis at full braking, as indicated by figure 6.12b and figure 6.12d.



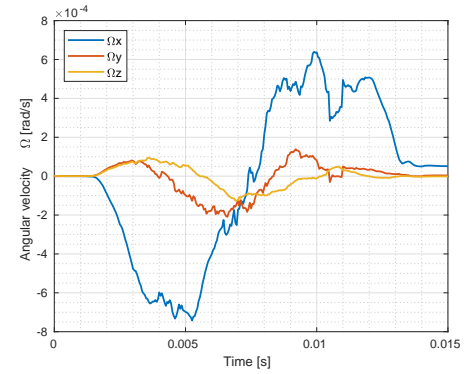
(a) Translation velocity-free rolling



(b) Angular velocity-free rolling



(c) Translation velocity-full braking

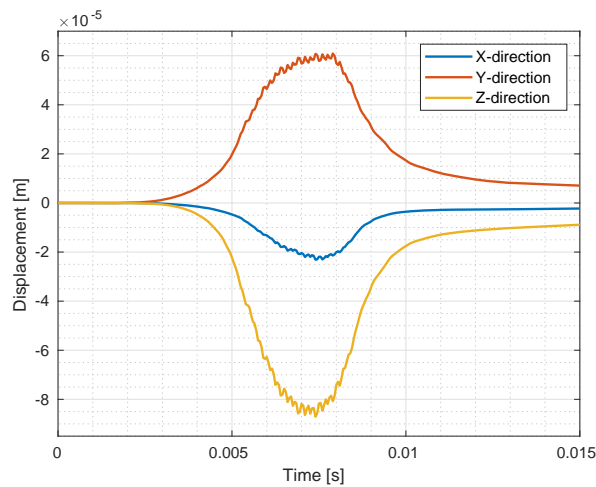


(d) Angular velocity-full braking

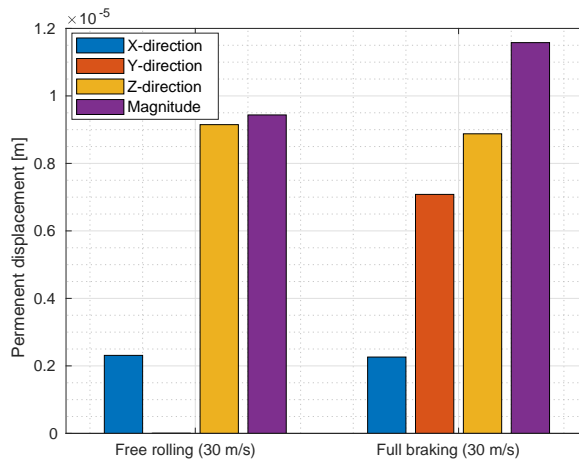
Figure 6.12: Average particle velocities for different tire rolling status

### 6.5.5 Particle movement characteristics

Additionally, the displacement of a single particle is investigated. Figure 6.13 shows the displacement evolution of one particle located on the layer surface center under both loading conditions. It can be found that the full braking condition causes an obvious longitudinal displacement component (Figure 6.13a) during the tire rolling process and a permanent displacement component (Figure 6.13b) along the y-axis after the tire rolling.



(a) Full braking (30 m/s)



(b) Comparison for the permanent displacement

Figure 6.13: Particle displacement for different tire rolling status

Tire rolling conditions including tire speed and rolling status are crucial in examining the mixture responses of asphalt surface layers. It is inevitable that tangential contact stresses are caused by the tire, particularly during braking or acceleration, which are crucial factors in asphalt mixture performance. The assumption of uniform contact stress is insufficient for predicting surface failures of asphalt mixtures, and it could lead to a misinterpretation of pavement degradation mechanisms under tire loads. The FEM-DEM coupling analysis described above offers insights into pavement surface design at the particle level by analyzing asphalt mixture responses under rolling tire loads using both continuum and discrete mechanics methods.

## 6.6 Conclusions of the chapter

The present chapter described a FEM-DEM coupling frame to study asphalt mixture responses at the particle level under real rolling tire loads. The main conclusions are drawn as follows:

An advanced FEM-DEM coupling algorithm was developed for the tire-pavement surface interaction process under rolling tire loads. Three procedures including tire imprint determination, tire contact force detection, and tire contact force application were performed continuously. The coupling simulation was performed to examine the response of the asphalt mixture layer to rolling tire load along the time step iterations.

As a result of applied tire-pavement contact stresses on the asphalt layer surface, particles move consistently in three directions, proving the effectiveness of the coupling method. In addition, there are differences in the contour color between particle displacements and applied contact stresses, which are caused by the non-uniformity of particle size distribution and particle contact-bearing capacity.

As the tire rolls on the asphalt layer surface, the particle force network evolves in a consistent way with the loading process, demonstrating the effectiveness of coupling simulations. In the study of the effect of tire velocity on mixture responses, it was found that low tire velocity results in a large permanent particle displacement, which might eventually result in a large non-recoverable permanent mixture deformation.

The effect of tire rolling state on asphalt mixture behavior has been demon-

strated in a study showing particle contact force at full braking is higher than that at free rolling. At the contact plane, full braking causes a great amount of shear, which may lead to early damage initiation. According to the particle displacement distribution, particles tend to flow and rotate along the longitudinal direction under full braking, resulting in structural disturbance. Moreover, due to tire boundary forces along the longitudinal direction under full braking, particles tend to have a large displacement component along this direction, which could result in severe permanent deformation.

The following paper summarizes the main results of this chapter:

Ge, H., Quezada, J. C., Le Houerou, V., & Chazallon, C. (2023). Three-dimensional FEM–DEM coupling simulation for analysis of asphalt mixture responses under rolling tire loads. *Construction and Building Materials*, 369, 130615. [198].

# Findings, conclusions and perspectives

---

## Contents

<b>7.1 Findings</b> . . . . .	<b>155</b>
7.1.1 Tire-pavement contact stresses . . . . .	155
7.1.1.1 Experimental measurements . . . . .	156
7.1.1.2 Numerical tire modeling . . . . .	156
7.1.2 Asphalt mixture modeling . . . . .	157
7.1.2.1 Constitutive law identification of asphalt mixture	157
7.1.2.2 DEM model of asphalt mixture . . . . .	157
7.1.3 Asphalt mixture responses under tire loads . . . . .	158
7.1.3.1 Tire-sensor-pavement coupling chain . . . . .	158
7.1.3.2 From macro to micro: FEM-DEM coupling . . . . .	158
<b>7.2 Conclusions</b> . . . . .	<b>160</b>
<b>7.3 Perspectives</b> . . . . .	<b>161</b>

---

In this study, a multi-scale FEM-DEM modeling strategy was developed for investigating tire-pavement interaction under non-uniform rolling tire loads. The main findings, conclusions, and perspectives for future works are given as follows:

## 7.1 Findings

### 7.1.1 Tire-pavement contact stresses

Experimental measurements and numerical tire modeling were used to obtain tire contact stresses on asphalt pavement surfaces in this study, as presented

in Chapter 3.

#### **7.1.1.1 Experimental measurements**

To measure tire contact stresses on pavement surfaces, the Tekscan system was used. It has been demonstrated that tire-pavement contact stresses are not uniform across the entire contact patch, and tire load and inflation pressure affect contact stress values and contact area.

The peak tire contact stress values are much higher than the tested tire inflation pressure and concentrated in the center of the tire imprint. Furthermore, as tire loads increase, the contact area extends from center-concentrated to side-flat, while the peak value of the contact stress increases slightly at two tire inflation pressures. In addition, increased tire inflation pressures also significantly increase tire-pavement contact stresses. Compared to tire load, tire inflation pressure seems to have a more significant impact on tire-pavement contact stress distribution.

#### **7.1.1.2 Numerical tire modeling**

Notably due to the limitation of experimental sensors in capturing tangential tire contact stresses on the pavement surface, a numerical tire modeling strategy and its calibration were developed to fully obtain tire-pavement contact stresses, refereed in Chapter 5.

Laser scanning and image processing techniques were used to reconstruct tire geometry. By using FEM, the tire structure model was built based on its function, and the relevant parameters were determined through experimental compression testing. Considering its performance and numerical stability in non-linear system simulations, the Contact Dynamics (CD) method was used for solving the tire-pavement contact condition through implicit contact formulation.

Under free-rolling and full-braking conditions, the tire induces three components of contact stresses (vertical, transverse, longitudinal) and they are all not uniform throughout the contact area. The vertical contact stress is much bigger than the other two tangential contact stresses for both free-rolling and full-braking conditions. In addition, under full braking, the tangential contact stress on the pavement surface is much higher than when free-rolling.

## 7.1.2 Asphalt mixture modeling

### 7.1.2.1 Constitutive law identification of asphalt mixture

The continuum mechanics framework was used to carry out macroscopic simulations of asphalt mixtures in consideration of the computational cost of asphalt pavement simulations, as introduced in Chapter 3.

In the numerical FEM simulations, the NOnLinear ViscoElastic (VENoL) model was used for characterizing the frequency- and temperature-dependent asphalt mixture properties.

According to the numerical simulation results, this model accurately describes the viscoelastic properties of the asphalt mixture under various temperatures and frequencies during the complex modulus test, as demonstrated by 2PB complex modulus measurements.

### 7.1.2.2 DEM model of asphalt mixture

As described in Chapter 4, due to the heterogeneous structure of asphalt mixtures, the DEM has been adopted to describe the internal asphalt mixture responses from a microscopic level, consistently, at the particle level.

A statistical analysis of the morphology features of aggregates was conducted using laser scanning and image processing. Results show that the elongation ratio, flatness ratio, and sphericity value of aggregates follow normal distributions.

Asphalt mixture specimens were generated by a tessellation method based on the particle morphology statistics including the average aspect ratio and the mean and standard deviation of the sphericity value.

The CD method is introduced to model asphalt mixtures because of its superior capability in polyhedron simulation. The Burgers contact model is adopted to mimic the viscoelastic behavior of asphalt mixtures. To validate the accuracy of the model, experimental and numerical complex modulus tests were conducted at different temperatures and frequencies. Results showed good agreement between the corresponding numerical master curves and the experimental results about dynamic modulus and phase angle.

Upon microscopic analysis resulting from DEM modeling, both the tangential force and normal force between particles appear to increase with decreasing



temperature and increased loading frequency. Further, comparing the tangential force and normal force between the particles during cyclic loading could provide insight into the mechanism of damage initiation for asphalt mixtures.

### **7.1.3 Asphalt mixture responses under tire loads**

#### **7.1.3.1 Tire-sensor-pavement coupling chain**

For the analysis of macroscopic asphalt mixture responses, a tire-sensor-pavement coupling chain was proposed based on continuum mechanics theory, referred to Chapter 4. The response of asphalt layers to different working conditions, including tire rolling velocity, tire load, inflation pressure, and external environment temperature, was examined. According to the results, the residual displacement of the asphalt layer surface increases with increasing tire loads and decreasing tire velocities, respectively; as a consequence of their two-sided opposing contributions to residual displacement, both tire load and contact area should be evaluated simultaneously for tire inflation pressure effects. A significant increase in residual displacement is observed at high temperatures (when the temperature surpasses 20 °C). The influencing zone of the residual displacement distribution field increases as the temperature increases, especially at high temperatures.

#### **7.1.3.2 From macro to micro: FEM-DEM coupling**

- Simulation under stationary tire loads:

In Chapter 5, we proposed a basic coupling strategy to analyze asphalt mixture responses under stationary non-uniform tire loads. Through building a series of rib elements on the asphalt DEM layer surface, the tire contact stresses derived from FEM simulations could be applied on the asphalt layer as a contact force field. By adjusting the number and size of elements within each rib element, the shape of the tire contact patch at a given load level could be considered.

Simulation results demonstrate that under full-braking conditions, particles inside the asphalt mixture tend to flow along the longitudinal direction and rotate ahead, which may lead to structural instability. The distribution of tangential force values under full-braking is higher

than that under free-rolling, based on particle contact force analysis. The results indicate that under full-braking conditions, particles in the mixture undergo greater shear than under free-rolling conditions, likely resulting in earlier damage initiation.

- Simulation under rolling tire loads:

In Chapter 6, an advanced FEM-DEM coupling method is developed to study asphalt mixture responses at the particle level under real rolling tire loads.

The kernel of FEM-DEM coupling is to detect corresponding particles on the asphalt layer that are in contact with tire-pavement contact area nodes. For this purpose, contact detection between particles and mesh nodes is carried out at two levels. First, a coarse detection is carried out using the bounding box algorithm in order to identify the particles in the neighboring of a reference mesh area. When a mesh node is inside the bounding box, a finer detection is performed using the cross-product method to determine which particle surface is in direct contact with the tire contact force nodal point. Following the tire contact nodal forces composed of three components being applied to the particles on the asphalt mixture layer surface, the coupling simulation was performed using time-iteration calculations.

The effectiveness of the coupling method is validated by combining the analysis of particle displacement distributions and tire-pavement contact stresses in three directions (transverse, longitudinal, and vertical).

During tire rolling over the asphalt layer surface, the particle force network evolves in a consistent manner, showing the effectiveness of coupling simulations. There was evidence that low tire velocity results in large residual particle displacement, which would eventually lead to permanent non-recoverable mixture deformation.

Similar results were observed as those in the stationary simulations mentioned before when evaluating the effect of tire rolling state on asphalt mixture behavior by particle contact force analysis. At the contact plane, full braking causes a significant amount of shear, which may lead to early damage initiation. Particles tend to flow and rotate along the longitudinal direction under full braking, which could result

in structural disturbances.

Moreover, particles under full braking tend to have a large displacement component along the longitudinal direction due to tire boundary forces, which could result in severe permanent deformation.

## 7.2 Conclusions

This study is dedicated to the modeling of tire-pavement interaction mechanisms from multi-scales. The main conclusions are summarized below.

There are two ways to obtain tire-pavement contact stresses: sensor measurements and numerical models. The numerical modeling method has priority since it can capture tire-pavement contact stresses in tangential directions, among other advantages.

For asphalt mixture modeling, FEM and DEM can be utilized for macro and micro scale simulations, respectively. In FEM modeling, asphalt mixtures are usually assumed to be homogeneous and complex constitutive material laws are typically required. The NOnLinear ViscoElastic (VENoL) model was successfully implemented in numerical simulations, and accuracy was achieved in predicting the properties of asphalt mixtures as a function of frequency and temperature. For characterizing heterogeneous asphalt mixture structures, the DEM modeling method presented in this study provides a basis for the high-precision simulation of asphalt mixtures containing multi-phases including irregular particles and asphalt mastic. In the numerical simulation, aggregate morphology and size distributions are incorporated into the asphalt mixture structure. Furthermore, the computational cost for preparing polyhedral samples is significantly reduced by using tessellation techniques. It can be seen as an appealing alternative to classic modeling methods in asphalt mixture simulations.

For investigating asphalt mixture responses under rolling tire loads, there are two main strategies that are suitable for different scales and purposes. At the macroscopic scale, finite element models using the tire-sensor-pavement coupling chain could be applied to investigate tire-pavement interaction processes as well as to investigate asphalt pavement response to different tire loading and environmental conditions. For tire-pavement contact zones in a macro pavement structure, the proposed FEM-DEM coupling strategy can

be used to conduct the tire-pavement interaction simulation at the microscopic scale. The coupling method incorporates the advantages that FEM can simulate contact stresses precisely on the asphalt pavement surface and that DEM is capable of examining internal responses of the asphalt mixture at the particle scale.

The present study provides a multi-scale simulation method incorporating FEM with DEM together to analyze tire-pavement interaction mechanisms under realistic rolling tire loads, which offers a promising way of understanding pavement surface deterioration and optimizing pavement surface design.

### 7.3 Perspectives

Due to the fact that tire geometry, structure, and tread configuration affect tire contact stress distributions, it is recommended to model more tire types including various structures and tread patterns to create a database of tire-pavement contact stresses. This database can be used as input boundary conditions for investigating asphalt pavement responses under tire loads.

The proposed DEM model for asphalt mixtures can be used further to investigate the effect of different particle sizes and morphology distribution and rheological properties of asphalt mixtures. Combined with the FEM-DEM coupling, the effects of asphalt mixture components (ex, aggregate gradation, asphalt mastic properties, etc) and external environmental conditions such as temperatures on asphalt mixture responses could be also examined under realistic rolling tire loads. It could therefore be possible to develop a comprehensive database of asphalt pavement responses based on various tire loading conditions, environmental conditions, and asphalt mixture characteristics including proprieties of internal components. In conjunction with computation methods such as artificial neural networks or machine learning, this database also has the potential to develop monographs for pavement design purposes based on input parameters from the tire, asphalt mixture, and environmental conditions.

Limited by the current computation capacity, this study conducted numerical simulations to examine asphalt mixture responses under a single tire loading cycle. Asphalt mixtures deteriorate under multiple tire overruns, and finally, induce cracks or permanent rutting deformation. The next step

consists to proceed further with particle-scale damage analysis and bridging it with macroscopic pavement performance predictions. Based on multi-scale FEM-DEM coupling simulations, a performance prediction model should be developed to include asphalt mixture damage mechanisms by using fatigue damage and/or fracture mechanics theory.

# Bibliography

- [1] Alvaro Gonzalez, Misko Cubrinovski, Bryan Pidwerbesky, and David Alabaster. Full-scale experiment on foam bitumen pavements in an accelerated testing facility. *Transportation research record*, 2094(1):21–29, 2009. (Cited on pages 2 and 30.)
- [2] ML Nguyen, P Hornych, XQ Le, M Dauvergne, L Lumière, C Chazallon, Mehdi Sahli, S Mouhoubi, D Doligez, and E Godard. Development of a rational design procedure based on fatigue characterisation and environmental evaluations of asphalt pavement reinforced with glass fibre grid. *Road Materials and Pavement Design*, 22(sup1):S672–S689, 2021. (Cited on pages 2 and 30.)
- [3] Sanghyun Chun, Kukjoo Kim, James Greene, and Bouzid Choubane. Evaluation of top-down cracking potential for asphalt pavements with 4.75 mm nominal maximum aggregate size mixture layer using full-scale field tests and finite element analysis. *Road Materials and Pavement Design*, 19(5):1089–1101, 2018. (Cited on pages xxx, 2, 30 and 31.)
- [4] Wentao Wang, Kang Zhao, Jianfeng Li, Rong Luo, and Linbing Wang. Characterization of dynamic response of asphalt pavement in dry and saturated conditions using the full-scale accelerated loading test. *Construction and Building Materials*, 312:125355, 2021. (Cited on pages xxx, 2, 30 and 31.)
- [5] Austroads. *Pavement design: A guide to the structural design of road pavements*. Austroads, 2004. (Cited on page 6.)
- [6] European Commission. Directorate-General Transport, European Cooperation in the Field of Scientific, and Technical Research (Organization). *COST 333: Development of New Bituminous Pavement Design Method: Final Report of the Action*, volume 18906. European Communities, 1999. (Cited on page 6.)
- [7] Johann Litzka, Bojan Leben, Francesca La Torre, Alfred Weninger-Vycudil, Maria de Lurdes Antunes, Darko Kokot, Goran Mladenovic, Stuart Brittain, and Helen Viner. *The Way Forward for Pavement Per-*

- formance Indicators Across Europe. COST Action 354: Performance Indicators for Road Pavements.* 2008. (Cited on page 6.)
- [8] Transportation Officials. Mechanistic-empirical pavement design guide: A manual of practice. *AASHTO: Washington, DC, USA*, 2008. (Cited on page 6.)
- [9] South African National Roads Agency Ltd. South african pavement engineering manual (sapem). *South Africa*, 2013. (Cited on page 6.)
- [10] D Cebon. Theoretical road damage due to dynamic tyre forces of heavy vehicles part 2: simulated damage caused by a tandem-axle vehicle. *Proceedings of the Institution of Mechanical Engineers, Part C: Journal of Mechanical Engineering Science*, 202(2):109–117, 1988. (Cited on page 6.)
- [11] David Cebon. Interaction between heavy vehicles and roads. Technical report, SAE Technical Paper, 1993. (Cited on page 6.)
- [12] MS Mamlouk. Vehicle-pavement interaction. state of the art. final report. Technical report, 1990. (Cited on page 6.)
- [13] Michael J Markow, J Karl Hedrick, Brian D Brademeyer, and Edward Abbo. Analyzing the interactions between dynamic vehicle loads and highway pavements. *Transportation Research Record*, (1196), 1988. (Cited on page 6.)
- [14] Shafi Ullah, Shanhong Wan, Chen Yang, Xianyong Ma, and Zejiao Dong. Self-stress and deformation sensing of electrically conductive asphalt concrete incorporating carbon fiber and iron tailings. *Structural Control and Health Monitoring*, 29(9):e2998, 2022. (Cited on page 6.)
- [15] Xianyong Ma, Zejiao Dong, and Yongkang Dong. Stiffness identification method for asphalt pavement layers and interfaces using monitoring data from built-in sensors. *Structural Health Monitoring*, page 14759217221077612, 2022. (Cited on page 6.)
- [16] Yang Hsien Huang et al. Pavement analysis and design. 1993. (Cited on pages 6 and 32.)

- 
- [17] Jean-François Corté and Marie-Thérèse Goux. Design of pavement structures: the french technical guide. *Transportation research record*, 1539(1):116–124, 1996. (Cited on page 6.)
- [18] Hechter L Theyse and M Muthen. Pavement analysis and design software (pads) based on the south african mechanistic-empirical design method. *SATC 2000*, 2000. (Cited on page 6.)
- [19] Tamás Király, Péter Primusz, and Csaba Tóth. Simulation of static tyre–pavement interaction using two fe models of different complexity. *Applied Sciences*, 12(5):2388, 2022. (Cited on page 7.)
- [20] M De Beer. Measurement of tyre/pavement interface stresses under moving wheel loads. *International Journal of Heavy Vehicle Systems*, 3(1-4):97–115, 1996. (Cited on pages 7 and 8.)
- [21] Dae-Wook Park, Emmanuel Fernando, and Joe Leidy. Evaluation of predicted pavement response with measured tire contact stresses. *Transportation Research Record*, 1919(1):160–170, 2005. (Cited on pages 7 and 44.)
- [22] Raj V Siddharthan, N Krishnamenon, Mohey El-Mously, and Peter E Sebaaly. Investigation of tire contact stress distributions on pavement response. *Journal of Transportation Engineering*, 128(2):136–144, 2002. (Cited on pages 7 and 44.)
- [23] Xin Jiang, Cheng Zeng, Xiaofeng Gao, Zhujun Liu, and Yanjun Qiu. 3d fem analysis of flexible base asphalt pavement structure under non-uniform tyre contact pressure. *International Journal of Pavement Engineering*, 20(9):999–1011, 2019. (Cited on pages 7 and 44.)
- [24] Imad L Al-Qadi, Hao Wang, Pyeong Jun Yoo, and Samer H Dessouky. Dynamic analysis and in situ validation of perpetual pavement response to vehicular loading. *Transportation Research Record*, 2087(1):29–39, 2008. (Cited on pages 7 and 44.)
- [25] Hao Wang, Hasan Ozer, Imad L Al-Qadi, and C Armando Duarte. Analysis of near-surface cracking under critical loading conditions using uncracked and cracked pavement models. *Journal of transportation engineering*, 139(10):992–1000, 2013. (Cited on pages 7, 32, 44 and 122.)



- 
- [26] Massimiliano Pau, Bruno Leban, and Antonio Baldi. Ultrasonic measurements of contact area and pressure distribution of a pneumatic tire on a rigid surface. *Tire Science and Technology*, 36(1):43–62, 2008. (Cited on page 8.)
- [27] Edem Yawo Manyo, Philippe Reynaud, Benoit Picoux, Remi Tautou, Daniel Nelias, Fatima Allou, and Christophe Petit. Towards fast modelling of the tire-pavement contact. *European Journal of Environmental and Civil Engineering*, 25(13):2396–2412, 2021. (Cited on pages 8 and 44.)
- [28] Morris De Beer and Colin Fisher. Stress-in-motion (sim) system for capturing tri-axial tyre-road interaction in the contact patch. *Measurement*, 46(7):2155–2173, 2013. (Cited on pages xxix and 8.)
- [29] Morris De Beer, James W Maina, Yvette Van Rensburg, and Jan M Greben. Toward using tire-road contact stresses in pavement design and analysis. *Tire Science and Technology*, 40(4):246–271, 2012. (Cited on page 8.)
- [30] Morris De Beer and Colin Fisher. Towards understanding tyre-pavement contact in apt research on flexible pavements. In *The Roles of Accelerated Pavement Testing in Pavement Sustainability*, pages 491–507. Springer, 2016. (Cited on pages 8 and 63.)
- [31] Ronald Blab and John T Harvey. Modeling measured 3d tire contact stresses in a viscoelastic fe pavement model. *The International Journal Geomechanics*, 2(3):271–290, 2002. (Cited on page 8.)
- [32] Y Oubahdou, ER Wallace, P Reynaud, B Picoux, J Dopeux, C Petit, and D Nélias. Effect of the tire-pavement contact at the surface layer when the tire is tilted in bend. *Construction and Building Materials*, 305:124765, 2021. (Cited on pages 8, 9, 44 and 108.)
- [33] Tongxu Wang, Zejiao Dong, Ke Xu, Shafi Ullah, Donghao Wang, and Yiheng Li. Numerical simulation of mechanical response analysis of asphalt pavement under dynamic loads with non-uniform tire-pavement contact stresses. *Construction and Building Materials*, 361:129711, 2022. (Cited on pages 8 and 34.)

- 
- [34] Hao Wang and Imad L Al-Qadi. Impact quantification of wide-base tire loading on secondary road flexible pavements. *Journal of Transportation Engineering*, 137(9):630–639, 2011. (Cited on pages 8, 32 and 108.)
- [35] N Korunović, M Trajanović, and M Stojković. Finite element model for steady-state rolling tire analysis. *Journal of the Serbian Society for Computational Mechanics/Vol*, 1(1):63–79, 2007. (Cited on page 9.)
- [36] Hao Wang, Imad L Al-Qadi, and Ilinca Stanciulescu. Simulation of tyre–pavement interaction for predicting contact stresses at static and various rolling conditions. *International Journal of Pavement Engineering*, 13(4):310–321, 2012. (Cited on pages xxix, 9, 10 and 108.)
- [37] Ines Wollny and Michael Kaliske. Numerical simulation of pavement structures with inelastic material behaviour under rolling tyres based on an arbitrary lagrangian eulerian (ale) formulation. *Road Materials and Pavement Design*, 14(1):71–89, 2013. (Cited on page 9.)
- [38] Ines Wollny, Ronny Behnke, Karl Villaret, and Michael Kaliske. Numerical modelling of tyre–pavement interaction phenomena: coupled structural investigations. *Road Materials and Pavement Design*, 17(3):563–578, 2016. (Cited on pages 9, 32, 60, 108 and 115.)
- [39] Minrui Guo and Xinglin Zhou. Tire-pavement contact stress characteristics and critical slip ratio at multiple working conditions. *Advances in Materials Science and Engineering*, 2019, 2019. (Cited on pages 9 and 108.)
- [40] Minrui Guo, Xiangwen Li, Maoping Ran, Xinglin Zhou, and Yuan Yan. Analysis of contact stresses and rolling resistance of truck-bus tyres under different working conditions. *Sustainability*, 12(24):10603, 2020. (Cited on pages 9, 108 and 115.)
- [41] EY Manyo, P Reynaud, B Picoux, R Tautou, F Allou, C Petit, and D Nélias. Tire–pavement tractive rolling contact under turning conditions: towards pavement top-down cracking. *International Journal of Pavement Engineering*, pages 1–10, 2020. (Cited on pages 9, 12 and 108.)

- 
- [42] Edem Yawo Manyo, Benoit Picoux, Philippe Reynaud, Rémi Tautou, Daniel Nelias, Fatima Allou, and Christophe Petit. Approach of pavement surface layer degradation caused by tire contact using semi-analytical model. *Materials*, 14(9):2117, 2021. (Cited on pages 9 and 108.)
- [43] EY Manyo, I Leandry, B Picoux, P Reynaud, F Allou, and C Petit. 3d modeling and measuring of tire-pavement contact pressure. In *Proceedings of 10th International Conference on the Bearing Capacity of Roads, Railways and Airfields, Athens, Greece, 2017*. (Cited on pages xxx and 11.)
- [44] Qiang Li, Danny X Xiao, Kelvin CP Wang, Kevin D Hall, and Yanjun Qiu. Mechanistic-empirical pavement design guide (mepdg): a bird’s-eye view. *Journal of Modern Transportation*, 19(2):114–133, 2011. (Cited on page 12.)
- [45] EN 12697-26. Bituminous mixtures. test methods for hot mix asphalt. stiffness, 2012. (Cited on pages 12, 13, 14, 46, 96, 114 and 138.)
- [46] Huanan Yu and Shihui Shen. A micromechanical based three-dimensional dem approach to characterize the complex modulus of asphalt mixtures. *Construction and Building Materials*, 38:1089–1096, 2013. (Cited on pages 12, 20 and 78.)
- [47] Huan Feng, Matteo Pettinari, Bernhard Hofko, and Henrik Stang. Study of the internal mechanical response of an asphalt mixture by 3-d discrete element modeling. *Construction and Building materials*, 77:187–196, 2015. (Cited on pages 12, 21 and 22.)
- [48] Juan Carlos Quezada and Cyrille Chazallon. Complex modulus modeling of asphalt concrete mixes using the non-smooth contact dynamics method. *Computers and Geotechnics*, 117:103255, 2020. (Cited on pages xxx, xxxiii, 12, 22, 24, 48, 91, 93 and 94.)
- [49] Haichuan Jia, Yanping Sheng, Hongli Lv, Y Richard Kim, Xiaorui Zhao, Jiandang Meng, and Rui Xiong. Effects of bamboo fiber on the mechanical properties of asphalt mixtures. *Construction and Building Materials*, 289:123196, 2021. (Cited on pages xxx and 12.)

- 
- [50] Manfred N Partl, Hussain U Bahia, Francesco Canestrari, Chantal De la Roche, Hervé Di Benedetto, Herald Piber, and Dariusz Sybilski. *Advances in interlaboratory testing and evaluation of bituminous materials: state-of-the-art report of the RILEM technical committee 206-ATB*, volume 9. Springer Science & Business Media, 2012. (Cited on page 14.)
- [51] Juan Carlos Quezada and Cyrille Chazallon. Discrete element modelling of hot mix asphalt complex modulus using realistic aggregate shapes. *Road Materials and Pavement Design*, 23(sup1):178–195, 2022. (Cited on pages xxx, 14 and 88.)
- [52] Mihai Marateanu and David Anderson. Time-temperature dependency of asphalt binders—an improved model (with discussion). *Journal of the Association of Asphalt Paving Technologists*, 65, 1996. (Cited on page 15.)
- [53] Salvatore Mangiafico. Linear viscoelastic properties and fatigue of bituminous mixtures produced with reclaimed asphalt pavement and corresponding binder blends. *ENTPE, Lyon*, 2014. (Cited on page 15.)
- [54] Lily D Poulikakos, Michel Pittet, Andre-Gilles Dumont, and Manfred N Partl. Comparison of the two point bending and four point bending test methods for aged asphalt concrete field samples. *Materials and Structures*, 48(9):2901–2913, 2015. (Cited on page 15.)
- [55] Yu Liu and Zhanping You. Accelerated discrete-element modeling of asphalt-based materials with the frequency-temperature superposition principle. *Journal of engineering mechanics*, 137(5):355–365, 2011. (Cited on pages xxx, 15, 22 and 23.)
- [56] Marinella Giunta and Aurora Angela Pisano. One-dimensional visco-elastoplastic constitutive model for asphalt concrete. *Multidiscipline Modeling in Materials and Structures*, 2006. (Cited on page 15.)
- [57] Shaopeng Wu, Hong Wang, and Yao Yao. Constitutive relationship of asphalt mixture for finite element method. In *ICCTP 2009: Critical Issues In Transportation Systems Planning, Development, and Management*, pages 1–6. 2009. (Cited on page 15.)

- 
- [58] Y Richard Kim. *Modeling of asphalt concrete*. McGraw-Hill Education, 2009. (Cited on page 15.)
- [59] Robert L Lytton, Jacob Uzan, Emmanuel G Fernando, Reynaldo Roque, Dennis Hiltunen, and Shelley M Stoffels. *Development and validation of performance prediction models and specifications for asphalt binders and paving mixes*, volume 357. Strategic Highway Research Program Washington, DC, 1993. (Cited on page 15.)
- [60] Qinwu Xu and Mansour Solaimanian. Modelling linear viscoelastic properties of asphalt concrete by the huet–sayegh model. *International Journal of Pavement Engineering*, 10(6):401–422, 2009. (Cited on page 15.)
- [61] Sassan Aflaki and Pouria Hajikarimi. Implementing viscoelastic rheological methods to evaluate low temperature performance of modified asphalt binders. *Construction and Building Materials*, 36:110–118, 2012. (Cited on page 15.)
- [62] Gao Lian-Sheng, Dan Han-Cheng, and Chen Jia-Qi. Research on predicting the rutting of asphalt pavement based on a simplified burgers creep model. *Mathematical Problems in Engineering*, 2017, 2017. (Cited on page 15.)
- [63] Roger N Nilsson, Piet C Hopman, and Ulf Isacsson. Influence of different rheological models on predicted pavement responses in flexible pavements. *Road Materials and Pavement Design*, 3(2):117–149, 2002. (Cited on page 15.)
- [64] Adriaan C Pronk. The huet-sayegh model: A simple and excellent rheological model for master curves of asphaltic mixes. In *Asphalt Concrete: Simulation, Modeling, and Experimental Characterization*, pages 73–82. 2006. (Cited on page 15.)
- [65] François Olard and Hervé Di Benedetto. General “2s2p1d” model and relation between the linear viscoelastic behaviours of bituminous binders and mixes. *Road materials and pavement design*, 4(2):185–224, 2003. (Cited on page 16.)
- [66] Léo Coulon, Georg Koval, Cyrille Chazallon, and Jean-Noël Roux. Modeling of t/c complex stiffness modulus test and non-linearity of

- asphalt concrete mixes. In *RILEM International Symposium on Bituminous Materials*, pages 1343–1350. Springer, 2020. (Cited on page 16.)
- [67] L Coulon, G Koval, C Chazallon, and J-N Roux. Analytical modelling of complex stiffness modulus tests in direct tension-compression on asphalt concrete and nonlinearity effect due to strain amplitude. *Road Materials and Pavement Design*, pages 1–31, 2021. (Cited on pages xxxi, 16, 51 and 52.)
- [68] Léo Coulon, G Koval, Cyrille Chazallon, and J-N Roux. Analytical modelling of thixotropy contribution during t/c fatigue tests of asphalt concrete with the venol model. *Road Materials and Pavement Design*, 22(sup1):S536–S559, 2021. (Cited on page 16.)
- [69] Y Lu and PJ Wright. Numerical approach of visco-elastoplastic analysis for asphalt mixtures. *Computers & structures*, 69(2):139–147, 1998. (Cited on page 16.)
- [70] Andrew C Collop, A Scarpas, Cor Kasbergen, and Arian de Bondt. Development and finite element implementation of stress-dependent elastoviscoplastic constitutive model with damage for asphalt. *Transportation Research Record*, 1832(1):96–104, 2003. (Cited on page 16.)
- [71] Eyad Masad, Samer Dessouky, and Dallas Little. Development of an elastoviscoplastic microstructural-based continuum model to predict permanent deformation in hot mix asphalt. *International Journal of Geomechanics*, 7(2):119–130, 2007. (Cited on page 16.)
- [72] Ma Ameri, Ab Mansourian, M Heidary Khavas, MRMc Aliha, and MR Ayatollahi. Cracked asphalt pavement under traffic loading—a 3d finite element analysis. *Engineering Fracture Mechanics*, 78(8):1817–1826, 2011. (Cited on page 16.)
- [73] Tao Bai, Zhen Cheng, Xiaodi Hu, Luis Fuentes, and Lubinda F Walubita. Viscoelastic modelling of an asphalt pavement based on actual tire-pavement contact pressure. *Road Materials and Pavement Design*, 22(11):2458–2477, 2021. (Cited on page 16.)
- [74] Rosario Fedele, Filippo Giammaria Praticò, and Gianfranco Pellicano. The prediction of road cracks through acoustic signature: Extended

- finite element modeling and experiments. *J. Test. Eval*, 49(4):20190209, 2019. (Cited on page 16.)
- [75] Xin He, Sherif Abdelaziz, Fangliang Chen, and Huiming Yin. Finite element simulation of self-heated pavement under different mechanical and thermal loading conditions. *Road Materials and Pavement Design*, 20(8):1807–1826, 2019. (Cited on page 16.)
- [76] Maoyun Li, Hao Wang, Guangji Xu, and Pengyu Xie. Finite element modeling and parametric analysis of viscoelastic and nonlinear pavement responses under dynamic fwd loading. *Construction and Building Materials*, 141:23–35, 2017. (Cited on page 16.)
- [77] Anyi Yin, Xinhua Yang, Chuanchuan Zhang, Guowei Zeng, and Zhenjun Yang. Three-dimensional heterogeneous fracture simulation of asphalt mixture under uniaxial tension with cohesive crack model. *Construction and Building Materials*, 76:103–117, 2015. (Cited on page 18.)
- [78] Jiaqi Chen, Hao Wang, and Liang Li. Virtual testing of asphalt mixture with two-dimensional and three-dimensional random aggregate structures. *International Journal of Pavement Engineering*, 18(9):824–836, 2017. (Cited on page 18.)
- [79] Can Jin, Feilong Zou, Xu Yang, and Kai Liu. 3-d virtual design and microstructural modeling of asphalt mixture based on a digital aggregate library. *Computers & Structures*, 242:106378, 2021. (Cited on page 18.)
- [80] Pengfei Liu, Jing Hu, Dawei Wang, Markus Oeser, Stefan Alber, Wolfram Ressel, and Gustavo Canon Falla. Modelling and evaluation of aggregate morphology on asphalt compression behavior. *Construction and Building Materials*, 133:196–208, 2017. (Cited on pages xxx, 18, 19, 83 and 86.)
- [81] Peter A Cundall. A computer model for simulating progressive, large-scale movement in blocky rock system. In *Proceedings of the International Symposium on Rock Mechanics, 1971*, 1971. (Cited on pages 19 and 79.)
- [82] Bernard Cambou, Michel Jean, and Farhang Radjaï. *Micromechanics of granular materials*. John Wiley & Sons, 2013. (Cited on page 19.)

- [83] M. Jean and J. J. Moreau. Dynamics in the presence of unilateral contacts and dry friction: A numerical approach. In G. Del Piero and F. Maceri, editors, *Unilateral Problems in Structural Analysis — 2*, pages 151–196, Vienna, 1987. Springer Vienna. (Cited on pages 19 and 79.)
- [84] W Cai, GR McDowell, and GD Airey. Discrete element visco-elastic modelling of a realistic graded asphalt mixture. *Soils and Foundations*, 54(1):12–22, 2014. (Cited on pages 20 and 78.)
- [85] Fangyuan Gong, Yu Liu, Xiaodong Zhou, and Zhanping You. Lab assessment and discrete element modeling of asphalt mixture during compaction with elongated and flat coarse aggregates. *Construction and Building Materials*, 182:573–579, 2018. (Cited on pages 20 and 78.)
- [86] Habtamu Melese Zelelew and Athanassios Tom Papagiannakis. Micromechanical modeling of asphalt concrete uniaxial creep using the discrete element method. *Road Materials and Pavement Design*, 11(3):613–632, 2010. (Cited on pages 20, 26 and 78.)
- [87] Yu Liu, Qingli Dai, and Zhanping You. Viscoelastic model for discrete element simulation of asphalt mixtures. *Journal of Engineering Mechanics*, 135(4):324–333, 2009. (Cited on pages 20 and 22.)
- [88] Mingfeng Chang, Jianzhong Pei, and Jiupeng Zhang. Influences of mesoscopic parameters on crack resistance of asphalt mixture. In *IC-CTP 2011: Towards Sustainable Transportation Systems*, pages 3324–3332. 2011. (Cited on page 20.)
- [89] Jingsong Shan, Yang Du, Dahai Fan, and Laiyao Guo. Determination of parameters of the discrete element bond model for asphalt mixture based on splitting test. *Advances in Civil Engineering*, 2019, 2019. (Cited on page 20.)
- [90] David Renteria, Shadi Saadeh, and Enad Mahmoud. Fracture behavior analysis of semi-circular bending test. In *MATEC Web of Conferences*, volume 271, page 03007. EDP Sciences, 2019. (Cited on page 20.)
- [91] Yong Peng and Li-jun Sun. Aggregate distribution influence on the indirect tensile test of asphalt mixtures using the discrete element



- method. *International Journal of Pavement Engineering*, 18(8):668–681, 2017. (Cited on page 20.)
- [92] Tengfei Nian, Jinguo Ge, Ping Li, Meng Wang, and Yu Mao. Improved discrete element numerical simulation and experiment on low-temperature anti-cracking performance of asphalt mixture based on pfc2d. *Construction and Building Materials*, 283:122792, 2021. (Cited on pages xxx and 21.)
- [93] Zhanping You and Yu Liu. Three-dimensional discrete element simulation of asphalt concrete subjected to haversine loading: An application of the frequency-temperature superposition technique. *Road materials and pavement design*, 11(2):273–290, 2010. (Cited on page 21.)
- [94] Zhanping You, Yu Liu, and Qingli Dai. Three-dimensional microstructural-based discrete element viscoelastic modeling of creep compliance tests for asphalt mixtures. *Journal of Materials in Civil Engineering*, 23(1):79–87, 2011. (Cited on page 21.)
- [95] Yu Liu, Zhanping You, and Yang Zhao. Three-dimensional discrete element modeling of asphalt concrete: Size effects of elements. *Construction and Building Materials*, 37:775–782, 2012. (Cited on page 22.)
- [96] William G Buttlar and Zhanping You. Discrete element modeling of asphalt concrete: microfabric approach. *Transportation Research Record*, 1757(1):111–118, 2001. (Cited on page 22.)
- [97] AC Collop, GR McDowell, and Y Lee. On the use of discrete element modelling to simulate the viscoelastic deformation behaviour of an idealized asphalt mixture. *Geomechanics and Geoengineering: An International Journal*, 2(2):77–86, 2007. (Cited on page 22.)
- [98] G Dondi, V Vignali, Matteo Pettinari, F Mazzotta, A Simone, and C Sangiorgi. Modeling the dsr complex shear modulus of asphalt binder using 3d discrete element approach. *Construction and building Materials*, 54:236–246, 2014. (Cited on page 22.)
- [99] Zhanping You and William G Buttlar. Application of discrete element modeling techniques to predict the complex modulus of asphalt–aggregate hollow cylinders subjected to internal pressure. *Transporta-*

- tion Research Record*, 1929(1):218–226, 2005. (Cited on pages 22 and 26.)
- [100] Zhanping You, Sanjeev Adhikari, and M Emin Kutay. Dynamic modulus simulation of the asphalt concrete using the x-ray computed tomography images. *Materials and Structures*, 42(5):617–630, 2009. (Cited on pages 22 and 27.)
- [101] Tao Ma, Hao Wang, Deyu Zhang, and Yao Zhang. Heterogeneity effect of mechanical property on creep behavior of asphalt mixture based on micromechanical modeling and virtual creep test. *Mechanics of Materials*, 104:49–59, 2017. (Cited on page 22.)
- [102] Jingsong Chen, Baoshan Huang, Feng Chen, and Xiang Shu. Application of discrete element method to superpave gyratory compaction. *Road materials and pavement design*, 13(3):480–500, 2012. (Cited on page 22.)
- [103] Fangyuan Gong, Xiaodong Zhou, Zhanping You, Yu Liu, and Siyu Chen. Using discrete element models to track movement of coarse aggregates during compaction of asphalt mixture. *Construction and Building Materials*, 189:338–351, 2018. (Cited on page 22.)
- [104] Maziar Moaveni, Enad Mahmoud, Eduardo Madrigal Ortiz, Erol Tutumluer, and Sheila Beshears. Use of advanced aggregate imaging systems to evaluate aggregate resistance to breakage, abrasion, and polishing. *Transportation Research Record*, 2401(1):1–10, 2014. (Cited on page 26.)
- [105] Thomas Bennert, L Allen Cooley Jr, Christopher Ericson, and Zoeb Zavery. Coarse aggregate angularity and its relationship to permanent deformation of gravel-aggregate hot-mix asphalt in New York State. *Transportation research record*, 2207(1):25–33, 2011. (Cited on page 26.)
- [106] Jian-Shiuh Chen, Weichou Hsieh, and Min-Chih Liao. Effect of coarse aggregate shape on engineering properties stone mastic asphalt applied to airport pavements. *International Journal of Pavement Research and Technology*, 6(5):595, 2013. (Cited on page 26.)

- 
- [107] Leonardo T Souza, Yong-Rak Kim, Flavio V Souza, and Leandro S Castro. Experimental testing and finite-element modeling to evaluate the effects of aggregate angularity on bituminous mixture performance. *Journal of Materials in Civil Engineering*, 24(3):249–258, 2012. (Cited on page 26.)
- [108] Daniel Castillo, Silvia Caro, Masoud Darabi, and Eyad Masad. Influence of aggregate morphology on the mechanical performance of asphalt mixtures. *Road Materials and Pavement Design*, 19(4):972–991, 2018. (Cited on page 26.)
- [109] Zhanping You and William G Buttlar. Discrete element modeling to predict the modulus of asphalt concrete mixtures. *Journal of materials in civil engineering*, 16(2):140–146, 2004. (Cited on page 26.)
- [110] Mohammad J Khattak, Ahmed Khattab, Hashim R Rizvi, Subasish Das, and Mohammad R Bhuyan. Imaged-based discrete element modeling of hot mix asphalt mixtures. *Materials and Structures*, 48(8):2417–2430, 2015. (Cited on page 26.)
- [111] Zhanping You, Sanjeev Adhikari, and Qingli Dai. Three-dimensional discrete element models for asphalt mixtures. *Journal of engineering mechanics*, 134(12):1053–1063, 2008. (Cited on page 26.)
- [112] Yanrong Fu, Linbing Wang, and Chuangbing Zhou. 3d clustering dem simulation and non-invasive experimental verification of shear localisation in irregular particle assemblies. *International Journal of Pavement Engineering*, 11(5):355–365, 2010. (Cited on page 26.)
- [113] Sanjeev Adhikari, Zhanping You, and M Emin Kutay. Prediction of dynamic modulus of asphalt concrete using two-dimensional and three-dimensional discrete element modeling approach. In *GeoCongress 2008: Characterization, Monitoring, and Modeling of GeoSystems*, pages 1020–1027. 2008. (Cited on page 26.)
- [114] J Wimmer, B Stier, J-W Simon, and S Reese. Computational homogenisation from a 3d finite element model of asphalt concrete—linear elastic computations. *Finite Elements in Analysis and Design*, 110:43–57, 2016. (Cited on pages 26 and 86.)

- [115] Yu Liu and Zhanping You. Visualization and simulation of asphalt concrete with randomly generated three-dimensional models. *Journal of Computing in Civil Engineering*, 23(6):340–347, 2009. (Cited on page 26.)
- [116] Dong Zhang, Xiaoming Huang, and Yongli Zhao. Algorithms for generating three-dimensional aggregates and asphalt mixture samples by the discrete-element method. *Journal of Computing in Civil Engineering*, 27(2):111–117, 2013. (Cited on page 26.)
- [117] Tao Ma, Deyu Zhang, Yao Zhang, Siqi Wang, and Xiaoming Huang. Simulation of wheel tracking test for asphalt mixture using discrete element modelling. *Road Materials and Pavement Design*, 19(2):367–384, 2018. (Cited on pages 26 and 34.)
- [118] Changhong Zhou, Xueyan Liu, Panos Apostolidis, A Tom Scarpas, and Liang He. Induction heating-assisted compaction in Porous Asphalt Pavements: A computational study. *Applied sciences*, 8(11):2308, 2018. (Cited on page 26.)
- [119] Bin Xue, Jianzhong Pei, Bochao Zhou, Jiupeng Zhang, Rui Li, and Fucheng Guo. Using random heterogeneous dem model to simulate the scb fracture behavior of asphalt concrete. *Construction and Building Materials*, 236:117580, 2020. (Cited on page 26.)
- [120] Xiaodong Zhou, Yu Liu, and Zhanping You. Heavy impact compaction modeling and analysis on unbound paving mixtures. In *International Conference on Discrete Element Methods*, pages 437–444. Springer, 2016. (Cited on page 26.)
- [121] Yu Liu, Xiaodong Zhou, Zhanping You, Shun Yao, Fangyuan Gong, and Hainian Wang. Discrete element modeling of realistic particle shapes in stone-based mixtures through matlab-based imaging process. *Construction and Building Materials*, 143:169–178, 2017. (Cited on pages xxx, 26 and 29.)
- [122] Bin Xue, Jing Xu, Jianzhong Pei, Jiupeng Zhang, and Rui Li. Investigation on the micromechanical response of asphalt mixture during permanent deformation based on 3d virtual wheel tracking test. *Construction and Building Materials*, 267:121031, 2021. (Cited on pages xxx, 28, 34 and 36.)

- 
- [123] Nivedita Das. *Modeling three-dimensional shape of sand grains using discrete element method*. University of South Florida, 2007. (Cited on page 27.)
- [124] F. Alonso-Marroquin and H. J. Herrmann. Calculation of the incremental stress-strain relation of a polygonal packing. *Phys. Rev. E*, 66:021301, Aug 2002. (Cited on page 27.)
- [125] Emilien Azéma, Farhang Radjai, and Gilles Saussine. Quasistatic rheology, force transmission and fabric properties of a packing of irregular polyhedral particles. *Mechanics of Materials*, 41(6):729–741, 2009. (Cited on pages 27, 100 and 142.)
- [126] D Jones, RZ Wu, and TJ Holland. *Accelerated traffic load testing of seismic expansion joints for the new San Francisco–Oakland Bay Bridge*. CRC Press Boca Raton, FL, USA, 2012. (Cited on page 29.)
- [127] Cong Lin and Wang Tongjing. Effect of fine aggregate angularity on skid-resistance of asphalt pavement using accelerated pavement testing. *Construction and Building Materials*, 168:41–46, 2018. (Cited on page 30.)
- [128] Songtao Lv, Long Hu, Chengdong Xia, Xiaofeng Wang, Milkos Borges Cabrera, Shuaicheng Guo, and Jie Chen. Development of fatigue damage model of asphalt mixtures based on small-scale accelerated pavement test. *Construction and Building Materials*, 260:119930, 2020. (Cited on page 30.)
- [129] M Zaumanis, M Arraigada, SA Wyss, K Zeyer, MC Cavalli, and LD Poulidakos. Performance-based design of 100% recycled hot-mix asphalt and validation using traffic load simulator. *Journal of Cleaner Production*, 237:117679, 2019. (Cited on pages xxx and 30.)
- [130] John B Metcalf. *Application of full-scale accelerated pavement testing*, volume 235. Transportation Research Board, 1996. (Cited on page 30.)
- [131] Xavier Chapeleau, Juliette Blanc, Pierre Hornych, Jean-Luc Gautier, and Jean Carroget. Use of distributed fiber optic sensors to detect damage in a pavement. *Asph. Pavements*, pages 449–457, 2014. (Cited on pages xxx, 30 and 31.)

- [132] Zhen Liu, Xingyu Gu, Hua Ren, Xiang Wang, and Qiao Dong. Three-dimensional finite element analysis for structural parameters of asphalt pavement: A combined laboratory and field accelerated testing approach. *Case Studies in Construction Materials*, page e01221, 2022. (Cited on pages xxx and 31.)
- [133] Benjamin Worel, Michael Vrtis, and R Buzz Powell. Guidance for the next generation accelerated pavement testing facilities. In *Accelerated Pavement Testing to Transport Infrastructure Innovation*, pages 40–48. Springer, 2020. (Cited on page 30.)
- [134] D de Jong, M Peutz, and A Korswagen. Computer program bisar, layered systems under normal and tangential surface loads. *Koninklijke/Shell Laboratorium, Amsterdam, Shell Research BV*, 1979. (Cited on page 32.)
- [135] Gordon F Hayhoe. *LEAF: A new layered elastic computational program for FAA pavement design and evaluation procedures*. Citeseer, 2002. (Cited on page 32.)
- [136] Jean Maurice Balay and Cécile Caron. Airfiels pavements characteristics design and evaluation: A rational design method for airfield pavements: the french alizé-airfield pavement software. *Europeanroads review RGRA*, (13):pp–4, 2008. (Cited on page 32.)
- [137] Jean-Martin Croteau, S Pianarosa, T HARRISON, C Slawinsky, and L Brissaud. Performance-based asphalt mixture development process to optimize material durability and pavement design. In *Proceedings of the Sixth-Second Annual Conference of the Canadian Technical Asphalt Association (CTAA): Halifax, Nova Scotia*, 2017. (Cited on page 32.)
- [138] Jaeseung Kim. General viscoelastic solutions for multilayered systems subjected to static and moving loads. *Journal of Materials in Civil Engineering*, 23(7):1007–1016, 2011. (Cited on page 32.)
- [139] James W Maina, Yoshiaki Ozawa, and Kunihiro Matsui. Linear elastic analysis of pavement structure under non-circular loading. *Road Materials and Pavement Design*, 13(3):403–421, 2012. (Cited on page 32.)
- [140] Sudhir Varma and M Emin Kutay. Viscoelastic nonlinear multilayered model for asphalt pavements. *Journal of Engineering Mechanics*,

- 142(7):04016044, 2016. (Cited on page 32.)
- [141] Imad L Al-Qadi and Hao Wang. Full-depth pavement responses under various tire configurations: Accelerated pavement testing and finite element modeling. *Journal of the Association of Asphalt Paving Technologists*, 78:721–760, 2009. (Cited on page 32.)
- [142] Zhoujing Ye, Yinghao Miao, Weidong Zhang, and Linbing Wang. Effects of random non-uniform load on asphalt pavement dynamic response. *International Journal of Pavement Research and Technology*, 14(3):299–308, 2021. (Cited on page 33.)
- [143] I Wollny, F Hartung, M Kaliske, P Liu, M Oeser, D Wang, G Canon Falla, S Leischner, and F Wellner. Coupling of microstructural and macrostructural computational approaches for asphalt pavements under rolling tire load. *Computer-Aided Civil and Infrastructure Engineering*, 35(11):1178–1193, 2020. (Cited on pages 34 and 108.)
- [144] Hancheng Dan, Liansheng Gao, Hao Wang, and Jin Tang. Discrete-element modeling of mean texture depth and wearing behavior of asphalt mixture. *Journal of Materials in Civil Engineering*, 34(4):04022027, 2022. (Cited on page 34.)
- [145] Sainan Xie, Junyan Yi, Hengting Wang, Shih-Hsien Yang, Meng Xu, and Decheng Feng. Mechanical response analysis of transverse crack treatment of asphalt pavement based on dem. *International Journal of Pavement Engineering*, 23(7):2206–2226, 2022. (Cited on pages xxx, 34 and 35.)
- [146] Hui Wang, Zhenghui Zhou, Weilin Huang, and Xinyu Dong. Investigation of asphalt mixture permanent deformation based on three-dimensional discrete element method. *Construction and Building Materials*, 272:121808, 2021. (Cited on page 34.)
- [147] Jacob Fish and Kamlun Shek. Multiscale analysis of composite materials and structures. *Composites Science and Technology*, 60(12-13):2547–2556, 2000. (Cited on page 37.)
- [148] Prasanna Raghavan, Suresh Moorthy, Somnath Ghosh, and NJ Pagano. Revisiting the composite laminate problem with an adap-

- tive multi-level computational model. *Composites Science and Technology*, 61(8):1017–1040, 2001. (Cited on page 37.)
- [149] Flavio V Souza and David H Allen. Multiscale modeling of impact on heterogeneous viscoelastic solids containing evolving microcracks. *International Journal for Numerical Methods in Engineering*, 82(4):464–504, 2010. (Cited on page 37.)
- [150] Siavouche Nemat-Nasser and Muneo Hori. *Micromechanics: overall properties of heterogeneous materials*. Elsevier, 2013. (Cited on page 37.)
- [151] IL Al-Qadi, MA Elseifi, PJ Yoo, and I Janajreh. Pavement damage due to conventional and new generation of wide-base super single tires. *Tire Science and Technology*, 33(4):210–226, 2005. (Cited on page 37.)
- [152] IM Gitman, Harm Askes, and LJ Sluys. Representative volume: Existence and size determination. *Engineering fracture mechanics*, 74(16):2518–2534, 2007. (Cited on page 37.)
- [153] Hiroki Yamashita, Guanchu Chen, Yeefeng Ruan, Paramsothy Jayakumar, and Hiroyuki Sugiyama. Hierarchical multiscale modeling of tire–soil interaction for off-road mobility simulation. *Journal of Computational and Nonlinear Dynamics*, 14(6), 2019. (Cited on pages xxxi, 37 and 38.)
- [154] Chun-Lai Zhao and Meng-Yan Zang. Application of the fem/dem and alternately moving road method to the simulation of tire-sand interactions. *Journal of Terramechanics*, 72:27–38, 2017. (Cited on page 37.)
- [155] Mark Michael, Frank Vogel, and Bernhard Peters. Dem–fem coupling simulations of the interactions between a tire tread and granular terrain. *Computer Methods in Applied Mechanics and Engineering*, 289:227–248, 2015. (Cited on pages xxxi, 37 and 39.)
- [156] Jo Sias Daniel and Aaron Lachance. Mechanistic and volumetric properties of asphalt mixtures with recycled asphalt pavement. *Transportation Research Record*, 1929(1):28–36, 2005. (Cited on pages 51 and 96.)
- [157] Y Richard Kim, S Joon Lee, Youngguk Seo, and Omar El-Haggan. A mechanistic approach to determine price reduction factors for density-deficient asphalt pavements. In *Airfield and Highway Pavement: Meet-*



- ing Today's Challenges with Emerging Technologies*, pages 1018–1029, 2006. (Cited on pages [51](#) and [96](#).)
- [158] R. Byron Bird and Pierre J. Carreau. A nonlinear viscoelastic model for polymer solutions and melts—i. *Chemical Engineering Science*, 23(5):427–434, 1968. (Cited on page [51](#).)
- [159] Kenji Yasuda. *Investigation of the analogies between viscometric and linear viscoelastic properties of polystyrene fluids*. PhD thesis, Massachusetts Institute of Technology, 1979. (Cited on page [51](#).)
- [160] Malcolm L Williams, Robert F Landel, and John D Ferry. The temperature dependence of relaxation mechanisms in amorphous polymers and other glass-forming liquids. *Journal of the American Chemical Society*, 77(14):3701–3707, 1955. (Cited on page [53](#).)
- [161] Huailei Cheng, Liping Liu, Lijun Sun, Yi Li, and Yue Hu. Comparative analysis of strain-pulse-based loading frequencies for three types of asphalt pavements via field tests with moving truck axle loading. *Construction and Building Materials*, 247:118519, 2020. (Cited on page [57](#).)
- [162] Yi Xiong. *In-plane Tire Deformation Measurement Using a Multi-Laser Sensor System*. Doctoral thesis, School of Engineering, 2016. (Cited on pages [60](#) and [116](#).)
- [163] IJM Besselink, AJC Schmeitz, and HB Pacejka. An improved magic formula/swift tyre model that can handle inflation pressure changes. *Vehicle System Dynamics*, 48(S1):337–352, 2010. (Cited on page [60](#).)
- [164] Minrui Guo, Xiangwen Li, Maoping Ran, Xinglin Zhou, and Yuan Yan. Analysis of contact stresses and rolling resistance of truck-bus tyres under different working conditions. *Sustainability*, 12(24), 2020. (Cited on page [60](#).)
- [165] SK Ahirwar and JN Mandal. Finite element analysis of flexible pavement with geogrids. *Procedia engineering*, 189:411–416, 2017. (Cited on page [62](#).)
- [166] Sercan Serin, Muhammed Ahmet Oğuzhanoglu, and Cafer Kayadelen. Comparative analysis of stress distributions and displacements in rigid and flexible pavements via finite element method. *Revista de la construcción*, 20(2):321–331, 2021. (Cited on page [62](#).)

- 
- [167] Haitao Ge, Juan Carlos Quezada, Vincent Le Houerou, Cyrille Chazallon, and Pierre Hornych. A new tire-sensor-pavement coupling chain for investigating asphalt mixture responses under rolling tire loads. *Road Materials and Pavement Design*, pages 1–18, 2023. (Cited on page 75.)
- [168] Martin H Sadd, Qingli Dai, Venkitanarayanan Parameswaran, and Arun Shukla. Microstructural simulation of asphalt materials: Modeling and experimental studies. *Journal of materials in civil engineering*, 16(2):107–115, 2004. (Cited on page 78.)
- [169] Peter Wriggers and Giorgio Zavarise. Computational contact mechanics. *Encyclopedia of computational mechanics*, 2004. (Cited on page 79.)
- [170] Peter A Cundall and Otto DL Strack. A discrete numerical model for granular assemblies. *geotechnique*, 29(1):47–65, 1979. (Cited on page 79.)
- [171] Michel Jean. The non-smooth contact dynamics method. *Computer methods in applied mechanics and engineering*, 177(3-4):235–257, 1999. (Cited on page 79.)
- [172] Jean J Moreau. Unilateral contact and dry friction in finite freedom dynamics. In *Nonsmooth mechanics and Applications*, pages 1–82. Springer, 1988. (Cited on page 79.)
- [173] Frédéric Dubois, Vincent Acary, and Michel Jean. The contact dynamics method: A nonsmooth story. *Comptes Rendus Mécanique*, 346(3):247–262, 2018. (Cited on page 79.)
- [174] Farhang Radjai and Vincent Richefeu. Contact dynamics as a nonsmooth discrete element method. *Mechanics of Materials*, 41(6):715–728, 2009. (Cited on page 81.)
- [175] Peter A Cundall. Formulation of a three-dimensional distinct element model—part i. a scheme to detect and represent contacts in a system composed of many polyhedral blocks. In *International Journal of Rock Mechanics and Mining Sciences & Geomechanics Abstracts*, volume 25, pages 107–116. Elsevier, 1988. (Cited on page 81.)
- [176] Erfan G Nezami, Youssef MA Hashash, Dawei Zhao, and Jamshid Ghaboussi. A fast contact detection algorithm for 3-d discrete element

- method. *Computers and Geotechnics*, 31(7):575–587, 2004. (Cited on page 81.)
- [177] Erfan G. Nezami, Youssef MA Hashash, Dawei Zhao, and Jamshid Ghaboussi. Shortest link method for contact detection in discrete element method. *International Journal for Numerical and Analytical Methods in Geomechanics*, 30(8):783–801, 2006. (Cited on page 81.)
- [178] Taleb Al-Rousan, Eyad Masad, Erol Tutumluer, and Tongyan Pan. Evaluation of image analysis techniques for quantifying aggregate shape characteristics. *Construction and Building Materials*, 21(5):978–990, 2007. (Cited on page 82.)
- [179] Tongyan Pan, Erol Tutumluer, and Samuel H Carpenter. Effect of coarse aggregate morphology on the resilient modulus of hot-mix asphalt. *Transportation Research Record*, 1929(1):1–9, 2005. (Cited on page 82.)
- [180] Erol Tutumluer and Tongyan Pan. Aggregate morphology affecting strength and permanent deformation behavior of unbound aggregate materials. *Journal of materials in civil engineering*, 20(9):617–627, 2008. (Cited on page 82.)
- [181] Iuri S Bessa, Verônica TF Castelo Branco, Jorge B Soares, and José A Nogueira Neto. Aggregate shape properties and their influence on the behavior of hot-mix asphalt. *Journal of Materials in Civil Engineering*, 27(7):04014212, 2015. (Cited on page 82.)
- [182] Yao Zhang, Tao Ma, Xiaoming Huang, Yongli Zhao, and Pengsen Hu. Algorithms for generating air-void structures of idealized asphalt mixture based on three-dimensional discrete-element method. *Journal of Transportation Engineering, Part B: Pavements*, 144(2):04018023, 2018. (Cited on page 82.)
- [183] Wenli Jia, Valeri Markine, Yunlong Guo, and Guoqing Jing. Experimental and numerical investigations on the shear behaviour of recycled railway ballast. *Construction and Building Materials*, 217:310–320, 2019. (Cited on page 82.)
- [184] Yifei Sun, Buddhima Indraratna, and S Nimbalkar. Three-dimensional characterisation of particle size and shape for ballast. *Géotechnique*

- Letters*, 4(3):197–202, 2014. (Cited on page 83.)
- [185] Haitao Ge, Aimin Sha, Zhenqiang Han, and Xiaowei Xiong. Three-dimensional characterization of morphology and abrasion decay laws for coarse aggregates. *Construction and Building Materials*, 188:58–67, 2018. (Cited on page 83.)
- [186] NF P 18-545:2011. Granulats – Éléments de définition, conformité et codification (in french)., 2011. (Cited on page 83.)
- [187] Hakon Wadell. Volume, shape, and roundness of quartz particles. *The Journal of Geology*, 43(3):250–280, 1935. (Cited on page 83.)
- [188] Laura Gaillard, Juan Carlos Quezada, Cyrille Chazallon, and Pierre Hornych. Resilient modulus prediction of rap using the contact dynamics method. *Transportation Geotechnics*, 24:100371, 2020. (Cited on pages 86 and 88.)
- [189] Romain Quey, PR Dawson, and Fabrice Barbe. Large-scale 3d random polycrystals for the finite element method: Generation, meshing and remeshing. *Computer Methods in Applied Mechanics and Engineering*, 200(17-20):1729–1745, 2011. (Cited on page 86.)
- [190] Romain Quey and Loïc Renversade. Optimal polyhedral description of 3d polycrystals: method and application to statistical and synchrotron x-ray diffraction data. *Computer Methods in Applied Mechanics and Engineering*, 330:308–333, 2018. (Cited on page 86.)
- [191] Haitao Ge, Juan Carlos Quezada, Vincent Le Houerou, and Cyrille Chazallon. Three-dimensional simulation of asphalt mixture incorporating aggregate size and morphology distribution based on contact dynamics method. *Construction and Building Materials*, 302:124124, 2021. (Cited on pages 105 and 113.)
- [192] Hiroki Yamashita. *Flexible multibody dynamics approach for tire dynamics simulation*. PhD thesis, University of Iowa, 2016. (Cited on page 109.)
- [193] Edem Yawo Manyo, Philippe Reynaud, Benoit Picoux, Remi Tautou, Daniel Nelias, Fatima Allou, and Christophe Petit. Towards fast modelling of the tire-pavement contact. *European Journal of Environmental and Civil Engineering*, pages 1–17, 2019. (Cited on page 110.)

- 
- [194] K. L. Johnson. *Contact Mechanics*. Cambridge University Press, 1985. (Cited on pages [xxxiii](#) and [112](#).)
- [195] Hans Pacejka. *Tire and vehicle dynamics, 2nd ed.* Butterworth-Heinemann, Oxford, UK, 2006, 2005. (Cited on page [115](#).)
- [196] Zejiao Dong and Xianyong Ma. Analytical solutions of asphalt pavement responses under moving loads with arbitrary non-uniform tire contact pressure and irregular tire imprint. *Road Materials and Pavement Design*, 19(8):1887–1903, 2018. (Cited on page [122](#).)
- [197] Haitao Ge, Juan Carlos Quezada, Vincent Le Houerou, and Cyrille Chazallon. Multiscale analysis of tire and asphalt pavement interaction via coupling fem–dem simulation. *Engineering Structures*, 256:113925, 2022. (Cited on page [129](#).)
- [198] Haitao Ge, Juan Carlos Quezada, Vincent Le Houerou, and Cyrille Chazallon. Three-dimensional fem–dem coupling simulation for analysis of asphalt mixture responses under rolling tire loads. *Construction and Building Materials*, 369:130615, 2023. (Cited on page [154](#).)

# Étude multi-échelle de l'interaction pneu-chaussée dans des conditions de roulement basée sur le couplage de la méthode des éléments finis et de la méthode des éléments discrets

## Multi-scale study of tire- pavement interaction under rolling conditions based on the coupling of Finite element method and Discrete element method

### Résumé

Alors que le trafic augmente à pas de géant, la détérioration des couches de surface en asphalte apparaît comme la première cause des coûts d'entretien du réseau routier. Une compréhension approfondie de l'interaction pneu-chaussée est essentielle pour optimiser la conception de la couche de surface des chaussées bitumineuses dans le contexte d'infrastructures vieillissantes et de ressources d'entretien limitées. Pour faire face aux difficultés découlant de la complexité et de l'inadéquation des méthodes d'essai expérimentales dans l'étude du système d'interaction pneu-chaussée, les approches numériques telles que la méthode des éléments finis (FEM) et la méthode des éléments discrets (DEM) sont apparues comme un moyen prometteur et efficace de mieux comprendre les performances des enrobés bitumineux au cours des dernières décennies. La plupart des études actuelles sur l'interaction entre le pneu et la chaussée ont été menées dans le cadre de la mécanique des milieux continus à l'aide de la méthode des éléments finis, qui présente des limites dans la modélisation de la nature discontinue des mélanges bitumineux. La DEM offre un moyen prometteur d'examiner les propriétés mécaniques des mélanges bitumineux à l'échelle des particules, mais elle est inadéquate pour modéliser la structure déformable des pneus et estimer les forces de contact réalistes des pneus sur la surface de la chaussée. Cette thèse est consacrée à l'étude du système d'interaction entre le pneu et la chaussée sur la base de simulations numériques. Deux méthodes numériques principales, FEM et DEM, sont utilisées pour modéliser ce système à plusieurs échelles, de manière différente. Pour l'examen des réponses de la couche de béton bitumineux sous des charges de roulement réalistes (pneus) à un niveau macroscopique, une nouvelle chaîne de couplage pneu-capteur-chaussée basée sur la FEM a été proposée pour intégrer la distribution réaliste de la contrainte de contact du pneu dans la modélisation mécanique de la couche bitumineuse. Les distributions de contraintes de contact du pneu lors de différentes conditions de chargement, incluant les charges et les pressions de gonflage du pneu, ont été obtenues en utilisant le système de mesure du capteur Tekscan. Le comportement des matériaux bitumineux en fonction de la température et de la fréquence a été décrit par le modèle VEnoL (NONLinear ViscoElastic). La

fiabilité du modèle a été validée à la fois numériquement et expérimentalement par des essais de module complexe. Enfin, les effets de diverses températures de chaussée, vitesses de roulement des pneus, charges des pneus et pressions de gonflage des pneus sur les réponses de la couche de béton bitumineux ont été étudiés. Les résultats indiquent que les réponses de la couche bitumineuse est considérablement influencée par les conditions de chargement des pneus. Pour la modélisation du mélange bitumineux à partir d'une échelle microscopique, la méthode DEM a été adoptée. Sur la base de l'acquisition des formes tridimensionnelles (3D) des agrégats par balayage laser, les caractéristiques morphologiques d'un grand nombre de particules ont été analysées statistiquement par la technologie de traitement des images. Des échantillons numériques de mélange d'asphalte ont été générés par des tessellations de Voronoï combinant la distribution de la taille des particules et les statistiques de morphologie. La fiabilité du modèle a été validée par la réalisation d'expériences et de simulations DEM basées sur la méthode de la dynamique de contact (CD) pour l'essai du module complexe. Grâce à cette procédure, la morphologie et la distribution de la taille des agrégats ont pu être incorporées dans les simulations numériques des mélanges bitumineux. En outre, la méthode proposée permet d'apprendre le possible micromécanisme d'initiation des dommages du mélange à l'échelle des particules. Pour faire face aux difficultés des mesures expérimentales des capteurs à mesurer les contraintes de contact tangentielles du pneu sur la surface de la chaussée, la FEM a été utilisée pour modéliser le pneu et déterminer les contraintes de contact résultantes entre le pneu et la chaussée. La méthode CD a été introduite pour imposer la condition de contact entre le pneu et la surface de la chaussée en raison de ses performances dans la simulation de systèmes de corps rigides ayant des lois de contact non linéaires. La géométrie du pneu a été reconstruite par balayage laser et par des techniques de traitement d'images. La structure du pneu a été construite par FEM et les paramètres pertinents ont été identifiés par un test de compression. Les distributions des contraintes de contact en cas de roulement libre et de freinage complet révèlent que le pneu induit des contraintes de contact dans trois directions (verticale, transversale, longitudinale) et qu'elles ne sont pas uniformes dans la zone de contact. La contrainte de contact tangentielle sur la surface de la chaussée en cas de freinage complet est beaucoup plus élevée que celle en cas de roulement libre, ce qui prouve la nécessité de considérer les contraintes de contact tangentielles du pneu comme des conditions limites dans l'examen des réponses du mélange bitumineux. Enfin, des simulations de couplage FEM-DEM ont été présentées pour étudier les réponses du mélange d'asphalte à l'échelle des particules, ce qui répond à l'objectif d'investigations multi-échelles des mécanismes d'interaction pneu-chaussée. La méthode de couplage incorpore les avantages que possède la FEM pour simuler les contraintes de contact du pneu avec précision sur la surface de la chaussée bitumineuse et la DEM pour estimer les réponses internes du mélange bitumineux à l'échelle des particules. En mettant en œuvre un modèle DEM d'un béton bitumineux avec des conditions réalistes de charge de roulement des pneus (à partir d'un modèle FEM), cette stratégie de couplage permet d'étudier l'évolution du réseau de chaînes de force des particules, les distributions des déplacements et des vitesses des particules, les mouvements des particules individuelles et les caractéristiques des forces de contact entre les particules à l'intérieur du béton bitumineux. La présente étude fournit une méthode de simulation multi-échelles incorporant la FEM et la DEM pour analyser les mécanismes d'interaction pneu-chaussée sous des charges de roulement réalistes, ce qui offre une voie prometteuse pour comprendre la détérioration de la surface de la chaussée et optimiser la conception de cette dernière.

**Mots-clés: interaction entre le pneu et la chaussée ; méthode de la dynamique des contacts ; approche multi-échelles ; modélisation par éléments finis ; modélisation par éléments discrets ; charge non uniforme du pneu ; réponses du mélange d'asphalte**

## Abstract

As traffic grows by leaps and bounds, deterioration of asphalt surface layers emerges as the primary cause of road network costs. A deep understanding of the tire-pavement interaction is essential for optimizing the surface design of asphalt pavements in the context of aging infrastructure and limited maintenance resources. To cope the difficulties rising from the complexity and inadequacy of experimental test methods in examining the tire-pavement interaction system, numerical approaches such as the Finite Element Method (FEM) and the Discrete Element Method (DEM) have emerged as a promising and effective way of gaining insight into asphalt mixture performance in recent decades. Most of the current tire-pavement interaction studies have been conducted in the continuum mechanics framework using FEM, which shows limitations in modeling the discontinuity nature of asphalt mixtures. DEM offers a promising way to examine the mechanical properties of asphalt mixtures at the particle level, but it is inadequate for modeling deformable tire structure and capturing realistic tire contact forces on the pavement surface. This thesis is dedicated to the investigation of the tire-pavement interaction system based on numerical simulations. Two main numerical methods, FEM and DEM, are used to model this system from multi-scales, differently. For the examination of asphalt layer responses under realistic tire rolling loads from a macroscopic level, a novel tire-sensor-pavement coupling chain based on FEM was proposed for integrating the realistic distribution of tire contact stress into the mechanical modeling of the asphalt layer. The tire contact stress distributions under different tire loading conditions including tire loads and tire inflation pressures were obtained by using the Tekscan sensor measuring system. The temperature- and frequency-dependent material behavior of asphalt mixes was described through the VENoL (NONLinear ViscoElastic) model. The model reliability was validated both numerically and experimentally via complex modulus tests. Finally, various pavement temperatures, tire driving speeds, tire loads, and tire inflation pressures were investigated for their effect on asphalt layer responses. The results indicate that asphalt layer responses are influenced considerably by tire loading conditions. For the modeling of asphalt mixture from a microscopic scale, DEM was adopted. Based on the acquisition of three-dimensional (3D) aggregate shapes using laser scanning, the morphological characteristics for a large number of particles were analyzed statistically by image processing technology. Numerical asphalt mixture samples were generated by Voronoi tessellations combining the particle size distribution and morphology statistics. The model reliability has been validated by conducting experiments and DEM simulations based on the Contact Dynamics (CD) method for the complex modulus test. Using this procedure, the aggregate morphology and size distribution could be incorporated in numerical simulations of asphalt mixtures. Furthermore, the possible micro-mechanism of mixture damage initiation might be revealed at the particle-scale by using the proposed method. To cope the difficulties of experimental sensor measurements in capturing tangential tire contact stresses on the pavement surface, FEM was utilized to model the tire and capture the resulting tire-pavement contact stresses. The CD method was introduced to enforce the contact condition between the tire and the pavement surface because of its performance in non-linear system simulation. The tire geometry was reconstructed via laser scanning and image processing techniques. The tire structure was built by FEM according to its function and the relevant parameters were identified with a compression test. The contact stress distributions under free-rolling and full-braking reveal that the tire induces contact stresses in three directions (vertical, transverse, longitudinal) that are not uniform across the contact area. The tangential contact stress on the pavement surface under full-braking is much higher than that under free-rolling, which proves the necessity of considering tangential tire contact stresses as boundary conditions in examining asphalt mixture responses. Finally, FEM-DEM coupling simulations were presented to investigate asphalt mixture responses at the particle level, which fulfills the goal of multi-scale investigations of tire-pavement interaction mechanisms. The coupling method incorporates the advantages that FEM can simulate tire contact stresses precisely on the asphalt pavement surface and DEM is capable of examining internal responses of the asphalt mixture at the particle scale. By implementing a DEM model of asphalt mixtures with realistic rolling tire load conditions (from a FEM model), this coupling strategy allows the investigation of particle force chain network evolution, particle displacement and velocity distributions, movements of individual particles, and particle contact force characteristics inside an asphalt mixture. The present study provides a multi-scale simulation method incorporating FEM with DEM together to analyze tire-pavement interaction mechanisms under realistic rolling tire loads, which offers a promising way of understanding pavement surface deterioration and optimizing pavement surface design.

**Keywords:** tire-pavement interaction; contact dynamics method; multiscale approach; finite element modeling; discrete element modeling; non-uniform tire load; asphalt mixture responses



